



## Investigating the Chemical and Thermal Based Treatment Procedures on the Clinoptilolite to Improve the Physicochemical Properties

Ezgi Bayrakdar Ates<sup>1\*</sup> 

<sup>1</sup>Yalova University, Energy Systems Engineering Department, Yalova, 77100, Turkey.

**Abstract:** Natural clinoptilolites have been preferred as promising catalysts and adsorption materials due to their low cost and important properties. However, they struggle with their cationic phases and impurities, weakening the physicochemical structure. The main approach is to improve the features of clinoptilolites by applying treatments such as acid modification and calcination. Here in clinoptilolites in two different particle sizes were pre-treated with acid, then, calcined at two different temperatures (300 and 500 °C) with different durations (2 and 3 h). The effects of pre-treatment were investigated with X-ray diffraction (XRD), X-ray fluorescence (XRF), Fourier transform infrared (FTIR), Thermogravimetry (TG-DTG), Differential Thermal Analysis (DTA), N<sub>2</sub> adsorption with Brunauer-Emmett-Teller (BET), Scanning Electron Microscopy (SEM) coupled with Energy Dispersion Spectroscopy (EDS) analyses. XRF analysis shows that cations and aluminum were removed due to pre-treatments and that the clinoptilolite, with a smaller particle size, had a higher Si/Al ratio. All clinoptilolites showed good thermal stability up to temperatures 600–800 °C with continuous mass-loss curves. It was determined that surface area and total pore volume increased in most of the samples without agglomeration by SEM-EDS and BET. The surface functional groups were investigated by FTIR and intensities of some bands showed a decrease due to decationization.

**Keywords:** Clinoptilolite, acid treatment, calcination, natural zeolite, heat treatment.

**Submitted:** March 29, 2022. **Accepted:** June 13, 2022.

**Cite this:** Bayrakdar Ates E. Investigating the Chemical and Thermal Based Treatment Procedures on the Clinoptilolite to Improve the Physicochemical Properties. JOTCSB. 2022;5(2):39–58.

\*Corresponding author. E-mail: [ezgi.bayrakdar@yalova.edu.tr](mailto:ezgi.bayrakdar@yalova.edu.tr).

### INTRODUCTION

Zeolites consist of various minerals and have great scientific and industrial applications in different areas. The larger surface area of zeolites due to porosity and their high thermal strength make them frequently preferred materials for different applications, especially adsorbents, catalysts (1-3), the water purification (4-6), microelectronics, optics, medicine, and agriculture. The most important features that make it a material that can be used in many different areas are listed as high adsorption ability, molecular sieve capacity, high selectivity, ion exchange capacity, strong resistance to acidic substances, and high thermal resistance (7). Zeolites are called hydrated aluminosilicates containing silicon and aluminum atoms bonded to each other with oxygen atoms, arranged in crystal structure and tetrahedral units, with a three-dimensional structure, which is generally characterized as natural or synthetic zeolite, with channels and spaces formed due to the microporous surface structure (1,7-12). The most important feature that distinguishes zeolite from other crystal structures and aluminosilicate-based materials is the presence of structural voids connected to each other by channels. The structure and size of these voids and channels are different for each zeolite and are considered characteristic features (4,10,13). Each aluminum atom causes one negative charge in the

zeolite structure which is generally balanced with an exchangeable cation (Ca<sup>2+</sup>, Mg<sup>2+</sup>, Na<sup>+</sup>, K<sup>+</sup>, etc). Considering the significant behaviors of the exchangeable cations, they affect the adsorption and thermal characteristics of the zeolites (9). The ion exchange characteristics of zeolite are sourced from exchangeable cations and provide the advantage of using it in many fields (2).

When the literature is examined, it is seen that zeolites, whose aluminum content has been diluted by dealumination, provide important advantages, especially in terms of catalysis. Despite its impurities, it has been determined that these zeolite-based catalysts, which have strict thermal stability, have high selectivity for different catalytic reactions, thanks to the alternatives brought by their chemical content and molecular structure. Compared to metal oxide catalysts, they exhibit higher activity, on the other hand, they are more stable than noble metal-based catalysts. Mesopores in natural zeolite structures provide an advantage in the diffusion of reactants into micropores where active centers occur (10,14-17). Similarly, Król and Jeleń (7) also stated that the inner surface area of the zeolites is large and has more than one active site. This feature of zeolites is especially important in catalytic applications both as a stand-alone catalyst and as catalyst support. Zeolites are usually dealuminated and removal of

cations from the framework by acid (HCl, HNO<sub>3</sub>, H<sub>2</sub>SO<sub>4</sub>, and CH<sub>3</sub>COOH) (2-4,9,18-23), steaming (3,10,24) and calcination (3,10,23,25-26). Utilization of an acidic mixture, which consists of phosphoric acid and citric acid, has already been carried out as an alternative (27). The main goal of acid pre-treatment is to remove the aluminum from the zeolite to create more pores in the structure (4,28). When the studies in the literature are examined, it may not be a very simple procedure to improve the properties of zeolite by treating it with acid. Because the types of zeolites can be so diverse, there may be some cases where the application and effect of each pretreatment are not the same for all species (4,19). Simple inorganic salts and alkalis are also used for the pretreatment process, allowing the cations to move away from the structure and increase the nSi/nAl ratio (10).

When both adsorption and catalytic properties of zeolites were examined, it was stated that these properties were not only affected by the type of out-of-frame cations (29) but were also significantly affected by the amount of water in the structure (7,25). When the literature studies are examined, problems are experienced during the use of natural zeolites due to high water demands (25,30-33). Therefore, the application of the calcination process (10,22,25,33-35), as preferred in this study, is of great importance. The high surface area of zeolites due to the porosity originating from micro and mesopores results in an increase in the water demand characteristics. Seraj et al. (25) stated that the high surface area feature of natural zeolites is often due to internal porosity. They explained the high water demand of natural zeolites by accepting that the water was adsorbed into the internal pores (34,36). Seraj et al. (25) stated that if the structure of the pores is changed in a way that prevents water adsorption, there will be a decrease in water demand. For this, they proposed calcination as a thermal pretreatment in the zeolite structure and examined its effect on the structure. It was emphasized that not only the decrease in water demand in the structure after calcination but also a significant improvement in the workability of the material will occur due to this decreasing demand. It has been stated that the calcination process will also be effective in removing the clay impurities that may increase the water demand by absorbing the water in the structure (37). However, Seraj et al. (25), Wang et al. (22) and Ates and Hardcre (3) reported that agglomeration occurred in the structure at high temperatures such as 600, 650, 700, 750, and 800 °C. Perraki et al. (26) explained that the thermal behavior of the zeolite when applied to a heat treatment such as calcination also depends on the amount of Al in its structure. They stated that since clinoptilolite is a zeolite with a Si/Al ratio greater than 4, its thermal resistance is high at temperatures above 450 °C. Considering these different studies, performing calcination and acid pretreatment together is very important in terms of improving the physicochemical properties of the zeolite. Considering these different studies, it is very important to carry out calcination and acid pretreatment together, as the author applied in her study, in terms of improving the physicochemical properties of the zeolite.

Clinoptilolite is one of the most common types of zeolites encountered in nature and is frequently used in different fields (8,12,35,38,39). Clinoptilolite is in the heulandite group and has the highest thermal resistance among the zeolites in this group. When the clinoptilolite structure is examined, it is seen that it consists of two types of channels

connected with eight-membered rings (9,38,40-43). Clinoptilolite has a significant cation exchange capacity due to the presence of extra framework cations in its structure (41,42,44,45).

Clinoptilolite generally includes impurities that could differ due to the region of the reserve and these impurities strict its utilization. In the literature, several treatment methods were improved and applied to remove these impurities and enhance the chemical and physical properties of different zeolite types. Clinoptilolites are widely used for catalytic and adsorption purposes as important structural properties such as surface area, total pore volume, pore diameter, chemical structure, water content, and porosity change as a result of pretreatment (8,9,46,47). The low cost of clinoptilolites has also been an important reason for their use for adsorption (9,48), environmental applications (48-50), and catalysts (43). With the removal of cations from the structure of clinoptilolites, which are pre-treated with acid, the voids formed in the structure increase the specific area and surface, and new acidic regions appear. While this situation changes the adsorption characteristics of the zeolite, on the other hand, if it is to be used as a catalyst instead of an adsorbent, the increased surface area causes an increase in both the catalytic activity and the selectivity of the products (41,52).

In this study, the effect of different calcination temperatures (300 and 500 °C) on two different clinoptilolite samples (with different particle sizes), as well as varying durations of calcination (2 and 3 h), were investigated after pretreatment with hydrochloric acid. Burris and Juenger (34) stated that the literature focused on examining the effect of calcination on zeolites used in cementitious mixtures compared to clinoptilolite. Therefore, this study is important not only in terms of the effects of pretreatment of clinoptilolite with calcination in the literature but also in terms of comparing the effects of different calcination temperatures and durations on clinoptilolite samples with different particle sizes. With the characterization tests, it is possible to compare the samples calcined at the same temperature and time, pre-treated at the same acid concentration, in terms of different particle sizes at the beginning, on the other hand, the effect of the changing pretreatment conditions on the physicochemical properties in the same sample was investigated. At the same time, considering the contribution of the acid and pre-treatment applied before the calcination process together with the calcination, as stated before, to the structure, it is seen that it has an important contribution to the improvement of the properties of the structure, especially by removing impurities. Although it is stated in the literature that calcination may cause surface agglomeration and sintering problems, especially if the calcination temperatures are selected high, it is clearly seen that the preferred temperatures in this study do not cause agglomeration in the structure, as supported by SEM analysis. In this case, it has been determined that the pretreatment with HCl applied before calcination is also important. When the obtained characterization results were examined, possible changes in the structure (change in cation concentration, dealumination, change in peak densities, etc.), especially after acidic pretreatment, were in line with the literature. In addition, as stated in the article, not using a high concentration of the acidic solution and sufficient contact time did not damage the crystalline structure, morphological features, and other characteristic features related to the structure. Burris and Juenger (34)

stated that the calcination temperature values recommended by the researchers vary according to the zeolite type and the optimum calcination detection scale, in other words, there is no single truth in this regard. From this point of view, it is thought that this study on clinoptilolite, in which fewer calcination effects are investigated, will make significant contributions to the literature. In addition, not many studies have been found in which the effect of calcination time has been examined together with the parameter of being a natural clinoptilolite obtained from the same region but having different particle sizes.

## MATERIALS AND METHODS

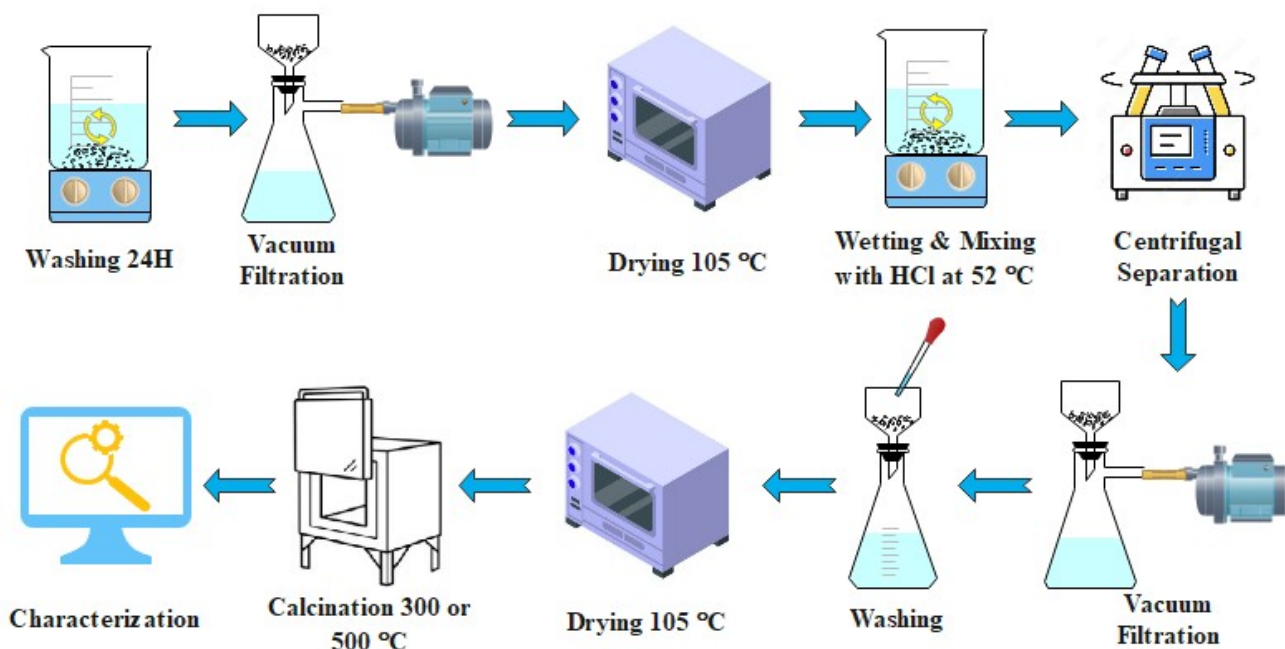
### Raw Materials and Reagents

Natural clinoptilolite samples from Gordes were used, supplied by Gordes Zeolite Mining Corporation. These clinoptilolite samples particle size are 50  $\mu$  (Clinoptilolite-A) and 150  $\mu$  (Clinoptilolite-B), respectively. The mineral acid,

HCl ( $\geq 37\%$ ), was supplied by Merck (Darmstadt, Germany) and all solutions were prepared by using deionized water.

### Pre-treatment Procedure for Natural Clinoptilolite

The procedure of the pre-treatment of natural clinoptilolites is shown in Figure 1. A required amount of the clinoptilolite was put into deionized water and stirred for 24 h using a magnetic stirrer in a three-neck round-bottomed flask at 30 °C. In the pre-treatment method, after the pre-mixing period, the clinoptilolite sample was filtered under vacuum and dried in a furnace at 105 °C for 2-3 hours. The HCl solution concentrations were fixed at 0.3 M and, these dried natural zeolite samples were wetted and stirred with HCl solution at 52 °C for 1 hour. According to preliminary experiments, the HCl solution amount was fixed at the optimum ratio of HCl solution/Clinoptilolite (v/w) 10:1. The acid-pre-treated sample was separated by centrifugation, then washed by using excess deionized water until the pH is 7 and then dried at 105 °C in a furnace for 2-3 h. The samples obtained were calcinated at 300 and 500 °C for both 2 and 3 h.



**Figure 1:** Procedure of the pre-treatment of natural clinoptilolites.

The pre-treated clinoptilolite samples belonging to (Clinoptilolite-A) were denoted as Clinoptilolite-A<sub>1</sub>, Clinoptilolite-A<sub>2</sub>, Clinoptilolite-A<sub>3</sub> and Clinoptilolite-A<sub>4</sub>, according to their corresponding 300°C for 2 h, 300°C for 3 h, 500°C for 2 h and 500°C for 3 h calcinations, respectively. In the same way, other pre-treated natural zeolite samples prepared from (Clinoptilolite-B) were named as Clinoptilolite-B<sub>1</sub>, Clinoptilolite-B<sub>2</sub>, Clinoptilolite-B<sub>3</sub> and Clinoptilolite-B<sub>4</sub>, calcined at 300°C for 2 h, 300°C for 3 h, 500°C for 2 h and 500°C for 3 h, respectively.

### Characterization

The chemical compositions of the natural clinoptilolite samples were determined on powdered samples with X-ray fluorescence (XRF, Spectro Xepos II).

X-ray powder diffraction (XRD) patterns of zeolites were recorded on a Panalytical Empyrean diffractometer using

nonmonochromotografic Cu K $\alpha$ 1-radiation (45 kV, 40 mA,  $k = 1.5 \text{ \AA}$ ). The scanning range was 4–90°(2 $\theta$ ) and with an incremental step size of 0.02° 2 $\theta$  and 2 s dwell time. Thermal behaviors were investigated using a Seiko, TG/DTA 6300 instrument (range: 25-900°C) under flowing nitrogen (150 mL min<sup>-1</sup>) at a heating rate of 10 °C min<sup>-1</sup> using approximately 5-5.5 mg of clinoptilolite samples in alumina crucibles. Physisorption isotherms were determined by the adsorption of N<sub>2</sub> at 77 K in a QANTACHROME AUTOSORB IQ2. High purity (99.99%) nitrogen was used in the adsorption measurements. The clinoptilolite samples were previously heated at a temperature of 160 °C under vacuum for 12 h to remove the volatile compounds in the structures, to provide more gas adsorption to the surfaces, and determine the surface area and pore size distributions more accurately. The pore size distributions and specific surface area of samples were calculated by the Barrett–Joyner–Halenda (BJH) and BET

methods, respectively. Infrared absorption measurements of the clinoptilolite samples were obtained using a Fourier transform infrared (FTIR) spectrometer (PERKIN ELMER-SPECTRUM 100). The FTIR spectra were recorded in the wavenumber range of 400–4000  $\text{cm}^{-1}$  at a resolution of 4  $\text{cm}^{-1}$  with the use of ATR technique. The morphological structures and elemental distributions were investigated by using scanning electron microscopy (SEM) with a JEOL Brand JSM 6610 model used with a system for elemental composition and elemental mapping analysis based on energy-assisted X-ray spectroscopy (EDS) system (Oxford Instruments Brand, Inca X-act model). Before the beginning of the SEM analysis, to provide the conductivity of all-natural and treated clinoptilolites, the surface of the samples (Quorum brand, SC-7620 model) was coated with argon gas environment for nearly 150 seconds with 99% purity gold (Au) at an approximate thickness of 200 angstroms. Images of the sample surfaces were recorded for different magnifications at an accelerating voltage of 15 kV in a vacuum, spot size of 30, and a working distance of approximately 12 mm. Elemental analysis was carried out for different points randomly determined on the clinoptilolite surfaces and the average of those found was shown.

## RESULTS AND DISCUSSION

### Elemental Composition (XRF Analysis)

The XRF analyses of the natural (Clinoptilolite-A and Clinoptilolite-B) and that of pre-treated (Clinoptilolite-A<sub>1</sub>, Clinoptilolite-A<sub>2</sub>, Clinoptilolite-A<sub>3</sub>, Clinoptilolite-A<sub>4</sub>, Clinoptilolite-B<sub>1</sub>, Clinoptilolite-B<sub>2</sub>, Clinoptilolite-B<sub>3</sub> and Clinoptilolite-B<sub>4</sub>) samples of clinoptilolites are presented in Table 1. The elements located at smaller concentrations compared to Al and Si were determined and recorded in oxide form. The XRF element analysis resulted in a significant amount of silicon (Si) in all of the samples (Table 1). It was found that SiO<sub>2</sub> concentrations showed a significant increase following the acid and calcination treatments. Both acid and calcination treatments did not cause any critical destruction of the crystal lattice in comparison with the natural clinoptilolites. The natural clinoptilolite samples (Clinoptilolite-A and Clinoptilolite-B) were quantified by the high amounts of potassium and calcium while magnesium, sodium, and phosphorus amounts are low. Additionally, iron is determined as iron oxides. According to Table 1, treatment of both acid-treated-clinoptilolites with increasing calcination temperature and calcination period resulted from the subtraction of cations (Ca<sup>2+</sup>, Mg<sup>2+</sup>, and K<sup>+</sup>) from the samples. Although the findings on cation concentrations are correlated to literature (2,3,9,10,43,48,53,54), two different types of zeolites and their pretreated samples showed different behaviors in dealumination. With increasing calcination temperature and duration, aluminum oxide concentration had a decreasing trend for Clinoptilolite-A and pre-treated samples except for Clinoptilolite-A<sub>1</sub>. Radosavljević-Mihajlović et al. (53) emphasized that a movement to framework could happen and dealumination takes place when the acid solution concentration is above 0.1 M (0.3 M acid solution used in this study) at treatment. Conversely, Clinoptilolite-A samples, small increases in aluminum oxide concentrations were observed for the four of the treated Clinoptilolite-B samples. This decreasing trend (for Clinoptilolite-A and its treated versions) and the increasing trend (for Clinoptilolite-B and its treated versions) showed a slightly reverse trend with the increase in time at the same calcination temperatures. Elaiopoulos et al. (10)

explained the unexpected dealumination problems as the existence of huge (hydrated) and effectively involved in ion-exchangeable cations at K3 (in the center of distorted 8-member rings) might prevent Al<sup>3+</sup> motion. Further dealumination could not be performed due to the other factor being the exposure of the acid-treated zeolite samples to high temperatures. While this high-temperature value was 700 °C in their study, the dealumination of all Clinoptilolite-B samples treated at both 300 and 500 °C in this study was below the expectation mentioned before. Additionally, Davarpanah et al., (41) and Sato et al. (55) explained that negligible change in Al content is correlated to dealumination coming true in the exchange (55). Miądlicki et al. (43) also indicated that an effective increase in dealumination could be determined with alkali pH values of the treatment solution. In higher acidic pH values such as above 0.1 M, dealumination could slightly occur as in our study.

### X-Ray Diffraction (XRD) Analysis

The XRD patterns of the natural and acid-treated resultant products (Clinoptilolite-A, Clinoptilolite-A<sub>1</sub>, Clinoptilolite-A<sub>2</sub>, Clinoptilolite-A<sub>3</sub>, Clinoptilolite-A<sub>4</sub>) exposed with a varying calcination temperature and time for thermal treatment are given in Figure 2, and other samples (Clinoptilolite-B, Clinoptilolite-B<sub>1</sub>, Clinoptilolite-B<sub>2</sub>, Clinoptilolite-B<sub>3</sub>, Clinoptilolite-B<sub>4</sub>) prepared with the same treatment procedure and conditions are given in Figure 3. The natural clinoptilolite XRD spectrum was correlated to the literature. The XRD graphics had typical peaks of clinoptilolite, according to JCPDS card 25–1349, for natural and acid-treated clinoptilolites ( $2\theta = 9.85^\circ, 11.19^\circ, 13.09^\circ, 16.92^\circ, 17.31^\circ, 19.09^\circ, 20.42^\circ, 22.48^\circ, 22.75^\circ, 25.06^\circ, 26.05^\circ, 28.02^\circ, 28.58^\circ, 29.07^\circ, 30.12^\circ, 31.97^\circ, 32.77^\circ$ ). The other four peaks ( $2\theta = 20.86^\circ, 26.6^\circ, 36.55^\circ, 39.45^\circ$ ) according to JCPDS card 85–0930 belonged to quartz, which is an impurity phase in natural clinoptilolite.

There are changes in XRD peak sharpness and intensity in all treated types of Clinoptilolite-A and all B-type clinoptilolites. It was clear that XRD patterns of the acid and temperature treated clinoptilolites clearly show differences in regard to both natural clinoptilolites. These differences, such as the sharpening of some peaks, enhanced due to higher calcination temperatures and time for especially Clinoptilolite-B and its treated ones in Figure 3. Compared to Clinoptilolite-A<sub>3</sub> and Clinoptilolite-A<sub>4</sub> samples, the intensity of the peaks of Clinoptilolite-A<sub>1</sub> and Clinoptilolite-A<sub>2</sub> samples (calcination temperature: 300 °C) are so near to Clinoptilolite-A. It was determined that intensities of clinoptilolite peaks show a decline with increasing calcination temperature for Clinoptilolite-A<sub>3</sub>, Clinoptilolite-A<sub>4</sub>, Clinoptilolite-B<sub>3</sub>, and Clinoptilolite-B<sub>4</sub>. The change in calcination time did not cause a great change in the clinoptilolite structure, at the same calcination temperatures for all treated clinoptilolites. However, it resulted from both XRD patterns that higher calcination temperature (500 °C) and longer calcination time at this temperature affect the crystal structures of all treated clinoptilolite samples compared to natural clinoptilolites and samples pretreated at lower calcination temperature (300 °C). The relative crystallinity of the clinoptilolite samples showed a decreasing trend with increasing calcination temperature. Burris and Juenger (34) observed that the changes in clinoptilolite phases due to calcination were so near for all samples as in our study. They also explained that calcination will cause a decrease in crystallinity, which will



be pointed out by a decrease in the heights of the characteristic clinoptilolite peaks. As in our study, a greater decrease was observed for the same peaks with the increase of the calcination temperature, compared to the decrease in the clinoptilolite peaks as a result of the calcination process performed at 300 °C. They also stated that for each clinoptilolite sample, the decrease in clinoptilolite crystallinity due to calcination varied with the increase in the original amorphous amount of the clinoptilolite. Elaiopoulos et al. (38) stated that after the heat treatment was applied at 350 °C, important peak points for zeolite can be greatly affected. Seraj et al. (25) also

determined a significant decrease in the intensity of clinoptilolite peaks in the XRD patterns for natural zeolite due to calcination. Florez et al. (35) determined that the amount of amorphous material increased as the calcination process temperature increased according to XRD analysis. They stated that calcination has thermal effects on natural zeolite such as water loss, collapse of the crystal structure and gradual amorphization. In many studies in the literature, a decrease in peak density was observed in zeolite samples pretreated with acid (2,3,22,39,43,56). In other words, the pretreatment carried out with acid also has an effect on the changes in crystallinity and peak densities in this study.

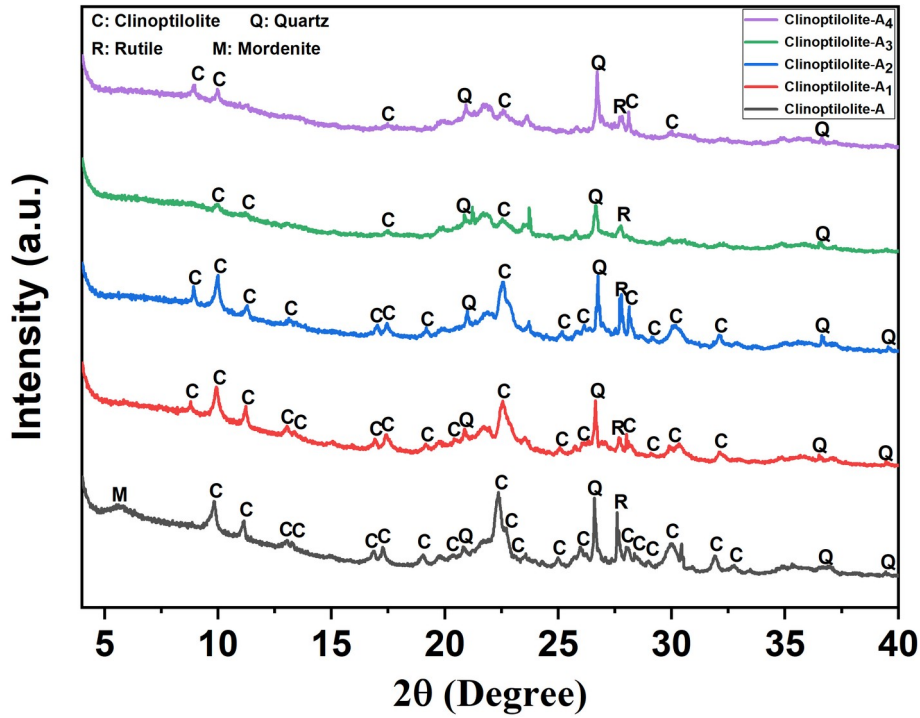


Figure 2: Typical peaks of the Clinoptilolite-A and acid-treated resultant products determined with XRD pattern.

**Table 1:** Chemical compositions (wt%) and SiO<sub>2</sub>/Al<sub>2</sub>O<sub>3</sub> ratios of natural and pretreated clinoptilolites determined by using XRF analysis.

Sample	SiO <sub>2</sub>	Al <sub>2</sub> O <sub>3</sub>	Fe <sub>2</sub> O <sub>3</sub>	CaO	MgO	K <sub>2</sub> O	Na <sub>2</sub> O	P <sub>2</sub> O <sub>5</sub>	SrO	TiO <sub>2</sub>	SiO <sub>2</sub> /Al <sub>2</sub> O <sub>3</sub>
Clinoptilolite-A	79.37	13.88	1.305	2.437	1.963	2.491	1.26	0.04	0.05	0.09	5.71
Clinoptilolite-A <sub>1</sub>	81.8	13.97	0.989	1.141	1.808	1.816	1.297	0.01	0.02	0.07	5.85
Clinoptilolite-A <sub>2</sub>	82.01	13.34	1.179	1.285	1.718	2.053	1.192	0.01	0.03	0.09	6.14
Clinoptilolite-A <sub>3</sub>	81.88	13.1	1.275	1.42	1.669	2.163	1.25	0.01	0.03	0.09	6.25
Clinoptilolite-A <sub>4</sub>	81.74	13.38	1.236	1.373	1.686	2.112	1.24	0.01	0.03	0.09	6.10
Clinoptilolite-B	77.87	14.61	1.628	2.426	1.74	3.217	1.198	0.03	0.03	0.09	5.32
Clinoptilolite-B <sub>1</sub>	80.64	14.67	1.172	1.243	1.611	2.46	0.979	0.01	0.01	0.09	5.49
Clinoptilolite-B <sub>2</sub>	80.48	15.23	1.025	1.086	1.719	2.127	1.16	0.01	0.01	0.06	5.28
Clinoptilolite-B <sub>3</sub>	80.8	14.66	1.17	1.225	1.649	2.36	0.924	0.01	0.01	0.07	5.51
Clinoptilolite-B <sub>4</sub>	80.62	15.2	1.042	1.076	1.791	2.112	0.959	0.01	0.01	0.08	5.30

Miądlicki et al. (43) indicated that clinoptilolite treated by using an acidic solution at a concentration of higher than 0.1 M (this is 0.3 M in our study) negatively affects the crystallinity of the sample. Considering Wang et al. (2) study, it can be explained that the changes in the 9.85 and 22.48°2θ peaks in the XRD patterns in this study were directly caused by the acidic treatment. This situation is explained by dealumination from the structure of clinoptilolite as a result of acid treatment. In our study, there

was no significant change in the intensity of quartz peaks for treated Clinoptilolite-A and Clinoptilolite-B samples. Wang et al. (2) stated that the structure of quartz changes and its crystallinity decreases when the zeolite is pretreated with alkali, not by pretreatment with acid (54). Kim et al. (57) found that clinoptilolites were more durable than heulandites (HEUs) despite high-temperature heat treatment and acid pretreatment.

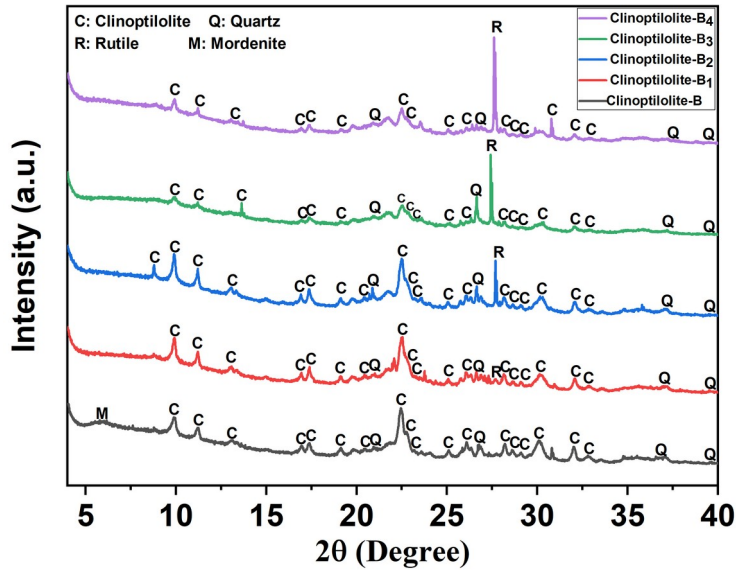


Figure 3: Typical peaks of the Clinoptilolite-B and acid-treated resultant products determined with XRD pattern.

**Fourier Transform Infrared Transmittance Spectra (FT-IR) Analysis**

FT-IR spectra could be used to put forth the structure of zeolite samples. The FTIR spectra of the natural and treated clinoptilolites investigated between the 400–4000 cm<sup>-1</sup> wavenumber are given in Figure 4 (Clinoptilolite-A,

Clinoptilolite-A<sub>1</sub>, Clinoptilolite-A<sub>2</sub>, Clinoptilolite-A<sub>3</sub>, Clinoptilolite-A<sub>4</sub>) and Figure 5 (Clinoptilolite-B, Clinoptilolite-B<sub>1</sub>, Clinoptilolite-B<sub>2</sub>, Clinoptilolite-B<sub>3</sub>, Clinoptilolite-B<sub>4</sub>). The exact points of the bands determined in every clinoptilolite are given in Table 2 (3,9,10,38,43,54,56).

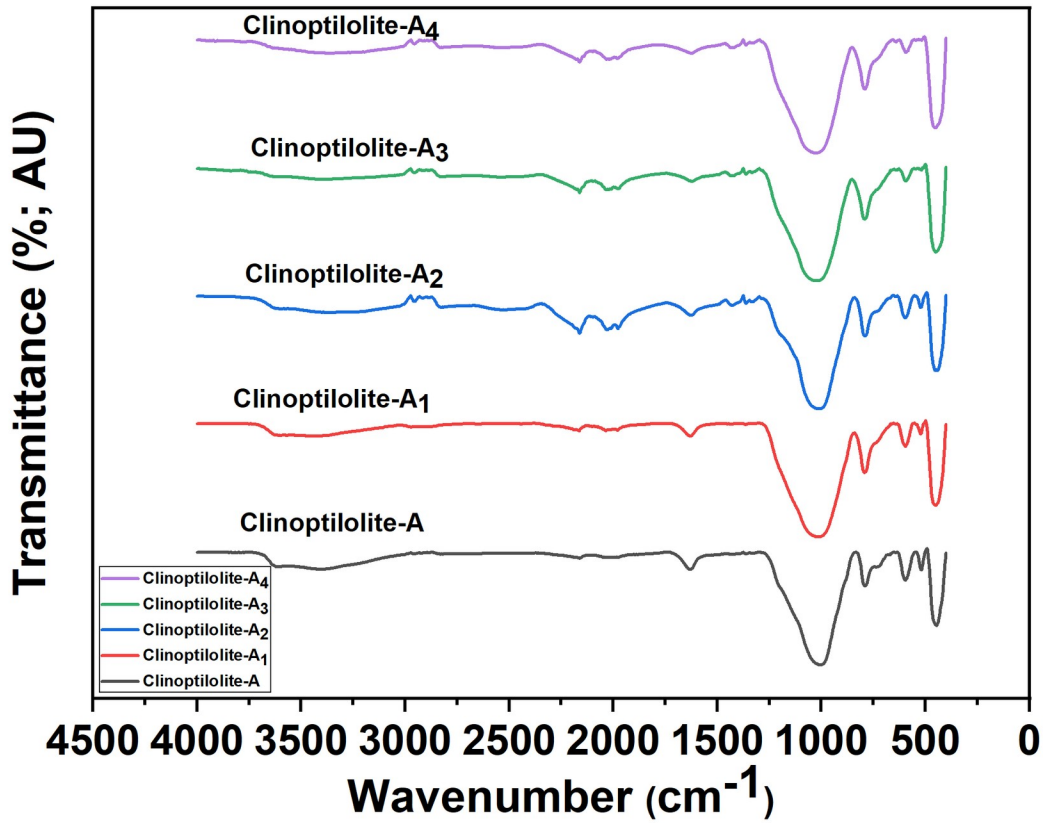


Figure 4: The FT-IR spectra of the Clinoptilolite-A and acid-treated resultant products.

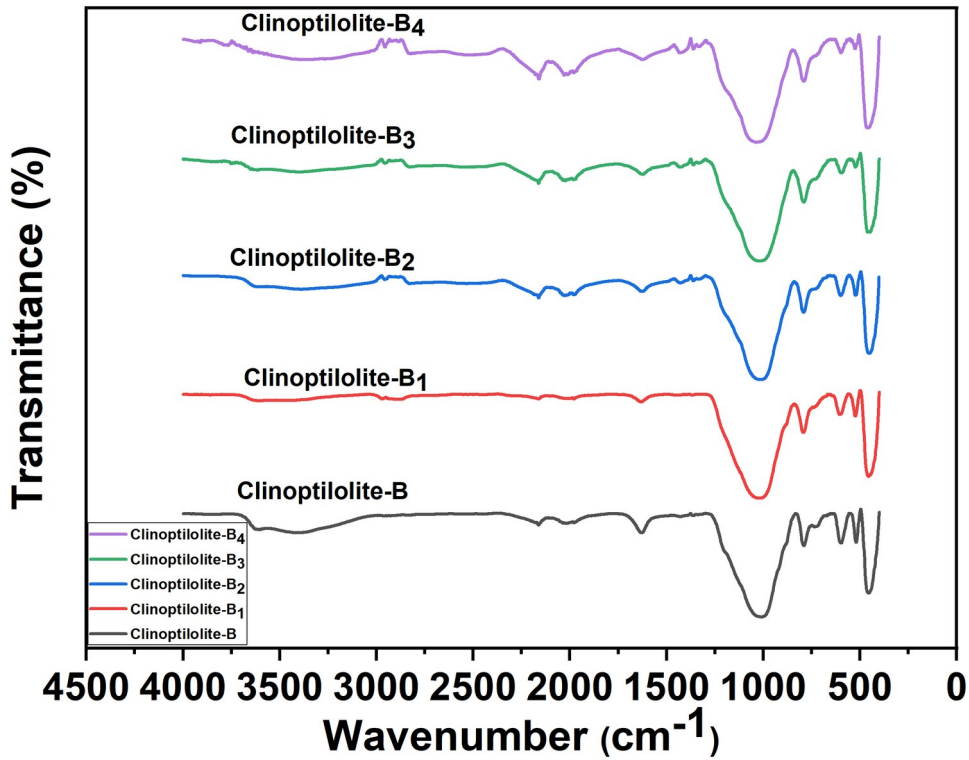


Figure 5: The FT-IR spectra of the Clinoptilolite-B and acid-treated resultant products.

**Table 2:** The peak wavenumber of bands determined in FT-IR analysis for natural and pretreated clinoptilolites.

Sample	T-O stretching vibration		T-O bending vibration	OH <sup>-</sup> Stretching	OH <sup>-</sup> Bending and/or NH <sub>3</sub>	Other
	Zeolite	SiO <sub>2</sub>				
Clinoptilolite-A	1004	790.58	446.91	3611.30, 3414.74	1629.41	595.97, 519.16
Clinoptilolite-A <sub>1</sub>	1015.22	792.21	448.33	3432.05	1629.85	595.76, 522.66
Clinoptilolite-A <sub>2</sub>	1010.97	790.66	442.77	3385.35,	1625.62,1430.99, 1362.37, 1331.90	597.18, 523.28
Clinoptilolite-A <sub>3</sub>	1023.97	792.28	450.63	3392.38	1621.85, 1434.79, 1361.88	595.46
Clinoptilolite-A <sub>4</sub>	1026.81	791.11	453.05	3362.40	1627.88, 1428.70, 1361.25	641.40, 593.16
Clinoptilolite-B	1009.52	789.87	456.02	3610.41, 3415.86	1629.90	596.28, 519.52
Clinoptilolite-B <sub>1</sub>	1021.03	793.04	455.94	3610.17	1629.96	524.50, 604.98
Clinoptilolite-B <sub>2</sub>	1015.25	791.12	451.09	3388.05	1628.15, 1428.01, 1361.43	599.31, 523.12,
Clinoptilolite-B <sub>3</sub>	1019.23	790.25	459.01, 447.28	3393.73	1623.05, 1427.09, 1361.63	598.52, 523.83
Clinoptilolite-B <sub>4</sub>	nd	789.11	460.25	3911.41, 3765.89, 3372.64	1626.06, 1431.03, 1360.39, 1330.25	599.86, 525.97

The characteristic bands in the range of 1600–3700 cm<sup>-1</sup> could be attributed to the water in clinoptilolite. According to Bilgiç (1), while the (4000-3000 cm<sup>-1</sup>) region in the FTIR spectrum indicates the presence of various OH groups, hydroxyl vibrations are observed in this region. Figure 4 and Figure 5 indicate three characteristic bands appearing in the spectra of all samples, at ~3414 cm<sup>-1</sup>, ~3610 cm<sup>-1</sup>, ~3910 cm<sup>-1</sup>, ~3765 cm<sup>-1</sup> and ~3380 cm<sup>-1</sup>. The band at 3910 cm<sup>-1</sup> is correlated to isolated silanol groups (Si-OH), the band at ~3414 cm<sup>-1</sup> is sourced from Si-O(H)-Al, and the band at ~3414 cm<sup>-1</sup> is assigned to hydrogen bonded Si-OH groups in nest deformities and hydrogen bonding of slouching kept water molecules (3,10,38,43,54,58-60). Isolated OH stretching at 3611.30 cm<sup>-1</sup> for Clinoptilolite-A, 3610.41 cm<sup>-1</sup> for Clinoptilolite-B and at 3610.17 cm<sup>-1</sup> for Clinoptilolite-B<sub>1</sub> was determined due to the interplay among the water hydroxyl and cations. Due to acid and heat treatments, the intensity of this band showed a decrease in all treated samples as a result of decationization and dealumination from the structure (3,10,61,62). Another bands are assigned to the hydrogen bonding in the water structure to surface oxygen (3414–3416 cm<sup>-1</sup>) and to the bending mode of water molecules (~1629 cm<sup>-1</sup>) (3,43,38,56). The bands at 1400–1450 cm<sup>-1</sup> could be attributed to NH<sub>3</sub> bound by Bronsted sites (10,56). Bilgiç (1) also determined a band at 1398 cm<sup>-1</sup> which belongs to NH<sub>4</sub><sup>+</sup>. Bands in the 1300-1450 cm<sup>-1</sup> wavelength range were not observed in natural clinoptilolites, Clinoptilolite-A<sub>1</sub>, and Clinoptilolite-B<sub>1</sub> samples, but were observed in Clinoptilolite-A<sub>2</sub>, Clinoptilolite-A<sub>3</sub>, Clinoptilolite-A<sub>4</sub>, Clinoptilolite-B<sub>2</sub>, Clinoptilolite-B<sub>3</sub>, Clinoptilolite-B<sub>4</sub> samples that were calcined at the same temperature for a longer time or whose calcination temperature was increased.

In the range of 1600–1450 cm<sup>-1</sup>, there are not extended bands and they are assigned to the bending mode of water. In this study, however, these bands were not determined in the all-natural and treated clinoptilolites. Ates and Hardacre (3) also stated that these bands could be determined in

slight transmittance or not existing for the treated samples. For the wavenumber 600–800 cm<sup>-1</sup>, the bands are assigned to pseudo-crystalline vibrations (3,54,63). In this interval; there is an intensity for the band at 789–794 cm<sup>-1</sup> which is assigned to Si-O stretching in all-natural and treated samples (3,43,51,54,60,64). This band is also sourced from amorphous silica or the opal CT-like phase generated with the zeolite phase solvation due to the treatments (3,51). The Si-O stretching vibrations of Clinoptilolite-A and Clinoptilolite-B are being moved to a higher wavenumber after acid and heat treatment. The band detected at near ~794 cm<sup>-1</sup> for Clinoptilolite-B<sub>1</sub> could be assigned to quartz or amorphous SiO<sub>2</sub>, which is confirmed by the XRD pattern and XRF analysis (54).

The dominant T-O stretching vibration bands are detected in the 1045–1070 cm<sup>-1</sup> region. The intensity of this band is proportionated with the Si/Al ratio (3,10,43,54). When the more Al<sup>3+</sup> atoms are removed from the clinoptilolite structure, this band is expected to give higher wavelengths in the FTIR spectra from ~1047 cm<sup>-1</sup> onwards. However, it was stated that samples with a high Al<sup>3+</sup> amount gave bands around ~1022 cm<sup>-1</sup> in some studies (10,38,43,54,56,57,60,66). They also explained that the force constant for the mode in the Al-O-Si bond is lower than the corresponding mode in a Si-O-Si bond because the bond between Al-O is weak and longer. This situation causes the wavelength of the clinoptilolite to be lower in these mentioned ranges if the Al<sup>3+</sup> content is high. In line with this, the bands detected in the range of 1016–1022 cm<sup>-1</sup> belong to stretching vibrations of the T-O band in Miądlicki et al. (43) study. In the author's study, it was determined that it gave bands in the range of ~1004-1024 cm<sup>-1</sup>, which is close to these band gaps but at a lower wavelength range. This is due to the fact that the dealumination could not be achieved at the desired rates, as supported by XRF analyses, and therefore the amount of Al<sup>3+</sup> present in the structure was higher than the target. However, an increase in the ratio of Si/Al in structure content carries the bands to



higher wavenumbers for especially Clinoptilolite-A<sub>1</sub>, Clinoptilolite-A<sub>2</sub>, Clinoptilolite-A<sub>3</sub>, Clinoptilolite-A<sub>4</sub>, Clinoptilolite-B<sub>1</sub> compared to natural clinoptilolites in this study. Compared to Clinoptilolite-B, incremental slip of wavenumbers in Clinoptilolite-B<sub>2</sub> and Clinoptilolite-B<sub>3</sub> could be explained by higher calcination time and calcination temperature, respectively. However, when evaluated in itself, the lower wavelength of the Clinoptilolite-B<sub>2</sub> and Clinoptilolite-B<sub>3</sub> samples compared to Clinoptilolite-B<sub>1</sub> may be due to the longer calcination time in the Clinoptilolite-B<sub>2</sub> sample compared to Clinoptilolite-B<sub>1</sub>, and the fact that the Clinoptilolite-B<sub>3</sub> sample calcination was carried out at the same time but at a higher temperature than Clinoptilolite-B<sub>1</sub>. In addition to all these, as given in other researches, all possible structures due to the presence of feldspars and amorphous species in non-high purity clinoptilolite samples may cause a wide peak formation in the 1250-850 cm<sup>-1</sup> region, which prevents determining the exact position of other important bands (10,56,63,65,67,68).

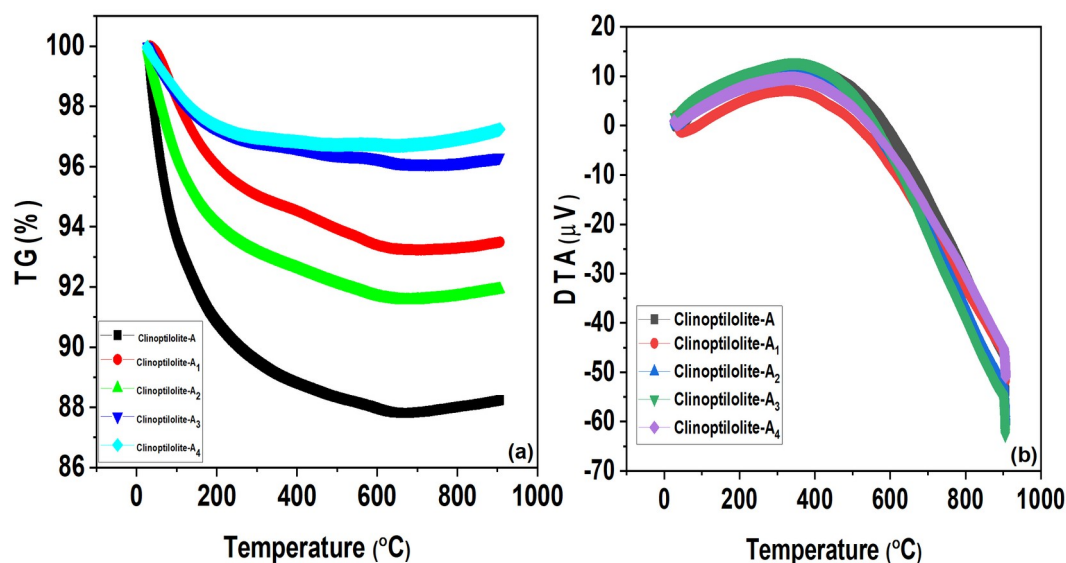
The band in ~437-470 cm<sup>-1</sup> region could be assigned to Si-O-Si or T-O bending band as mentioned in several studies (10,38,41,54). The band intensity showed differences from structure to structure, pointing out that there is a possibility of overlapping from bands assigned to amorphous structures and/or exchangeable cations. Compared to Clinoptilolite-A<sub>1</sub>, Clinoptilolite-A<sub>2</sub>, Clinoptilolite-B<sub>1</sub>, and Clinoptilolite-B<sub>2</sub>; higher wavelength values were determined in this range for Clinoptilolite-A<sub>3</sub>, Clinoptilolite-A<sub>4</sub>, Clinoptilolite-B<sub>3</sub>, and Clinoptilolite-B<sub>4</sub> samples that were pretreated with a higher calcination temperature and longer time. This can be explained by the change in the state of the amorphous structure and exchangeable cations as a result of pretreatment with acid and calcination.

The bands at 519.16 (at Clinoptilolite-A), 522.66 (at Clinoptilolite-A<sub>1</sub>), 523.28 (at Clinoptilolite-A<sub>2</sub>), 519.52 (at Clinoptilolite-B), 523.12 (Clinoptilolite-B<sub>2</sub>), 523.83 (Clinoptilolite-B<sub>3</sub>), and 525.97 (Clinoptilolite-B<sub>4</sub>) are attributed to extra-framework cations in the structures of

samples (41,58). According to these studies in the literature, since these cations are removed in the samples treated by acid solutions with a concentration of 0.5 M and above, no band is observed in this wavelength range, while these bands are existence in the FTIR spectrum of samples pretreated by an acidic solution with a concentration of less than 0.5 M. The weak band determined at 604.98 cm<sup>-1</sup> in Clinoptilolite-B<sub>1</sub> belongs to bending vibrations among tetrahedra, especially to double ring vibrations (41). Korkuna et al. (56) also stated that the bands detected between 500-700 cm<sup>-1</sup> belong to pseudo-lattice vibrations in the structure.

#### Thermogravimetry and Differential Thermal Analysis (TGA-DTA) and Thermal Characteristics

TGA and DTA results are given in Figure 6 (Clinoptilolite-A, Clinoptilolite-A<sub>1</sub>, Clinoptilolite-A<sub>2</sub>, Clinoptilolite-A<sub>3</sub>, Clinoptilolite-A<sub>4</sub>) and Figure 7 (Clinoptilolite-B, Clinoptilolite-B<sub>1</sub>, Clinoptilolite-B<sub>2</sub>, Clinoptilolite-B<sub>3</sub>, Clinoptilolite-B<sub>4</sub>). Clinoptilolite (natural and treated) had high thermal stability (up to temperatures 600–800 °C) (4,34,48) and showed continuous mass-loss curves as a function of temperature up to 600 °C. The main structural changes, due to especially water loss, occurred at temperatures below or around 300-400°C. Therefore, weight loss (%) of the natural and pretreated clinoptilolites determined using TGA-DTA analysis at different temperature ranges up to 600 °C are shown in Table 3. The major amount of water in the clinoptilolite structure could be removed by heating at temperatures lower than 450 °C without damaging the structure (7,34,38,48,54,56). Additionally, when the TG curves were examined, it was stated that they showed a regular weight loss up to 700 °C due to water loss. It has been determined that the DTA curves of all treated/untreated clinoptilolites have a strong endothermic effect at ~350 °C. It is correlated to the removal of physically adsorbed water. In literature, different researchers (48,56,69) determined the endothermic effects in the DTA curves due to the removal of water up to 200°C.



**Figure 6:** Comparison of thermal behaviors due to (a) TGA and (b) DTA of the Clinoptilolite-A and acid-treated resultant products.

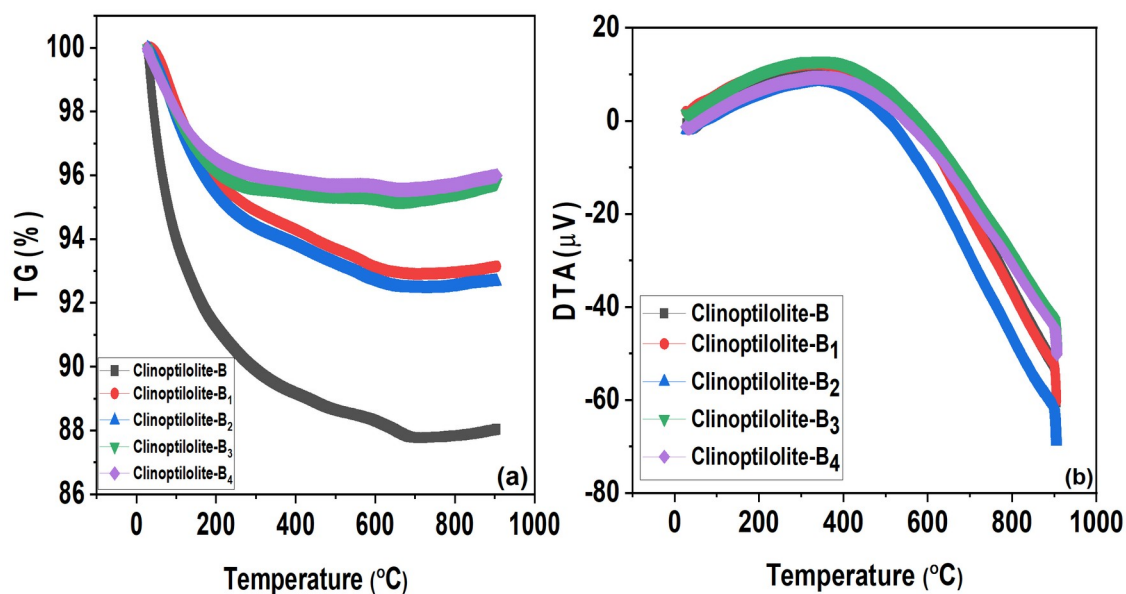


Figure 7: Comparison of thermal behaviors due to (a) TGA and (b) DTA of the Clinoptilolite-B and acid-treated resultant products.

Table 3: Weight loss (%) of the natural and pretreated clinoptilolites determined using TGA at different temperature ranges.

Sample	Weight Loss % 30-100°C	Weight Loss % 100-200°C	Weight Loss % 200-300°C	Weight Loss % 300-400°C	Weight Loss % 400-500°C	Weight Loss % 500-600°C	Total
Clinoptilolite-A	6.327	2.832	1.297	0.731	0.476	0.369	12.032
Clinoptilolite-A <sub>1</sub>	1.746	2.209	0.997	0.517	0.597	0.541	6.607
Clinoptilolite-A <sub>2</sub>	3.582	2.278	0.96	0.551	0.504	0.436	8.311
Clinoptilolite-A <sub>3</sub>	1.623	1.125	0.437	0.197	0.236	0.119	3.737
Clinoptilolite-A <sub>4</sub>	1.777	1.388	0.403	0.056	0.099	0.004	3.727
Clinoptilolite-B	5.999	2.73	1.368	0.733	0.525	0.34	11.695
Clinoptilolite-B <sub>1</sub>	1.764	2.308	1.037	0.593	0.604	0.563	6.869
Clinoptilolite-B <sub>2</sub>	2.099	2.42	1.103	0.554	0.58	0.546	7.302
Clinoptilolite-B <sub>3</sub>	2.149	1.71	0.521	0.14	0.111	0.07	4.701
Clinoptilolite-B <sub>4</sub>	1.977	1.509	0.514	0.192	0.132	0.018	4.342

Decationization and dealumination of pre-treated clinoptilolites, which is supported by the results of XRF analysis, cause a decrease in the hydrophilic characteristics of clinoptilolites. In general, the abundance of the clinoptilolite phase provides a stable structure up to 700 °C. All treatment operations resulted in a decline for clinoptilolite content and removing the cations (especially acid treatment is significant for this), causing higher water removal (22,48,70). When weight loss (%) was totally examined, the weight loss values decreased inversely with the increase of calcination temperature and calcination time applied to both acid-treated clinoptilolite species. Among the pretreated samples, the highest total weight loss was observed in Clinoptilolite-A<sub>2</sub> and Clinoptilolite-B<sub>2</sub> samples, which had the lowest calcination temperature and time, while the lowest total weight loss was detected in Clinoptilolite-A<sub>4</sub> and Clinoptilolite-B<sub>4</sub> samples. When

examined in general, the weight loss of Clinoptilolite-B<sub>1</sub>, Clinoptilolite-B<sub>3</sub> and Clinoptilolite-B<sub>4</sub> samples are higher than that of pretreated Clinoptilolite-A samples, except for the Clinoptilolite-B<sub>2</sub> sample. This could be explained by the fact that the high Si/Al ratio observed in the pre-treated Clinoptilolite-A samples, as seen in the XRF analysis results, ensures the preservation of the crystal structure (54).

The weight loss in samples exposed to temperatures between 30–100 °C occurs as a result of the desorption of physisorption water. The results differ according to the type of zeolite, acid treatment, calcination temperature and calcination time: Clinoptilolite-A<sub>2</sub>> Clinoptilolite-B<sub>3</sub>> Clinoptilolite-B<sub>2</sub>> Clinoptilolite-B<sub>4</sub>> Clinoptilolite-A<sub>4</sub>> Clinoptilolite-B<sub>1</sub>> Clinoptilolite-A<sub>1</sub>> Clinoptilolite-A<sub>3</sub>. For all treated Clinoptilolite-A samples, weight loss was greater at

longer duration of calcination at both calcination temperatures. The decrease in weight loss also depends on the decrease in water absorption due to acid pretreatment, as indicated in Ates and Hardacre (3) and Elaiopoulos et al. (38).

Between 100-200 °C, for both clinoptilolite types, the highest weight loss was observed in the samples that were calcined at 300 °C for 3 hours (Clinoptilolite-A<sub>2</sub> and Clinoptilolite-B<sub>2</sub>). When calcined at 500 °C, the weight loss decreased due to the increasing calcination time in the acid-pre-treated Clinoptilolite-B<sub>4</sub> sample, while the weight loss increased while the calcination time increased in the pre-treated Clinoptilolite-A<sub>4</sub> sample. The remarkable weight losses for all samples were determined between 30-200 °C due to the removal of physically adsorbed water, the water existing into the clinoptilolite cavities, and cations at the structure (26,48,70).

Compared to the first two temperature ranges, the weight loss values decreased between 200-300 °C. From 200-300 °C, the slope of TG curves started to fall for all samples in Figures 6 and 7 (3,38,48). When examined in itself, it was determined that the weight loss decreased with increasing calcination temperature and calcination time in both clinoptilolite samples. Wang et al. (22) stated that weight loss values decrease due to the increasing calcination temperatures. They also explained that calcination could significantly carry out the removal of water from the surface/structure of zeolites. This indicates that the heat treatment reduces the silanol slot-derived water content in the zeolite structure. Only the Clinoptilolite-B<sub>2</sub> sample showed a slight increase due to the increasing time compared to the other sample calcined at the same temperature in our study.

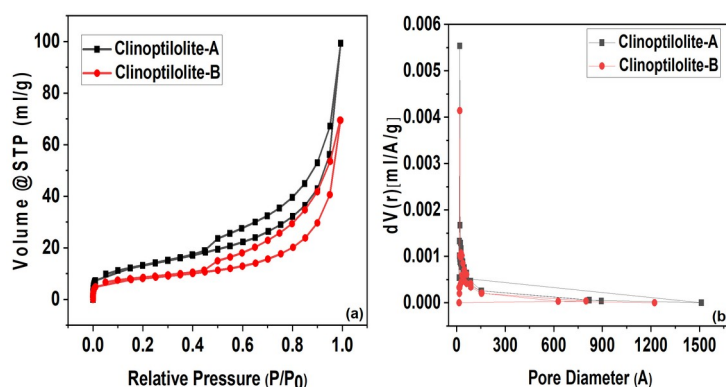
Weight loss values were less in the range of 300-400 °C. When investigated in itself, it has resulted that the weight loss decreased with increasing calcination temperature and calcination time in both clinoptilolite samples, except for Clinoptilolite-A<sub>2</sub> and Clinoptilolite-B<sub>4</sub>. Compared to the first three temperature range values, weight losses were lower between 400-500 °C, as in the temperature range of 300-400 °C. The same situation for the two the temperature range observed in other studies (38,48). The temperature range of 500-600 °C is the range where the lowest weight losses were seen for all treated samples, except for the Clinoptilolite-A<sub>1</sub> sample, and all of the water remaining in

the structure was removed during this interval and afterward. The slope of the TG curves was slighter compared to lower temperature ranges (<500°C) (3,34).

According to the examination of analysis results, the water structures that appeared in clinoptilolites could be divided into three versions: physisorbed water (<100 °C), water correlated to extra-framework cations and aluminum (100–400 °C), and water correlated to silanol nests (>400 °C) (22,34).

#### Brunauer-Emmett-Teller (BET) Analysis

The nitrogen adsorption and desorption isotherms and pore size distributions of natural and pre-treated clinoptilolites are given to explain the structural characteristics of porous samples in Figures 8, 9, and 10. According to the IUPAC (International Union of Pure and Applied Chemistry) classification, the clinoptilolites have Type 4 isotherms with the hysteresis loop. The surface characteristics calculated are shown in Table 4. Zeolites are generally microporous structures, but the primary micropores formed due to the specific crystal structure of the zeolite itself may not be able to reach and adsorb N<sub>2</sub> gas into these pores due to the inhibition of large cations (10,71,72). Due to the acid treatment and calcination, it was determined an increase in the specific surface areas of clinoptilolites (except Clinoptilolite-A<sub>3</sub> and Clinoptilolite-B<sub>1</sub>). The increase in surface area and total pore volume as a result of acid pretreatment has been detected in many studies in the literature (2,3,10,22,39,48). These changes in the surface properties such as surface area, micropore volume, and total pore volume could be correlated to removal of the metal cations, dealumination, and some impurities. Pre-treatments cause the generation of defects and voids left by the removed aluminum (2,3,10,22,43,73). Contrary to this, it was stated that adsorption-desorption isotherms are seldomly affected by acid pre-treatment (3). Elaiopoulos et al. (10) stated that it would not be possible to hold all changes in some physicochemical characteristics responsible for the change in the pore structure. Miądlicki et al. (43) also explained that very high acid concentrations above 1 M can damage the crystal structure, resulting in a lower BET surface area and pore volume. This is the reason why the author did not study at very high acid concentration values (used HCl solution concentration was 0.3 M) in the author's study, and the results obtained (except for Clinoptilolite-A<sub>3</sub> and Clinoptilolite-B<sub>1</sub>) did not show a decrease in BET surface area and pore volume.



**Figure 8:** Nitrogen adsorption and desorption isotherms and pore size distributions of Clinoptilolite-A and Clinoptilolite-B according to BET analysis.

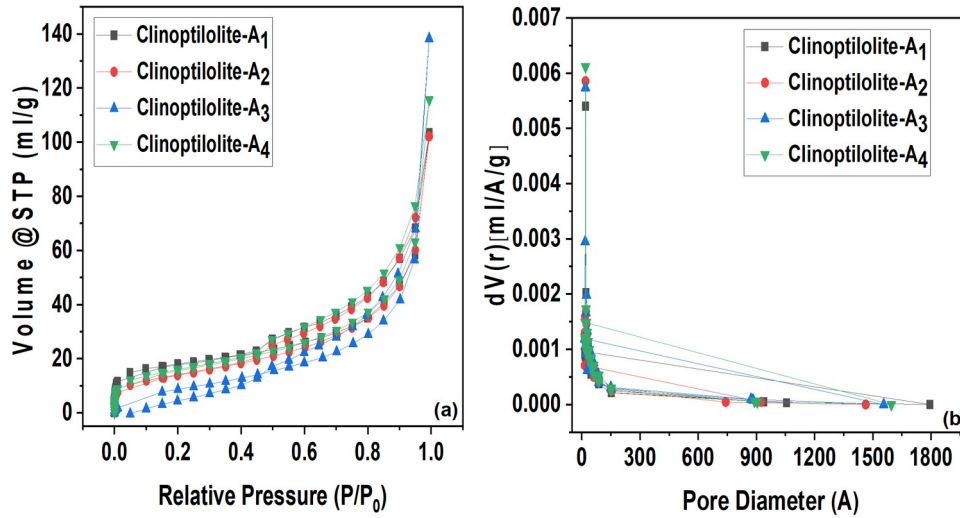


Figure 9: Nitrogen adsorption and desorption isotherms and pore size distributions of the acid-treated clinoptilolites (modified from Clinoptilolite-A) according to BET analysis.

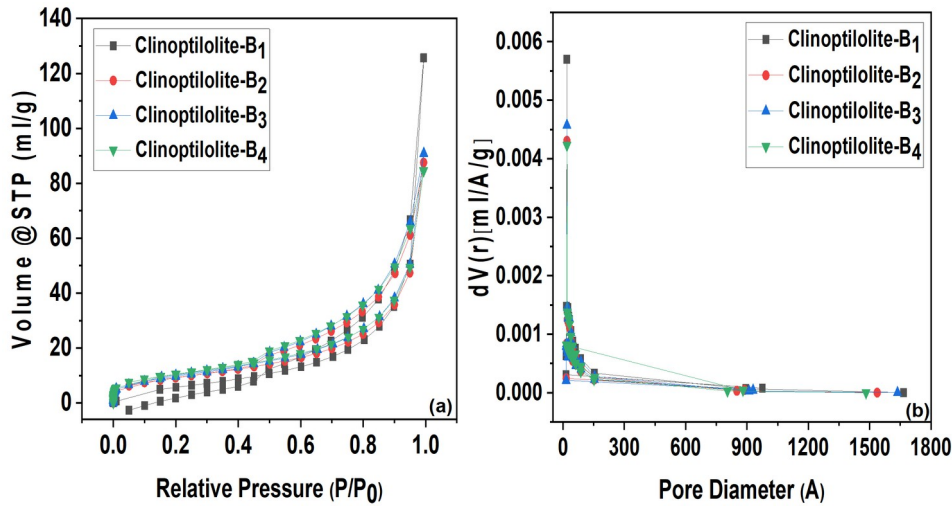


Figure 10: Nitrogen adsorption and desorption isotherms and pore size distributions of the acid-treated clinoptilolites (modified from Clinoptilolite-B) according to BET analysis.

Table 4: Structural parameters calculated for natural and treated clinoptilolites from adsorption–desorption isotherms of nitrogen at 77 K in BET analysis.

Sample	BET Surface Area(m <sup>2</sup> /g)	Total pore volume (cm <sup>3</sup> /g)	Average Pore Diameter (Å)
Clinoptilolite-A	46.534	0.1538	132.16
Clinoptilolite-A <sub>1</sub>	60.318	0.1600	106.06
Clinoptilolite-A <sub>2</sub>	49.092	0.1580	128.76
Clinoptilolite-A <sub>3</sub>	34.286	0.2140	249.7
Clinoptilolite-A <sub>4</sub>	54.594	0.1789	131.1
Clinoptilolite-B	28.246	0.1075	152.26
Clinoptilolite-B <sub>1</sub>	26.302	0.1944	295.64
Clinoptilolite-B <sub>2</sub>	33.077	0.1355	163.8
Clinoptilolite-B <sub>3</sub>	36.037	0.1408	156.24
Clinoptilolite-B <sub>4</sub>	36.869	0.1308	141.86

When the pore size distributions of both clinoptilolites (both natural and pre-treated) are examined, it is seen that there is an increase in microporosity due to acid treatment and calcination. This situation can be explained by dealumination due to acid treatment, and it is possible to

reach micropores, especially with cations removed from the structure. It was also stated that treatment with acid has a significant effect on pore size distributions (3,9).

When the graphs of both clinoptilolite samples are examined, it is seen that the adsorption values increase, mostly in Clinoptilolite-A<sub>3</sub> and Clinoptilolite-B<sub>1</sub>, depending on the increase in relative pressure. Çakıcıoğlu-Özkan and Ülkü (9) also determined this situation in their own studies and stated that the temperature during the HCl pretreatment application was also effective on adsorption. They observed that as this temperature increased, the adsorption decreased especially in the samples that were pretreated with acid at around 100 °C. In our study, no decrease in adsorption values was observed due to the fact that the acid pretreatment application temperature was worked with a value that was almost half of this temperature value.

When the Clinoptilolite-A sample, which was supplied with a smaller pore size, is compared with the Clinoptilolite-B sample with a larger pore size, although the amount of N<sub>2</sub> they adsorbed seems to be close, the Clinoptilolite-A sample adsorbed more N<sub>2</sub> at low pressures as in Figure 8. Similarly, when the pre-treated samples belonging to Clinoptilolite-A were examined in Figure 9, it was determined that Clinoptilolite-A<sub>3</sub> and especially the Clinoptilolite-A<sub>4</sub> sample, which was pretreated by applying a higher calcination temperature, adsorbed more N<sub>2</sub> for lower pressures. When pre-treatment was applied to Clinoptilolite-B, which has larger pores, it was seen that Clinoptilolite-B<sub>2</sub>, Clinoptilolite-B<sub>3</sub>, and Clinoptilolite-B<sub>4</sub> adsorb N<sub>2</sub> very closely at smaller pressures, but Clinoptilolite-B<sub>4</sub> adsorbs more nitrogen, albeit with a relatively small difference. This situation, especially in the Clinoptilolite-A<sub>4</sub> and Clinoptilolite-B<sub>4</sub> samples, is explained by their lower average pore diameters compared to the diameter of Clinoptilolite-A and Clinoptilolite-B as seen in Table 4. Such a difference was also detected in samples with smaller pore diameters in the Elaiopoulos et al. (10) study, and it was stated that there was too little difference to be seen in the differential pore volume distribution curves. Desorption curves of isotherms show a decrease from  $P/P_0 \sim 0.45$  for Clinoptilolite-A<sub>3</sub> and Clinoptilolite-B<sub>1</sub> and Clinoptilolite-B<sub>3</sub> samples. In this case, it was stated by Elaiopoulos et al. (10) that as the pressure decreases, the separation of smaller pores may occur, and when the critical pressure value is lowered to a value, the separation of these micropores will be managed with a much slower progressing kinetics. It was stated that the equilibrium to be established between the adsorption and desorption phases would take longer time.

In this study, although there are differences in the surface morphology, area, total pore volume, and adsorption characteristics between the samples with the calcination process we applied, it is seen that the changes in the calcination temperature and time do not create very large differences between the pretreated samples. In their study, Elaiopoulos et al. (10) and Burris and Juenger (34) explained the calcination temperatures around 500-550 °C as moderate calcination temperatures and stated that the changes in the structure could be less at these calcination temperatures compared to higher temperatures. Burris and Juenger (34) stated that they observed a little decrease in the surface area and in the total pore volume depending on the calcination temperature values increasing from the calcination temperature of 300 °C. Although changes were observed after the calcinations performed at 300 and 500 °C, very large changes occurred after the calcination processes above 500 °C. Although it is stated that agglomeration can be seen in the structure as a result of sintering at temperatures, especially below 800 °C in their

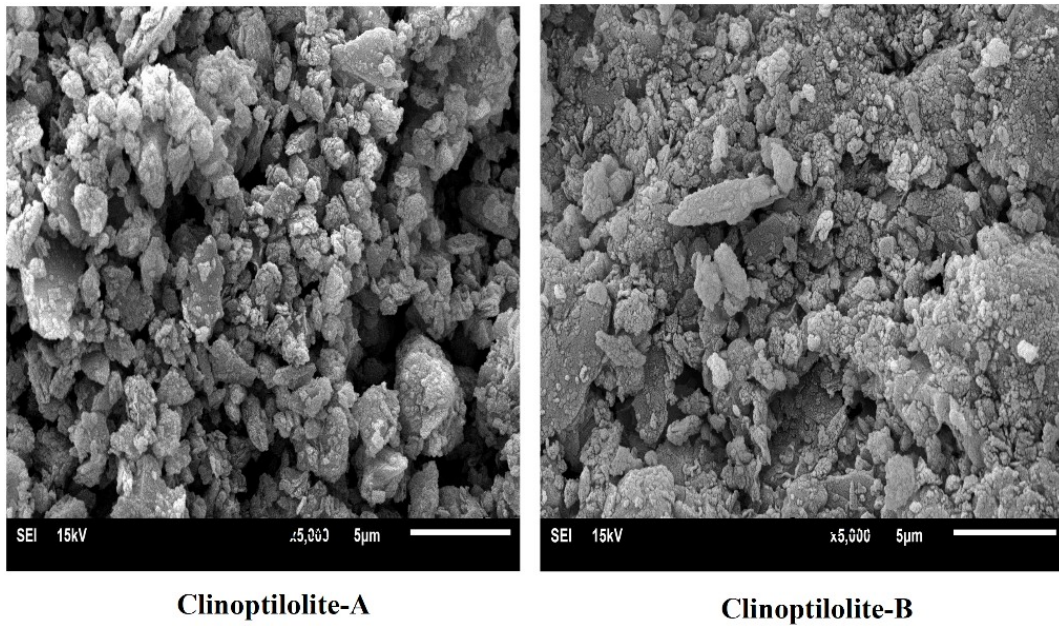
study, agglomeration did not occur at both calcination temperatures, as can be clearly seen in the SEM results of the author's study. Wang et al. (22) found that samples calcined at 800 °C had larger pore diameter and lower pore volume compared to samples calcined at 400 °C and 600 °C. Emphasizing that low calcination temperatures have negligible negative effects on the zeolite structure, they explained that increasing calcination temperatures damage the morphological structure. Elaiopoulos et al. (10) also determined that both agglomeration in the structure and a decrease in crystallinity can be observed due to the high temperature (above 550 °C) as a result of calcination. They stated that pores and channels may be clogged or damaged due to high-temperature-calcination. Depending on the increasing calcination temperatures, the calcination temperature of 300 and 500 °C was accepted to prevent both a decrease in the surface area and the agglomeration in the structure for this study. Unlike the Burris and Juenger (34) study, in this study, an increase in the surface area (except for Clinoptilolite-B<sub>1</sub> and Clinoptilolite-A<sub>3</sub> samples) and total pore volume was observed despite increasing calcination temperatures and time, thanks to the pre-treatment with acid before calcination. As mentioned before, pretreatment with acid provides these increases in surface area and total pore volume. Different researchers (22,25,35) also found a decrease in zeolite surface areas as a result of calcination. Florez et al. (35) emphasized that increasing calcination temperatures causes a reduction in total pore volume. Seraj et al. (25) stated that the decrease in the surface area is due to the destabilization of the zeolitic structure, the pores in the internal structure negatively affected, and the aggregation of the zeolite particles as a result of sintering. When this information is taken into account, the decrease in the surface area of the Clinoptilolite-A<sub>3</sub> and Clinoptilolite-B<sub>1</sub> samples in this study may have been caused by the instability of the zeolite structure or especially the pores in the internal structure negatively affected as a result of the calcination process. In other respects, as seen in Table 4, Clinoptilolite-B<sub>2</sub> and Clinoptilolite-B<sub>3</sub> samples show an increase in surface area compared to natural clinoptilolite sample (Clinoptilolite-B) with increasing calcination time and temperature despite the increasing pore diameter. This can be explained by the increase in the surface due to porosity in the material structure. Miądlicki et al. (43) reported that there may be an increase in porosity in acid-pretreated clinoptilolite samples. In addition, as seen in Clinoptilolite-B<sub>3</sub> SEM analysis, tabular, platy, and coffin-shaped structures in the samples may cause an increase in the surface area. According to Seraj et al. (25), since the BET surface area results take into account both the outer and inner surface area, it can also give an idea of the porosity of the material if the particle size distribution of the material is also known, as given in this study. When the samples with known BET surface area and particle size distribution are compared, the samples with larger pore diameters have a higher surface area, contrary to what it should be, which indicates that this material has more porosity.

#### Scanning Electron Microscopy (SEM) and Energy Dispersion Spectroscopy Analysis

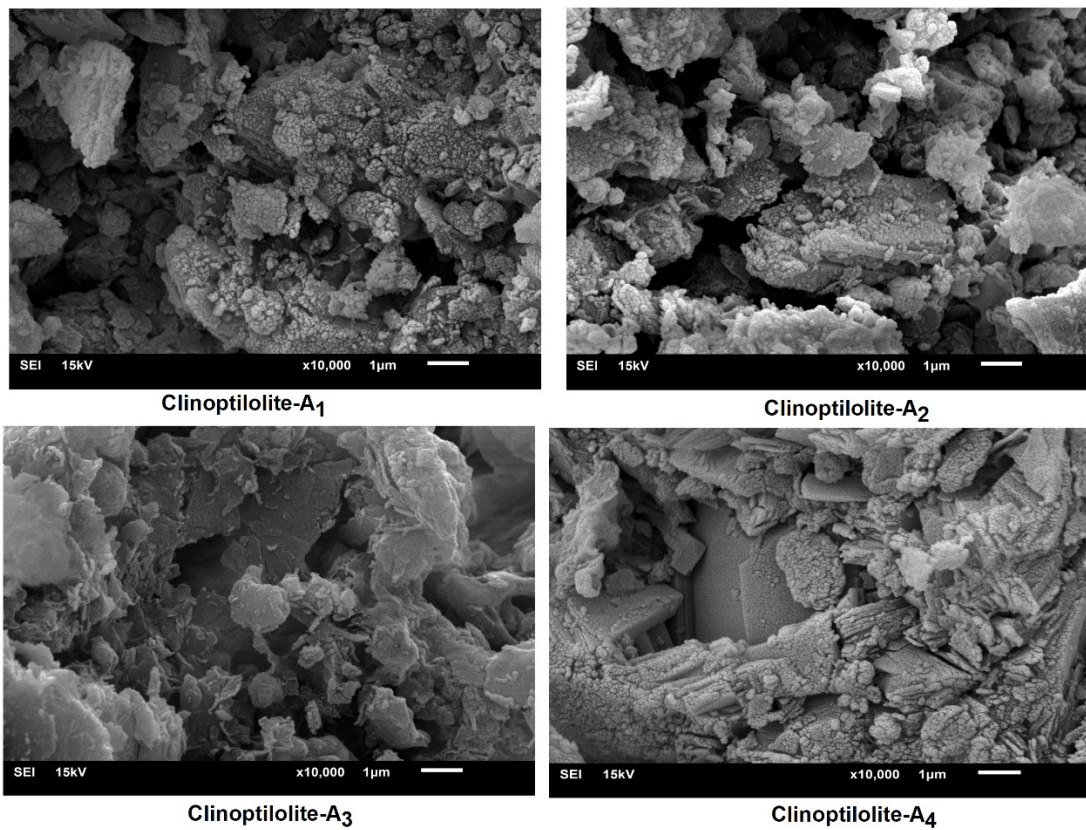
The scanning electron microscopy images and EDS experiments were performed to examine the morphological properties and elemental composition belonging to the natural and treated clinoptilolites. SEM and EDS results for each sample are shown in Figures 11, 12, and 13 comparatively. Also, the average elemental compositions of



natural and treated clinoptilolites determined by EDS analysis are presented in Table 5.



**Figure 11:** Morphological characterization determined with SEM for Clinoptilolite-A and Clinoptilolite-B.



**Figure 12:** Morphological characterization determined with SEM for acid-treated clinoptilolites (modified from Clinoptilolite-A).

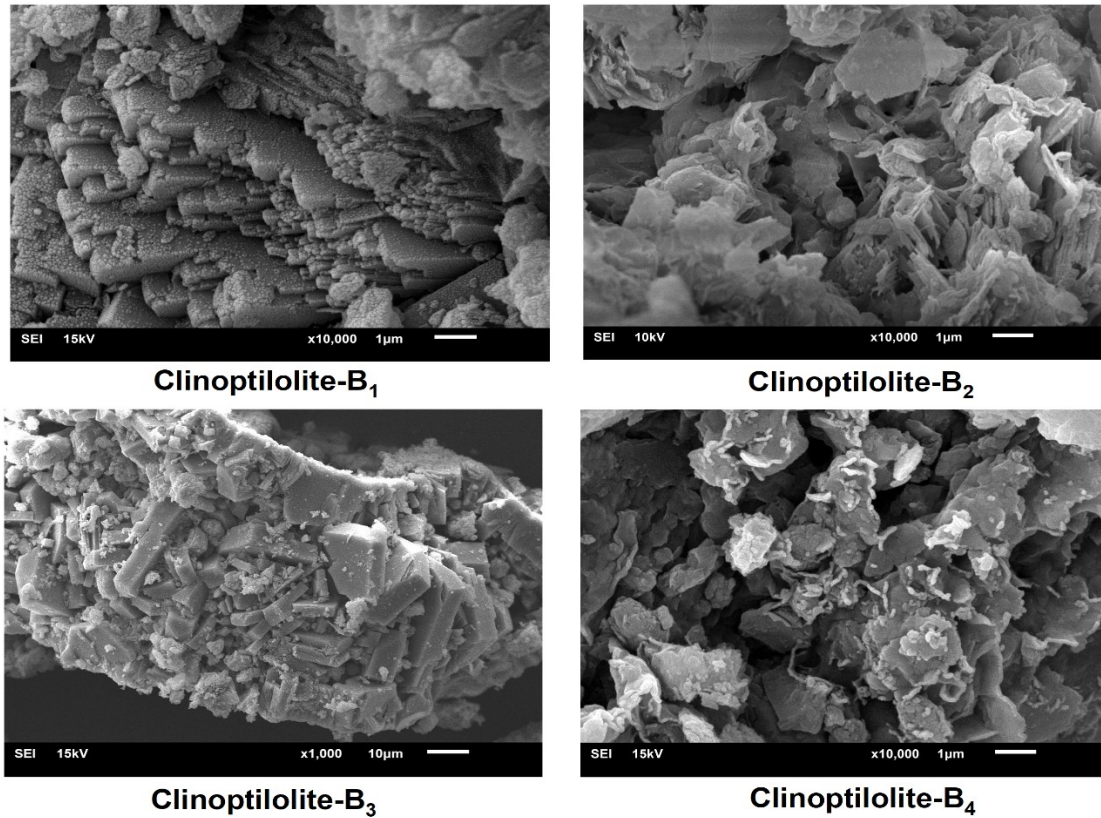


Figure 13: Morphological characterization determined with SEM for acid-treated clinoptilolites (modified from Clinoptilolite-B).

Table 5: Average elemental composition of natural and pre-treated clinoptilolites determined by EDS analysis.

Sample	O	Al	Si	Fe	Ca	K	C	Mg
Clinoptilolite-A	43.9	4.1	31.5	-	0.7	2.6	16.7	0.4
Clinoptilolite-A <sub>1</sub>	40.3	4.9	30.6	1.7	0.9	1.5	19.6	0.5
Clinoptilolite-A <sub>2</sub>	35.4	2.4	33.0	-	-	-	29.1	-
Clinoptilolite-A <sub>3</sub>	46.1	4.5	23.4	0.9	0.4	1.5	22.8	0.4
Clinoptilolite-A <sub>4</sub>	47.1	5.0	28.4	1.2	0.6	1.4	15.7	0.5
Clinoptilolite-B	41.5	5.5	27.4	2.0	1.6	2.8	18.7	0.4
Clinoptilolite-B <sub>1</sub>	37.8	7.9	43.1	6.2	1.1	2.9	-	0.9
Clinoptilolite-B <sub>2</sub>	42.3	5.0	27.2	1.8	0.7	2.0	20.5	0.4
Clinoptilolite-B <sub>3</sub>	51.2	5.4	23.6	-	1.3	2.4	15.8	0.4
Clinoptilolite-B <sub>4</sub>	44.6	5.4	25.5	2.0	0.7	1.5	19.7	0.6

Compared to natural zeolite samples; although there were differences in the morphological structure of the samples calcined at lower temperatures (300 °C) for both zeolite types, more significant changes were detected in the surface structure of the clinoptilolites calcined at higher temperatures (500 °C). In Figure 11, natural clinoptilolites are shown and, the particle structure of both is spherical and morphologically very similar to each other. After acid treatment and then calcination, except for the Clinoptilolite-A<sub>1</sub> sample, changes occurred in the structure with the increase in calcination temperature and time. When the calcination temperature was 500 °C, the particle structure began to transform from spherical to rod-shaped as seen in Figure 12. Compared to Clinoptilolite-A sample, although there were changes in the structure from the first calcination temperature for Clinoptilolite-B sample, significant changes occurred with the increase in calcination temperature and time. As in the other clinoptilolite sample, rod-shaped particles (especially Clinoptilolite-B<sub>4</sub>) were detected more

clearly when the calcination temperature was 500 °C in Figure 13. Additionally, tabular, platy, and coffin-shaped structures appeared in SEM images of Clinoptilolite-A<sub>4</sub>, Clinoptilolite-B<sub>1</sub>, and Clinoptilolite-B<sub>3</sub> as in several studies (10,38). It is seen that for both clinoptilolites, significant changes in the structure occur with the increase of the effect of calcination. Agudelo et al. (74) and Wang et al. (2) stated in their study that acid pretreatment did not cause significant changes in zeolite morphology. Also, Mortazavi et al. (12) carried out a different pretreatment using cations, amines, and ionic liquids and determined that there was no significant morphological difference between the pre-treated samples and natural clinoptilolites. In the study of Burris and Juenger (34), they detected agglomeration in the morphological structure of natural clinoptilolite after calcination at very high temperatures such as 965 °C. They determined that after all calcination processes at 300, 500, 800, and 965 °C, small particles were found on the larger zeolite structures in SEM images. In our study,



agglomeration was not observed after calcination, and the occurrence of smaller structures on large particles either did not occur or was negligible. Since the agglomeration seen in the structure is an important feature that restricts the use, and reduces the catalytic activity and selectivity, especially for catalytic purposes, it is very important to choose the most suitable pretreatment method for clinoptilolite and to determine the optimum conditions for this method. In addition, as we encountered in this study, the transformation of shapes of the particle into rod, platy or tabular structures as a result of the pre-treatment processes performed as an alternative to the spherical classical particle structure in the structure can provide advantages in different areas, especially for catalytic use.

The elemental compositions of the natural clinoptilolite and its treated versions were investigated with EDS carried out at 2 different random points. According to Table 5, the major elements of the natural clinoptilolite samples were O, Si, Al, and K additionally small amounts of Mg and Ca. It could be resulted from Table 5 that the amount of Ca and K decreased due to acid treatments and calcination. In the EDS analysis of the Clinoptilolite-B<sub>1</sub> a significant iron and aluminum content was determined compared to other samples. Only, Fe, Ca, K, and Mg content were not identified in Clinoptilolite-A<sub>2</sub>. Mg content is similar to each other for all samples (except Clinoptilolite-A<sub>2</sub>) correlated to XRF analysis results.

## CONCLUSION

The effects of the pre-treatment procedure consisted of acid pretreatment and different calcination temperatures and durations on the main features of clinoptilolites were investigated by comparing with the characteristic features of the natural clinoptilolite sample. Treatment of clinoptilolite with HCl caused mild dealumination, removal of some cations, and impurities, resulting in an increase in surface area and total pore volume. Contrary to many studies in the literature, the suitability of calcination temperature and times in this study is an important result in that calcination does not adversely affect the surface properties of clinoptilolites. Treatment with HCl and calcination resulted in increased BET surface area and decreased mean pore diameter. As a result of pretreatment, there was a strong increase in N<sub>2</sub> adsorption isotherms, thanks to the removal of Al<sup>3+</sup> cations, possible amorphous structures, and impurities from the structure. The increased surface area values can be explained primarily by the presence of micropores. Depending on the increasing Si/Al ratios, an increase in BET surface areas was observed especially in Clinoptilolite-A<sub>1</sub>, Clinoptilolite-A<sub>2</sub>, Clinoptilolite-A<sub>4</sub>, and Clinoptilolite-B<sub>3</sub> samples. In particular, the results of SEM and BET analysis support the conclusion that the pre-treatment method proposed in this study allows the preparation of non-agglomerated, non-sintered, large surface area clinoptilolites suitable for use as a catalyst, catalyst support, or adsorbent. The improvement of properties such as surface area and total pore volume were greater in the sample with smaller particle sizes. In addition, according to the results of thermogravimetric analysis, the weight loss of Clinoptilolite-B (except Clinoptilolite-B<sub>2</sub>) with larger particle size and its pretreated modifications is higher than the pretreated Clinoptilolite-A samples. Although the untreated versions of both natural clinoptilolite samples gave chemically similar results, particle size differences resulted in differences in XRF results with applied

pretreatments. These show that besides chemical or heat treatment, particle size and properties also determine the effect of these treatments on the structure. In future studies, we plan to apply for different uses of these pre-treated zeolites for catalyst, catalyst support, and hydrogen storage.

## CONFLICT OF INTEREST

The author declares that she has no known competing financial interests or personal relationships that could have appeared to influence the work reported in this paper.

## ACKNOWLEDGMENTS

This study was supported by the Yalova University Scientific Research Projects Unit through project No: 2019/AP/0014. I would like to express my sincere thanks to Gordes Zeolite Mining Corporation for their support in the supply of natural clinoptilolite samples. I also would like to thank Prof. Dr. Sibel BASAKCILARDAN KABAKCI for sharing her technical devices such as centrifuge and precision scales. I sincerely would like to thank Dr. Ozlem TUNA for her general support on the some technical issues.

## REFERENCES

1. Çolak A, MiñdiVan F, Göktaş M. İndirgenmiş Grafen Oksit Katkılı UHMWPE Kompozitin Kuru ve Sulu Ortamlarda Aşınma Davranışlarının Karşılaştırılması. Nevşehir Bilim ve Teknoloji Dergisi. 2019 Dec 15;12–20. <DOI>.
2. Wang C, Leng S, Guo H, Cao L, Huang J. Acid and alkali treatments for regulation of hydrophilicity/hydrophobicity of natural zeolite. Applied Surface Science. 2019 Jun;478:319–26. <DOI>.
3. Ates A, Hardacre C. The effect of various treatment conditions on natural zeolites: Ion exchange, acidic, thermal and steam treatments. Journal of Colloid and Interface Science. 2012 Apr;372(1):130–40. <DOI>.
4. Silva M, Lecus A, Lin Y, Corrao J. Tailoring Natural Zeolites by Acid Treatments. MSCE. 2019;07(02):26–37. <DOI>.
5. Wang S, Peng Y. Natural zeolites as effective adsorbents in water and wastewater treatment. Chemical Engineering Journal. 2010 Jan 1;156(1):11–24. <DOI>.
6. Adinehvand J, Shokuhi Rad A, Tehrani AS. Acid-treated zeolite (clinoptilolite) and its potential to zinc removal from water sample. Int J Environ Sci Technol. 2016 Nov;13(11):2705–12. <DOI>.
7. Król MK, Jeleń P. The Effect of Heat Treatment on the Structure of Zeolite A. Materials. 2021 Aug 18;14(16):4642. <DOI>.
8. de Souza V, Villarroel-Rocha J, de Araújo M, Sapag K, Pergher S. Basic Treatment in Natural Clinoptilolite for Improvement of Physicochemical Properties. Minerals. 2018 Dec 14;8(12):595. <DOI>.
9. Cakicioglu-Ozkan F, Ulku S. The effect of HCl treatment on water vapor adsorption characteristics of clinoptilolite rich natural zeolite. Microporous and Mesoporous Materials. 2005 Jan;77(1):47–53. <DOI>.

10. Elaiopoulos K, Perraki Th, Grigoropoulou E. Monitoring the effect of hydrothermal treatments on the structure of a natural zeolite through a combined XRD, FTIR, XRF, SEM and N<sub>2</sub>-porosimetry analysis. *Microporous and Mesoporous Materials*. 2010 Oct;134(1–3):29–43. [<DOI>](#).
11. Koshy N, Singh DN. Fly ash zeolites for water treatment applications. *Journal of Environmental Chemical Engineering*. 2016 Jun;4(2):1460–72. [<DOI>](#).
12. Mortazavi N, Bahadori M, Marandi A, Tangestaninejad S, Moghadam M, Mirkhani V, et al. Enhancement of CO<sub>2</sub> adsorption on natural zeolite, modified clinoptilolite with cations, amines and ionic liquids. *Sustainable Chemistry and Pharmacy*. 2021 Sep;22:100495. [<DOI>](#).
13. Moshoeshoe M, Nadiye-Tabbiruka MS, Obuseng V. A review of the chemistry, structure, properties and applications of zeolites. *Am J Mater Sci*. 2017;7(5):196–221.
14. Dickerson T, Soria J. Catalytic Fast Pyrolysis: A Review. *Energies*. 2013 Jan 21;6(1):514–38. [<DOI>](#).
15. Anand R, Khaire SS, Maheswari R, Gore KU. Alkylation of biphenyl with t-butylalcohol over modified Y zeolites. *Journal of Molecular Catalysis A: Chemical*. 2004 Aug;218(2):241–6. [<DOI>](#).
16. Ivanova II, Kuznetsov AS, Yuschenko VV, Knyazeva EE. Design of composite micro/mesoporous molecular sieve catalysts. *Pure and Applied Chemistry*. 2004 Sep 30;76(9):1647–57. [<DOI>](#).
17. Cherif L, El-Berrichi FZ, Bengueddach A, Tougne P, Fraissard J. Structural evolution of calcium-exchanged (NH<sub>4</sub>)<sub>2</sub>SiF<sub>6</sub>-dealuminated Y zeolite after various chemical treatments. *Colloids and Surfaces A: Physicochemical and Engineering Aspects*. 2003 Jun;220(1–3):83–9. [<DOI>](#).
18. Rivera A, Farías T, de Mênorval LC, Autié-Pérez M, Lam A. Natural and Sodium Clinoptilolites Submitted to Acid Treatments: Experimental and Theoretical Studies. *J Phys Chem C*. 2013 Feb 28;117(8):4079–88. [<DOI>](#).
19. Valdiviés-Cruz K, Lam A, Zicovich-Wilson CM. Full Mechanism of Zeolite Dealumination in Aqueous Strong Acid Medium: Ab Initio Periodic Study on H-Clinoptilolite. *J Phys Chem C*. 2017 Feb 9;121(5):2652–60. [<DOI>](#).
20. Panda AK, Mishra BG, Mishra DK, Singh RK. Effect of sulphuric acid treatment on the physico-chemical characteristics of kaolin clay. *Colloids and Surfaces A: Physicochemical and Engineering Aspects*. 2010 Jun;363(1–3):98–104. [<DOI>](#).
21. Apelian MR, Fung AS, Kennedy GJ, Degnan TF. Dealumination of Zeolite β via Dicarboxylic Acid Treatment. *J Phys Chem*. 1996 Jan 1;100(41):16577–83. [<DOI>](#).
22. Wang C, Cao L, Huang J. Influences of acid and heat treatments on the structure and water vapor adsorption property of natural zeolite. *Surf Interface Anal*. 2017 Dec;49(12):1249–55. [<DOI>](#).
23. Chen X, Srubar WV. Sulfuric acid improves the reactivity of zeolites via dealumination. *Construction and Building Materials*. 2020 Dec;264:120648. [<DOI>](#).
24. Ong LH, Dömök M, Olindo R, van Veen AC, Lercher JA. Dealumination of HZSM-5 via steam-treatment. *Microporous and Mesoporous Materials*. 2012 Dec;164:9–20. [<DOI>](#).
25. Seraj S, Ferron RD, Juenger MCG. Calcining natural zeolites to improve their effect on cementitious mixture workability. *Cement and Concrete Research*. 2016 Jul;85:102–10. [<DOI>](#).
26. Perraki T, Kontori E, Tsivilis S, Kakali G. The effect of zeolite on the properties and hydration of blended cements. *Cement and Concrete Composites*. 2010 Feb;32(2):128–33. [<DOI>](#).
27. Li X, Qiao K, He L, Liu X, Yan Z, Xing W, et al. Combined modification of ultra-stable Y zeolites via citric acid and phosphoric acid. *Appl Petrochem Res*. 2014 Oct;4(4):343–9. [<DOI>](#).
28. Matias P, Lopes JM, Ayraut P, Laforge S, Magnoux P, Guisnet M, et al. Effect of dealumination by acid treatment of a HMCM-22 zeolite on the acidity and activity of the pore systems. *Applied Catalysis A: General*. 2009 Aug;365(2):207–13. [<DOI>](#).
29. Jentys A, Warecka G, Derewinski M, Lercher JA. Adsorption of water on ZSM 5 zeolites. *J Phys Chem*. 1989 Jun;93(12):4837–43. [<DOI>](#).
30. Ahmadi B, Shekarchi M. Use of natural zeolite as a supplementary cementitious material. *Cement and Concrete Composites*. 2010 Feb;32(2):134–41. [<DOI>](#).
31. Bilim C. Properties of cement mortars containing clinoptilolite as a supplementary cementitious material. *Construction and Building Materials*. 2011 Aug;25(8):3175–80. [<DOI>](#).
32. Lilkov V, Petrov O, Petkova V, Petrova N, Tzvetanova Y. Study of the pozzolanic activity and hydration products of cement pastes with addition of natural zeolites. *Clay miner*. 2011 Jun;46(2):241–50. [<DOI>](#).
33. Perraki T, Kontori E, Tsivilis S, Kakali G. The effect of zeolite on the properties and hydration of blended cements. *Cement and Concrete Composites*. 2010 Feb;32(2):128–33. [<DOI>](#).
34. Burris LE, Juenger MCG. Effect of calcination on the reactivity of natural clinoptilolite zeolites used as supplementary cementitious materials. *Construction and Building Materials*. 2020 Oct;258:119988. [<DOI>](#).
35. Florez C, Restrepo-Baena O, Tobon JI. Effects of calcination and milling pre-treatments on natural zeolites as a supplementary cementitious material. *Construction and Building Materials*. 2021 Dec;310:125220. [<DOI>](#).
36. Roussel N, Lemaître A, Flatt RJ, Coussot P. Steady state flow of cement suspensions: A micromechanical state of the art. *Cement and Concrete Research*. 2010 Jan;40(1):77–84. [<DOI>](#).
37. Fernandez R, Martirena F, Scrivener KL. The origin of the pozzolanic activity of calcined clay minerals: A comparison between kaolinite, illite and montmorillonite. *Cement and Concrete Research*. 2011 Jan;41(1):113–22. [<DOI>](#).
38. Elaiopoulos K, Perraki Th, Grigoropoulou E. Mineralogical study and porosimetry measurements of zeolites from Scaloma area, Thrace, Greece. *Microporous and Mesoporous Materials*. 2008 Jul;112(1–3):441–9. [<DOI>](#).

39. Erdoğan B, Dikmen G. Effect of the acid type on clinoptilolite-rich tuff for hydrogen storage. *International Journal of Hydrogen Energy*. 2020 Jan;45(3):2017–21. [<DOI>](#).
40. Dzedzicka A, Sulikowski B, Ruggiero-Mikołajczyk M. Catalytic and physicochemical properties of modified natural clinoptilolite. *Catalysis Today*. 2016 Jan;259:50–8. [<DOI>](#).
41. Davarpanah E, Armandi M, Hernández S, Fino D, Arletti R, Bensaid S, et al. CO<sub>2</sub> capture on natural zeolite clinoptilolite: Effect of temperature and role of the adsorption sites. *Journal of Environmental Management*. 2020 Dec;275:111229. [<DOI>](#).
42. Kennedy DA, Mujčin M, Abou-Zeid C, Tezel FH. Cation exchange modification of clinoptilolite –thermodynamic effects on adsorption separations of carbon dioxide, methane, and nitrogen. *Microporous and Mesoporous Materials*. 2019 Jan;274:327–41. [<DOI>](#).
43. Miądlicki P, Wróblewska A, Kielbasa K, Koren ZC, Michalkiewicz B. Sulfuric acid modified clinoptilolite as a solid green catalyst for solvent-free  $\alpha$ -pinene isomerization process. *Microporous and Mesoporous Materials*. 2021 Sep;324:111266. [<DOI>](#).
44. Ackley MW, Giese RF, Yang RT. Clinoptilolite: Untapped potential for kinetics gas separations. *Zeolites*. 1992 Sep;12(7):780–8. [<DOI>](#).
45. Pabalan RT, Bertetti FP. Cation-Exchange Properties of Natural Zeolites. *Reviews in Mineralogy and Geochemistry*. 2001 Jan 1;45(1):453–518. [<DOI>](#).
46. Moradi M, Karimzadeh R, Moosavi ES. Modified and ion exchanged clinoptilolite for the adsorptive removal of sulfur compounds in a model fuel: New adsorbents for desulfurization. *Fuel*. 2018 Apr;217:467–77. [<DOI>](#).
47. Groen JC, Jansen JC, Moulijn JA, Perez-Ramirez J. Optimal Aluminum-Assisted Mesoporosity Development in MFI Zeolites by Desilication. *ChemInform [Internet]*. 2004 Nov 9 [cited 2022 Jun 13];35(45). [<DOI>](#).
48. Erdoğan Alver B. A comparative adsorption study of C<sub>2</sub>H<sub>4</sub> and SO<sub>2</sub> on clinoptilolite-rich tuff: Effect of acid treatment. *Journal of Hazardous Materials*. 2013 Nov;262:627–33. [<DOI>](#).
49. Nezamzadeh-Ejhieh A, Moazzeni N. Sunlight photodecolorization of a mixture of Methyl Orange and Bromocresol Green by CuS incorporated in a clinoptilolite zeolite as a heterogeneous catalyst. *Journal of Industrial and Engineering Chemistry*. 2013 Sep;19(5):1433–42. [<DOI>](#).
50. Nezamzadeh-Ejhieh A, Amiri M. CuO supported Clinoptilolite towards solar photocatalytic degradation of p-aminophenol. *Powder Technology*. 2013 Feb;235:279–88. [<DOI>](#).
51. Christidis G. Chemical and thermal modification of natural HEU-type zeolitic materials from Armenia, Georgia and Greece. *Applied Clay Science*. 2003 Nov;24(1–2):79–91. [<DOI>](#).
52. Allen SJ, Ivanova E, Koumanova B. Adsorption of sulfur dioxide on chemically modified natural clinoptilolite. *Acid modification. Chemical Engineering Journal*. 2009 Oct 15;152(2–3):389–95. [<DOI>](#).
53. Radosavljevic-Mihajlovic A, Dondur V, Dakovic A, Lemic J, Tomasevic-Canovic M. Physicochemical and structural characteristics of HEU-type zeolitic tuff treated by hydrochloric acid. *J Serb Chem Soc*. 2004;69(4):273–82. [<DOI>](#).
54. Sakızci M, Özgül Tanrıverdi L. Influence of acid and heavy metal cation exchange treatments on methane adsorption properties of mordenite. *Turk J Chem*. 2015;39:970–83. [<DOI>](#).
55. Sato K, Nishimura Y, Matsubayashi N, Imamura M, Shimada H. Structural changes of Y zeolites during ion exchange treatment: effects of Si/Al ratio of the starting NaY. *Microporous and Mesoporous Materials*. 2003 May;59(2–3):133–46. [<DOI>](#).
56. Korkuna O, Lebeda R, Skubiszewska-Zięba J, Vrublevs'ka T, Gun'ko VM, Ryczkowski J. Structural and physicochemical properties of natural zeolites: clinoptilolite and mordenite. *Microporous and Mesoporous Materials*. 2006 Jan;87(3):243–54. [<DOI>](#).
57. Hyeon Kim M, Hwang UC, Nam IS, Gul Kim Y. The characteristics of a copper-exchanged natural zeolite for NO reduction by NH<sub>3</sub> and C<sub>3</sub>H<sub>6</sub>. *Catalysis Today*. 1998 Sep;44(1–4):57–65. [<DOI>](#).
58. Ruiz-Serrano D, Flores-Acosta M, Conde-Barajas E, Ramírez-Rosales D, Yáñez-Limón JM, Ramírez-Bon R. Study by XPS of different conditioning processes to improve the cation exchange in clinoptilolite. *Journal of Molecular Structure*. 2010 Sep;980(1–3):149–55. [<DOI>](#).
59. Favvas EP, Tsanaksidis CG, Sapalidis AA, Tzilantonis GT, Papageorgiou SK, Mitropoulos Ach. Clinoptilolite, a natural zeolite material: Structural characterization and performance evaluation on its dehydration properties of hydrocarbon-based fuels. *Microporous and Mesoporous Materials*. 2016 May;225:385–91. [<DOI>](#).
60. Nezamzadeh-Ejhieh A, Shirzadi A. Enhancement of the photocatalytic activity of Ferrous Oxide by doping onto the nano-clinoptilolite particles towards photodegradation of tetracycline. *Chemosphere*. 2014 Jul;107:136–44. [<DOI>](#).
61. Sánchez NA, Saniger JM, d'Espinose de la Caillerie JB, Blumenfeld AL, Fripiat JJ. Dealumination and surface fluorination of H-ZSM-5 by molecular fluorine. *Microporous and Mesoporous Materials*. 2001 Dec;50(1):41–52. [<DOI>](#).
62. López-Fonseca R, de Rivas B, Gutiérrez-Ortiz JI, Aranzabal A, González-Velasco JR. Enhanced activity of zeolites by chemical dealumination for chlorinated VOC abatement. *Applied Catalysis B: Environmental*. 2003 Mar;41(1–2):31–42. [<DOI>](#).
63. Blancovarela M, Martinezramirez S, Erena I, Gener M, Carmona P. Characterization and pozzolanicity of zeolitic rocks from two Cuban deposits. *Applied Clay Science*. 2006 Jul;33(2):149–59. [<DOI>](#).
64. Aghadavoud A, Rezaee Ebrahim Saraee K, Shakur HR, Sayyari R. Removal of uranium ions from synthetic wastewater using ZnO/Na-clinoptilolite nanocomposites. *Radiochimica Acta*. 2016 Nov 1;104(11):809–19. [<DOI>](#).



65. Mozgawa W. The relation between structure and vibrational spectra of natural zeolites. *Journal of Molecular Structure*. 2001 Sep;596(1–3):129–37. [<DOI>](#).
66. Ramishvili T, Tsitsishvili V, Chedia R, Sanaia E, Gabunia V, Kokiashvili N. Preparation of ultradispersed crystallites of modified natural clinoptilolite with the use of ultrasound and its application as a catalyst in the synthesis of methyl salicylate. *American Journal of Nano Research and Applications*. 2017;5(3–1):26–32.
67. Mozgawa W, Fojud Z, Handke M, Jurga S. MAS NMR and FTIR spectra of framework aluminosilicates. *Journal of Molecular Structure*. 2002 Sep;614(1–3):281–7. [<DOI>](#).
68. Lutz W, Rüscher CH, Heidemann D. Determination of the framework and non-framework [SiO<sub>2</sub>] and [AlO<sub>2</sub>] species of steamed and leached faujasite type zeolites: calibration of IR, NMR, and XRD data by chemical methods. *Microporous and Mesoporous Materials*. 2002 Sep;55(2):193–202. [<DOI>](#).
69. Perraki Th, Orfanoudaki A. Mineralogical study of zeolites from Pentalofos area, Thrace, Greece. *Applied Clay Science*. 2004 Apr;25(1–2):9–16. [<DOI>](#).
70. Akbelen M, Ezber Ç. Investigation of thermal and structural properties of nitric, hydrochloric and sulphuric acid-treated zeolite. *Eskişehir Technical University Journal of Science and Technology A - Applied Sciences and Engineering [Internet]*. 2019 Dec 16 [cited 2022 Jun 13]; [<DOI>](#).
71. Kowalczyk P, Sprynskyy M, Terzyk AP, Lebedynets M, Namieśnik J, Buszewski B. Porous structure of natural and modified clinoptilolites. *Journal of Colloid and Interface Science*. 2006 May;297(1):77–85. [<DOI>](#).
72. Elizalde-González MP, Mattusch J, Wennrich R, Morgenstern P. Uptake of arsenite and arsenate by clinoptilolite-rich tuffs. *Microporous and Mesoporous Materials*. 2001 Aug;46(2–3):277–86. [<DOI>](#).
73. Segawa K, Shimura T. Effect of dealumination of mordenite by acid leaching for selective synthesis of ethylenediamine from ethanolamine. *Applied Catalysis A: General*. 2000 Mar;194–195:309–17. [<DOI>](#).
74. Agudelo JL, Hensen EJM, Giraldo SA, Hoyos LJ. Influence of steam-calcination and acid leaching treatment on the VGO hydrocracking performance of faujasite zeolite. *Fuel Processing Technology*. 2015 May;133:89–96. [<DOI>](#).



## Simulation of Hydrogen Production from Hydrolysis of Ammonia Borane for Hydrogen Fuel Cell Applications through Aspen HYSYS

Sefa Aras<sup>1</sup> , Derya Ünlü<sup>1\*</sup> 

<sup>1</sup> Bursa Technical University, Chemical Engineering Department, Bursa, 16310, Turkey

**Abstract:** Hydrogen is an efficient, clean, and sustainable energy carrier with high energy density and zero emission, which can find important applications in fuel cells. Hydrolysis of ammonia borane is an enormous alternative to produce hydrogen. In this study, the hydrogen production via hydrolysis of ammonia borane for hydrogen fuel cell applications was investigated by using ASPEN HYSYS. Firstly, the thermodynamic method and suitable reactor were specified with depending on hydrogen production rate. The influences of reaction temperature and feed mass flow rate of water on the hydrogen production rate were studied. Hydrogen was acquired in the act of mixture with ammonia, boric acid, and unreacted water at the end of the reaction. First of all, solid boric acid was removed from the product mixture. Hydrogen would be purified from ammonia and water by using the separatory equipment. The goal of this study is to obtain the high production rate and high purity of hydrogen for hydrogen fuel cell applications. The optimum operation parameters were determined as 30°C of reaction temperature and 0.1 of feed water concentration. 99.9% purity of hydrogen was obtained at 30°C. The obtained results show that ASPEN HYSYS could be successfully applied for the determination of optimum reaction conditions and appropriate equipment for high production rate and purity hydrogen production from hydrolysis of ammonia borane.

**Keywords:** Ammonia borane, Aspen HYSYS, Hydrogen, Simulation

**Submitted:** June 04, 2022. **Accepted:** July 15, 2022.

**Cite this:** Aras S, Ünlü D. Simulation of Hydrogen Production from Hydrolysis of Ammonia Borane for Hydrogen Fuel Cell Applications through Aspen HYSYS. JOTCSB. 2022;5(2):59-66.

\*Corresponding author. E-mail: [derya.unlu@btu.edu.tr](mailto:derya.unlu@btu.edu.tr).

### INTRODUCTION

In parallel with technological developments and population growth, the energy requirements of countries are increasing gradually. In this respect, energy has strategic importance worldwide. Energy is directly related to the economic development of countries as well as their security. The researches for new and alternative energy sources and integration with existing energy systems are important steps for sustainability (1-2). Fossil-based fuel reserves are gradually decreased and caused environmental pollution (3-5). Hydrogen production is a suitable environmental solution. Because, hydrogen-based energy systems which are high-quality, efficient, clean, reliable, and sustainable, sufficiently meets the conditions expected from an energy source (6-7).

Hydrogen is considered the clean fuel of the future due to its advantages such as high energy density ( $142 \times 10^3$  kJ / kg) and electronegative properties. In addition to these, the reasons such as high heat conversion, energy power, and no harmful wastes when burned with oxygen, being natural and renewable, unlimited, being used in industry, houses and vehicles, makes it advantageous among the alternative energy sources (7-9).

Fuel cells use hydrogen to convert chemical energy into electrical energy. Depending on evolution of fuel cells, studies about storage and production of hydrogen are also being performed (10-11).

The biggest advantage of systems using chemical hydrides for hydrogen production is that hydrogen is not storable, but generable when needed. By using this system, all risks and difficulties of hydrogen storage are eliminated. Among the chemical

hydrides, sodium boron hydride and ammonia borane have promising potential for using hydrogen energy in vehicles as solid hydrogen storage materials. When these two materials are compared, ammonia borane contains more hydrogen than sodium boron hydride (sodium boron hydride contains 10.8 wt.% H<sub>2</sub>, ammonia borane contains 19.6 wt. % H<sub>2</sub>). Also, the aqueous solution of sodium boron hydride is unstable and a base is added to the solution for stabilization. In contrast, ammonia borane has higher solubility and a more stable structure in an aqueous solution. Non-toxic, safe storage, high solubility in water, high stability in aqueous solution, and dehydrogenation in low temperature are other advantages of ammonia borane. Due to such prominent properties, it is possible to use ammonia borane as a high-density hydrogen generator in portable fuel cells (12-16).

Hydrogen generation is carried out by hydrolysis of ammonia borane. 1 mol of ammonia borane reacts and 3 mol of hydrogen occurs (16). The hydrolysis reaction of ammonia borane was given in the following equation.



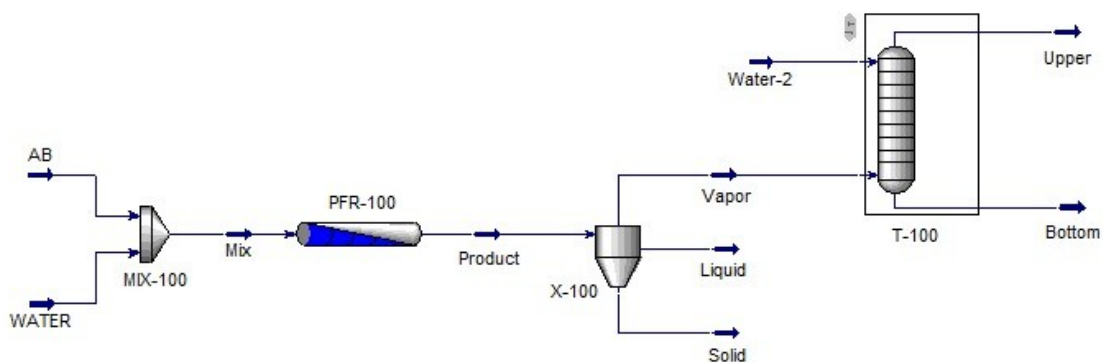
By using this method, rapid and controllable hydrogen production is possible. Hydrogen

production by hydrolysis method in catalytic systems directly depends on the active substance and surface area of the catalyst. The biggest advantage of this method is that hydrogen can be produced quickly and at low temperatures (17-18).

In literature, there are lots of experimental studies about the hydrolysis of ammonia borane. According to the author’s knowledge, this is the first study on simulation of hydrogen production from hydrolysis of ammonia borane by using Aspen HYSYS. In this research, suitable reactor for the reaction was selected and designed in Aspen HYSYS. The convenient thermodynamic method for the reaction was specified. After that, the details of simulation were given. The optimum reaction conditions such as reaction temperature and feed flow rate of water were determined. By the determination of optimum process conditions, hydrogen synthesis from hydrolysis of ammonia borane process design was simulated.

**SIMULATION MODELING**

Hydrogen production from hydrolysis of ammonia borane was investigated with ASPEN HYSYS. The scheme of simulation of the hydrogen production process is shown in Figure 1.



**Figure 1:** Scheme of simulation of hydrogen production.

The list of equipment was given in Table 1.

**Table 1:** Equipment list in simulation.

Equipment Code	Equipment Description	Duty
MIX-100	Mixer	Mixing of feed components
PFR-100	Plug flow reactor	Hydrogen production from hydrolysis of ammonia borane
T-100	Absorption column	Purification of hydrogen

Water and ammonia borane at different feed flow rates were fed to the mixer and stirred. After the mixer, the mixture of water-ammonia borane entered the plug flow reactor. The hydrogen synthesis from hydrolysis of ammonia borane was operated in a plug flow reactor. At the end of the reaction; hydrogen, boric acid, unreacted water

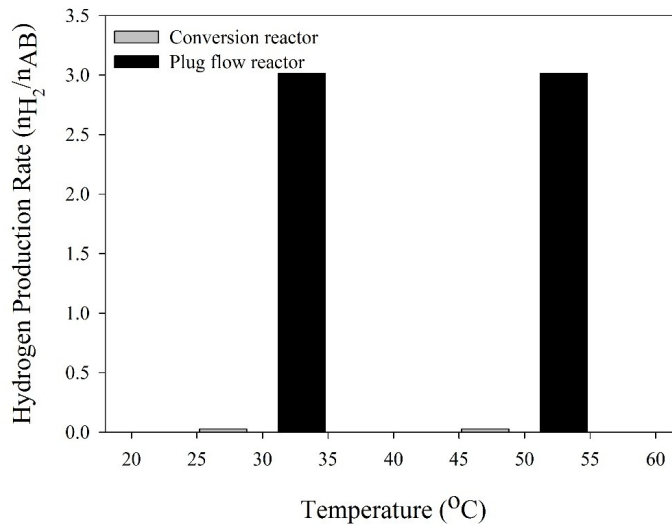
were obtained. The reaction products were initially sent to the simple solid separator. Boric acid was removed from the mixture in this equipment. Vapor phase, which contained hydrogen, water, and ammonia, was sent to the absorption column. Finally, hydrogen was purified by using an absorption column and obtained as pure.

## RESULTS AND DISCUSSION

### Selection of Reactor Type

The appropriate reactor type was determined according to the hydrogen production rate.

Hydrolysis reaction of ammonia borane was carried out by using a conversion reactor and a plug flow reactor. Determination of appropriate reactor type was investigated on hydrogen production rate ( $n_{H_2}/n_{AB}$ ) with the changing temperature.



**Figure 2:** Selection of reactor type in different temperature.

Figure 2 shows the hydrogen production rate in conversion and plug flow reactor. Hydrogen production rate in the plug flow reactor is higher than that of the hydrogen production rate in the conversion reactor. This result is related to the working principle of reactors. Plug flow reactor is based on reaction mechanism and used catalyst features. As ammonia borane and water flow and reacted along the reactor, hence, the axial change in concentration value observed. The conversion reactor is only based on conversion and stoichiometric ratio. Conversion values are defined to the reactor by the user. Reaction continues until the particular conversion has been acquired. However, PFR calculates the reaction yield according to reaction mechanism and catalytic properties. In experimental studies, catalyst has an important effect for the reaction. From all reasons above, PFR was used to simulate hydrogen production. Due to the more production of hydrogen, a plug flow reactor was used for all processes. The reaction is exothermic, so there is no effect of temperature increment on the hydrogen production rate.

While the obtained hydrogen production rate was 0.0270 in the conversion reactor, this value was 3.014 for the plug flow reactor.

### Selection of Thermodynamic Model

Thermodynamic methods are utilized to show the phase equilibrium and energy level of components

in the systems. There are five types of property methods in ASPEN HYSYS. The equations of state, activity models, Chao-Seader based empirical methods, vapor pressure models, and miscellaneous methods are available as thermodynamic models. The equations of state are generally recommended for oil, gas, and petrochemical applications. It can be used for single, two, and three-phased systems. The model calculates the properties with high efficiency. The Activity Models is mostly preferred for non-ideal systems. The Chao-Seader is an older and semi-empirical method. Vapor Pressure model is to be utilized for ideal mixtures at low pressure values. The Miscellaneous methods are preferred if the groups previously mentioned do not fit.

In this study, equations of state and activity models were tested. Soave-Redlich-Kwong (SRK), Peng Robinson (PENG-ROB), Peng-Robinson Stryjek Vera (PRSV) in equations of state and Non-Random-Two-Liquid (NRTL), Wilson, UNIVERSAL QUASI Chemical (UNIQUAC) in activity models are applied. The activity methods are resulted in low hydrogen composition according to the EOS. Besides that, byproduct amounts increased while the activity models were used due to the formation of low hydrogen amount. Especially, formation of more ammonia is an undesired state for fuel cell applications. Therefore, the low amount byproduct formation was chosen. The obtained results were given in Table 2.

**Table 2:** The selection of thermodynamic method.

Property Package	Model	Hydrogen Composition
Equations of State	PENG-ROB	0.9347
	SRK	0.9306
	PRSV	0.9229
Activity Models	NRTL	0.8647
	WILSON	0.8456
	UNIQUAC	0.8586

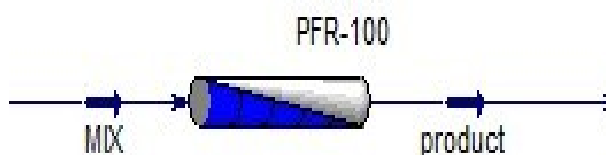
All thermodynamic methods were examined in 30 °C of reaction temperature, 0.01 kg/h of water mass flow rate and 1 bar of pressure. According to Table 2, Peng Robinson method was selected was chosen as an appropriate thermodynamic model. Also, hydrogen synthesis reaction from hydrolysis of ammonia borane results in the formation of solid, liquid, and vapor phase products. Therefore, the usage of equations of state is appropriate for this process. Because these methods can be used for single, two and three phase systems. Among equations of state models, the Peng Robinson model has been chosen as an appropriate thermodynamic model.

### Simulation Details of Hydrogen Production from Hydrolysis of Ammonia Borane

Hydrogen production from hydrolysis of ammonia borane has not been examined previously in the ASPEN HYSYS simulation programme. No study is available in the literature on the Hydrogen production

from hydrolysis of ammonia borane by using ASPEN HYSYS. According to the author's knowledge, this is the first study on ASPEN HYSYS simulation of hydrogen production from hydrolysis of ammonia borane.

According to the stoichiometric ratio, excess water was fed to the reactor. Also, usage of diluted ammonia borane in reaction has some advantages such as the formation of low byproduct, the decrement of the increase in ambient temperature due to the exothermic reaction. 1 mol of ammonia borane reacts and 3 mol of hydrogen occurs (16, 19). At the first stage of the process, water and ammonia borane were stirred in a mixer at 30 °C and 1 bar. Ammonia borane is a solid component, mixed with water and was dissolved, liquid mixture was achieved. The mixed stream was obtained and sent to plug flow reactor. Plug Flow Reactor (PFR) which is shown in Figure 3 is used for hydrogen generation.

**Figure 3:** Plug flow reactor.

Plug flow reactor was operated 30 °C and 1 bar. The usage of appropriate catalyst plays a significant part on the hydrogen generation rate. The used catalyst was a ruthenium based catalyst. The researches in literature confirmed that ruthenium-based catalysts

are one of the most productive catalysts for the ammonia borane hydrolysis reaction (20-24). The features of the used catalyst can be seen in Table 3. These values are also defined in simulation programme.

**Table 3:** The catalyst data.

Particle Diameter	3.8e-009 m
Particle Sphericity	1
Solid Density	0.5 kg/m <sup>3</sup>
Bulk Density	0.15 kg/m <sup>3</sup>
Solid Heat Capacity	10 kJ/kg°C

The feed molar flow rates of ammonia borane and water are  $1.5 \times 10^{-6}$  and  $5.55 \times 10^{-3}$  kmol/h. The conversion of ammonia borane was 100%. There is no ammonia borane in product stream. The produced

hydrogen molar flow rate is  $5.542 \times 10^{-3}$  kmol/h. The hydrogen production rate ( $n_{H_2}/n_{AB}$ ) was calculated as 0.19. The molar composition of the product stream was given in Table 4.

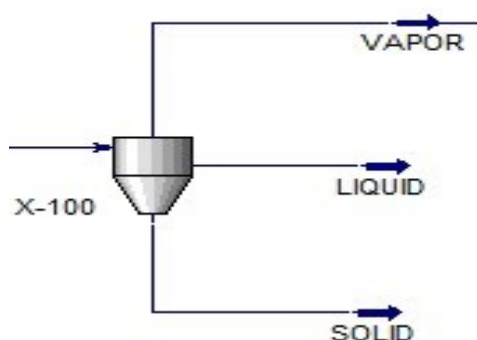


**Table 4:** The molar composition of the product stream.

Components	Mole Fraction
H <sub>3</sub> BO <sub>3</sub>	0.0003
Hydrogen	0.0008
H <sub>2</sub> O	0.9986
AB	0.0003
NH <sub>3</sub>	0.0027

The products of hydrogen synthesis reaction are H<sub>3</sub>BO<sub>3</sub>, NH<sub>3</sub>, H<sub>2</sub> and unreacted water. The H<sub>3</sub>BO<sub>3</sub> was obtained as a solid phase at the end of the reaction. Therefore, the removal of H<sub>3</sub>BO<sub>3</sub> gains importance

for the obtain pure hydrogen. For this purpose, solid separator was used. The simple solid separator equipment is shown in Figure 4.

**Figure 4:** Simple solid separator.

The solid phase was completely separated. Due to the no hydrogen in a liquid phase, the vapor phase

was sent to the separator. The molar composition of each stream in the exit side was given in Table 5.

**Table 5:** The molar composition of the product stream.

Components	Solid	Vapor	Liquid
H <sub>3</sub> BO <sub>3</sub>	1	0.0000	0.0000
Hydrogen	0.0000	0.9915	0.0000
H <sub>2</sub> O	0.0000	0.0077	0.9973
AB	0.0000	0.000	0.000
NH <sub>3</sub>	0.0000	0.0008	0.0027

Vapor stream includes Hydrogen, H<sub>2</sub>O and NH<sub>3</sub> components. Hydrogen should be purified from water and NH<sub>3</sub>. Therefore, the separator should be used in the process. For that purpose, an absorption column was used and a high purify of hydrogen was obtained. The used absorption column is shown in Figure 5.

The additional water stream was given in the absorption column. Ammonia was dissolved easily in water, and separated from hydrogen. 99.15 wt. % hydrogen purity was obtained in the upper stream.

### Investigation of Reaction Parameters

#### Effect of temperature

To investigate the effect of temperature on the hydrogen production reaction from hydrolysis of ammonia borane, the temperature range was chosen as 20-50 °C with 10 °C of increment. The observed mass fraction of hydrogen and ammonia were given in Figure 6.

Figure 5: Absorption column.

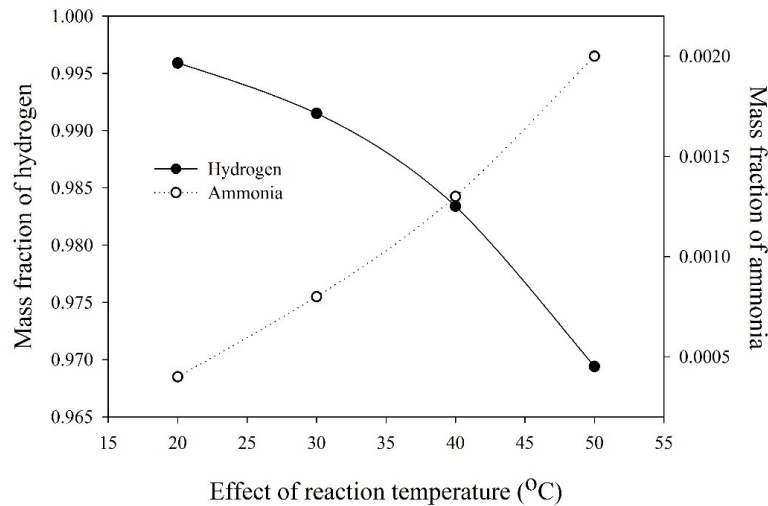
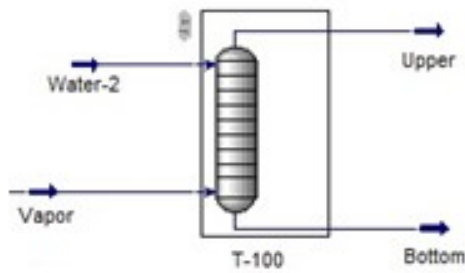


Figure 6: Effect of reaction temperature.

The hydrogen production from hydrolysis of ammonia borane is an exothermic reaction. Therefore, an increase in temperature results in low hydrogen concentration (7, 17, 25). With the raise in reaction temperature from 20 °C to 50 °C, the mass fraction of hydrogen decreases from 0.9959 to 0.9694. Besides, the mass composition of ammonia increased from 0.0004 to 0.0022. The maximum H<sub>2</sub> mass composition was acquired at 20 °C. This is the expected result.

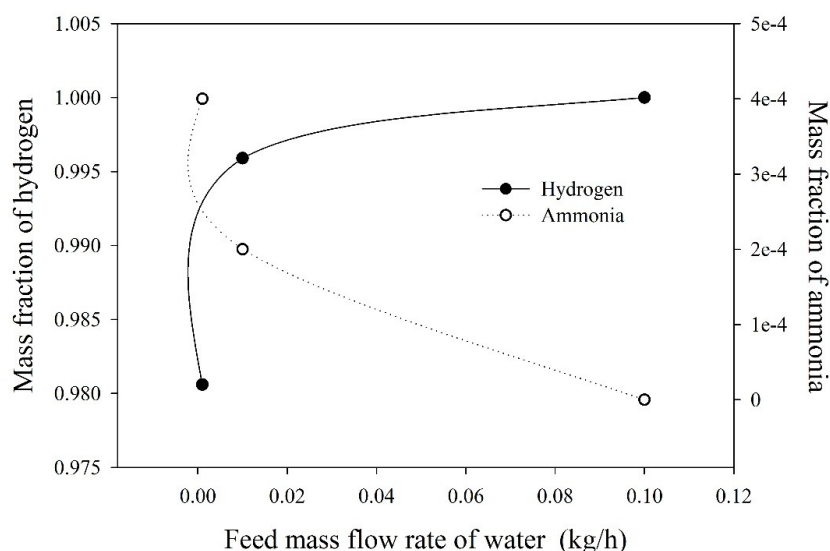
*Effect of feed mass flow rate of water*

To investigate the effect of the feed mass flow rate of water on the mass fraction of hydrogen and ammonia in the hydrolysis of ammonia borane, the water at different ratios were fed to the system. The dependence of the feed mass flow rate of water on the mass fraction of hydrogen and ammonia is investigated by varying the mass flow rate of water from 0.001 kg/h to 0.1 kg/h, and the results are shown in Figure 7.

With the increase of the feed mass flow rate of water, the mass fraction of hydrogen increased. When the feed mass flow rate of water was 0.1 kg/h, the highest hydrogen composition was obtained. As the water concentration increased in the feed mixture, ammonia borane in the feed mixture was diluted. In experimental studies, diluted ammonia borane was used for the reaction.

As the increment of dilution of the ammonia borane, the formation of ammonia had been decreased. This result was supported by the literature. It can be explained that the use of dilute Ammonia borane solution reduces the increase in ambient temperature as a result of the exothermic reaction, thus reducing the formation of ammonia (26-27).

As seen in Figure 7, when the feed mass flow rate of water was increased from 0.001 to 0.1 kg/h, the mass fraction of hydrogen increased from 0.9806 to 1. Under the same conditions, ammonia concentration decreased from 0.0004 to 0.



**Figure 7:** Effect of feed mass flow rate.

## CONCLUSION

The hydrogen production from hydrolysis of ammonia borane had been carried out in conversion and Plug flow reactor. The highest hydrogen mass composition was achieved in plug flow reactor. Plug flow reactor calculates the reaction yield according to the reaction mechanism and catalytic properties. Therefore, a plug flow reactor was preferred for hydrogen synthesis. Peng Robinson as the thermodynamic model was selected. Peng Robinson is one of the equations of state model. It can be utilized for multiple phase systems. Then, the general simulation design was investigated. The details of each equipment were explained. After that, the effects of temperature and feed mass flow rate of water were investigated. Firstly, the effect of temperature on the mass fraction of hydrogen was examined. A decrement of hydrogen fraction was detected in high temperature values. This result is related to the exothermic behavior of the reaction. The optimum temperature was found as 20 °C. The feed mass flow rate of water was also investigated. The mass fraction of hydrogen increased with increasing water amount in the feed mixture. As the increment of dilution of the ammonia borane, the formation of ammonia had been decreased. Therefore, the optimum feed mass flow rate was chosen as 0.1 kg/h. Also, the hydrogen was purified with absorption column. At the end of the purification, hydrogen was achieved as 99.15 vol % purity at 1 bar and 30 °C. The study conducted show that ASPEN HYSYS can be used to hydrogen production from hydrolysis of ammonia borane.

## CONFLICT OF INTEREST

The author declares that there is no conflict of interest.

## REFERENCES

1. Gielen D, Boshell F, Saygin D, Bazilian MD, Wagner N, Gorini R. The role of renewable energy in the global energy transformation. *Energy Strategy Rev.* 2019; 24:38–50. [<URL>](#).
2. Caruso G, Colantonio E, Gattone SA. Relationships between Renewable Energy Consumption, Social Factors, and Health: A Panel Vector Auto Regression Analysis of a Cluster of 12 EU Countries. *Sustainability.* 2020; 12(7):2915. [<URL>](#).
3. Parthasarathy P, Narayanan KS, Hydrogen production from steam gasification of biomass: Influence of process parameters on hydrogen yield–A review. *Renew Energy.* 2014; 66:570–579. [<URL>](#).
4. Koroneos C, Dompros A, Roumbas G. Hydrogen production via biomass gasification-a life cycle assessment approach. *Chem Eng Process* 2008; 47:1261-1268. [<URL>](#).
5. Yüksel Alpaydın C, Gülbay SK, Colpan OC. A review on the catalysts used for hydrogen production from ammonia borane. *Int J Hydrogen Energy* 2019; 45(5):3414-3434. [<URL>](#).
6. Dutta S. A review on production, storage of hydrogen and its utilization as an energy resource. *J Ind Eng Chem.* 2014; 20:1148–1156. [<URL>](#).
7. Ozay O, Inger E, Aktas N, Sahiner N. Hydrogen production from ammonia borane via hydrogel template synthesized Cu, Ni, Co composites. *Int J Hydrogen Energy.* 2011; 36:8209–8216. [<URL>](#).
8. Kantürk FA. Improved catalytic performance of metal oxide catalysts fabricated with electrospinning

- in ammonia borane methanolysis for hydrogen production. *Int J Hydrogen Energy*. 2019; 44: 8451-28462. [<URL>](#).
9. Ozay H, Ilgin P, Ozay O. Hydrogen production via copper nanocatalysts stabilized by cyclen derivative hydrogel networks from the hydrolysis of ammonia borane and ethylenediamine bisborane. *Int J Hydrogen Energy*. 2020; 45(35): 17613-17624. [<URL>](#).
10. Staffell I, Scamman D, Velazquez AA, Balcombe P, Dodds PE, Ekins, P, Ward KR. The role of hydrogen and fuel cells in the global energy system. *Energy Environ Sci*. 2019; 12:463-491. [<URL>](#).
11. Manoharan Y, Hosseini SE, Butler B, Alzahrani H, Senior BTF, Ashuri T, Krohn J. Hydrogen Fuel Cell Vehicles; Current Status and Future Prospect. *Appl Sci*. 2019; 9(11):2296. [<URL>](#).
12. Metin Ö, Şahin Ş, Özkar S, Water-soluble poly(4-styrenesulfonic acid-co-maleic acid) stabilized ruthenium(0) and palladium(0) nanoclusters as highly active catalysts in hydrogen generation from the hydrolysis of ammonia-borane. *Int J Hydrogen Energy*. 2009; 34:6304-6313. [<URL>](#).
13. Rakap M, Özkar S, Hydrogen generation from the hydrolysis of ammonia borane using intrazeolite cobalt (0) nanoclusters catalyst. *Int J Hydrogen Energy*. 2010; 35:3341-3346. [<URL>](#).
14. Shang N, Zhou X, Feng C, Gao S, Wu Q, Wang C. Synergetic catalysis of Ni Pd nanoparticles supported on biomass-derived carbon spheres for hydrogen production from ammonia borane at room temperature. *Int J Hydrogen Energy*. 2017; 42:5733-5740. [<URL>](#).
15. Inoue H, Yamazaki T, Kitamura T, Shimada M, Chiku M, Higuchi E. Electrochemical hydrogen production system from ammonia borane in methanol solution. *Electrochimica Acta*. 2012; 82:392-396. [<URL>](#).
16. Lai SW, Park JW, Yoo SH, Ha JM, Song EH, Cho SO. Surface synergism of Pd/H<sub>2</sub>Ti<sub>3</sub>O<sub>7</sub> composite nanowires for catalytic and photocatalytic hydrogen production from ammonia borane. *Int J Hydrogen Energy*. 2016; 41:3428-3435. [<URL>](#).
17. Mohajeri N, T-Raissi A, Adebisi O. Hydrolytic cleavage of ammonia borane complex for hydrogen production. *J. Power Sources*. 2007; 167:482-485. [<URL>](#).
18. Liu CH, Wu YC, Chou CC, Chen BH, Hsueh CL, Ku JR, Tsau F. Hydrogen generated from hydrolysis of ammonia borane using cobalt and ruthenium based catalysts. *Int J Hydrogen Energy*. 2012; 37:2950-2959. [<URL>](#).
19. Gil-San-Millan R, Grau-Atienza A, Johnson DT, Rico-Francés S, Serrano E, Linares N, García-Martínez J. Improving hydrogen production from the hydrolysis of ammonia borane by using multifunctional catalysts. *International Journal of Hydrogen Energy*. 2018; 43(36):17100-17111. [<URL>](#).
20. Navlani-García M, Mori K, Nozaki A, Kuwahara Y, Yamashita H. Highly efficient Ru/carbon catalysts prepared by pyrolysis of supported Ru complex towards the hydrogen production from ammonia borane. *Appl Catal A*. 2016; 527:45-52. [<URL>](#).
21. Can H, Metin Ö. A facile synthesis of nearly monodisperse ruthenium nanoparticles and their catalysis in the hydrolytic dehydrogenation of ammonia borane for chemical hydrogen storage. *Appl Catal B*. 2012; 125:304-310. [<URL>](#).
22. Ma H, Na C. Isokinetic Temperature and Size-Controlled Activation of Ruthenium-Catalyzed Ammonia Borane Hydrolysis. *ACS Catalysis*. 2015; 5(3):1726-1735. [<URL>](#).
23. Chen G, Desinan S, Rosei R, Rosei F, Ma D. Synthesis of Ni-Ru Alloy Nanoparticles and Their High Catalytic Activity in Dehydrogenation of Ammonia Borane. *Chemistry - A European Journal*. 2012; 18(25):7925-7930. [<URL>](#).
24. Wright WRH, Berkeley ER, Alden LR, Baker, RT, Sneddon LG. (2011). Transition metal catalysed ammonia-borane dehydrogenation in ionic liquids. *Chem Comm*. 2011; 47(11):3177-3179. [<URL>](#).
25. Chou CC, Lee DJ, Chen BH. Hydrogen production from hydrolysis of ammonia borane with limited water supply. *Int J Hydrogen Energy*. 2012; 37:15681-15690. [<URL>](#).
26. Tunç N, Rakap M. Preparation and characterization of Ni-M (M: Ru, Rh, Pd) nanoclusters as efficient catalysts for hydrogen evolution from ammonia borane methanolysis. *Renew Energy*. 2020; 155:1222-1230. [<URL>](#).
27. Ramachandran PV, Gagare PD. Preparation of ammonia borane in high yield and purity, methanolysis and regeneration. *Inorg Chem*. 2007; 46:7810-7817. [<URL>](#).



## Dye Removal from Aqueous Solutions Using Natural and Biochar Butt: Full Factorial Design Approach

Sevda Esma Darama\* , Semra Çoruh , Yusuf Tibet 

Ondokuz Mayıs University, Faculty of Engineering, Department of Environmental Engineering, Samsun, Turkey

**Abstract:** High concentrations of dye-containing wastewater are generated from industries that produce intense dyes, such as textiles. These wastewaters cause serious environmental and human health problems when they are discharged into natural environments without adequate treatment. Adsorption is a frequently used, effective, and easy method to prevent this situation. However, commercial activated carbon, which is used as an adsorbent material, is often needed to be regenerated, and, this creates economic problems. This study investigated the usability of cigarette butts as an inexpensive alternative to commercial activated carbon. Cigarette butts in natural and biochar forms were used to remove malachite green dyestuff.  $2^3$  full factorial modeling was used to model the adsorption efficiency. Because of this modeling, the parameters that have the main effect on adsorption have been revealed. In the experiments, 3 factors were examined at 2 levels. These are, adsorbent amount (0.005 g/30 mL and 0.1 g/30 mL), initial dye concentration (50 mg/L and 500 mg/L), and adsorbent type (natural and biochar butts). The dyestuff removal efficiency was obtained in the study, up to 96%. According to the results of the model graphics, the factor that has the most effect on adsorption is the adsorbent type. The biochar form gave very high efficiency results compared to the natural form. It was seen that the adsorbent dose was the factor with the lowest effect on the adsorption efficiency.

**Keywords:** Adsorption, biochar, butt, dye, full factorial design.

**Submitted:** May 14, 2022. **Accepted:** July 18, 2022.

**Cite this:** Darama SE, Çoruh S, Tibet Y. Dye Removal from Aqueous Solutions Using Natural and Biochar Butt: Full Factorial Design Approach. Journal of the Turkish Chemical Society, Section B: Chemical Engineering. 2022;5(2):67-76.

\*Corresponding author. E-mail: [sevda.akkaya@omu.edu.tr](mailto:sevda.akkaya@omu.edu.tr).

### INTRODUCTION

Dyes are widely used in various industries, such as textiles, paper, plastics, cosmetics, ceramics, and leather, for coloring their final products. To remove dyes from aqueous solutions, many chemical or biological treatments have been used either individually or together (1-2). There are several methods for dye removal, such as adsorption, oxidation-ozonation, coagulation, coagulation-flocculation, and biological methods. Among these removal methods, adsorption is an attractive alternative method. Many adsorbents have been tested on the possibility to lower concentrations from aqueous solutions, such as active carbon, peat, olive oil waste, chitin, red mud, calcite, clay, natural

zeolites, bentonite, sepiolite, perlite, iron oxide coated sand, burnside, and others (3).

Malachite green is a toxic chemical often used to dye materials such as fabric, leather, and paper. Although it causes many health problems, it is widely used today due to its cheapness and ease of use. Malachite green is found in many industrial wastewater-containing dyes. Due to its harmful effects on nature and human health, its treatment is mandatory. Therefore, malachite green was chosen as the dyestuff in this study.

Industrial and technological progress required massive consumption of natural energy resources in recent years. For this reason, energy resources



have started to decrease rapidly. Biomass is much more than firewood or just another fuel source. Electrical or stationary energy can be provided by hydro, solar, thermal, geothermal, wind, wave, and even nuclear power in a post-fossil fuel and C-constrained economy (4-5). Biomass can produce primary gas, liquids, solids, or the C-based chemicals we currently obtain from fossil supplies. It is worth noting that during its growth phase, biomass contributes significantly to providing ecosystem services, other organisms' biodiversity, and recreational values. The energy stored in biomass can be used to produce renewable electricity, thermal energy, or transportation fuels (6).

Previous studies have reported the application of hydrochar as adsorbents for the removal of metals (7), dyes (8), drugs (9) and herbicides (10) from aqueous solutions. However, restrictions on applying hydrocarbons for adsorption processes cause low adsorption capacity, generally due to low porosity and specific area. For more efficient use of these materials, hydrochars should be subjected to an activation process to increase their adsorption capacity (11). The activating agent plays a vital role in forming the pore structure and determining the physicochemical properties of the resulting hydrocarbons. Typical activation approaches can be divided into physical and chemical activation. It has many advantages such as chemical activation, low operating temperature, short activation time, well-developed pore structure and high efficiency (12).

In this study, butts with high waste capacity were selected as biomass. Disposed of cigarette filters, in the form of cigarette butts, are a major waste disposal and environmental pollution hazard, mainly because they contain biodegradable cellulose

acetate; Worldwide, 5.8 trillion cigarettes are smoked annually and 4 million 800 thousand tons of cigarette butts are produced (13). In addition to causing litter, cigarette butts contain pollutants such as toxic heavy metals that may leak into waterways, potentially damaging humans and wildlife. To convert hazardous wastes into high-value products, this study investigates the evaluation of smoked cigarette filters/butts disposed of (14). In addition, the large amount and waste state of butts make it a more economical adsorbent option. Adsorption studies with butts are also very limited in the literature. For all these reasons, butts were chosen as an adsorbent in this study.

This study investigated the efficiency of large cigarette butts in the form of waste in removing malachite green with activated hydrochar forms. The conditions under which the removal efficiency depends on the selected adsorption conditions were examined by applying to the full factorial model.

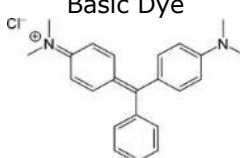
## MATERIAL AND METHOD

### Materials

The remaining cigarette butts after consumption were used as adsorbents. Cigarette butts collected by our means were separated from the paper and prepared for experiments with only filter parts remaining.

Basic dye form of Malachite Green ( $C_{23}H_{26}ClN_2$ ) was selected for adsorption studies. The stock solution of 1000 mg/L was prepared by dissolving accurately weighed amounts of malachite green in 1000 mL distilled water. Table 1 shows some properties of the dye. All experiments were performed in duplicate and the average values were used for data analysis.

**Table 1:** Some properties of malachite green dye.

Basic Dyes Properties	Malachite green
C.I. No	42000
CAS No	5596-64-2
Chemical Formula	$C_{23}H_{26}ClN_2$
Molecular Weight (g/mol)	364.92
Melting Point (°C)	164
C.I. Name	Basic Dye
Molecular Structure	

## Method

### Hydrochar production

Butts separated from paper to be converted into hydrocarbons: The experiment was carried out by

mixing 1:8 (solid: liquid) with pure water in a 250-mL fully enclosed steel reactor.

80 mL of purified water was placed in the reactor with 10 g of butts. After completely closing the

reactor, it was left in the ash oven at 250°C for 5 hours. At the end of the time, the reactor was removed from the furnace and cooled with cold water. The slurry sample was taken into the washing paper and dried in the oven at 50-60 °C for 24 hours. The result was a black powder of hydrochar.

#### Chemical activation phase

The dry hydrocarbon tobacco was activated by mixing in a pyrolysis mechanism at 600 °C with 1:4 KOH and washing with acid; KOH in dry pellets was pulverized using a pestle, mixed with 10 g of hydrochars and 40 g of powdered KOH. The mixture was pyrolyzed at 600 °C, 5 °C/min, one hour residence time, and 100 mL/min nitrogen gas flow rate. The product obtained after pyrolysis was placed in vacuum filtration apparatus and washed with 2 M hydrochloric acid (HCl) dropwise. After the reaction with acid, it was washed several times with purified water to neutralize. After washing, it was dried in the oven at 50-60 °C for 24 hours. As a result of all these processes, approximately 2-3 g of product is obtained.

#### Adsorption study and full factorial modeling

In this study, a Full Factorial Design of the Experiment was designed to investigate the effect of adsorbent amount, initial dye concentration and adsorbent type on the removal of malachite green

dye ions with natural and biochar butts. The samples were mixed at predetermined periods at a temperature of 23 °C in a shaker at 150 rpm until equilibrium was reached. The concentrations of the dyes were determined using a UV/Vis Spectrophotometer.

The removal efficiency (E) of natural and biochar butt on malachite green dye was calculated according to the following formula (Eq. 1):

$$E(\%) = (C_0 - C_e) / C_0 \times 100 \quad (1)$$

Where  $C_0$  is the initial concentration of the dye solution and  $C_e$  is the final concentration of the dye solution.

Full Factorial Design of Experiments examines every possible combination of factors at the levels tested (15-16). The general notation for a full factorial design run at b levels is  $b^k$  Runs, where k is the number of factors (17).

This study aims to maximize the removal of malachite green dye ions (response variable). In this respect, experimental factors, which are adsorbent amount, initial dye concentration, and adsorbent type, were selected as possible candidates affecting the removal percentage. By considering the earlier studies, two levels for each factor were determined. The  $2^3$  factorial design with high and low levels of factors are given in Table 2 (b=2 and k=3).

**Table 2:** The levels of experimental factors.

Factor	Low Level (-1)	High Level (+1)
Adsorbent Amount (g/30 mL) (A)	0.005	0.1
Dye Concentration (mg/L) (B)	50	500
Adsorbent type (C)	Natural butt	Biochar butt

The results of each run with duplicate tests are shown in Table 3. Interaction is a variation among

the differences between means for varying levels of one factor over different levels of the other factor.

**Table 3:** Experimental design matrix of malachite green dye removal efficiency.

Run No.	Factor			Efficiency (%)		Average
	A	B	C	Replicate I	Replicate II	
1	-1	-1	-1	22.88	21.59	22.24
2	+1	-1	-1	30.83	29.72	30.28
3	-1	+1	-1	5.26	4.82	5.04
4	+1	+1	-1	8.42	11.07	9.75
5	-1	-1	+1	92.03	87.69	89.86
6	+1	-1	+1	98.30	94.60	96.45
7	-1	+1	+1	70.04	65.69	67.87
8	+1	+1	+1	73.52	75.15	74.34

Using plus and minus signs to represent high and low levels of a factor, main effects given in Table 4 were calculated by using the following general equation (18-19).

**Table 4:** Estimated Effects and Coefficients for malachite green dye removal efficiency.

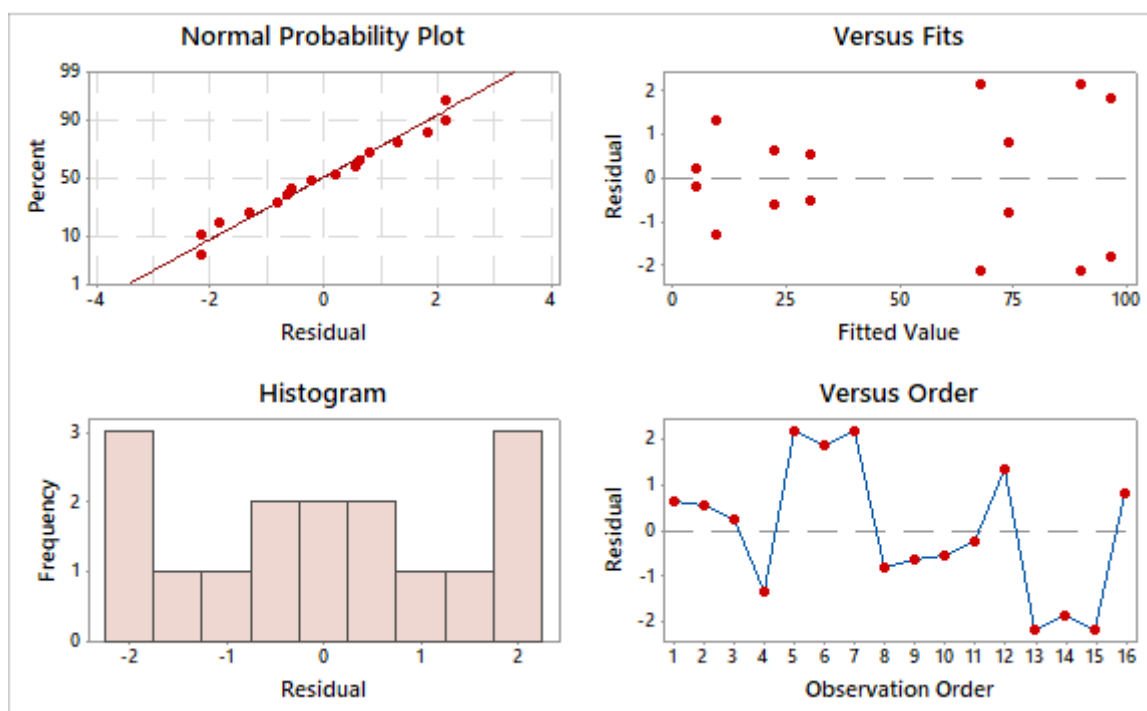
Term	Effect	Coeff.	SE Coeff.	T	P
Constant		49.477	0.501	98.82	0.00
Adsorbent Amount	6.451	3.226	0.501	6.44	0.00
Initial Concentration	-20.45	-10.23	0.501	-20.4	0.00
Adsorbent Type	65.303	32.651	0.501	65.21	0.00
Adsorbent Amount* Initial Concentration	-0.864	-0.432	0.501	-0.86	0.41
Adsorbent Amount* Adsorbent Type	0.079	0.040	0.501	0.08	0.93
Initial Concentration* Adsorbent Type	-1.596	-0.798	0.501	-1.59	0.15
Adsorbent Amount* Initial Concentration* Adsorbent Type	0.805	0.402	0.501	0.80	0.44

S=2.00276, R-Sq=99.83%, R-Sq(pred)=99.32%, R-Sq(adj)=99.68%

**RESULTS AND DISCUSSION**

The residuals also appraised the sufficiency of the models. The observed residuals are plotted against the expected values, given by a normal distribution

in Figure 1. Trends seen in Figure 1 reveal reasonably well-behaved residuals. In these graphics, the residuals seem to be randomly scattered.



**Figure 1:** Residual plots for methyl red dye removal efficiency.

The Cube Plot in Figure 2 shows the predicted removal efficiency at combinations of the low and high levels for experimental factors. In the study, the highest expected value for the response variable is obtained at methyl red initial concentration at a high level, adsorbent amount at low level and adsorbent type at biochar butt.

The R-square of the model (99.83%) was higher than the predicted value (99.32) % and fit well the model's results. These results argued good agreements between the predicted and experimental values of malachite green dye removal efficiency (Table 3).

The most critical parameters affecting the efficiency of an adsorption process are adsorbent type, initial

concentration and adsorbent amount. To determine the effects of these parameters, experiments were performed at different combinations of the physical parameters using statistically designed experiments.

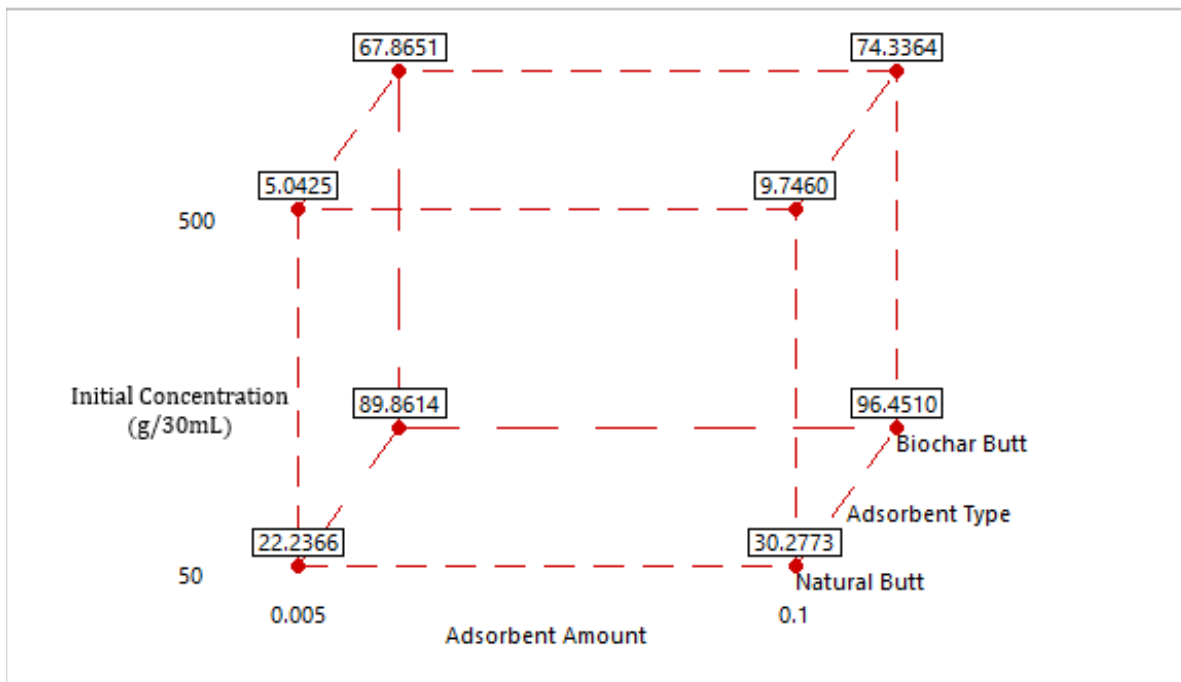


Figure 2: Cube plot malachite green dye removal efficiency.

A normal probability plot of the standardized effects, the aim of which is to determine the statistical significance of both the main and interaction effects, is given in Figure 3. The insignificant effects will fall along a line; however, the significant effects will stray farther from the line. According to Figure 3 and Figure 4, the main effects C, B and A are

statistically significant. Since C and A lie on the right-hand side of the line, their contributions positively affect the model. The reverse is valid for the rest of the significant results, which lie on the left-hand side. The adsorbent type appears to have the largest effect because it lies furthest from the line.

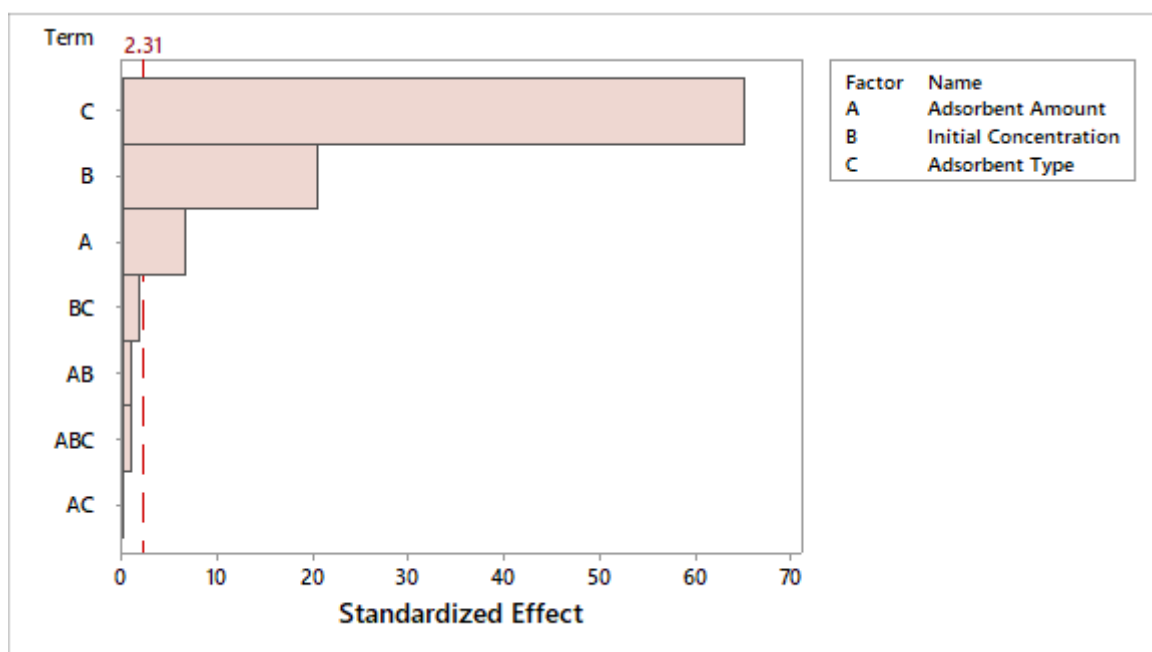


Figure 3: Pareto chart of the standardized effects for malachite green removal.

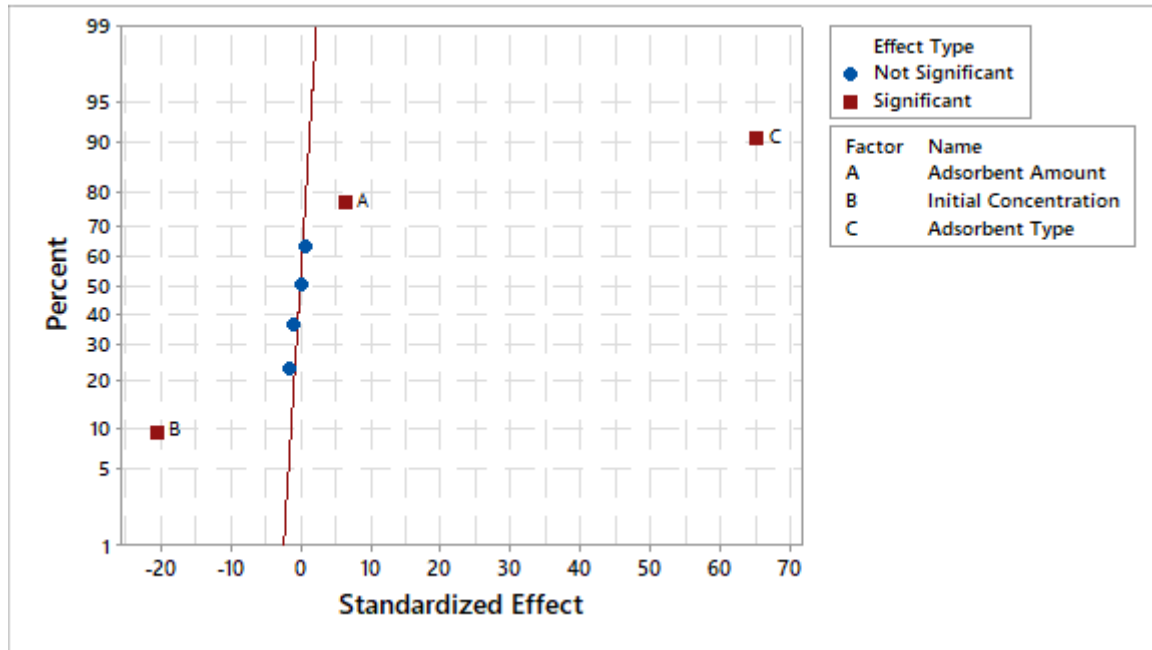


Figure 4: Normal plot of the standardized effects for malachite green removal.

Figure 5 shows the main effects plot, offering the effect of each variable on the response factor. The main effect is significant if the mean for one level of

the factor is sufficiently different from the mean for another level of the factor.

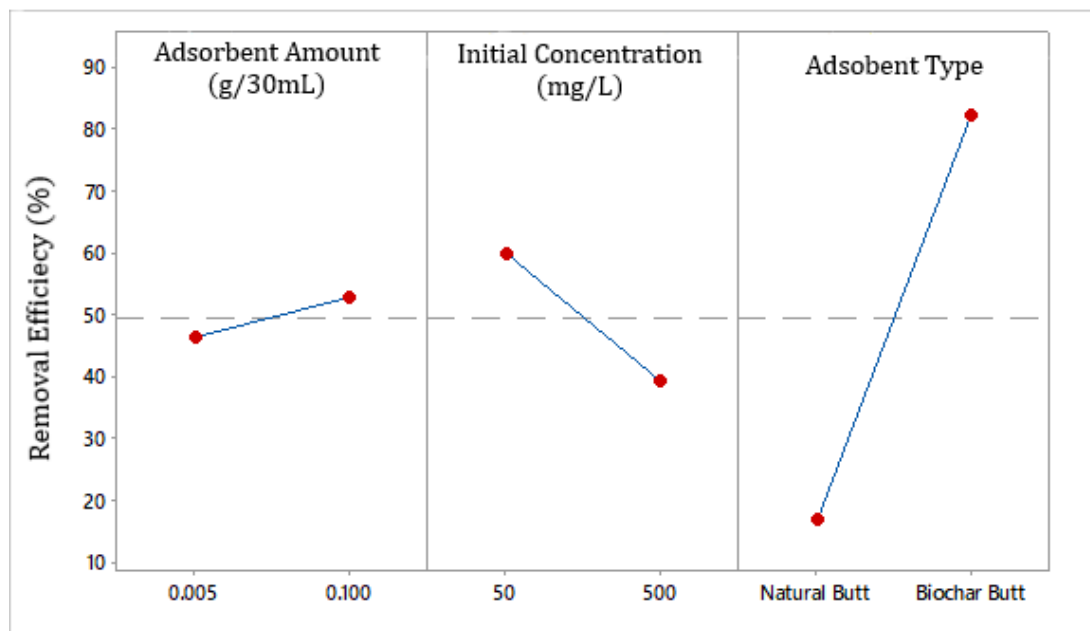
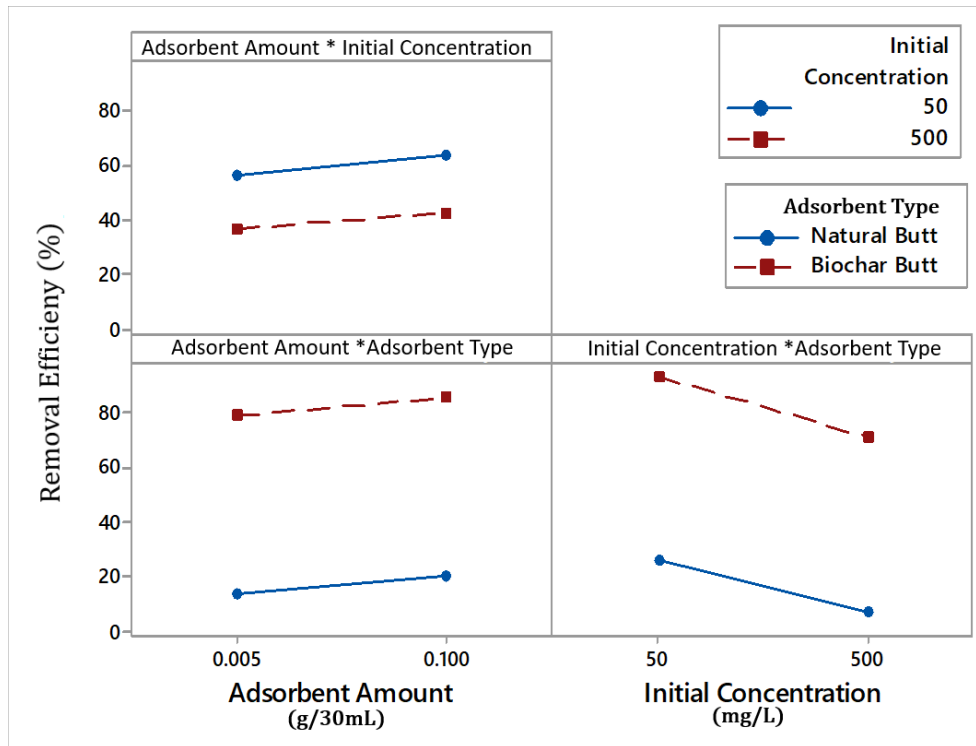


Figure 5: Main Effects plot for malachite green removal efficiency from aqueous solutions.

That is, lines with steeper slopes (up or down) have a more significant impact on the output means than lines with little or no slope (horizontal). This type of figuration shows the contribution to the response factor of changing one of the influential variables. When the effect of a factor is negative, removal

efficiency decreases as the factor changes from low to high levels. In contrast, if the effect is positive, removal efficiency increases for a high level of the same factor. If the magnitude of the main effect is small, the slope would be close to zero.



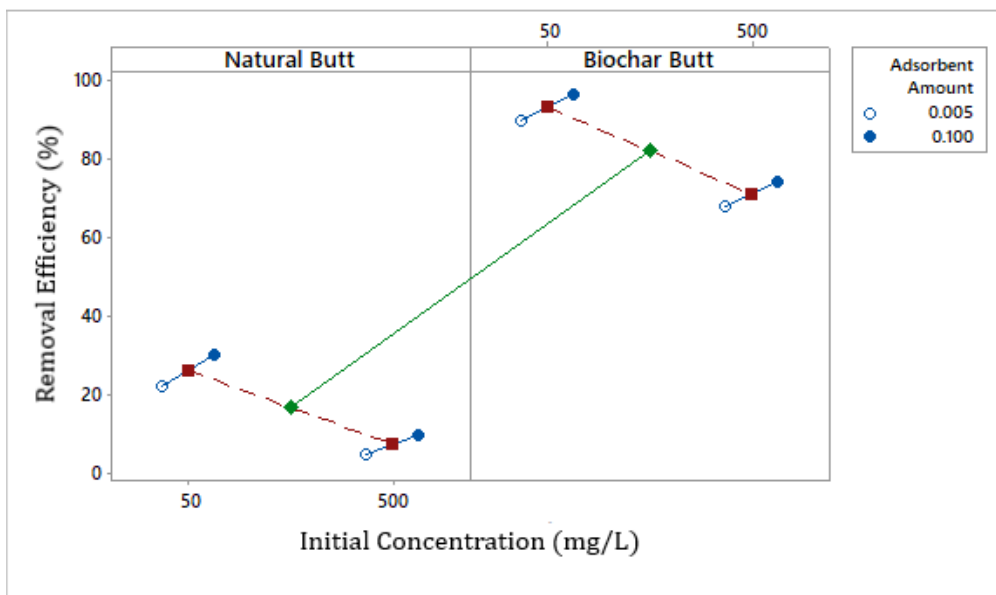


**Figure 6:** Interaction plot for malachite green removal efficiency from aqueous solutions.

The plot shows the possible interaction between the mean responses of the factors under assessment. An interaction plot circumstances the impact that the act of changing the settings of one factor has on another factor. Graphically, two parallel lines of factors indicate no interaction between them; however, non-parallel lines suggest that the two factors interact together. The interaction plot in

Figure 6 confirms that there is no interaction between the factors.

In order to see the effects of interactions between experimental factors, a multi-vari chart was generated (Figure 7). This chart shows that the effect of adsorbent type is clearly observed for the biochar butt is more efficient than the natural butt.



**Figure 7:** Multi-Vari Chart for malachite green removal efficiency from aqueous solutions.

## CONCLUSION

The scope of this study was to investigate the effectiveness of the natural and biochar butts in removing malachite green dye ions from aqueous solutions. For this purpose, a 2<sup>3</sup> full factorial design was employed to evaluate the importance and interactions of adsorbent amount, initial dye concentration and adsorbent type. Full factorial design model used some experimental data to predict the response of the experiments at new similar conditions for the problem of malachite green dye by natural and biochar butts. The factorial design results show that "adsorbent type (factor C)" had the most potent effect on the removal efficiency of malachite green dye. The negative coefficient means that increasing initial concentration (factor B) decreases removal efficiency.

On the other hand, the positive sign of adsorbent type (factor C) and adsorbent amount (factor A) means that there is a direct relation between these factors and the response. The results of this study clearly show that adsorbent type, initial dye concentration, and adsorbent amount were significant for the removal efficiency of malachite green dye. The proposed modeling method also decreases the number of experiments to remove the adsorption efficiency for removing malachite green dye ions. This decreases the cost of the experimental studies.

## REFERENCES

- Bingol D, Tekin N, Alkan M. Brilliant Yellow dye adsorption onto sepiolite using a full factorial design. *Applied Clay Science* [Internet]. 2010 Nov [cited 2022 Jul 18];50(3):315–21. Available from: [<URL>](#).
- Iram M, Guo C, Guan Y, Ishfaq A, Liu H. Adsorption and magnetic removal of neutral red dye from aqueous solution using Fe<sub>3</sub>O<sub>4</sub> hollow nanospheres. *Journal of Hazardous Materials* [Internet]. 2010 Sep [cited 2022 Jul 18];181(1–3):1039–50. Available from: [<URL>](#).
- Nayak A, Bhushan B, Gupta V, Sharma P. Chemically activated carbon from lignocellulosic wastes for heavy metal wastewater remediation: Effect of activation conditions. *Journal of Colloid and Interface Science* [Internet]. 2017 May [cited 2022 Jul 18];493:228–40. Available from: [<URL>](#).
- Kosinkova J, Doshi A, Maire J, Ristovski Z, Brown R, Rainey TJ. Measuring the regional availability of biomass for biofuels and the potential for microalgae. *Renewable and Sustainable Energy Reviews* [Internet]. 2015 Sep [cited 2022 Jul 18];49:1271–85. Available from: [<URL>](#).
- Tibet Y, Çoruh S. Immobilisation and Leaching Performance of Lead-Acid Batteries Smelting Slag Using Natural and Waste Materials. *Global NEST Journal* [Internet]. 2017 Oct 27 [cited 2022 Jul 18];19(4):562–73. Available from: [<URL>](#).
- Blankenship LS, Mokaya R. Cigarette butt-derived carbons have ultra-high surface area and unprecedented hydrogen storage capacity. *Energy Environ Sci* [Internet]. 2017 [cited 2022 Jul 18];10(12):2552–62. Available from: [<URL>](#).
- Zhou N, Chen H, Feng Q, Yao D, Chen H, Wang H, et al. Effect of phosphoric acid on the surface properties and Pb(II) adsorption mechanisms of hydrochars prepared from fresh banana peels. *Journal of Cleaner Production* [Internet]. 2017 Nov [cited 2022 Jul 18];165:221–30. Available from: [<URL>](#).
- Li Y, Meas A, Shan S, Yang R, Gai X. Production and optimization of bamboo hydrochars for adsorption of Congo red and 2-naphthol. *Bioresource Technology* [Internet]. 2016 May [cited 2022 Jul 18];207:379–86. Available from: [<URL>](#).
- Fernandez ME, Ledesma B, Román S, Bonelli PR, Cukierman AL. Development and characterization of activated hydrochars from orange peels as potential adsorbents for emerging organic contaminants. *Bioresource Technology* [Internet]. 2015 May [cited 2022 Jul 18];183:221–8. Available from: [<URL>](#).
- Flora JFR, Lu X, Li L, Flora JRV, Berge ND. The effects of alkalinity and acidity of process water and hydrochar washing on the adsorption of atrazine on hydrothermally produced hydrochar. *Chemosphere* [Internet]. 2013 Nov [cited 2022 Jul 18];93(9):1989–96. Available from: [<URL>](#).
- Mohan D, Sarswat A, Ok YS, Pittman CU. Organic and inorganic contaminants removal from water with biochar, a renewable, low cost and sustainable adsorbent – A critical review. *Bioresource Technology* [Internet]. 2014 May [cited 2022 Jul 18];160:191–202. Available from: [<URL>](#).
- Zhu X, Liu Y, Qian F, Zhou C, Zhang S, Chen J. Role of Hydrochar Properties on the Porosity of Hydrochar-based Porous Carbon for Their Sustainable Application. *ACS Sustainable Chem Eng* [Internet]. 2015 May 4 [cited 2022 Jul 18];3(5):833–40. Available from: [<URL>](#).
- Ennil Köse T. Agricultural residue anion exchanger for removal of dyestuff from wastewater using full factorial design. *Desalination* [Internet]. 2008 Mar [cited 2022 Jul 18];222(1–3):323–30. Available from: [<URL>](#).
- Lima HHC, Maniezzo RS, Kupfer VL, Guilherme MR, Moises MP, Arroyo PA, et al. Hydrochars based on cigarette butts as a recycled material for the adsorption of pollutants. *Journal of Environmental Chemical Engineering* [Internet]. 2018 Dec [cited 2022 Jul 18];6(6):7054–61. Available from: [<URL>](#).
- Ai M, Yang G, Zhang R. Minimum aberration blocking of regular mixed factorial designs. *Journal of Statistical Planning and Inference* [Internet]. 2006 Apr [cited 2022 Jul 18];136(4):1493–511. Available from: [<URL>](#).
- Yin Y, Zhou J. Minimax design criterion for fractional factorial designs. *Ann Inst Stat Math* [Internet]. 2015 Aug [cited 2022 Jul 18];67(4):673–85. Available from: [<URL>](#).
- Erbas SO, Olmus H. Deney düzenleri ve istatistik analizleri. Ankara: Gazi Kitabevi; 2006. ISBN: 9799756009030.

18. Montgomery DC, Runger GC, Hubele NF. Engineering statistics. 4th ed. Hoboken, NJ: John Wiley; 2007. 487 p. ISBN: 978-0-471-73557-1.
19. Zhao S, Chen X. Mixed two- and four-level fractional factorial split-plot designs with clear effects. Journal of Statistical Planning and Inference [Internet]. 2012 Jul [cited 2022 Jul 18];142(7):1789–93. Available from: [<URL>](#).





## Improved Oil-Water Separation Performance of Polylactic Acid by Halloysite Nanotube Incorporation

Filiz Uğur Nigiz<sup>1</sup> 

<sup>1</sup>Çanakkale Onsekiz Mart University, Chemical Engineering Department, Çanakkale, 17020, Turkey

**Abstract:** In this study, polylactic acid (PLA)-based nanocomposite membranes were prepared and used for the purification of simulated oil/water based wastewater. The lubricant oil (lubricating oil) was chosen as model oil. In order to increase the hydrophilicity of the membrane and improve its filtration performance, 0-20 wt.% of Halloysite nanotubes (HNT) were added into the PLA matrix. The effects of the HNT ratio on the oil/water swelling ratios (adsorption ratio), water flux, and oil rejection were determined. According to the results, optimal flux-oil rejection results were obtained with 5 wt.% of HNT incorporated nanocomposite membranes. The highest oil rejection of 94.9% was obtained using 5 wt.% of HNT incorporated membrane with a flux value of 1542.9 LMH.

**Keywords:** Nanocomposite membrane, polylactic acid membrane, halloysite nanotube, oil- water separation, lubricating oil.

**Submitted:** April 21, 2022. **Accepted:** July 18, 2022.

**Cite this:** Nigiz FU. Improved Oil-Water Separation Performance of Polylactic Acid by Halloysite Nanotube Incorporation. JOTCSB. 2022;5(2):77-84.

**\*Corresponding author. E-mail:** [filiz.ugur@comu.edu.tr](mailto:filiz.ugur@comu.edu.tr).

### INTRODUCTION

Depending on the environmental impact of the global population rise and industrialization, the consumption of earth resources is increasing. Although three-quarters of the earth's surface is covered with water, the amount of freshwater that is suitable for human use is limited. Rapid urbanization, industrialization, and agricultural developments lead to consumption of large amounts of freshwater. Therefore, water production from natural sources or wastewater treatment technology becomes essential (1).

Industrial wastewater contains many contaminants, including heavy metals, dissolved salts, polymeric fibers, metals, alloys, and oils. These contaminants must be kept in limit values and must be cleaned before discharging. Wastewater treatment consists of many stages and each component is disposed of at a different stage. The nature of the wastewater treatment system varies depending on the content of the wastewater to be cleaned. One of the basic components found in industrial wastewater is oil. While the vegetable and animal oils present in the

discharging of the food sector, lubricating and motor oils include in the wastewater of machinery containing sectors. Petrochemical-based oils and other industrial oily wastewaters pollute water resources irreversibly.

Waste oils must be handled appropriately. Oil/water mixes are classified into three types based on the droplet size of the dispersed phase: oil/water emulsion, free oil/water mixture, and oil/water dispersion (2, 3). Compared to emulsified oils, it is easy to remove free oil and dispersion from the water. For the removal of emulsified oil, advanced techniques are used (4). Well-known oil-water treatment techniques are gravity separation, dissolved air flotation, coagulation-flocculation (5), adsorption (6), biological treatment (7,8), electrochemical treatment (9), and membrane filtration (10). Membrane-based technology is prominent for treating oily wastewater due to its simplicity, ease of use, and low energy consumption. The separation efficiency of the membrane-based system is directly related to the structure and property of the membrane. Intensive studies are carried out to prepare high-performance



membranes for the oil/water separative membranes.

Membranes used in the oil-water treatment are classified as polymeric (organic), inorganic and mixed (composite) membranes according to their structures. According to the material affinity they can be defined as hydrophilic, hydrophobic, oleophilic, oleophobic, etc. (11). It is essential to use appropriate material with the appropriate pore size for filtration experiments. In the literature, MF and UF membranes are prepared with polyvinylidene fluoride (PVDF) (12), polyacrylonitrile (PAN), polydimethyl siloxane (PDMS) (13), cellulose acetate (CA) (14), polysulfone (PS), polyethersulfone (PES) (15) polymers are widely used in oil-water treatment studies (16). Composite membranes have recently attracted great interest in oil-water separation studies. By incorporating different inorganic fillers into the polymeric (organic) membrane matrix, higher flux and selectivity values, longer lifetime, less contamination, and better performance can be achieved (17-19).

In this study, a hydrophobic polylactic acid membrane was prepared for oily water separation. The main polymer matrix, polylactic acid, is a bio-based polymer. It can be obtained from natural sources such as corn starch, sugar cane, and other renewable biomass products or waste. They have high strength and can be used in biomedical applications and a wide variety of engineering applications. There are limited studies in which this polymer is used in oil-water separation (20, 21). In the present study, in order to enhance the water separation capability of the membrane, halloysite nanotubes (HNT) were added to the PLA matrix at different ratios. Halloysite nanotubes have multi-walled structures, and their morphology is like carbon nanotubes (22, 23). Since the attraction force between the particles of HNTs is lower than those of carbon nanotubes, they can be easily distributed homogeneously in a polymeric matrix (24). HNTs are environmentally friendly nanoparticulate materials. Bioplastics and membranes can be produced by adding HNTs to biodegradable polymers (25). There are several studies in the literature in which HNT was added to PLA polymer except for separation membranes (21, 26, 27)

In the present study different amounts of HNTs (from 1 wt.% to 20 wt.%) were added to the PLA matrix to remove the water from emulsified oil-containing water solution. Lubricant oil was chosen as the model oil in the present study. Lubricating oil, in other words lubricant, is a type of synthetic oil that is used to reduce the friction between the engine and parts of vehicles. The use of lubricating oils is increasing in proportion to the number of vehicles. Lubricant oil is refined from crude oil or is

synthesized in the laboratory. It is used in most important machines and vehicles (28).

Scanning electron microscopy (SEM) and Fourier transform infrared spectroscopy (FTIR) were used to investigate the physical and chemical structures of nanocomposite membranes. The affinity of the composite membranes to the oil and water was determined using water-oil uptake studies. Vacuum filtration experiments were conducted to determine the filtration capability of the membranes. The effect of HNT concentration in the matrix, oil types, and the downstream pressure on the water flux and oil rejection were investigated. According to the author's knowledge, HNT loaded PLA membranes were first time prepared as a membrane and were used for oil-water separation.

## EXPERIMENTAL SECTION

Polylactic acid (PLA) was supplied from the Turkish distributor of Nature Works (2003D)., N, N-dimethylformamide (DMF, with >99% purity), chloroform, and methanol (>99% purity) were purchased from Merck Chemicals. Halloysite nanotube was kindly supplied from the ESAN, Eczacıbasi, Turkey.

### Membrane Preparation

For the preparation of the plain PLA membrane, a DMF/chloroform solution containing 10% PLA was prepared. The membrane solution was stirred at 50 °C for four hours until a homogeneous mixture was obtained. The mixture was poured onto a Teflon sheet and semi-dried at room temperature for an hour. Then the casting solution was immersed in a water bath for two minutes. The membrane was taken from the bath and washed for a couple of times. Parameters such as the temperature of the water bath and the retention time affect the pore structure of the membrane.

For the preparation of the HNTs loaded nanocomposite membrane, 5-20 wt.% of HNTs were dissolved in 10 mL of DMF in an ultrasonic bath for 10 minutes. Then, the well-mixed HNTs-DMF solution was mixed with the PLA-DMF-chloroform solution containing 10% PLA. The solution was stirred for 2 hours at room temperature and was poured onto a Teflon layer. The casting solution was dried at room temperature for an hour. It was immersed in a water bath for two minutes.

Fourier transform infrared spectroscopy (Perkin Elmer) was used to determine the chemical properties of nanocomposite membranes (FTIR-Perkin Elmer). The test was carried out in the range of 4000–650  $\text{cm}^{-1}$  wavelength.

### Oil/Water Uptake

The affinity of all prepared membranes to water and oils was determined by adsorption tests. For the

uptake test, 1 cm<sup>2</sup> of membrane samples were kept in water and lubricating oil for 24 hours. The weights of the membranes were recorded hourly and were waited to reach constant weight. The uptake percentage was calculated from the weight of the dry ( $W_i$ ) and swollen membranes ( $W_f$ ). The calculation is given in Equation 1.

$$Uptake(\%) = \frac{W_f - W_i}{W_i} * 100 \quad (1)$$

### Vacuum filtration test

The schematic representation of the vacuum filtration test system is shown in Figure 1a. The prepared membranes are seen in Figure 1b. The experiments were carried out at room temperature by preparing lubricating oil-water emulsions containing 1 wt.% oil. Prior to the vacuum filtration experiments, the oil-water emulsion was sonicated for one hour and a milk-like color was obtained as shown in Figure 1c. Experiments were done at room temperature with 100 mL of oil-water solution. The

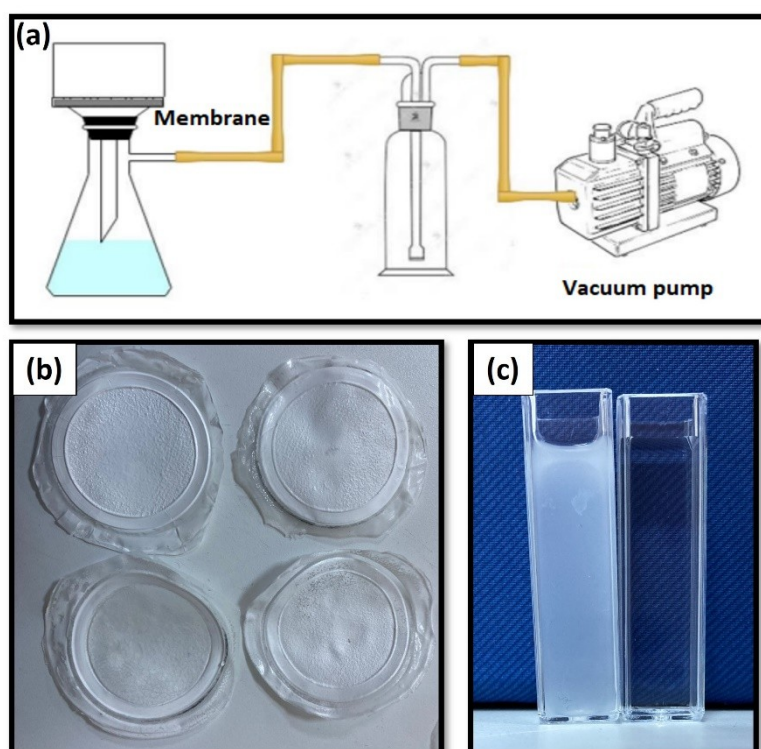
time-dependent permeate weight was recorded and the concentration of the permeate sample was analyzed using a UV-visible spectrophotometer (Shimadzu, 1800) at 420 nm.

The volumetric flow rate or flux ( $F$ ) (L/m<sup>2</sup>.h) was calculated from the volume of the permeate (Equation 2) and the oil rejection ( $R$ )(%) was calculated from the oil concentrations of the feed and permeate (Equations 3).

$$F = \frac{M}{t \cdot A} \quad (2)$$

$$R(\%) = \frac{C_f - C_p}{C_f} * 100 \quad (3)$$

where L (Liter) represents the volume of the permeate,  $t$  (h) represents the duration of filtration, and  $A$  (m<sup>2</sup>) represents effective membrane area. On the feed and permeate sides,  $C_f$  and  $C_p$  are the concentrations of the oil-water solution.



**Figure 1:** Vacuum filtration test unit (a), prepared nanocomposite membranes (b), and the oil-water mixture before (left) and after (right) vacuum filtration (c).

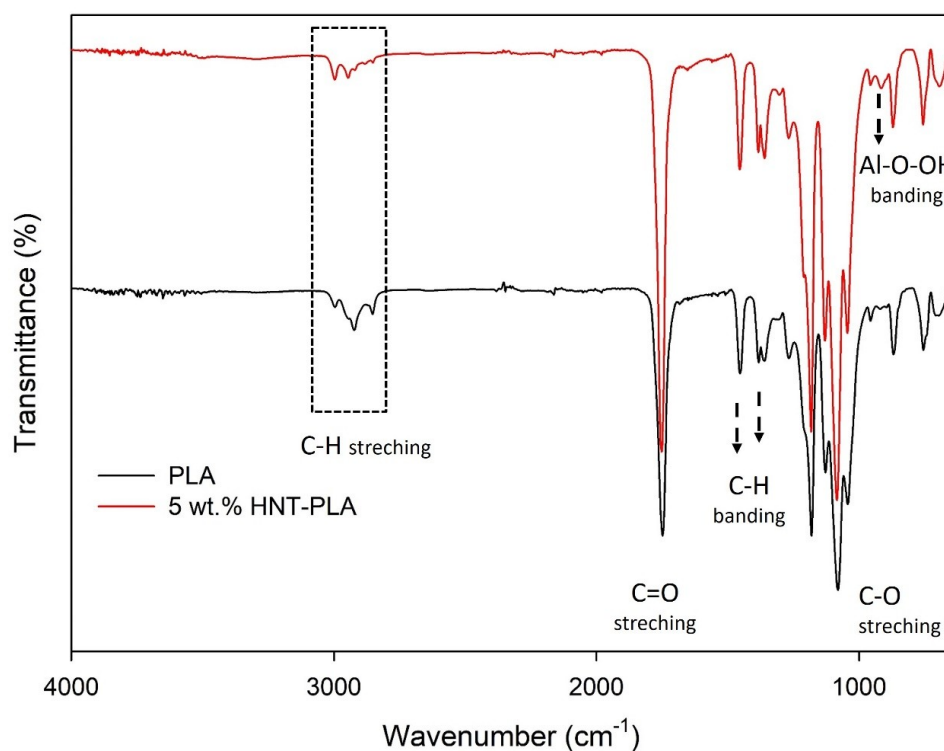
## RESULTS AND DISCUSSION

### Membrane Characterization

FTIR spectroscopy was used to investigate the chemical structures of plain PLA and HNT-PLA nanocomposite membranes. Figure 2 shows the spectra of unfilled and nanocomposite membrane. PLA has asymmetric and symmetric -CH groups,

which have stretching vibration peaks around 2998 cm<sup>-1</sup> and 2922 cm<sup>-1</sup>, respectively. The place of -CH stretching peaks are shifting 2996 cm<sup>-1</sup> and 2945 cm<sup>-1</sup> due to HNT addition into PLA. The C=O bond strains in PLA is observed about 1750 cm<sup>-1</sup>. The asymmetric and symmetric -CH<sub>3</sub> groups have bending frequencies of 1450 cm<sup>-1</sup> and 1385 cm<sup>-1</sup>,

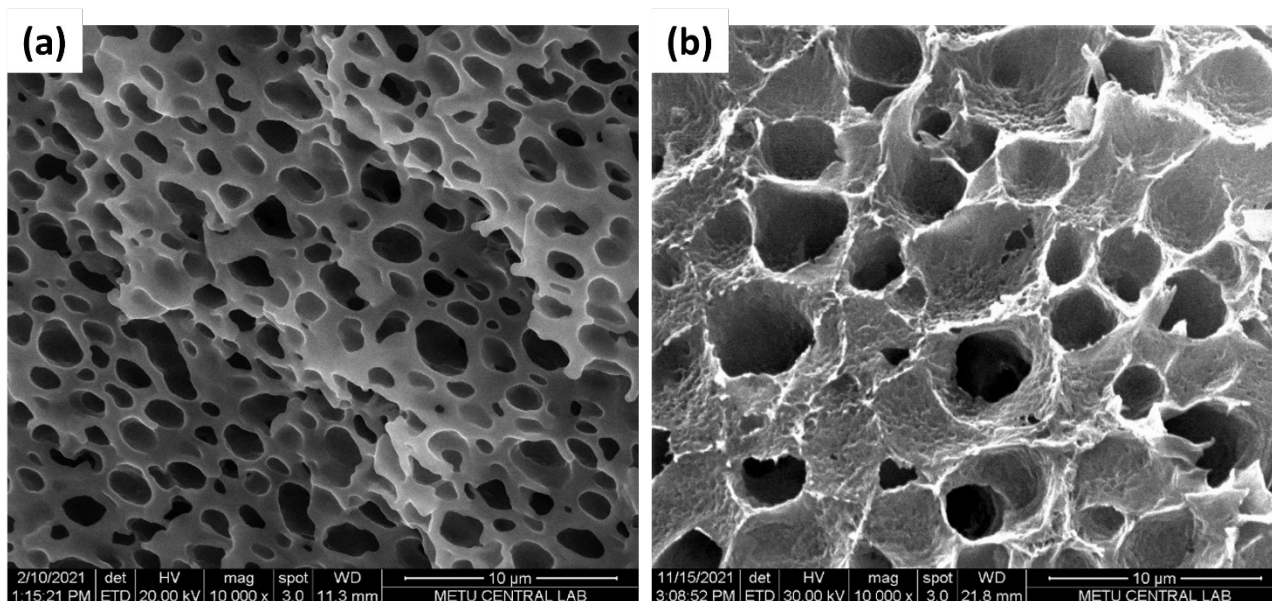
respectively. The absorption peak at  $910\text{ cm}^{-1}$  is corresponding to Al-O-OH bending of HNT (29, 30).



**Figure 2.** FTIR analysis of the plain PLA-and HNT-filled nanocomposite membranes.

Figure 3a and Figure 3b show the pore size and distribution of the plain and HNT loaded PLA membranes. The pore size of the plain PLA membrane varying between  $1\text{ }\mu\text{m}$  to  $3\text{ }\mu\text{m}$ . Unlike the plain membrane, the number of pores decreased, and the size of the pores increased in the nanocomposite membrane. The possible reason

for this is the strong interaction between the PLA matrix and HNT. This interaction may cause a decrease in the density of pore formation during the phase inversion stage. HNT particles are clearly seen within the polymer matrix. It is seen that HNT changes the membrane's structure. The distribution of HNT in the matrix is homogeneous.



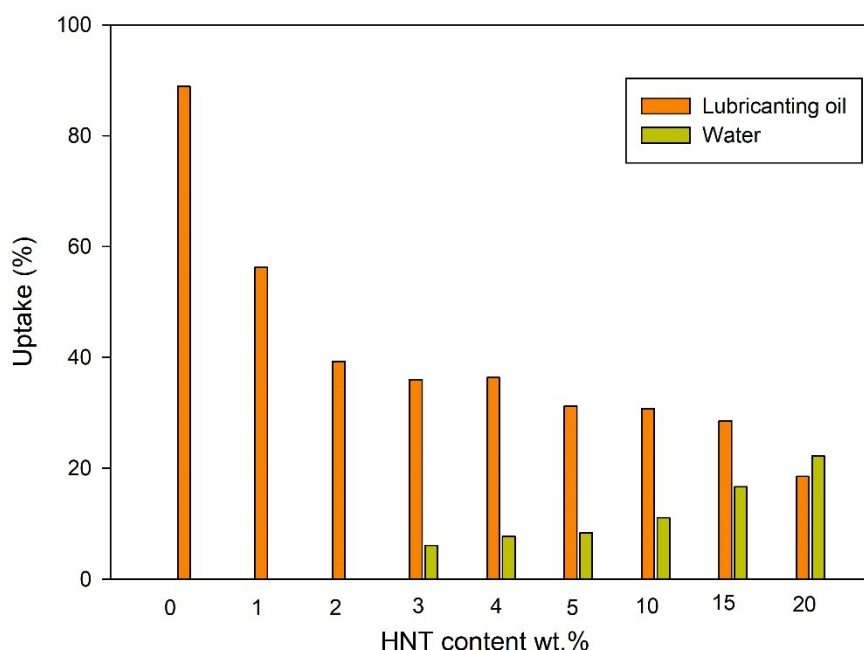
**Figure 3.** Cross-sectional SEM micrographs of the plain PLA (a)- and 5 wt.% of HNT-loaded PLA membranes.

### Oil and water uptake

In this study, it was aimed to improve the separation performance of the PLA membrane by adding HNT to the matrix. HNT is an environmentally friendly material that exhibits biocompatible hydrophilicity, stable dispersion in the polymer, and high water adsorption capacity. In the literature, it was reported that the hydrophilicity of the PLA-based materials was strongly increased by the addition of HNT depending on the hydroxyl groups in its structure (31). It was also reported that the separation performance of membranes in water-oil solution was significantly improved by HNT addition (32). A dramatic improvement in hydrophilicity and separation performance of membranes have been achieved depending on the HNT modification.

In Figure 4, the effect of HNT addition on uptake values is illustrated. The HNT concentration was

varied from 0 wt% to 20 wt%. The highest oil uptake results were obtained by using the plain PLA membrane. The plain membrane did not adsorb water. As the HNT concentration increased from 3 wt.% to 20 wt.%, the water uptake capacity of the plain membrane gradually increased. According to these results, it could be concluded that the HNT significantly increased the water uptake capacity of the hydrophobic PLA membrane. Halloysite clay is a mineral of volcanic origin consisting of layered aluminosilicate with a high surface area and aspect ratio (26). Like other kaolinite minerals, it adsorbs water, but unlike montmorillonite, this ratio is not high and does not cause an increase in polymer volume (swelling effect). As seen in the figure, the addition of HNT increased the water uptake only after 3% addition. However, swelling values in oily waters decreased significantly as the HNT content increased. According to these results, it can be predicted that the HNT could improve the water flux and oil rejection, simultaneously.



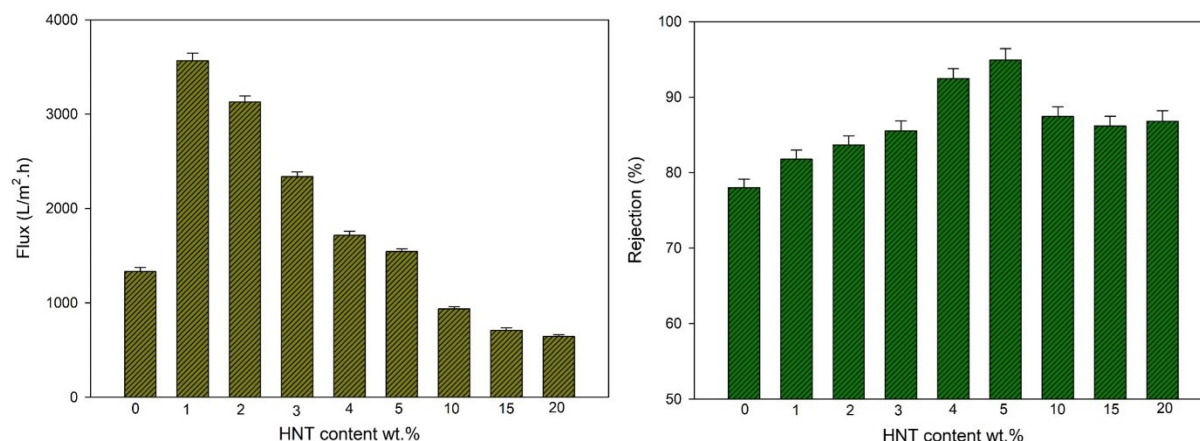
**Figure 4.** Effect of HNT ratio on uptake.

### Filtration performance of membranes

The flux and rejection results of the lubricant oil-water emission as a function of HNT content are shown in Figure 5. Very high flux values were obtained with the prepared membranes. Fluxes were remarkably improved by the addition of HNT. Flux increases occurred due to the high water holding and transfer capacity of HNT. When the HNT ratio was increased from 0 wt.% to 1 wt.%, flux increased from 1330.9 LMH to 3566.5 LMH when the vacuum pressure was 10 mbar (985 mbar

gauge pressure). However, after this loading, a significant decrease in flux was observed. This decrease is attributed to the closing of active separation sites by overloading of HNT. The pore-blocking effect may be occurred due to the highest amount of HNT which was also reported in the literature (32). Additionally, decrease in flux is also related to the reduced the number of the pores depending on the HNT addition as also confirmed by SEM image.





**Figure 5.** Effect of HNT content on the flux and lubricating oil rejection results.

The membranes also exhibited excellent rejection results for the water/lubricating oil emulsion. Although the flux values of membranes were improved compared to the plain membrane, there was no reduction in oil rejection values until the HNT loading ratio of 5 wt.%. Therefore, it can be assumed that the trade-off trend between the flux-rejection was overcome. The highest lubricating oil rejection of 94.9% was achieved with a flux of 1542.9 LMH using 5 wt.% of HNT loaded membrane. After that point, rejection decrease depending on the enlarged pore size of membrane which was confirmed by the SEM image.

Table 1 includes the results of oil-water separation studies. The cited studies are selected according to the high rejection results (greater than 90% oil rejection). When compared with the literature, it is seen that the results are quite good. Therefore, it is possible to consider that the produced membrane has the potential to be commercialized as a microfiltration membrane. Also, considering that both the polymer and the additive used are natural and cheap sources, promising results were obtained in the study.

**Table 1.** Comparison of the results with the literature.

Membrane	Oil Type	Flux (LMH)	Rejection (%)	Reference
Kaolin	-	123.8	97.3	(10)
PMDS/SiO <sub>2</sub>	Kolza	1800	97.2	(4)
PMDS/SiO <sub>2</sub>	Engine oil	1900	97.3	(4)
PS/PVA/Bentonite	Petroleum	312	97	(33)
PSf/PEG	-	120	95	(34)
Cellulose	Petroleum	1591	>96.5	(35)
PLA/TiO <sub>2</sub>	Lubricating oil	963	99	(20)
PVDF/PVP/TiO <sub>2</sub>	-	70.48	99.7	(36)
PSf	-	245	95.9	(37)
PVDF/Bentonite	Lubricating oil	1800	96.5	(38)
PLA/PDA	-	2664	98.4	(3)
PLA/HNT	Lubricating oil	1542.9	94.9	This work

## CONCLUSION

In this study, bio-based PLA-HNT nanocomposite membranes were produced and their performance in oil-water separation was investigated. It has been seen in the SEM analyses that the HNT material can be added to the membrane homogeneously. Although the number of pores decreased in membranes with HNT added, they exhibited excellent water separation performances. A

significant increase in water flux values was observed in HNT-loaded nanocomposite membranes. In addition, oil rejection values increased significantly. It has been observed that the most suitable HNT concentration was up to 5 wt.%, and the flux value was lower compared to the plain PLA after this ratio. When the HNT watio was 5 wt.%, the highest oil rejection of 94.8% and a reasonable flux value of 1542.9 LMH were obtained. These results were higher than many studies in the



literature. As a result, it has been seen that the HNT-doped PLA membrane was very successful for separation of emulsified oily wastewater using microfiltration technique.

### CONFLICT OF INTEREST

The author confirmed that there is no declaration of interest.

### ACKNOWLEDGMENTS

This research is financially supported by The Scientific Research Coordination Unit of Çanakkale Onsekiz Mart University (Grant Number: FBA-2021-3598).

### REFERENCES

1. Shamaei L, Khorshidi B, Islam MA, Sadrzadeh M. Development of antifouling membranes using agro-industrial waste lignin for the treatment of Canada's oil sands produced water. *Journal of Membrane Science*. 2020 Oct;611:118326. <URL>.
2. Wu M, Mu P, Li B, Wang Q, Yang Y, Li J. Pine powders-coated PVDF multifunctional membrane for highly efficient switchable oil/water emulsions separation and dyes adsorption. *Separation and Purification Technology*. 2020 Oct;248:117028. <URL>.
3. Liu W, Cui M, Shen Y, Zhu G, Luo L, Li M, Li J. Waste cigarette filter as nanofibrous membranes for on-demand immiscible oil/water mixtures and emulsions separation. *Journal of Colloid and Interface Science*. 2019 Aug;549:114-22. <URL>.
4. Sun Y, Zong Y, Yang N, Zhang N, Jiang B, Zhang L, Xiao X. Surface hydrophilic modification of PVDF membranes based on tannin and zwitterionic substance towards effective oil-in-water emulsion separation. *Separation and Purification Technology*. 2020 Mar;234: 116015. <URL>.
5. You Z, Xu H, Sun Y, Zhang S, Zhang L. Effective treatment of emulsified oil wastewater by the coagulation-flotation process. *RSC Advances*. 2018 Dec;8(71):40639-46. <URL>..
6. Guo X, Qu L, Zhu S, Tian M, Zhang X, Sun K, Tang X. Preparation of three-dimensional chitosan-graphene oxide aerogel for residue oil removal. *Water Environment Research*. 2016 Aug;88(8):768-78. <URL>.
7. Chen WT, Chen KF, Surmpalli RY, Zhang TC, Ou JH, Kao CM. Bioremediation of trichloroethylene-polluted groundwater using emulsified castor oil for slow carbon release and acidification control. *Water Environment Research*. 2022 Jan;94(1):e1673. <URL>.
8. Bilici Z, Ozay Y, Ozbey Unal B, Dizge N. Investigation of the usage potential of calcium alginate beads functionalized with sodium dodecyl sulfate for wastewater treatment contaminated with waste motor oil. *Water Environment Research*. 2021 Jul;93(11):2623-36. <URL>.
9. Akarsu C, Bilici Z, Dizge N. Treatment of vegetable oil wastewater by a conventional activated sludge process

coupled with electrocoagulation process. *Water Environment Research*. 2022 Feb;94(2):e10692. <URL>.

10. Shalaby MS, Sołowski G, Abbas W. Recent Aspects in Membrane Separation for Oil/Water Emulsion. *Advanced Materials Interfaces*. 2021 Sep;8(20):2100448. <URL>.
11. Doshi B, Sillanpää M, Kalliola S. A review of bio-based materials for oil spill treatment. *Water Research*. 2018 May;135:262-77. <URL>.
12. Ismail NH, Salleh WNW, Awang NA, Ahmad SZN, Rosman N, Sazali N, Ismail AF. PVDF/HMO ultrafiltration membrane for efficient oil/water separation. *Chemical Engineering Communications*. 2021 Oct;208(4):463-73. <URL>.
13. Shin JH, Heo JH, Jeon S, Park JH, Kim S, Kang HW. Bio-inspired hollow PDMS sponge for enhanced oil-water separation. *Journal of Hazardous Materials*. 2019 Mar; 365: 494-501. <URL>.
14. Wang W, Lin J, Cheng J, Cui Z, Si J, Wang Q, Turng LS. Dual super-amphiphilic modified cellulose acetate nanofiber membranes with highly efficient oil/water separation and excellent antifouling properties. *Journal of Hazardous Materials*. 2020 Mar;385:121582. <URL>.
15. Prince, JA, Bhuvana S, Anbharasi V, Ayyanar N, Boodhoo KVK, Singh G. Ultra-wetting graphene-based PES ultrafiltration membrane—a novel approach for successful oil-water separation. *Water Research*. 2016 Oct;103:311-318. <URL>.
16. Bolto B, Zhang J, Wu X, Xie Z. A review on current development of membranes for oil removal from wastewaters. *Membranes*. 2020 Apr;10(4):65. <URL>.
17. Ikhsan SNW, Yusof N, Aziz F, Misdan N, Ismail AF, Lau WJ, Hairon NHH. Efficient separation of oily wastewater using polyethersulfone mixed matrix membrane incorporated with halloysite nanotube-hydrous ferric oxide nanoparticle. *Separation and Purification Technology*, 2018 Jun;199:161-9. <URL>.
18. Amid M, Nabian N, Delavar M. Fabrication of polycarbonate ultrafiltration mixed matrix membranes including modified halloysite nanotubes and graphene oxide nanosheets for olive oil/water emulsion separation. *Separation and Purification Technology*. 2020 Nov;251:117332. <URL>.
19. Abdalla O, Wahab MA, Abdala A. Mixed matrix membranes containing aspartic acid functionalized graphene oxide for enhanced oil-water emulsion separation. *Journal of Environmental Chemical Engineering*. 2020 Oct;8(5);104269. <URL>.
20. Xiong Z, Lin H, Zhong Y, Qin Y, Li T, Liu F. Robust superhydrophilic polylactide (PLA) membranes with a TiO<sub>2</sub> nano-particle inlaid surface for oil/water separation. *Journal of Materials Chemistry A*. 2017 Mar;5(14):6538-6545. <URL>.
21. Liu M, Zhang Y, Zhou C. Nanocomposites of halloysite and polylactide. *Applied Clay Science*. 2013 May;75: 52-59. <URL>.

22. Joussein E, Petit S, Churchman J, Theng B, Righi D, Delvaux B. Halloysite clay minerals—a review. *Clay minerals*. 2005 Dec;40(4): 383-426. <URL>.
23. Saif MJ, Asif HM, Naveed M. Properties and modification methods of halloysite nanotubes: a state-of-the-art review. *Journal of the Chilean Chemical Society*. 2018 Sep;63(3):4109-4125. <URL>.
24. Grylewicz A, Mozia S. Polymeric mixed-matrix membranes modified with halloysite nanotubes for water and wastewater treatment: A review. *Separation and Purification Technology*. 2021 Feb;256:117827. <URL>.
25. Ünügül T, Nigiz FU. Evaluation of Halloysite Nanotube-Loaded Chitosan-Based Nanocomposite Membranes for Water Desalination by Pervaporation. *Water, Air, & Soil Pollution*. 2022 Feb; 233(2):34. <URL>.
26. Guo X, Qu L, Zhu S, Tian M, Zhang X, Sun K, Tang X. Preparation of three-dimensional chitosan-graphene oxide aerogel for residue oil removal. *Water Environment Research*. 2016 Aug;88(8): 768-78. <URL>.
27. Wu F, Zheng J, Li Z, Liu M. Halloysite nanotubes coated 3D printed PLA pattern for guiding human mesenchymal stem cells (hMSCs) orientation. *Chemical Engineering Journal*. 2019 Mar;359:672-83. <URL>.
28. Mohammed RR, Ibrahim IA, Taha AH, McKay G. Waste lubricating oil treatment by extraction and adsorption. *Chemical Engineering Journal*. 2013 Mar; 220:343-51. <URL>.
29. Barot T, Rawtani D, Kulkarni P. Physicochemical and biological assessment of silver nanoparticles immobilized Halloysite nanotubes-based resin composite for dental applications. *Heliyon*. 2020 Mar;6(3):e03601. <URL>.
30. Dong Y, Marshall J, Haroosh HJ, Mohammadzadehmoghadam S, Liu D, Qi X, Lau KT. Polylactic acid (PLA)/halloysite nanotube (HNT) composite mats: Influence of HNT content and modification. *Composites Part A: Applied Science and Manufacturing*. 2015 Sep;76: 28-36. <URL>.
31. Czarnecka-Komorowska D, Bryll K, Kostecka E, Tomasiak M, Piesowicz E, Gawdzińska K. The composting of PLA/HNT biodegradable composites as an eco-approach to the sustainability. *Bulletin of the Polish Academy of Sciences: Technical Sciences*. 2021;69(2): e136720. <URL>.
32. Ikhsan Wan SN, Yusof N, Mat Nawi NI, Bilad MR, Shamsuddin N, Aziz F, Ismail AF. Halloysite nanotube-ferrihydrite incorporated polyethersulfone mixed matrix membrane: effect of nanocomposite loading on the antifouling performance. *Polymers*. 2021 Jan;13(3):441. <URL>.
33. Kumar S, Mandal A, Guria C. Synthesis, characterization and performance studies of polysulfone and polysulfone/polymer-grafted bentonite based ultrafiltration membranes for the efficient separation of oil field oily wastewater. *Process Safety and Environmental Protection*. 2016 Jul;102:214-28. <URL>.
34. Yuan T, Meng J, Hao T, Zhang Y, Xu M. (2014). Polysulfone membranes clicked with poly (ethylene glycol) of high density and uniformity for oil/water emulsion purification: effects of tethered hydrogel microstructure. *Journal of Membrane Science*. 2014 Nov;470:112-24. <URL>.
35. Zhou K, Zhang QG, Li HM, Guo NN, Zhu AM, Liu, QL. Ultrathin cellulose nanosheet membranes for superfast separation of oil-in-water nanoemulsions. *Nanoscale*. 2014 Jul;6(17):10363-9. <URL>.
36. Ong CS, Lau WJ, Goh PS, Ng BC, Ismail AF. Preparation and characterization of PVDF-PVP-TiO<sub>2</sub> composite hollow fiber membranes for oily wastewater treatment using submerged membrane system. *Desalination and Water Treatment*. 2015; 53(5):1213-23. <URL>.
37. Shen C, Zhang Q, Meng Q. PSU-g-SBMA hollow fiber membrane for treatment of oily wastewater. *Water Science and Technology*. 2021 Dec;84(12): 3576-85. <URL>.
38. Nigiz FU, Yucak AI, Hilmioglu ND. Purification of emulsified oil by Bentonite loaded polyvinylidene fluoride/polyvinylpyrrolidone membrane. *Water Practice and Technology*, 2020 Jun;15(2): 394-403. <URL>.



## Polymer Fractionation by Automated Laboratory System with Laser Optical Probe (L.A.F.P.)

Mustafa Tolay<sup>1\*</sup> , Cemil Koyunoğlu<sup>2</sup> , P. Cinquina<sup>3</sup>

<sup>1</sup>Tolay Energy Consulting, 19 Mayıs Mah. Halaskargazi Cad. Feza Apt. No: 192, D:8, Şişli, 34360, İstanbul, Turkey

<sup>2</sup>Energy Systems Engineering Department, Engineering Faculty, Cinarcik Road 5<sup>th</sup> km, Central Campus, Yalova University, 77200, Yalova, Turkey

<sup>3</sup>Istituto Guido Donegani, Enichem, Via G.Fauser, 4, 28100 Novara-Italia

**Abstract:** By examining the composition of copolymers and the distribution of their molecular weights, one can get an idea about their various properties. It is necessary to obtain homogeneous samples from fractions of different molecular weights of copolymers. Fractionation processes are quite difficult and time consuming. In this study, a type of ethylene-propylene copolymer was fractionated depending on molecular weight with a system based on laser turbidity measurement. The copolymer was dissolved in diphenylmethane at a certain temperature. The temperature of the system and the adjustment of other parameters are made with the developed computer-controlled system. When the temperature of the solution was lowered slowly and in a controlled manner, the separation of fractions with certain molecular weights could be achieved. The solution turbidity formed during the separation was measured and controlled by the developed laser system. Molecular weights, viscosities and IR analyses of the copolymer and its fractions were tried to find the properties of the fractions.

**Keywords:** Polymer fractionation, molecular distribution, laser probes, laboratory automation, batch chemical reactors.

**Submitted:** January 10, 2022. **Accepted:** July 26, 2022.

**Cite this:** Tolay M, Koyunoğlu C, Cinquina P. Polymer Fractionation by Automated Laboratory System with Laser Optical Probe (L.A.F.P.). JOTCSB. 2022;5(2):85–90.

\*Corresponding author. E-mail: [drmtolay@libero.it](mailto:drmtolay@libero.it).

### INTRODUCTION

The ethylene-propylene copolymers, their derivatives, and similar polymers are among interesting elastomers both from the theoretical and commercial point of view. It is very well known that the physical-mechanical and application properties of copolymers are strongly dependent on their structure. Included in the structure are, generally, the molecular weights and their distributions, the average composition and its variations around the average value and, finally, the chain sequences and their microstructure. The prevailing influence of some of these, instead of others, can explain the conflicting results and conclusions drawn from

studies based average values of molecular weights and composition of different raw materials. The problem, therefore of separating homogeneous species concerning both the molecular weights and composition, is presently of great interest (1-4).

SEC chromatography has been recently useful in helping to solve problems in which some structural parameters overlap each other. Many years ago, the use of appropriate combinations of detectors has been a powerful tool in solving complicated molecular structures like polymer chain branching (5-8).

Where for homopolymers it is possible to obtain, in selected conditions, molecular weight distribution very close to real ones, the same may not be true for copolymers. It is necessary to take into account, possible compositional inhomogeneities that could influence the univocity of a correct calibration relationship between the retention volume and the molecular weight of eluted species. The same could be true concerning the concentration of molecular species if an RI detector is used. If the composition does not show variations over the whole range of molecular weight, the same assumption used for homopolymers can be applied also to the copolymers. However, this situation is unusual for most copolymers.

Otherwise, it is very important to choose a solvent which minimizes the  $dn/dc$  difference between the copolymers (5), in order to eliminate or to drastically reduce the influence of composition. Taking all these things into account, we tried to check the validity and reliability of some proposed relationships (9-11) for the copolymers under investigation.

For this reason, it has been necessary to prepare fractions which are homogeneous both in respect to molecular weight and composition to represent the real polymer distribution. In this study, a fractionation method is reported which separates the raw copolymer mainly as a function of its molecular weight mass. For this study, also a laser probe and an automated laboratory system (L.A.F.P.) are reported to developed for this polymer fractionation method was used (12-15).

## EXPERIMENTAL STUDIES

### Sample

The sample used in the experiment was a commercial (BUNA AP 301) ethylene-propylene copolymer (Table 1) from Chemische Werke Hüls Ag.

**Table 1:** Properties of BUNA AP 301 Copolymer.

$[\eta]$ (dL/g)	Mw	MWD	C <sub>3</sub> (%wt)	Mooney M <sub>L4</sub> (at 100 °C)
1.8	230,000	2.6	43.8	75

### Fractionation Process

Fractionation process was carried out using a single solvent at certain temperature ranges. The sample dissolved in the solvent at a certain temperature was separated into its fractions by slowly decreasing the solution temperature. The fractionation process was carried out in a jacketed fractionation device with automatic temperature control with a computer. Diphenylmethane was used as the

solvent and the polymer concentration was chosen as 1%. In order to prevent polymer degradation, 0.1% mixture of Irganox 1076 and Irganox 1010 was added to the polymer solution as a stabilizer. After the polymer solution to be fractionated was prepared, it was heated up to a maximum of 160 °C. No visible degradation was observed at this temperature. For the fractionation process, the temperature of the solution was lowered slowly, and according to the experimental plan, the fractions were set at the temperatures given in Table 2. A special thermostatic system (L.A.P.F.-Laboratorio Automatico per Il Frazionamento Polymer) developed for the fractionation process and controlled by a computer was used (Figure 1) (12-15). The solution turbidity formed during the separation of the fractions was measured and controlled with the developed laser probe (Figure 2) (12-15). Samples separated at each temperature range were weighed and stored for analysis. After each step of the separation process, the mixing process was continued while the temperature of the solution was lowered. Mixing was stopped to perform separation only after the desired temperature was reached. The fraction number was determined according to the molecular weight distribution of the polymer and the selected temperature range. During the whole fractionation process, it was worked in a nitrogen gas atmosphere.

### Viscosity Measurements

The actual viscosity  $[\eta]$  values of the starting crude copolymer and its fractions were measured with o-dichlorobenzene at 135 °C. Actual viscosities are the viscosity values measured at four different concentrations,  $h_{spec}/C$  was found by extrapolation to zero concentration. Measurements were made with a Desreux-Bischoff capillary viscometer (16).

### SEC Analysis

Average molecular weights of the starting crude polymer and its fractions and their distributions were determined by gel permeation chromatography method. Four PL GEL 10  $\mu$  (103 - 104 - 105 - 106 Å) mounted Waters 150-C ALC/GPC instruments were used with a differential refractive index detector. Analyses were performed at 135 °C using o-dichlorobenzene. Thus, the  $dn/dc$  ratio is minimized when EPR copolymers are used (10). The calibration curve was made according to the Mark-Houwink equations proposed by Benoit et al. (17).

### IR Analysis

The composition of the starting crude copolymer and its fractions was determined with the PERKIN-ELMER 1800 Mod.FTIR instrument. 2723  $cm^{-1}$  absorption band (-CH<sub>3</sub> symmetrical slope) was used as the calibration curve (Tables 1, 2, and 3).

### Automated Laboratory System

L.A.F.P. developed for the fractionation process and controlled by a computer was used (Figure 1). The Automated Laboratory System is also used for the automatic execution of batch or semi-batch chemical reactions. Automated Laboratory System is an automated lab reactor whereby a constant temperature is maintained within a system and the heat flux to or from the system is measured by computer control. The reactor is equipped with precise and rapid temperature control. The agitator motor that drives the standard agitators (anchor agitator, propeller, or turbine agitator, etc.) has an adjustable speed control. In addition, other process parameters such as dosing, pH of the reaction medium, pressure, etc. are measured and controlled (Figure 1) (11-14).

### Laser Optical Probe System

With the computer-controlled laser probe, which measures and controls the solution turbidity that occurs during fractionation of polymers, the efficient operation of the system has been increased and homogeneous fractions have been obtained. To enable continuous detection of solution concentration without stopping the operation of the equipment. A cylindrical probe 3 is provided with a slit portion 3' to which lenses 4 and 4' are attached. When the probe 3 is charged, the inside of the slit portion 3' is filled with the solution. Then, the beam  $f$  emitted from the laser 21 is split into beams  $f$  2 and  $f$  3. The beam  $f$  3 then becomes beams  $f$  4 to  $f$  9 and is reflected by the reflecting device 7 and becomes a beam  $f$  10 and merges with the beam  $f$  2. Then, the differential amplifier 10 is connected via the photosensor 8 and the current / voltage converter 9. The signal 11 representing the solution concentration is output by being input to the input terminal and compared with the reference signal 12 (Figure 2) (14).

## RESULTS

If a copolymer dissolved in a single solvent (high temperature-resistant organic solvent) is fractionated due to a temperature difference, the fractionation process occurs by the effects between the polymer and the solvent. The separation process depends on the molecular weight of the copolymer, its composition, or a combination thereof. The

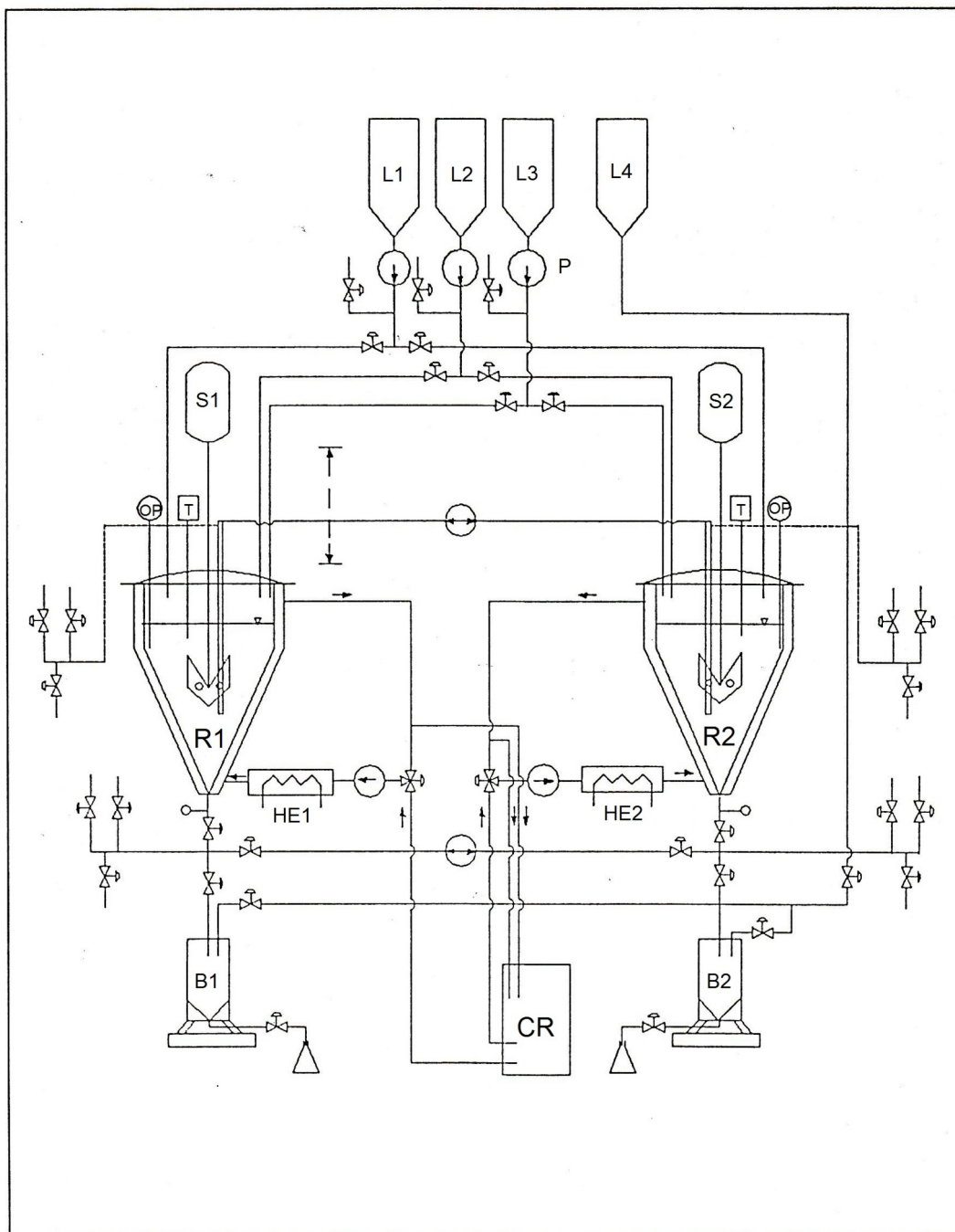
distribution of copolymer molecules in the two equilibrium phases is expressed by the following equation (11):

$$V' / V = \exp [P(\sigma - Kw)] \quad (1)$$

Here,  $V'$  and  $V$  define the volume fraction of a single component that is in solution and decomposes sequentially.  $P$  indicates the degree of polymerization,  $\sigma$  the fractionation parameter, and  $w$  the polymer composition. The  $K$  value for a single solvent system is defined as:

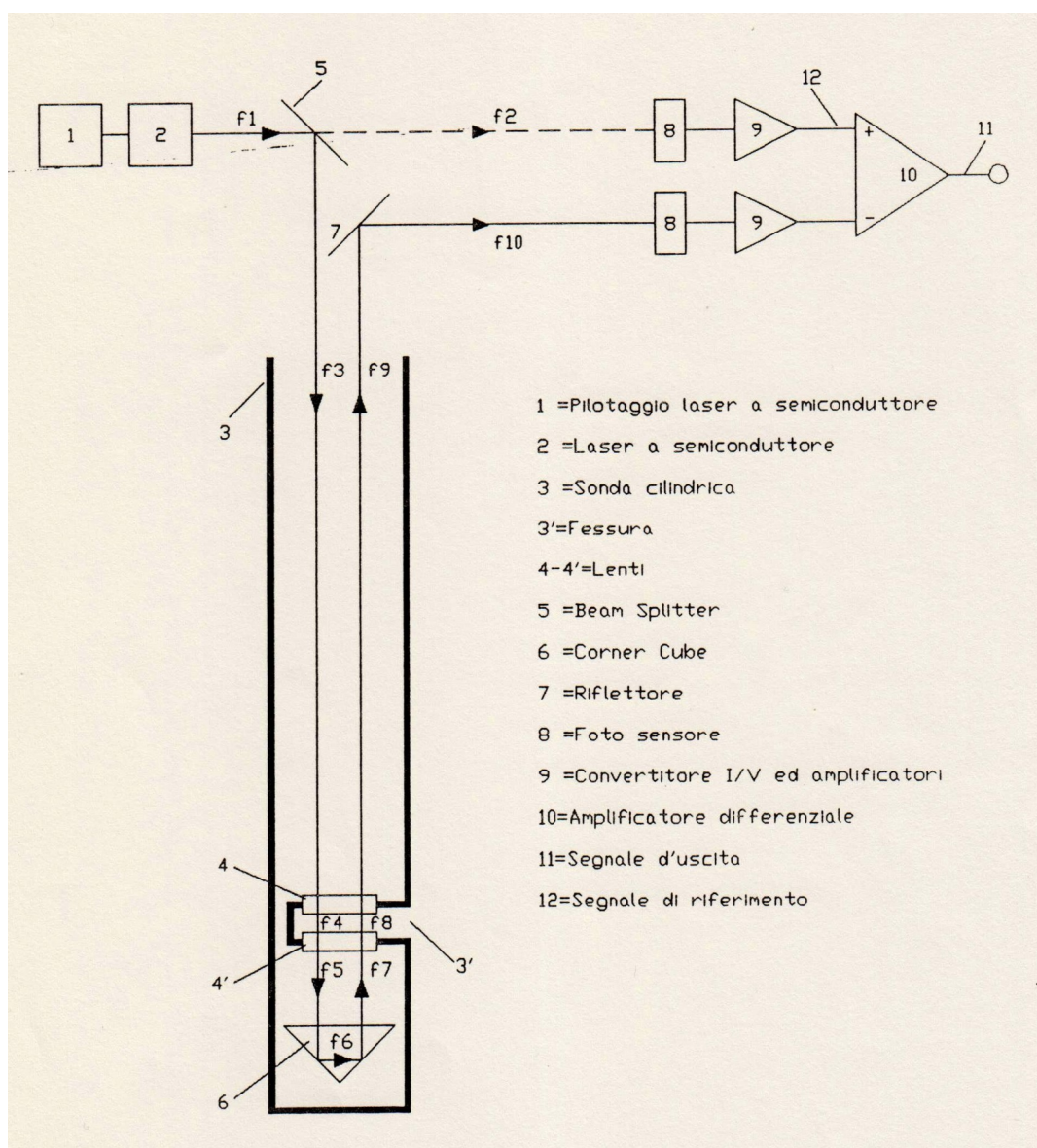
$$K = (V' - V) (X_A - X_B) \quad (2)$$

Here, the terms  $X_A$  and  $X_B$  refer to the interaction between the A and B copolymer units and the solvent. If  $X_A = X_B$ , then the  $K$  value will naturally be zero. The fractionation process is completely dependent on molecular weight (1-4). Composition and MWD values [Molecular weight distribution of polymers; degree of polydispersion ( $M_w/M_n$ )] of BUNA AP 301 copolymer and its fractions are given in Table 2. The molecular weight distribution of the fractions obtained in this study was evaluated according to the Tung and Scholte methods given in the literature (9,10). Table 3 shows the molecular weight distributions of the copolymer fractions obtained as a result of fractionation and their evaluation according to Tung and Scholte methods. In the evaluation made according to the Tung method, the molecular weight distribution is mostly in the form of Gaussian. In contrast, the Scholte assessment is more limited than the Tung assessment since linear macromolecules with short side chains are considered. However, as can be seen in Table 3, the results of both evaluations are close to each other with a difference of  $\pm 10\%$ . When the molecular weight distributions, MWD, viscosity values and other evaluations are examined together, it is seen that this fractionation system (L.A.F.P.) developed is quite effective. Especially with the computer-controlled laser probe, which measures and controls the solution turbidity that occurs during fractionation, the efficient operation of the system has been increased and homogeneous fractions have been obtained. With this method, a large amount of fractions with different molecular weights required for copolymer studies are obtained.



**Figure 1.** Computer-Controlled Automatic Laboratory System Used in Polymer Fractionation (L.A.F.P.), European Patent No: 911044370.1, 20.03.1991 [12,13,14,15] (R: Reactors for Polymer Fractionations, L: Polymer Solutions Sample Tanks, CR: Reactor Cooling and Heating System, HE: Heat Exchangers for Reactors, B: Samples Collection Tanks and Balance, S: Reactor Stirrers, T: Thermometers, OP: Laser Probe Systems).





**Figure 2.** Laser Probe System with Computer Controlled Automatic Laboratory System Used in Polymer Fractionation (L.A.F.P.), European Patent No: 911044370.1, 20.03.1991 (12-15).

**Table 2:** Properties of Fractions of BUNA AP 301 Copolymer Obtained From Diphenylmethane Solution.

No	(°C)	Fraction	(%wt)	(dL/g)
1	120	0.2000	2.5	42.6
2	117	0.2033	2.3	44.4
3	114	0.0656	1.6	43.4
4	112	0.1092	1.8	43.8
5	110	0.0687	1.6	44.0
6	106	0.0862	1.3	44.0
7	95	0.1501	1.4	43.3
8	90	0.0479	1.4	42.9
9	80	0.0231	1.6	42.2
10	70	0.0251	1.5	44.2
11	25	0.0208	2.5	n.d.
BUNA AP 301	-	-	2.6	43.8

**Table 3:** Analysis Results of Samples Obtained by Fractionation Evaluation

Fraction No	M <sub>w</sub> (PE)	M <sub>w</sub> (PP)	C <sub>3</sub> (% wt)	M <sub>w</sub> (Tung)	M <sub>w</sub> (Scholte)
1	305,000	556,000	42.6	394,000	356,000
2	217,000	350,000	44.4	269,000	255,000
3	205,000	334,000	43.4	254,000	240,000
4	167,000	271,000	43.8	207,000	196,000
5	149,000	240,000	44.0	183,000	174,000
6	131,000	211,000	44.0	161,000	153,000
7	97,000	156,000	43.3	119,000	114,000
8	70,000	112,000	42.9	85,000	82,000
9	57,000	92,000	42.2	70,000	67,000
10	38,000	60,000	44.2	46,000	44,000
11	19,000	31,000	n.d.	24,000	22,000
BUNA AP 301	187,000	302,000	43.8	230,000	220,000

n.d. : not measured, MWD: Molecular weight distribution of polymers; degree of polydispersion (Mw/Mn), Mw: average molecular weight, Mn: number average molecular weight. %C<sub>3</sub> : percent polypropylene content (from IR analysis). [η] : the actual viscosity of the polymer.

## ACKNOWLEDGMENT

We would like to thank Dott. Fabio Garbassi, Dott. Giangaleazzo Triulzi, Dott. Mariano Tacchi Venturi, Dott. Paolo Palagi, Ing. Paolo Bovio, Ing. Antonio Giuliani (Istituto Guido Donegani, Enichem, Novara, Italy) who helped us in this study, for their contribution.

## REFERENCES

- Patterson G. Physical chemistry of macromolecules [Internet]. Boca Raton: CRC Press; 2007 [cited 2022 Jul 26]. Available from: <http://www.crcnetbase.com/isbn/9781420014501>
- Misra GS. Introductory polymer chemistry. New York: J. Wiley & Sons; 1993. 253 p.
- Collins EA, Bareš J, Billmeyer FW. Experiments in polymer science. New York: Wiley; 1973. 530 p.
- Gouw TH. Guide to modern methods of instrumental analysis [Internet]. New York: Wiley-Interscience; 1972 [cited 2022 Jul 26]. Available from: <http://books.google.com/books?id=1HhOQAIAIAA>
- Mendelson RA, Bowles WA, Finger FL. Effect of molecular structure on polyethylene melt rheology. I. Low-shear behavior. J Polym Sci A-2 Polym Phys. 1970 Jan;8(1):105–26.
- Zimm BH, Kilb RW. Dynamics of branched polymer molecules in dilute solution. J Polym Sci. 1959 May;37(131):19–42.
- Ram A, Miltz J. New method for MWD determination in branched polymers. J Appl Polym Sci. 1971 Nov;15(11):2639–44.
- Schärfl W, Schärfl W. Light scattering from polymer solutions and nanoparticle dispersions. Berlin: Springer; 2007. (Springer laboratory manuals in polymer science).
- Tung LH. Block copolymer molecular weight by GPC. J Appl Polym Sci. 1979 Aug 15;24(4):953–63.
- Scholte ThG, Meijerink NLJ, Schoffeleers HM, Brands AMG. Mark–Houwink equation and GPC calibration for linear short-chain branched polyolefines, including polypropylene and ethylene–propylene copolymers. J Appl Polym Sci. 1984 Dec;29(12):3763–82.
- Flory PJ. Principles of polymer chemistry. 19. print. Ithaca, NY: Cornell Univ. Press; 2006. 672 p.
- Tolay M, Cinquina P, Triulzi G. (L.A.P.F.)-Laboratorio Automatico per Il Frazionamento Polimeri. Novara, Italy: Istituto Guido Donegani, Gruppo Enichem; 1990 May.
- Cinquina P, Triulzi G, Garbassi F. Procedure for the Continuous Fractionation of Polymers and Relative Equipment. Novara; 19778A/90.
- Tolay M, Cinquina P, Triulzi G. Optical Probe to Determine the Turbidity of a Solution by Immersion. Novara; 911044370.1, 1991.
- Tolay M, Cinquina P, Triulzi G. Optical Probe to Determine The Turbidity of a Solution of Polymers by Immersion (L. A. F. P.). In Istanbul, Turkey; 1996.
- Desreux V, Bischoff J. Viscosimètres capillaires modifiés. Bull Soc Chim Belges. 2010 Sep 1;59(1–2):93–101.
- Benoit H, Grubisic Z, Rempp P, Decker D, Zilliox JG. Étude par chromatographie en phase liquide de polystyrènes linéaires et ramifiés de structures connues. J Chim Phys. 1966;63:1507–14.



## Tetrazolium-Based Rapid Colorimetric Assay to Determine Bacteriocin Activity

Nedim ALBAYRAK 

Hitit University Faculty of Engineering, Department of Food Engineering, Çorum, Turkey.

**Abstract:** The aim of this study is to develop a simple, rapid, and accurate method for quantitative determination of bacteriocin activity. The method involves the use of 2,3,5-triphenyltetrazolium chloride (TTC), which is a colorless water-soluble salt. Only viable cells take up the compound and reduce it intracellularly to its red-colored and water-insoluble formazan dye. Bacteriocin, nisin and lactacin-A were assayed using the sensitive indicator *Lactobacillus delbrueckii* subsp. *lactis* ATCC 4797 whereas pediocin PO2 was assayed against *Lactobacillus bulgaricus* OSU 135. The major factors affecting the reduction of TTC, such as the reagent concentration, incubation period, temperature, and pH were adjusted so that optimal reduction of TTC by the indicator microorganisms could be achieved. Two-fold dilutions of the bacteriocins were mixed with a standardized indicator culture and incubated for 30 min. Then 0.2% TTC was added and the mixture (pH 6.0) was incubated at 37 °C for 20 min. After the incubation, formazan was extracted from the cells with methanol and the absorbance was measured at 485 nm. The amount of formazan formed by the survivor cells was compared with survivor counts and zone of inhibition method. The dose-response plot for the TTC-based bacteriocin assay was linear over a wide range bacteriocin concentration. A high correlation ( $R^2 > 0.95$ ) was between viable cell count and TTC reduction for three of the bacteriocins tested. The new assay can be completed in one hour, compared to one or two days with microbiological assays. Overall, the procedure is simple and easy to carry out.

**Key words:** Bacteriocin; 2,3,5-triphenyltetrazolium chloride (TTC); TTC-based bacteriocin assay, Nisin, Lactacin A

**Submitted:** August 30, 2022. **Accepted:** September 16, 2022.

**Cite this:** Albayrak N. Tetrazolium-Based Rapid Colorimetric Assay For Bacteriocin Activity. JOTCSB. 2022;5(2):91-110.

**\*Corresponding author. E-mail:** [nedimalbayrak@hitit.edu.tr](mailto:nedimalbayrak@hitit.edu.tr).

### INTRODUCTION

By definition, bacteriocins are ribosomally synthesized proteinaceous compounds showing a bactericidal mode of action against sensitive cells (1,2). Most LAB bacteriocins are active against a wide range of gram positive bacteria (3).

Although various bacteriocins have been discovered, isolated, and identified, methods for quantifying bacteriocin activity have remained with limited precision. The limitations of the available bacteriocin

assay methods have been recognized in several review articles (1,4-8). Almost all methods for qualitative or quantitative determinations of bacteriocin activity are based on the microbiological assays (7). Microbiological assays depend on the inhibition of the growth of the sensitive microorganism to determine the concentration of an inhibitory substance (9,10). The methods used for determination of bacteriocin activity are usually derived from those for antibiotics. However, bacteriocins differ from antibiotics especially due to the chemical compositions and mode of actions. The

majority of antibiotics are bacteriostatic, thus they only affect the growth rate of bacteria rather than killing them. Bacteriocins, on the other hand, are protein in nature and exhibit a very rapid killing effect. Therefore, the methods used for antibiotics might not be appropriate for bacteriocins.

Most widely used methods for bacteriocin activity are modifications of agar diffusion assays (spot, well, disc diffusion) and turbidimetric assays. Since standard reference compounds for bacteriocins are not generally available, critical dilution methods are more often applied with arbitrary units to express the activity. This method is a semi-quantitative, provides only a discontinuous scale for activity and always requires a complete series of dilutions to estimate activity (11). Although this method is simple and easy to use, detection of the inhibition zone, corresponding to the highest two-fold dilution, is error-prone. There is always an uncertainty of the decisive end-point, which leads to great inaccuracy in the calculations of bacteriocin activity (4,12). In turbidimetric measurements, the main drawback is that the curve rises sharply from low to high responses within a very short dilution span, which significantly limits the useful dose range and the accuracy of the method (10,11).

Any method that is used to detect bacterial growth or cell viability can be applied to the measurement of the interaction between antimicrobial agents and bacteria. Even though cell viability is conventionally defined as the reproductive capability of the cell, several characteristics of viable cells could be measured and used to estimate the reproductive ability (13–15). For instance, the determinations of membrane integrity and/or membrane potential can be associated with viability (15). In a broad sense, the alternative approaches to viability assays include measurements of metabolic activities, redox potential, electrical conductivity, microcalorimetry, radiometry, and bioluminescence (5).

Tetrazolia have been known as vital stains and employed in histochemistry particularly for localizing oxidative enzymes in biological systems (9,16). Reduction of tetrazolium salts in living organisms is caused by enzyme activity (16–18). These salts accept electrons from oxidized substrates such as NADH and NADPH (19) by means of intracellular dehydrogenase activity of viable cells (15,20). In this system, tetrazolium salts are taken by bacterial cells and reduced into its original red-colored formazan products. Even though the tetrazolium salts can enter both viable and dead cells, only viable organisms (metabolically active) have the ability to reduce these salts into formazan (4,11,15).

The presence of cell membrane potential attracts TTC to enter the cells. TTC has one positive charge and three phenyl groups around the four-nitrogen-containing ring. Thus, the molecule possesses lipid-like and fat-like properties, which helps TTC first attracted to cells and then enter the membrane. Uptake of tetrazolium salts depends on the basic cellular structure of bacteria. Between charged and uncharged state there is potential (O/R potential) about - 0.08 V. Due to the potential difference TTC is attracted to the cells. The potential difference across the bacterial membrane is typically 0.1-0.2 V (15). In bacteria, the enzymes of energy metabolism are located on the inner surface of the cytoplasmic membrane where the reducing power (NADH) of the metabolism is converted into ATP (21,22). When H is removed from NADH (oxidation) by a particular dehydrogenase enzyme (e.g., lactate dehydrogenase), H is taken by the tetrazolium salt (reduction) leading to the formation of formazan which no longer possesses the positive charge nor the bond between the nitrogen atoms (23). It was found that most cellular reduction of tetrazolium salts was dependent on the reduced pyridine nucleotides, NADH and NADPH (17). After reduction, formazan deposits, coalesces, and becomes larger deposits located in the cytoplasm (24).

Our goal was to develop a rapid and accurate quantitative assay for bacteriocin activity. We mainly propose that the characteristic of 2,3,5,-triphenyltetrazolium chloride (TTC) can be applied to quantitate the bacteriocin activity in liquid environment. The absorbance of red-colored formazan after extraction from the cells can be determined spectrophotometrically. If the sensitive cells are exposed to the bacteriocin in a range of concentrations, a correlation should exist between the viable cell counts (survivor count) and survivors' ability to reduce TTC into formazan. Such a method should allow rapid, accurate, and more sensitive determination of the bacteriocin activity.

## MATERIALS AND METHODS

### Media and Indicator Microorganisms

MRS broth was prepared by dissolving 55 g of Lactobacilli MRS (Difco) in 1 L of distilled water. Portions of 50 mL of MRS broth in 160-mL milk dilution bottle (Fisher Scientific, Pittsburgh, PA) were autoclaved at 120 °C for 20 mins. MRS agar and MRS soft agar were prepared by adding 15 and 7.5 g/L of agar (Difco) in MRS broth, respectively.

*Lactobacillus delbrueckii* subsp. *lactis* ATCC 4797 was used as a sensitive indicator for nisin and lacidin A (25), and *Lactobacillus bulgaricus* OSU 135 was the indicator for pediocin PO2 (26). Cultures were

obtained from the culture collection of the Food Microbiology Laboratory, The Ohio State University, Columbus, OH. The cultures were maintained in MRS containing 10% glycerol and stored at -18 °C. The cultures were propagated twice in MRS and incubated at 37 °C for 18 hours before use.

MRS broth was inoculated with an overnight culture at a rate of 0.1% ( $10^4$ - $10^5$  CFU /mL). The inoculated medium was incubated for 12 hours in a water bath at 37 °C. After 12 h of incubation, portions of the culture were centrifuged at 10,000 rpm for 5 mins at 20 °C. The supernatant was removed and the cell pellet was resuspended to the original volume using phosphate buffer at pH 6. An amount of 700 µL of the resuspended culture was dispensed into a microcentrifuge tube for the TTC-based bacteriocin assay.

### Preparation of Bacteriocins

A commercial preparation of nisin was obtained from Sigma Chemical. The preparation contains 2.5% nisin, which provides  $10^6$  IU nisin per g (27). Stock solution of nisin were prepared by adding 0.1 g of the powder to 1 mL of 0.05 M citrate-phosphate buffer at pH 4. The solution was filter-sterilized using a 0.22 µm pore size filter (Gelman Sciences). This solution was used to prepare various dilutions of nisin using the former buffer.

The bacteriocins Lacidin A and pediocin PO2 were produced by *L. acidophilus* OSU 133 and *Pediococcus acidolactisi* PO2, respectively. The bacteriocins were partially purified using a chloroform extraction. Stock solutions of the purified bacteriocins, or dilutions thereof, were made using phosphate buffer (pH 6). All the stock solutions and dilutions were kept frozen until use.

### TTC solutions

The reagent 2,3,5,-triphenyltetrazolium chloride (TTC) was obtained from Fisher Scientific in a dehydrated state. Stock solution 1% (w/v) was prepared using 0.05 M phosphate buffer at pH 6.0. The solution was filter-sterilized using a 0.22 µm pore size filter and kept frozen in the dark. The assay solution concentration was 0.2% (w/v) and prepared from the stock solution with the same sterile buffer.

### Optimizing Assay Conditions

#### *TTC and culture viability*

Experiments were done to test the susceptibility of indicator cultures to TTC. The cell suspension of strain 4797 was prepared as indicated earlier, and equal volumes (750 µL each) of 1% TTC solution and the culture were mixed. The mixtures were incubated in a water bath at 37 °C. Sample tubes were removed after 10, 20 and 90 minutes of incubation and plate

count on MRS agar was performed. The experiment included two replicates of the test and blank samples which received the TTC solution and pH 6 phosphate buffer, respectively.

#### *Culture growth*

MRS broth (50 mL) was inoculated with  $\sim 10^4$  CFU/mL from the culture 4797, which has been transferred twice. The inoculated MRS broth was incubated in a water bath at 37 °C. Samples were taken at 1-h intervals, and tested for cell count, turbidity, and TTC-reducing capacity by following the TTC reduction procedure.

#### *TTC concentration*

In order to determine the optimum TTC concentration, a broad range of concentrations was studied. Cell suspension of indicator microorganism was prepared and divided into six portions. The concentrations of 25, 50, 100, 500, 1000, 2000, 4000, and 5000 ppm of TTC were prepared from the stock solution using phosphate buffer (pH 6) as a diluent. Each of these concentrations was used as the TTC assay solution in the TTC reduction procedure and the results were compared.

#### *Incubation period*

The minimum time necessary for the uptake of TTC and its reduction to the formazan particulate was studied. The indicator culture 4797 was mixed with TTC assay solution and tested using the TTC reduction assay as indicated earlier. After 10, 20, 30, 40, 50 and 60 minutes of incubation, samples corresponding to the incubation period were removed from the water bath and tested according to the TTC reduction procedure. Five replicates of this experiment were performed using the same batch of the culture.

#### *pH*

In order to determine the effect of pH during the course of TTC reduction, pH values in the range of 3 to 9 were tested. Buffers with pHs of 3, 4, 5, 6, 7, 8, and 9 were prepared. For pH 3.0, 4.0, and 5.0, citrate-phosphate buffer was used (made by mixing 0.05 M solutions of citric acid monohydrate (Fisher) and dibasic phosphate (Mallinckrodt) until the desired pH is reached). For pH 6.0 and 7.0, phosphate buffer was used (made by mixing 0.05 M solutions of monobasic (Mallinckrodt) and dibasic phosphates until the desired pH is obtained). For pH 8.0 and 9.0, Tris buffer was used (made by mixing 0.05 M solutions of Tris (Fisher) and Trizma base (Sigma) until the desired pH is adjusted). A pH meter (Fisher Scientific) was used in all pH adjustments and measurements. These buffers were used for the pH adjustments of the indicator culture and the preparation of TTC solutions. The indicator microorganism was propagated as indicated and divided into seven portions. Each portion was centrifuged to remove the



medium, and the cells were resuspended in the buffer solution of desired pH. For each pH, three replicates were prepared. The stock solution of 1% TTC was also prepared in the buffer solutions of the desired pH values. Same buffers solutions were used to prepare 0.2% TTC assay solutions. Procedure for TTC reduction was done at different pH values.

#### Reduction Procedure of TTC

A portion (750  $\mu$ L) of the indicator microorganism cell suspension was mixed with 750  $\mu$ L of TTC assay solution. The mixture was incubated at 37 °C for 20 minutes in the dark. After the incubation, the cells (containing the red-colored formazan particulates) were centrifuged at 10,000 rpm for 5 min at 20 °C and supernatant was removed. Formazan in the cell pellet was extracted using 750  $\mu$ L of methanol with grinding and agitation. The mixture was centrifuged at 10,000 rpm for 5 min to remove cell debris. The amount of the reduced dye in the extract was measured at OD<sub>485</sub> against methanol as a reference solution.

Absorbance was measured using a spectrophotometer (Spectronic 1201). For the removal of the medium from the culture, SS-34 Rotor of Sorvall RC-5B Refrigerated Superspeed Centrifuge was used. For other centrifugations, a microcentrifuge (Biofuge A) was used.

#### TTC-based Bacteriocin Assay Procedure

The cell suspension of culture (700  $\mu$ L) and the bacteriocin solution (100  $\mu$ L) were mixed in microcentrifuge tubes and incubated at 37 °C for 30 min. After the incubation, 100  $\mu$ L volume of the mixture was removed for survivor count. TTC assay solution (700  $\mu$ L) was added to the remaining volume of bacteriocin-treated culture in the tubes. The mixture was incubated at 37 °C for 20 min in the dark. After the incubation, the mixture was centrifuged at 10,000 rpm for 5 mins to collect the cells. The cell pellets were received with 700  $\mu$ L of methanol and were grinded with a pellet pestle (Science ware Micro Centrifuge Sample Pestle, Fisher) to extract formazan from cells. The solvent culture mixture was centrifuged at 10,000 rpm for 5 mins to remove cell debris. The absorbance of the extracted red color was measured at OD<sub>485</sub> against methanol as a reference.

#### Survivor Count Method

For the determination of Colony Forming Unit (CFU) / mL, 100  $\mu$ L of the culture was mixed with 900  $\mu$ L of sterile peptone-water saline (0.85% NaCl, and 0.1% peptone-water (Difco)). Additional decimal dilutions were prepared similarly. Portions (100  $\mu$ L) of the desired dilutions were spread onto MRS agar in triplicates. The CFU counts were obtained by counting

the plates having colonies between 30 and 300 after the incubation for 48 hours at 37 °C.

#### Critical Dilution Method

Overnight culture of the sensitive microorganisms (*Lactobacillus delbrueckii* subsp. *lactis* ATCC 4797 or *Lactobacillus bulgaricus* OSU 135) were used to seed the liquefied soft agar at ca. 10<sup>6</sup> CFU/per mL of soft agar. The tubes were mixed well and 5 mL amounts were overlaid onto the MRS agar in petri dishes. The prepared petri dishes were refrigerated for 1 h and thereafter were spotted with the appropriate bacteriocin dilutions. Two-fold dilutions of bacteriocins were prepared as indicated earlier and 5  $\mu$ L from each dilution was spotted onto the agar overlay. The plates were incubated at 37 °C for 24 hours (3). Bacteriocin activity was measured using the highest dilution showing complete inhibition zone of the indicator lawn. Bacteriocin potency was expressed as activity units, AU/mL (27,28). The results were also read as diameters of inhibition zones in mm and calculated as area of inhibition zone.

#### Data Analysis

Statistical analysis of the results was done using the Minitab software. The significance was determined by one way (ANOVA) and means were compared using Tukey's pairwise comparisons at 0.05 probability level. The linear regression equations and correlation coefficients obtained were used for estimation of bacteriocin concentrations.

## RESULTS

#### Assay Development

Applying TTC as a tool to estimate the number of viable cells, rather than qualitative measure of viability, requires an understanding of the process of TTC reduction by the cultures. Thus, prior to developing TTC-based assay for bacteriocins, several parameters that may affect the reduction were studied. During the study, the factors in question were varied one at a time. After each step, the preliminary assay conditions were modified and standardized so as to serve as an ultimate procedure for the determination of bacteriocin activity. Although TTC reduction may measure intracellular dehydrogenase activity, our goal was to use this reaction as an indication of viability under standardized conditions of TTC concentration, incubation temperature, pH and culture age. The following are the factors of significance to the assay development and the obtained results.

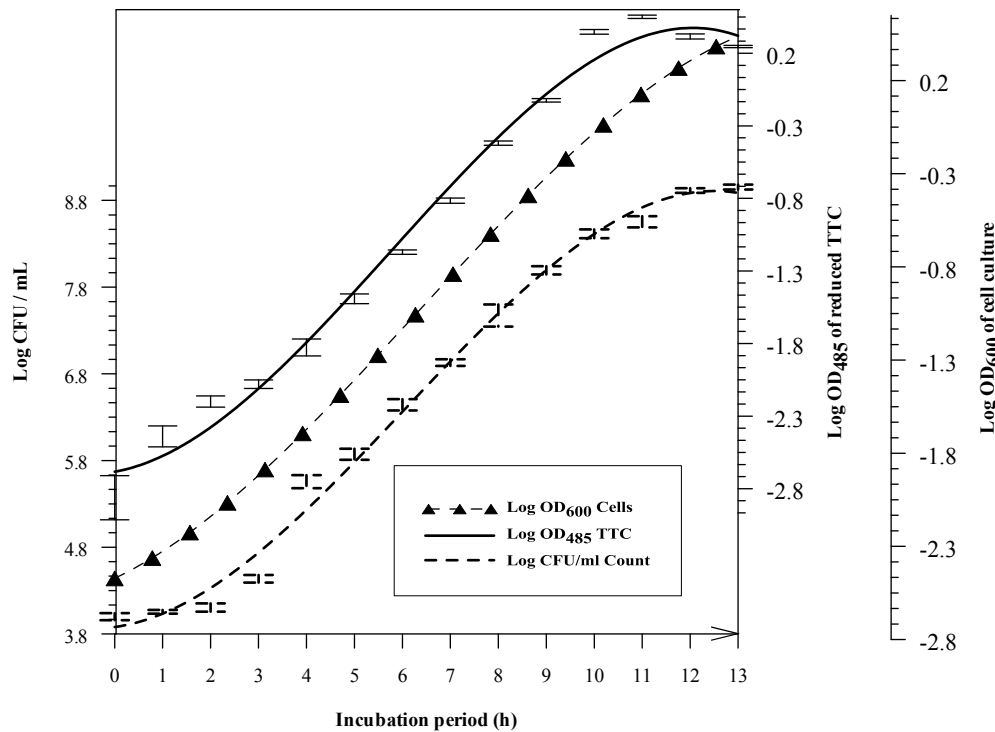
#### Optimization of Assay Parameters

The growth of *L. delbrueckii* subsp. *lactis* ATCC 4797 was monitored for 14 hours of incubation by three methods, (a) plate count (CFU/mL), (b) absorbance at



OD<sub>600 nm</sub>, and (c) TTC reduction (OD<sub>485 nm</sub>). Since the growth of microorganisms follows first order kinetics, the logarithm of the responses of three methods were

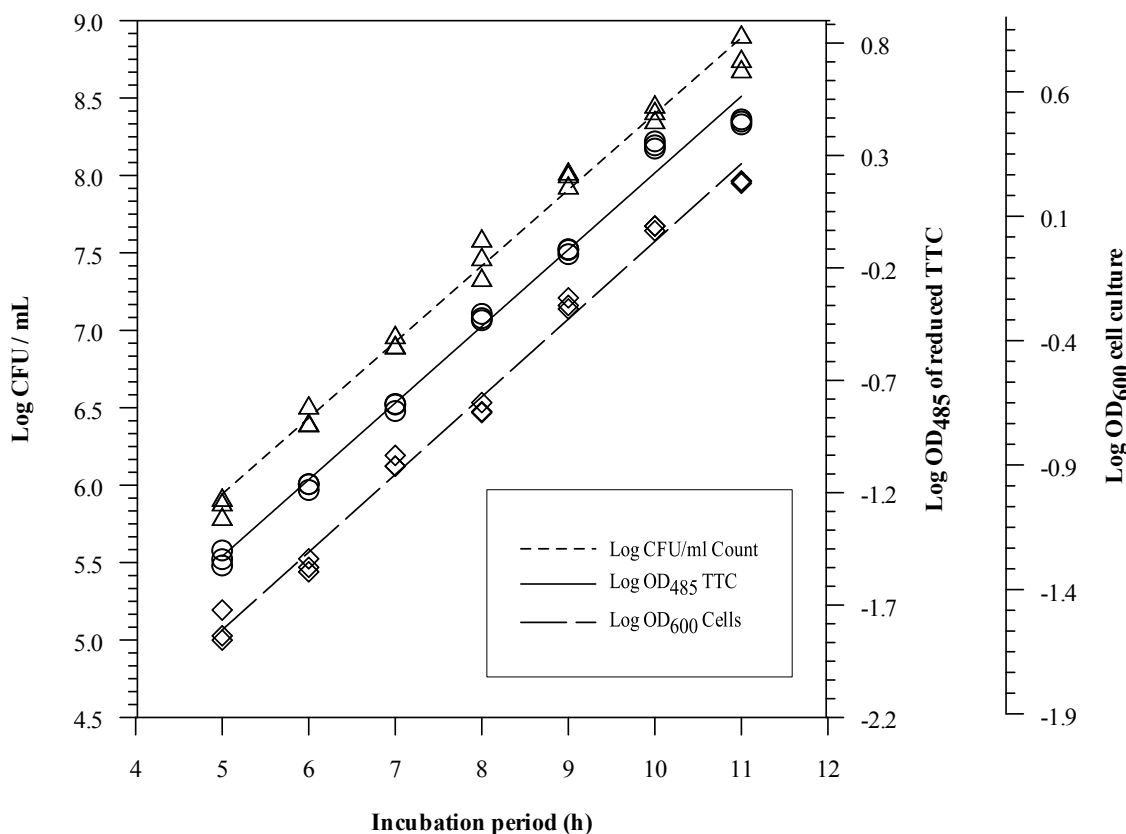
plotted against incubation period (Figure 1). The culture displayed regular batch growth kinetics.



**Figure 1:** Growth of *Lactobacillus delbrueckii* subsp. *lactis* ATCC 4797 culture monitored by plate counting (log CFU/mL), optical density (log OD at 600 nm) and TTC reduction (log OD at 485nm) after 20 min of incubation with 0.2% TTC at 37 °C. The curves indicate the best fit obtained by polynomial regression analysis of the results of three trials. The error bars show the standard deviations of the counts and TTC reduction.

The change in log CFU/mL during the first four hours was insignificant ( $P > 0.05$ ). During that time, TTC reductions were low (absorbance between 0.001 and 0.01). The low cell count may cause this small TTC reduction and large variability in results. During the

same period, OD<sub>600 nm</sub> increased from 0.007 to 0.02, but this change was not significant. In fact, OD<sub>600</sub> did not significantly change from the initial value until the CFU reached the 10<sup>6</sup> level (data not shown).



**Figure 2:** Growth of *Lactobacillus delbrueckii* subsp. *lactis* ATCC 4797 culture between fifth and eleventh hours as measured by plate counting (CFU/mL), optical density (OD at 600 nm) and TTC reduction (OD at 485 nm after 20 min incubation with 0.2% TTC at 37 °C), (results of three independent trials).

At approximately the fifth hour of incubation, the culture began the exponential phase as indicated by the changes in log CFU/mL. This phase lasted about six hours (Figure 2). TTC reduction and OD<sub>600</sub> increased with increasing plate counts until the log of CFU reached 8.5 - 8.8, which was approximately the late exponential phase of the growth. During the exponential phase, the linear growth can be clearly seen by means of the three methods (Figure 2), in which the correlation coefficients as log of response versus time were the highest ( $R^2 > 0.99$ ). After the eleventh hour, the changes in plate counts were not significant ( $P > 0.05$ ) and the number remained almost constant for two hours (Figure 1). However, a slight but gradual decline was observed with TTC reduction, which probably resulted from a decrease in the amounts of NADH during the stationary phase. The turbidity, on the other hand, continued to increase at a slower rate (Figure 1). When the experiment was repeated using different inoculation rates and TTC concentrations, similar results were observed (data not shown).

coefficient between log CFU and log OD<sub>600</sub> was 0.96, and log CFU and log OD<sub>485</sub> was 0.97 (data not shown). During the exponential growth, both  $R^2$  results were 0.99. Overall, these results suggest that TTC reduction can be used to monitor growth instead of conventional methods. Considering the range of the linear growth (Figure 1) where metabolic activity of the culture is uniform and constant, the results were found very promising that TTC reduction could be applied to monitor viable cell counts when the number of cells is reduced by a bactericidal agent.

Based on the results of this experiment, the 12-h-old culture has the maximum TTC reduction ability. Therefore, twelve-hour-old cultures, prepared with the same inoculation rate, were used for the entire study and during all trials of bacteriocin testings. By doing so, the variations in TTC reduction associated with culture age and metabolic activity were minimized. In this state, cells possess maximum activity of reducing enzymes as well as NADH (29), which are the primary cause of the TTC reduction.

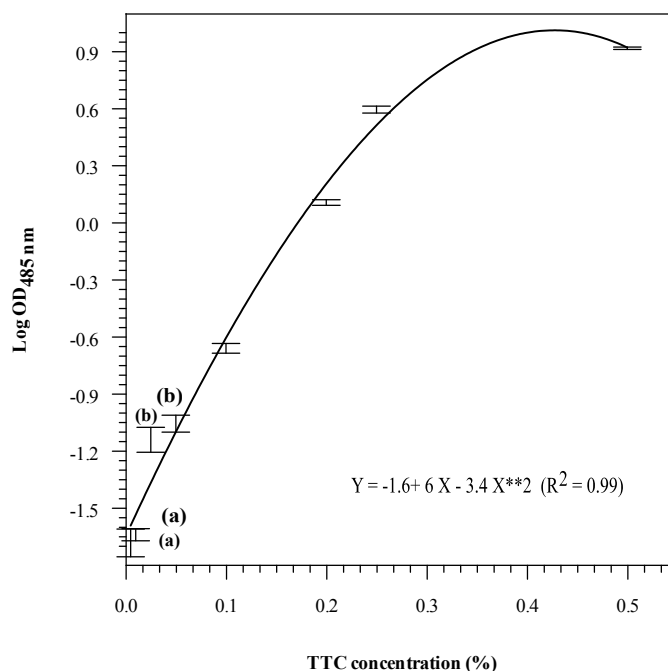
During the entire growth period, the correlation

Even though tetrazolium salts have been recognized

as vital stains, they are also known to have some inhibitory effect (15). Thus, in order to rule out any inhibitory effect of TTC, the culture 4797 prepared as indicated in earlier was treated with 1% TTC and the count was monitored for up to 120 min. However, the difference in count between the treatment and control was insignificant ( $P > 0.05$ ).

The effect of TTC concentrations was tested. As TTC concentration increased, color formation first increased rapidly then slowed down and leveled off (Fig 3). The results were best described by power 2 polynomial regression ( $R^2 > 0.99$ ), which probably suggest that the reduction of TTC resembles the

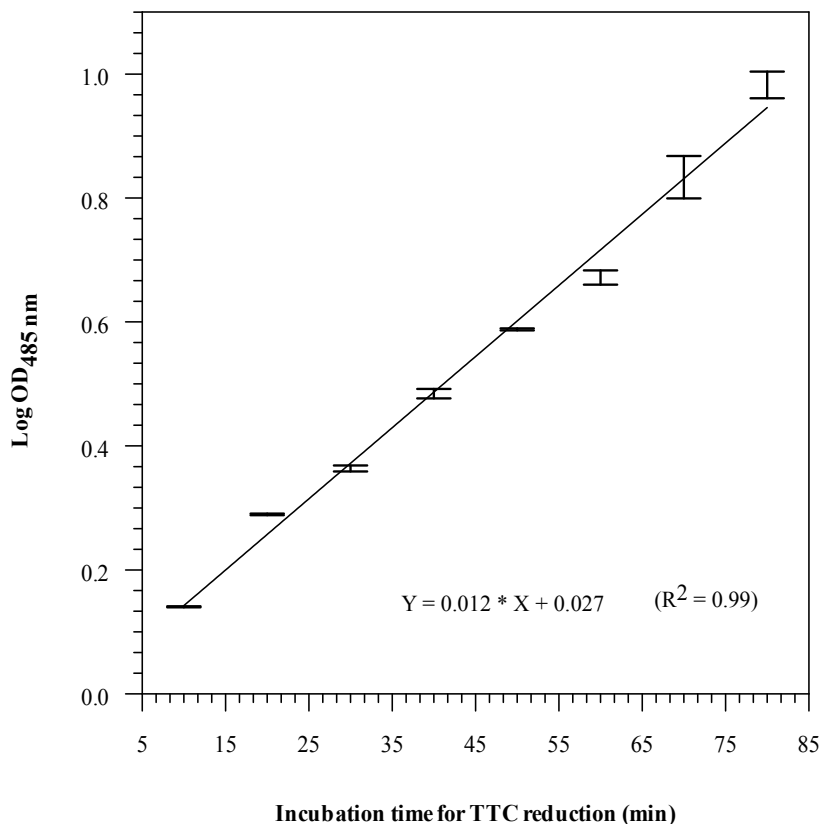
substrate effect on enzymatic reactions where the reaction follows the first order kinetics at low substrate concentrations (i.e., when substrate is limiting). At higher concentrations, however, the enzyme becomes a limiting factor and reaction follows zero order kinetics (8). Although TTC reduction may measure intracellular dehydrogenase activity, our goal is to use this reaction as an indication of viability under standardized conditions of TTC concentration, incubation temperature, pH and culture age. Therefore, 0.2% TTC concentration was chosen as an optimum concentration for measurable color formation under the standardized conditions.



**Figure 3:** Color formation (measured at OD 485nm) when the cells of *Lactobacillus delbrueckii* subsp. *lactis* ATCC 4797 were treated with different concentrations with of TTC. Error bars indicate standard deviations from the mean of three trials. Data points with similar superscripts were not statistically different ( $P > 0.05$ ).

Incubation period for TTC refers to the time permitted for the uptake of the salt by the cells and its reduction to the colored dye. Experiments were performed to determine a minimum time necessary for this process. The reduction of TTC increased with increasing incubation periods (Figure 4). 20 minutes of

incubation were chosen as a suitable period for adequate formation of formazan. The results were best described by linear regression ( $R^2 > 0.99$ ) suggesting that the reaction of TTC at 0.1% concentration follows zero order kinetics.



**Figure 4.** Reduction of 0.1% TTC, measured as color formation at OD 485nm, by *Lactobacillus delbrueckii* subsp. *lactis* ATCC 4797 after different periods of incubation at 37 °C. Error bars indicate the standard deviations from the means of two trials.

TTC reduction at pH values in the range of 3 to 9 was tested. The color formation reached the maximum at pH 6. Overall, the curve resembles to general effect of pH on enzyme activity where the activity increases as pH increases from low to optimum, and decreases as pH increases from its optimum point (data not shown).

For accurate spectrophotometric determination of the color resulting from intracellular reduction of TTC, extraction of formazan from the cells is necessary. Several solvents including methanol, ethanol, and acetone were compared in effectiveness and speed of extracting the color. Methanol was the most effective and the fastest color extractor among solvents tested (data not shown).

#### TTC-based Bacteriocin Assay

By taking the former factors into account, the TTC reduction procedure was standardized for the application in bacteriocin activity estimation. Bacteriocin activity was assayed by three methods (a) zone of inhibition, (b) survivor count method, and (c) TTC reduction. The responses obtained from the three methods were compared over a wide range of bacteriocins potency (two-fold dilutions). The results for nisin, lacidin A and pediocin PO<sub>2</sub> are summarized in Tables 1, 2 and 3, respectively. The unknown potency of bacteriocins were determined by critical dilution method. The results are expressed as AU/mL, which is determined from the reciprocal of the highest dilution possessing a clear zone (13,30). The AU/mL results as independent variable were used in dose-response curves (Figs. 5, 6 and 7).

**Table 1:** The survivor responses as log CFU/mL, log OD at 485 nm and diameter of inhibition zone (mm) obtained from two-fold dilution of nisin when used against *Lactobacillus delbrueckii* subsp. *lactis* ATCC 4797. Decline in responses are subtracted values of each survivor response from the last significant survivor response.

Two-fold Nisin dilution	Survivor Response (Log)		Decline in Response (Log)(*)		Zone Diameter (mm)	
	CFU/mL	OD <sub>485</sub>	CFU/ml	OD <sub>485</sub>	without TTC	with TTC
2 <sup>0</sup>	5.20 ± 0.07	-2.02 ± 0.07 <sup>(a)</sup>	3.84	2.62	23.33 ± 0.28	22.83 ± 0.28
2 <sup>-1</sup>	6.17 ± 0.05	-1.95 ± 0.16 <sup>(a)</sup>	2.86	2.55	22.16 ± 0.28	21.83 ± 0.28
2 <sup>-2</sup>	7.80 ± 0.05	-0.81 ± 0.08	1.23	1.41	19.66 ± 0.57	19.83 ± 0.28
2 <sup>-3</sup>	8.76 ± 0.03	0.32 ± 0.04	0.27	0.28	15.66 ± 1.52	17.50 ± 0.50
2 <sup>-4</sup> (**)	9.04 ± 0.05 <sup>(b)</sup>	0.60 ± 0.02 <sup>(c)</sup>	0.00	0.00	10.33 ± 1.15 <sup>(d)</sup>	12.66 ± 0.57 <sup>(e)</sup>
2 <sup>-5</sup>	9.08 ± 0.03	0.62 ± 0.01			0.00 ± 0.00	0.00 ± 0.00

(\*) Decline in Response = { Log of Survivor Response to the last significant dose (b or c) - Log of Survivor Response to a dose }  
{e.g., Decline in "Log CFU/ml" at 2<sup>-1</sup> dilution =(9.04 - 5.20) = 3.84 } or {e.g., Decline in "log OD<sub>485</sub>" at the same dilution =[ 0.60 - (-1.95) ] = 2.55

(\*\*) The highest dilution corresponding to last detectable zone of inhibition (d or e).

<sup>(a)</sup> The change in absorbance was not significant (P > 0.05).

<sup>(b, c)</sup> The last significant survivor response. At higher dilutions, change in responses were insignificant (P > 0.05).

<sup>(d, e)</sup> The last detectable zone of inhibition.

The zones of inhibition determinations were obtained from the agar plates that were used to determine AU/mL by the critical dilution method. This was done for comparison purposes and illustration of the diffusion characteristics of different bacteriocins. As zone diameters and standard deviations seen from the Table 1, 2 and 3, different bacteriocins displayed different agar diffusion kinetics. Nisin diffused very well and produced the largest and well-defined zones among the bacteriocins tested (Table 1). Nevertheless, this large zone decreased rapidly in size as the bacteriocin became more dilute. As nisin's dose was lowered by two-fold dilutions, the decline in diameter of the zone of inhibition was greater than the other bacteriocins. The fourth dilution was the last zone displaying always at least 10 mm zone diameter

(Table 1). Lacidin A preparation produced zones that also decreased in size with dilution but at a smaller rate than with nisin (Tables 1 and 2). The zones of lacidin A lasted until the sixth dilution (Table 2). Pediocin PO<sub>2</sub> (Table 3) showed similar diffusion and zone characteristics like lacidin A. The highest concentration of nisin (2<sup>4</sup> × 200 = 3200 AU/mL) produced ~ 23 mm zone of inhibition and 3.8 log CFU reduction (Table 1). On the other hand, lacidin A at the highest concentration (2<sup>6</sup> × 200 = 12800 AU/mL) showed ~ 18 mm zone of inhibition and 5.2 log CFU reduction. Thus, based on these results, the presence of less potency of nisin or the presence of relatively high potency of lacidin A did not seem to be reflected as zones of inhibition.

**Table 2:** The survivor responses as log CFU/mL, log OD at 485 nm and diameter of inhibition zone (mm) obtained from two-fold dilution of **lacidin-A** when used against *Lactobacillus delbrueckii* subsp. *lactis* ATCC 4797. Decline in responses are subtracted values of each survivor response from the last significant survivor response.

Two-fold Lac.-A dilution	Survivor Response (log)		Decline in Response (Log)(*)		Zone Diameter (mm)	
	CFU/mL	OD <sub>485</sub>	CFU/ml	OD <sub>485</sub>	without TTC	with TTC
2 <sup>0</sup>	3.53 ± 0.12	0.04 ± 0.009	5.26	0.54	17.50 ± 0.50	18.66 ± 0.57
2 <sup>-1</sup>	4.20 ± 0.08	0.13 ± 0.009	4.59	0.45	17.33 ± 0.57	16.50 ± 0.50
2 <sup>-2</sup>	5.30 ± 0.04	0.23 ± 0.006	3.50	0.35	15.83 ± 0.76	15.66 ± 0.57
2 <sup>-3</sup>	6.13 ± 0.12	0.33 ± 0.009	2.66	0.25	14.66 ± 0.57	14.33 ± 0.57
2 <sup>-4</sup>	6.64 ± 0.12	0.49 ± 0.007	2.15	0.09	12.66 ± 0.57	13.33 ± 0.57
2 <sup>-5</sup>	8.08 ± 0.13	0.55 ± 0.011	0.71	0.03	8.66 ± 1.15 <sup>(c)</sup>	9.33 ± 0.76
2 <sup>-6</sup> (**)	8.80 ± 0.07 <sup>(a)</sup>	0.59 ± 0.014 <sup>(b)</sup>	0.00	0.00	0.00 ± 0.00	5.66 ± 2.08 <sup>(d)</sup>
2 <sup>-7</sup>	8.94 ± 0.05	0.60 ± 0.009			0.00 ± 0.00	0.00 ± 0.00

(\*) Decline in Response = { Log of Survivor Response to the last significant dose (b or c) - Log of Survivor Response to a dose }  
 {e.g., Decline in “Log CFU/ml” at 2<sup>-3</sup> dilution = (8.80 - 6.13) = 2.66 } or {e.g., Decline in “log OD<sub>485</sub>” at 2<sup>-1</sup> dilution = ( 0.59 - 0.13) = 0.45 }

(\*\*) The highest dilution corresponding to last detectable zone of inhibition (d).

(a, b) The last significant survivor response. At higher dilutions, change in responses were insignificant (P > 0.05).

(c, d) The last detectable zone of inhibition.

**Table 3:** The survivor responses as log CFU/mL, log OD at 485 nm and diameter of inhibition zone (mm) obtained from two-fold dilution of pediocin PO<sub>2</sub> when used against *Lactobacillus bulgaricus* OSU 135. Decline in responses are subtracted values of each survivor response from the last significant survivor response.

Two-fold Ped.PO <sub>2</sub> dilution	Survivor Response (log)		Decline in Response (Log)(*)		Zone Diameter (mm)	
	CFU/mL	OD <sub>485</sub>	CFU/ml	OD <sub>485</sub>	without TTC	with TTC
2 <sup>0</sup>	6.08 ± 0.08	-0.89 ± 0.015	3.27	1.12	12.16 ± 0.3	12.63 ± 0.3
2 <sup>-1</sup>	6.97 ± 0.05	-0.64 ± 0.015	2.38	0.87	11.00 ± 0.0	10.83 ± 0.2
2 <sup>-2</sup>	7.54 ± 0.09	-0.40 ± 0.006	1.81	0.63	9.16 ± 0.2	9.17 ± 0.2
2 <sup>-3</sup>	8.07 ± 0.07	-0.22 ± 0.007	1.28	0.28	8.00 ± 0.0	8.16 ± 0.2
2 <sup>-4</sup>	9.11 ± 0.03	0.14 ± 0.005	0.24	0.08	6.16 ± 0.2 <sup>(c)</sup>	6.66 ± 0.1
2 <sup>-5</sup> (**)	9.35 ± 0.03 <sup>(a)</sup>	0.22 ± 0.003 <sup>(b)</sup>	0.00	0.00	0.00 ± 0.0	5.17 ± 0.2 <sup>(d)</sup>
2 <sup>-6</sup>	9.38 ± 0.02	0.23 ± 0.002			0.00 ± 0.0	0.00 ± 0.0

(\*) Decline in Response = { Log of Survivor Response to the last significant dose (b or c) - Log of Survivor Response to a dose }  
 {e.g., Decline in “Log CFU/ml” at 2<sup>-2</sup> dilution = (9.35 - 7.54) = 1.81 } or {e.g., Decline in “log OD<sub>485</sub>” at 2<sup>-1</sup> dilution = [ 0.22 - (-0.64) ] = 0.87 }

(\*\*) The highest dilution corresponding to last detectable zone of inhibition (d) with TTC.

(a, b) The last significant survivor response. At higher dilutions, change in responses were insignificant (P > 0.05).

(c, d) The last detectable zone of inhibition.

As indicated earlier, the TTC reduction and survivor counts were determined using the same set of dilutions of bacteriocins. Means and standard deviations of survivors' response determined by plate counts (log CFU/mL) and TTC reduction (log OD at 485 nm), are also displayed in Tables 1, 2, and 3. The

significance of each response (i.e., change of response as change of dose in two fold) corresponding to the same dilution were verified by analysis of variance (one-way ANOVA).

For a meaningful comparison of the results from these



different method results, survivor responses were converted into relative values, and expressed as the decline in response. Decline in response is obtained by subtraction of the  $\log_{10}$  of the response of a given dose from the  $\log_{10}$  of the response of the zero dose. This relative value can also be called as 'the proportionate response' (10). In our experiments, the last detectable response was considered as the response to zero dose.

Since the area of inhibition ( $\text{mm}^2$ ) is more relevant than zone diameter (mm) (31), the zone area values were used to compare with other methods. For calculation of the area of zone of inhibition, the radius of the zone, obtained from the critical dilution method with TTC, were squared and multiplied by 3.14,  $\pi$ -value. The area of zone of inhibition were plotted against AU/mL in Figs. 5, 6 and 7 for nisin, lacidin A and pediocin PO<sub>2</sub>, respectively.

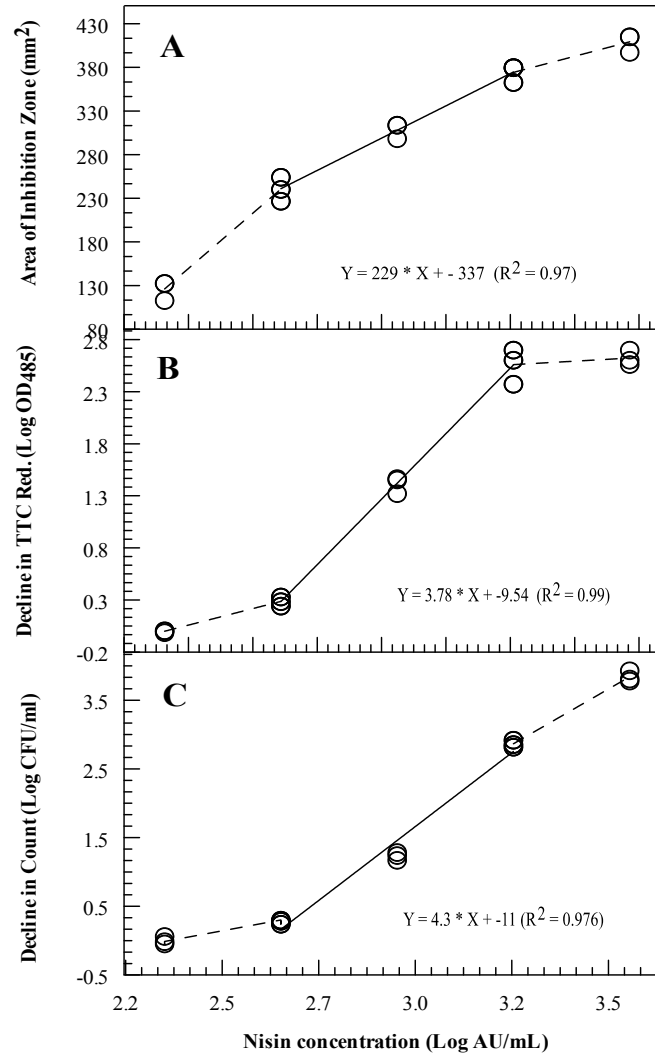
### Comparison of Different Methods

The decline in cell count and TTC reduction were plotted against the concentrations of bacteriocin (log AU/mL obtained from the critical dilution method). The dose-response curve of nisin, lacidin A, and pediocin PO<sub>2</sub> were shown in Figures 3, 4, and 5, respectively. The correlation coefficients ( $R^2$ ) and equations among the responses of the methods compared were summarized in Table 4. Overall, all of the responses of the methods shared the curvature characteristic of dose response curves. This was clearly observed with nisin (Figure 3). Therefore, the

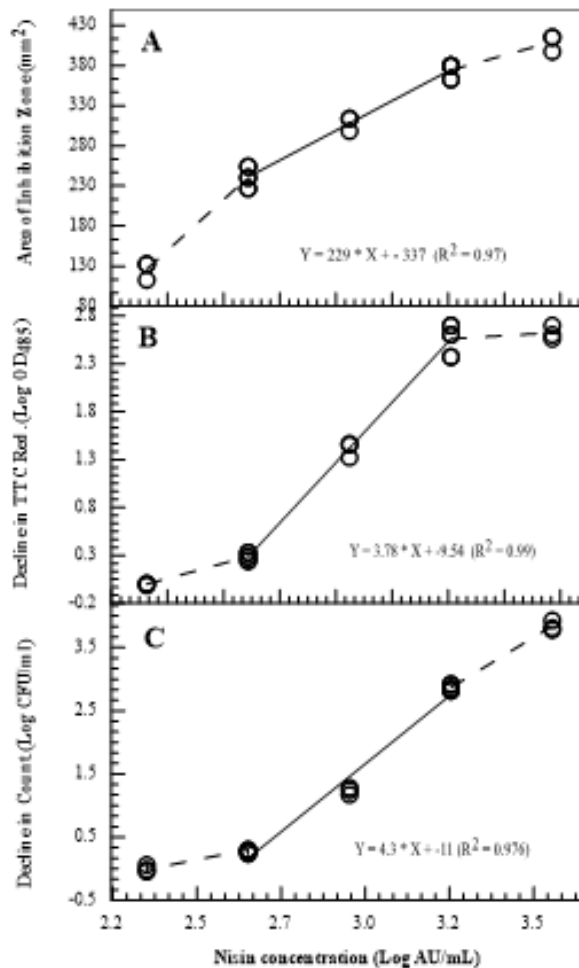
linear regression fit for nisin was established by only using three data points in the central range. However, in the case of lacidin-A (Figure 4) and pediocin PO<sub>2</sub> (Figure 5), the difference between the linear and polynomial regressions was negligibly close. Therefore, the linear fits were obtained by including all of the significant responses and used to describe the dose-response curves.

Based on the results of nisin dose-response curves, the correlation coefficients for TTC reduction, CFU count, and area of inhibition zone were 0.99, 0.98 and 0.97, respectively (Figure 5). Even though TTC reduction showed the best result in the central regions, the change in OD<sub>485</sub> from zero to first dilution was not significant ( $P > 0.05$ ) where CFU decline was evident (Figure 5A). Thus, this result probably suggests that the curve of TTC-based assay may not be useful at high doses of nisin. Overall, the correlations (Table 4) of the TTC reduction result with CFU and with the area of inhibition zone suggest that TTC-based assay provides apparent comparable results with the other methods despite the fact that higher and lower doses showed variations.

Unlike nisin, lacidin-A and pediocin PO<sub>2</sub> probably have a different killing kinetics, where the similar two-fold change in doses was reflected as a smaller rate of change in response. In other words, the linear dose-response curve of nisin was steeper than those of the other bacteriocins.



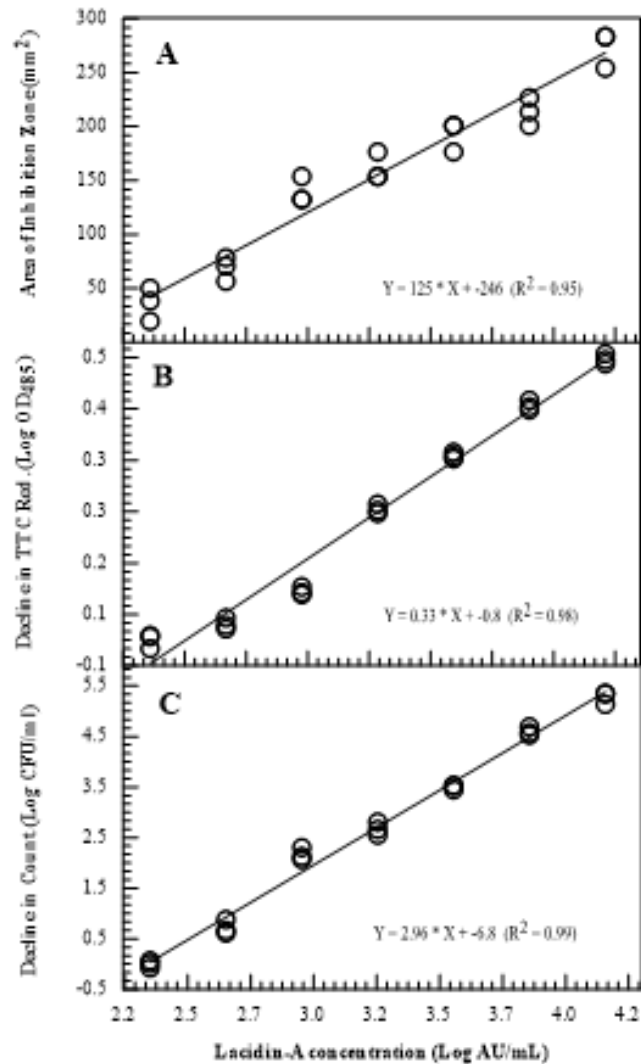
**Figure 5.** Nisin dose vs. area of inhibition zone (A), and decline in the responses of TTC reduction (B) and cell count (C) against indicator culture *L. delbrueckii* subsp. *lactis* ATCC 4797. Nisin activity (AU/mL) was calculated from the reciprocal of the highest dilution corresponding to the last detectable zone on agar medium with TTC. Symbols indicate the results of three independent trials, and the solid lines were obtained by linear regression fit with excluding the responses from the highest and the lowest nisin dilutions.



**Figure 6.** Lacidin-A dose vs. area of zone of inhibition (A), and the decline in responses of TTC reduction (B) and cell count (C) against indicator culture *L. delbrueckii* subsp. *lactis* ATCC 4797. Lacidin A activity (AU/mL) was calculated from the reciprocal of the highest dilution corresponding to the last detectable zone of inhibition on agar medium containing TTC. Symbols indicate the results of three independent trials.

Considering the dose-response curves for Lacidin-A (Figure 6), correlation coefficients ( $R^2$ ) for CFU count, TTC reduction and the area of zone diameter were 0.99, 0.98, and 0.95. With small variations, a linear change was apparent in CFU (Figure 6A). Although the TTC reduction results (Figure 6B) were described by a linear fit, a gradual leveling off can be seen at lower dose levels. At higher dose levels, the data fit into an almost straight line. The lacidin-A was partially purified and the highest possible doses were applied

yet the sigmoid shoulder at higher dose levels was not detected. This result probably suggest that TTC-based assay may provide linear responses at higher dose levels than that we used. The relationship between the relative TTC and CFU responses (Table 4) was highly correlated ( $R^2 = 0.96$ ), but the correlation was lower ( $R^2 = 0.90$ ) with the area of inhibition zone. Thus, TTC-based assay of lacidin-A provided comparable results with the cell count method.



**Figure 7.** Pediocin PO<sub>2</sub> dose vs. area of inhibition zone (A), and the decline in responses of TTC reduction (B) and cell count (C) against indicator culture *L. bulgaricus* OSU 135. Pediocin PO<sub>2</sub> activity (AU/mL) was calculated from the reciprocal of the highest dilution corresponding to the last detectable zone of inhibition on agar medium containing TTC. Symbols indicate the results of three independent trials.

Overall, pediocin PO<sub>2</sub> dose-response curves and correlations were similar to those of lacidin-A. As shown in Figure 7, the correlation coefficients of CFU count at part A and TTC reduction at part B were high (0.98). The area of the zone of inhibition had relatively lower correlation coefficients (0.96). Like lacidin-A, a sigmoid shoulder at higher dose levels

pediocin PO<sub>2</sub> seemed undetectable. Overall, the correlation coefficients between the TTC reduction result and log CFU/mL (Table 4) were high ( $R^2 = 0.97$ ) and with the area of zone of inhibition was relatively close yet lower ( $R^2 = 0.95$ ). Thus, TTC-based assay for pediocin PO<sub>2</sub> produced highly comparable results with the other methods.

**Table 4.** The correlation coefficients of the methods, TTC represents Decline in TTC reduction (log OD at 485 nm), CFU represents Decline in cell count (log CFU/mL) and MM<sup>2</sup> represents the area of zone of inhibition (mm<sup>2</sup>). The results were obtained from two-fold dilution of nisin and lacidin-A against *Lactobacillus delbrueckii* subsp. *lactis* ATCC 4797; pediocin PO<sub>2</sub> against *Lactobacillus bulgaricus* OSU 135. The equations and correlation coefficients were generated from the corresponding data in Tables 1, 2, and 3.

Correlations of the methods			
Bacteriocins	X: CFU vs. Y: TTC	X: TTC vs. Y: MM <sup>2</sup>	X: CFU vs. Y: MM <sup>2</sup>
Nisin	Y = 0.86 * X + 0.17 (R <sup>2</sup> = 0.97)	Y = 58.5 * X + 225 (R <sup>2</sup> = 0.97)	Y = 50.3 * X + 235 (R <sup>2</sup> = 0.95)
Lacidin-A	Y = 0.11 * X + -0.045 (R <sup>2</sup> = 0.96)	Y = 369 * X + 63 (R <sup>2</sup> = 0.90)	Y = 42.2 * X + 41 (R <sup>2</sup> = 0.95)
Pediocin PO <sub>2</sub>	Y = 0.35 * X + -0.031 (R <sup>2</sup> = 0.97)	Y = 66 * X + 19 (R <sup>2</sup> = 0.96)	Y = 24 * X + 16 (R <sup>2</sup> = 0.95)

In conclusion, TTC-based assay for lacidin-A and pediocin PO<sub>2</sub>, compared with the count method, can produce measurable responses at a wide range of doses of the bacteriocins. TTC-based assay for nisin provides better results at narrower range and lower dose levels. Overall, TTC reduction results were better correlated with log counts than that of with the area of inhibition zone. Under the testing conditions, it could also be concluded that different bacteriocins displayed not only different agar diffusion characteristics but probably different killing kinetics as well.

## DISCUSSION

The most commonly used agar plate assay to estimate the unknown potency of bacteriocins is the critical dilution method where the end-point determination is considered (4). Although it is quite simple, this method has limitations and lacks precision. Detection of the inhibition zone, corresponding to the highest two-fold dilution, is error-prone. This leads to impreciseness in the calculations of bacteriocin activity (4). In fact, this inherent uncertainty of the decisive end-point can be considered as the biggest problem of this assay (12).

In this study, we determined bacteriocin activity (AU/mL) using the critical dilution method. The same indicator culture (4797) and MRS agar medium were used for nisin and lacidin A in the critical dilution method. Therefore, the comparison of these two bacteriocins may reveal relative degrees of susceptibility, different killing effects or different diffusion characteristics. Nisin activity was 3200 AU/mL which revealed larger zone of inhibition than

that of lacidin A with activity of 12800 AU/mL. As the result, potency cannot be compared by diameters of inhibition zones. Therefore, the absolute value (mm) of zone of inhibition should not be used to compare the efficacy or potency of different bacteriocins.

TTC was used in the detection and counting of bacteria and it was reported that maximum dose of TTC allowing growth of gram positive and negative bacteria are 0.001% and 0.05%, respectively (16). Eidus et al., (32) investigated the effect of the concentrations of four different tetrazolia. The level for optimal staining occurred at about 50% of the toxic level. Tetrazolia varied in staining patterns, optimal concentration and toxicity to organisms. It was indicated that TTC is the least toxic to cells.

Tetrazolia were used for viability observations and qualitative determinations without solubilization or extraction of the colored formazans (4,24,33). In commercial cell proliferation kits that insoluble formazan of MTT (3-[4,5-dimethylthiazol-2-yl]-2,5-diphenyl tetrazolium bromide) needs to be solubilized by dimethyl sulfoxide before the determination of color by an ELISA reader. Similarly, without solubilization, we could not have achieved sensitive absorbance measurements. Thus, we tried to solubilize the color with several solvents. It was found that methanol was the most effective.

Colorimetric procedures is based on the extraction of the biologically produced insoluble formazan by organic solvents and measurement of absorbance with spectrophotometers (18). There have been various colorimetric viability assays developed using various tetrazolium salts for different cell line or tissue

cell cultures of animal and plant origin for different purposes (34–39). For example, by employing MTT (3-[4,5-dimethylthiazol-2-yl]-2,5-diphenyl tetrazolium bromide), Morgan (39) was reported a colorimetric procedure to evaluate viability of tissue culture. It was indicated that water-soluble MTT is taken up by the viable cells and produced water-insoluble blue formazan by the action of mitochondrial dehydrogenases. The formazan was extracted by organic solvents. Similar to our observations, it was found that formazan production is directly proportional to cell number. Despite coinciding basic approach and taking the benefit of tetrazolium, our study differs from previous assay for direct evaluation for bacteriocin activity and comparison with currently used methods.

After examining the factors that affect the reduction of TTC by bacterial cells, a TTC-based bacteriocin assay was developed. The assay was applied for the estimation of bacteriocin activity in conjunction with survivor count and agar diffusion methods.

Microbiological assay is defined as a technique whereby the potency of an antimicrobial agent may be determined by its effect on the growth of a microorganism (10). Based on this definition, the TTC-based bacteriocin assay should not be considered as a microbiological assay due to the fact that it does not depend on the growth inhibition of the sensitive culture nor is the culture permitted to grow in liquid or agar medium. Instead, the proportion of the cells survived the treatment as a function of bacteriocin concentration is evaluated indirectly by the survivors' ability to reduce TTC. However, the procedure shares some disadvantages of microbiological assays in that survivors' viability is involved. Furthermore, this procedure could not be defined as a chemical method either, because it measures the activity of bacteriocin on the sensitive culture. Therefore, it does not share the disadvantages of chemical procedures in which reflection of activity of the compound on the culture is missing.

In recent years, new methods for quantification of nisin have been investigated. Assay methods based on the release of ATP from sensitive indicator cells, use of antibodies developed against purified nisin, and HPLC analysis have been investigated (27,29). Amount of nisin, measured by chemical means, may not correlate well with the activity of the bacteriocin. For example, nisin is quite stable to pH changes, yet the activity of nisin is greatly affected by pH (27), which may not be verified by chemical methods. This considerations have long been the case with antibiotics where bioassays have remained as the standard method for years (10). In the case of antibody-based enzyme assays which are currently

developed, the minimum detectable concentration of bacteriocin is quite high, e.g, for nisin and pediocin, it was found 19,000 and 32,000 AU/mL, respectively (40).

There have been some confusions about the definition or interpretation of a quantitative assay. Some defined it as a measurable response such as mm zone inhibition of unknown potency (28,41). Others only defined it as the comparison of the responses at the same range between standard reference compound and the sample whose potency is to be determined (10). However, the standard procedures only use the term 'quantitative' when the reference standard is employed. For instance, the current procedure for the estimation of nisin in processed cheese is based on the agar diffusion and formation of zone of inhibition by the sample extract and the reference standard of nisin (12,41).

The microbiological assays, e.g., zone of inhibition measurements and turbidimetric determinations, can provide quantitative results only when a reference standard is used (4,10). Thus, any method can provide quantitative results as long as reference is used in conjunction with samples. There are several possibilities for expressing the results of the TTC-based bacteriocin assay. Bacteriocin potency may be expressed quantitatively as g/mL or ppm, but this requires the reference standard of bacteriocins. When the pure bacteriocins are available, TTC based assay can become a powerful tool to estimate the potency of bacteriocins. In the absence of a standard, one may express the bacteriocin activity using TTC-based assay to estimate AU/mL directly from the equations established in the dose-response curves. Then, measured AU can be expressed as IU (1 IU nisin = about 100 AU) for nisin and other bacteriocins (27,42).

Another arbitrary option could be a determination of some type of a median response. Median response is generally used in turbidimetric assays and defined as the dose of the inhibitory substance that permits the growth of the organism to 50% level of the zero dose under specified conditions (10). In the case of bacteriocidal agents, the median response is usually referred as a lethal unit, the level of 50% killing. Considering the highly significant correlation ( $R^2 > 0.95$ ) between the number of cells remained viable and their ability to reduce TTC for the three bacteriocins we tested (Table 4), one can easily convert one measurement to another. Thus, the unknown potency is then quantified as the number of cells killed under the standardized test conditions.

The results of the TTC based assay can also be expressed as the amount of formazan formed by



indicator cells with or without bacteriocin when TTC reduction is tested under standardized conditions. The amount of formazan can be deduced from the standard curve depicting 2,3,5-triphenyl formazan concentration vs absorbance at 485 nm. In fact, this standard curve was obtained yet not used (data not shown). In this study, we used changes in OD<sub>485</sub> to measure the activity of bacteriocins.

When compared to the current bacteriocin potency determination methods, the TTC based procedure is simple and easy to perform. Moreover, the procedure is not costly; TTC is one of the least expensive tetrazolia available. It also does not require expensive equipment nor high skills. In practice, a variety of assay volumes of tube size can be used. However, we preferred using 1.5 mL microcentrifuge tubes because of two centrifugation steps in the procedure. Thus, the centrifugations can be made directly without any transfer of assay liquid. The usage of small volumes allowed rapid heat transfer in water bath, and the use of micropipettes for all transfers. The filter sterilized stock TTC solutions can be stored frozen in small volumes and diluted with sterilized buffer to the desired assay concentration in one step.

Time saving is main advantage of TTC-based bacteriocin assay. With the other methods, using either agar or broth medium, the bioassay requires 24-48 h not including the time for preparation of the culture. In the TTC-based assay, all steps other than culture preparation, take about one hour. The ability to estimate bacteriocin potency in a short period provides great convenience for studies on bacteriocin purification, and in the determination of the optimum growth conditions (e.g., media, temperature, pH) and the productivity of bacteriocin producer strains. In these steps, investigator specifically looks forward to obtaining results in short period to be able to make necessary modifications earlier than the time is taken with current methods. There are some semi-automatic and automatic microbiological methods which are based on turbidity determinations. It was indicated that automation shortens the time up to 6 h and offers a potential for less technical errors and increase in accuracy (5,27). On the other hand, automatic methods do not assess microbial killing well. For many microorganisms, two to three log kill cannot be detected. TTC-based assay has several advantages over automatic and regular turbidimetric assays. In addition to time saving, TTC-based assay is more accurate than turbidimetric assays in that only viable cells contribute to the color formation. TTC-based method can detect up to five log decrease in count due to the action bacteriocin. Lastly, the results of TTC-based assay are less likely to be affected by bacterial clumping or aggregation.

Zone of inhibition and critical dilution tests cannot be used to differentiate whether the bacteriocins have bactericidal or bacteriostatic effect (5,7). Additionally, the diffusion of highly hydrophobic antimicrobial agents on agar becomes limited (10,12,32,43). Measuring the bactericidal effect, in general, requires the use of viable or survivor count method (4,7). Survivor count method provides measurable responses to a wider range of dose levels compared to other methods. Due to the higher detectable range of response, survivor count methods are considered more accurate than the other methods (9,32,43). The linear range is the most useful portion of dose-response curves for the assay purposes, yet generally it corresponds to only a narrow range of dose levels, which is the major problem with turbidimetric analysis (9,10,32). A clear medium is necessary for absorbance measurements otherwise the supplements of the medium may mislead the results (1). This point becomes very important in the case of opaque supplements of medium which are often required by fastidious microorganisms (5). However, in order to detect the changes in turbidity in liquid culture by spectrophotometer, at least 10<sup>6</sup> CFU / mL of indicator suspension is generally required (5,13,32). Formation of the clumps and chains affects the results of viable counts and turbidimetric methods (10,13,44).

Flamentation can result in an increase in turbidity where aggregation of bacterial cells can be caused by some antimicrobial agents as the number of viable cells decrease (5). Absorbance measurements can correlate with the number of cells in suspension, but it is unlikely to discriminate viable from non-viable cells (44). In this regard, optical measurements were found to be proportional to the dry weight of the culture rather than the number of viable cells (4,44).

In the TTC-based assay the metabolic activity of the culture is used as a measure of viability. It is well known that metabolic activity of the sensitive culture can change greatly with changes in the growth state. However, if the culture is harvested while the cells at the same growth phase, the metabolic response will be related directly to the number of viable cells, which is a function of the potency of the bacteriocin.

In terms of detection limits of bacteriocins, results from the TTC based assay cannot be compared with others in literature because of differences in assay conditions, sensitive strains, extraction procedure, and pH of media. For example, in the case of nisin, even though the actual nisin concentration in two-fold dilutions can be calculated from the original preparation, the effectiveness of the extraction of nisin from the commercial powder (containing 2.5% nisin) could not be determined. Thus, the results were not expressed as IU or µg of nisin /mL. For

comparison purposes, the expression AU/mL was thought to be more accurate. The equivalent of nisin was 14,300 IU/ per mL of cells at the highest concentration. The detection limit was the fourth dilution exhibiting last zone of inhibition from the critical dilution of the commercial nisin. This result agreed with the CFU count and TTC reduction in which CFU and absorbance increments were significant ( $P < 0.05$ ) up to the fifth dilution. After that dilution, the changes were not significant suggesting that the three procedure provided similar detection limits.

Assays for antimicrobial agents usually show a sigmoidal dose-response curve when the dose has a wide range. To apply these assay methods, it is critical to choose dose levels within the linear intermediate concentrations or 'sensitive region' of the response curve where small changes in concentration give maximum change in response (10). Therefore, the linear equation for nisin dose-response curve was obtained using only the central region (Figure 3). For lacidin A and pediocin PO2, the linear fits were obtained by using all of the significant responses of TTC-based assay. Even though polynomial regressions showed higher  $R^2$  than those of linear, the difference between the regressions were negligibly close in the central region of the plot.

In the case of TTC-based assay, the response can be obtained over a wide range of bacteriocin concentrations. The survivor cell concentration, however, should be high enough to produce a detectable color. Test sensitivity decreases when cell concentrations are lower than  $10^6$ . Therefore, cell concentration of  $10^7$  and higher is preferable. It is worth to note that the parameters can easily be modified for different conditions such as low number of cells versus either increasing incubation time with TTC or higher concentration of TTC. If the number of initial indicator cells is reduced, lower bacteriocin concentrations can be detectable and the assay may become more sensitive.

## REFERENCES

1. Jack RW, Tagg JR, Ray B. Bacteriocins of Gram-Positive Bacteria. *Microbiol Reivew* [Internet]. 1995;59(2):171-200.
2. Klaenhammer TR. Bacteriocins of lactic acid bacteria. *Biochimie*. 1988;70(3):337-49.
3. Mayr-Harting A, Hedges AJ, Berkeley RCW. Methods for Studying Bacteriocins. *Methods Microbiol*. 1972;7(April):315-422.
4. Mattila T. A modified Kelsey-Sykes method for testing disinfectants with 2,3,5-triphenyltetrazolium chloride reduction as an indicator of bacterial growth. *J Appl Bacteriol*. 1987;62(6):551-4.
5. Provonchee RB, Zinner SH. Rapid method for determining serum bactericidal activity. *Appl Microbiol*. 1974;27(1):185-6.
6. Tagg JR, Dajani AS, Wannamaker LW. Bacteriocins of gram positive bacteria. *Bacteriol Rev*. 1976;40(3):722-56.
7. Vistica DT. Tetrazolium-based assays for cellular viability: A critical examination of selected parameters affecting formazan production. In: *Cancer Research*. 1991. p. 2515-20.
8. Skyttä E, Mattila-Sandholm T. A quantitative method for assessing bacteriocins and other food antimicrobials by automated turbidometry. *J Microbiol Methods*. 1991;14(2):77-88.
9. Hewitt W, Vincent S. Theory and Application of Microbiological Assay [Internet]. San Diego, California.: Elsevier; 1989. 1-202 p.
10. Hoover DG, Harlender SK. Screening Methods for Detecting Bacteriocin Activity. In: *Bacteriocins of Lactic Acid Bacteria* [Internet]. Academic Press, INC; 1993. p. 23-39.
11. Piddock LJV. Techniques used for the determination of antimicrobial resistance and sensitivity in bacteria. *J Appl Bacteriol*. 1990;68(4):307-18.
12. Hurst A. Nisin. In: *Advances in applied microbiology* [Internet]. 1981. p. 85-123.
13. Cavalieri SJ, Harbeck RJ, McCarter YS, Ortez JH, Rankin ID, Sautter RL, et al. Manual of Antimicrobial Susceptibility Testing [Internet]. Marie B. Coyle (University of Washington), editor. American Society For Microbiology. 2005. 1-241 p.
14. Cutler RR, Wilson P, Clark F V. Evaluation of a radiometric method for studying bacterial activity in the presence of antimicrobial agents. *J Appl Bacteriol* [Internet]. 1989;67(6):515-21.
15. Shuler M, Kargi F. *Bioprocess Engineering Basic Concepts*. Second Edi. Englewood Cliffs, New Jersey: Prentice Hall PTR; 2002. 61-172 p.
16. Nissen-Meyer J, Holo H, Havarstein LS, Sletten K, Nes IF. A novel lactococcal bacteriocin whose activity depends on the complementary action of two peptides. *J Bacteriol*. 1992;174(17):5686-92.
17. Berridge MV, Tan AS, McCoy KD, Wang R. The Biochemical and Cellular Basis of Cell Proliferation Assays That Use Tetrazolium Salts. *Biochemica*. 1996;4:14-9.
18. Stockert JC, Horobin RW, Colombo LL, Blázquez-Castro A. Tetrazolium salts and formazan products in Cell Biology: Viability assessment, fluorescence imaging, and labeling perspectives. *Acta Histochem* [Internet]. 2018;120(3):159-67.
19. Worsfold M, Marshall MJ, Ellis EB. Enzyme detection using phenazine methosulphate and tetrazolium salts:

- Interference by oxygen. *Anal Biochem.* 1977;79(1-2):152-6.
20. Sahl HG, Kordel M, Benz R. Voltage-dependent depolarization of bacterial membranes and artificial lipid bilayers by the peptide antibiotic nisin. *Arch Microbiol.* 1987;149(2):120-4.
21. Nineham AW. The Chemistry of Formazans and Tetrazolium Salts. *Chem Rev [Internet].* 1955 Apr 1;55(2):355-483.
22. Şenöz H. Formazanlar ve Tetrazolyum Tuzlarının Kimyası. *Hacettepe J Biol Chem.* 2012;40(3):293-301.
23. Debnam PM, Shearer G. Colorimetric assays for substrates of NADP+-dependent dehydrogenases based on reduction of a tetrazolium dye to its soluble formazan. *Anal Biochem.* 1997;250(2):253-5.
24. Zimmermann R, Iturriaga R, Becker-Birck J. Simultaneous determination of the total number of aquatic bacteria and the number thereof involved in respiration. *Appl Environ Microbiol.* 1978;36(6):926-35.
25. Liao CC, Yousef AE, Chism GW, Richter ER. Inhibition of *Staphylococcus aureus* in buffer, culture media and foods by lacidin A, a bacteriocin produced by *Lactobacillus acidophilus* OSU 133. *J Food Saf [Internet].* 1994 May;14(2):87-101.
26. Liao CC, Yousef AE, Richter ER, Chism GW. *Pediococcus acidilactici* PO2 Bacteriocin Production in Whey Permeate and Inhibition of *Listeria monocytogenes* in Foods. *J Food Sci.* 1993;58(2):430-4.
27. Ray B. Nisin of *Lactococcus Lactis* ssp. *Lactis* as a Food Biopreservative. In: *Food Biopreservatives of Microbial Origin.* 1992. p. 207-64.
28. Parente E, Brienza C, Moles M, Ricciardi A. A comparison of methods for the measurement of bacteriocin activity. *J Microbiol Methods.* 1995;22(1):95-108.
29. Voet D, Voet JG. *Biochemistry.* 2nd ed. John Wiley and Sons; 1995.
30. Cabo ML, Murado MA, González MP, Pastoriza L. A method for bacteriocin quantification. *J Appl Microbiol.* 1999;87(6):907-14.
31. Roszak DB, Colwell RR. Survival strategies of bacteria in the natural environment. *Microbiol Rev [Internet].* 1987 Sep;51(3):365-79.
32. Eidus L, Diena BB, Greenberg L. Observations on the use of tetrazolium salts in the vital staining of bacteria. *Can J Microbiol.* 1959;5(3):245-50.
33. Weibuli C. Observations On The Staining Of *Bacillus Megaterium* With Triphenyltetrazolium. *J Bacteriol [Internet].* 1953 Aug;66(2):137-9.
34. Vistica DT, Skehan P, Scudiero D, Monks A, Pittman A, Boyd MR. Tetrazolium-based assays for cellular viability: a critical examination of selected parameters affecting formazan production. *Cancer Res [Internet].* 1991 May 15;51(10):2515-20.
35. Denizot F, Lang R. Rapid colorimetric assay for cell growth and survival. Modifications to the tetrazolium dye procedure giving improved sensitivity and reliability. *J Immunol Methods.* 1986;89(2):271-7.
36. Mosmann T. Rapid colorimetric assay for cellular growth and survival: Application to proliferation and cytotoxicity assays. *J Immunol Methods [Internet].* 1983 Dec;65(1-2):55-63.
37. Takeuchi H, Baba M, Shigeta S. An application of tetrazolium (MTT) colorimetric assay for the screening of anti-herpes simplex virus compounds. *J Virol Methods.* 1991;33(1-2):61-71.
38. Carmichael J, DeGraff WG, Gazdar AF, Minna JD, Mitchell JB. Evaluation of a tetrazolium-based semiautomated colorimetric assay: assessment of radiosensitivity. *Cancer Res [Internet].* 1987 Feb 15;47(4):943-6.
39. Morgan DM. Tetrazolium (MTT) assay for cellular viability and activity. *Methods Mol Biol.* 1998;79(4):179-83.
40. Bhunia AK. Monoclonal antibody-based enzyme immunoassay for pediocins of *Pediococcus acidilactici*. *Appl Environ Microbiol.* 1994;60(8):2692-6.
41. Benkerroum N, Ghouati Y, Sandine WE, Tantaoui-Elaraki A. Methods to demonstrate the bactericidal activity of bacteriocins. *Lett Appl Microbiol.* 1993;17(2):78-81.
42. Ray B. *Pediocin(s)* of *Pediococcus acidilactici* as a food biopreservatives. In: *Food Biopreservatives of Microbial Origins.* 1992. p. 265-319.
43. Davidson PM, Parish ME. Methods for testing the efficacy of food antimicrobials. *Food Technol.* 1989;43(1):148-55.
44. Daeschel MA. Procedures To Detect Antimicrobial Activities Of Microorganisms. In: *Food Biopreservatives of Microbial Origin.* Florida.: CRC Press; 1992. p. 58-77.





## Determination of Reactor Operational Mode for Concentrated Fungicide Production

Zeynep Yilmazer Hitit<sup>1\*</sup> , Pinar Aygener<sup>1</sup> , Seda Teymur<sup>1</sup> , Beyza Akiska<sup>1</sup> ,  
Kemal Kesenci<sup>2</sup> , Suna Ertunc<sup>1</sup> , and Bulent Akay<sup>1</sup> 

<sup>1</sup>Ankara University, Department of Chemical Engineering, 06100, Ankara, Turkey.

<sup>2</sup>Safa Tarim AS, Konya, Turkey.

**Abstract:** An aqueous solution of phosphorous acid ( $H_3PO_3$ ) and potassium hydroxide (KOH) is an example of a phosphonic acid neutralization reaction where potassium salts are formed. This study aimed to design the reactor and the process, which is a problem encountered in the industry, arising from the need to develop a safe and efficient production process. It was found that the production process carried out under exothermic conditions should be in a temperature-controlled reactor at optimum acid/base initial concentration ratios and feed flow rates as 1/1.5, 22800 mL/min, respectively. Due to the thermal safety and risk accidents at the batch reactor, a tubular flow reactor (TFR) has been designed to increase the controllability and the yield of the products produced in the batch reactor having some advantages as to feeding, sampling, and measuring from different points at different times.

**Keywords:** Fungicide production; phosphorous acid potassium salts; tubular flow reactor; neutralization reaction; mono and dipotassium phosphite.

**Submitted:** June 24, 2022. **Accepted:** September 23, 2022 .

**Cite this:** Hitit ZY, Aygener P, Teymur S, Akiska B, Kesenci K, Ertunc S, et al. Determination of Reactor Operational Mode for Concentrated Fungicide Production. JOTCSB. 2022;5(2):110-26.

\*Corresponding author. E-mail: [zyilmazer@ankara.edu.tr](mailto:zyilmazer@ankara.edu.tr)

### INTRODUCTION

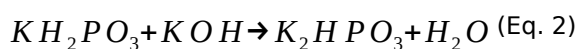
Fungal microorganisms are the structures that cause plant diseases and need to be kept under control. The most effective method to keep these structures under control is the application of fungicides to the plant (1). Phosphite compounds in the  $HPO_3$  structure are widely used in agriculture as fertilizer or fungicide. For an accurate hazard identification and risk assessment, it is crucial to recognize the toxic effects of fungicides and increase the benefits of fungicides while reducing toxic effects (2). Fungicides are used in the treatment of fungi that are formed or likely to occur in plants. Additionally, phosphite salts are pH-neutral chemical compounds and can show healing properties like fungicides in plants.

Although phosphite ( $PO_3^{3-}$ ) and phosphate ( $PO_4^{3-}$ ) compounds have similar chemical structures, they have different effects on plants and fungi. Phosphorous acid ( $H_3PO_3$ ) and its salt (phosphite) contain higher P concentrations (39%) than

conventional phosphate-based ( $H_3PO_4$ ) fertilizer (32% P) (3). It is used as a fungicide in the agricultural sector. It also has fertilizer properties and is used to strengthen the immune system of plants and overcome various infections. In addition, it has various uses such as having a direct antifungal effect on plant pathogens, controlling root-borne diseases, increasing yields, and organic farming. The mono-potassium and di-potassium salts of phosphorous acid, the active ingredient, have direct toxic effects on plant pathogens. They also activate the natural defense mechanisms of plants through disease suppression or eradication. Thus, they provide a double effect mode. However, as in the case of all commercial chemicals and especially environmentally friendly chemicals such as fungicides, a much more improved effect with a small amount is aimed, so improved performance is always required at the same dose. Thus, potassium phosphite will be particularly useful as it will provide potassium as a second precious nutrient besides the other two critical plant nutrients. Moreover, a

polyphosphite is expected to provide the known slow-release advantages of polyphosphate.

Currently available commercial methods for the preparation of fertilizer grade potassium phosphite ( $\text{KH}_2\text{PO}_3$  and  $\text{K}_2\text{HPO}_3$ ) include a stirred tank (usually a batch reactor) equipped with a stirrer and cooling jacket, using an aqueous solution of potassium hydroxide as seen in Equations 1 and 2.



Batch reactors are widely used and preferred in industry and their type is frequently preferred in the pharmaceutical industry. The performance of a batch reactor can be determined through mass and energy balances. At the beginning of the reaction, the inputs (substrates) are fed into the reactor and there is no material feeding and/or discharging during the reaction. Temperatures and concentrations are observed over time by the differential equations created with the help of mass and energy balances. In a batch reactor system, it may not be possible in all cases to maximize the product yield, as well as determining the reaction rate, which determines the variation of the concentration over time (4). Since the sudden feeding of the inputs to the reactor changes the temperature and reaction rate abruptly, the batch mode is not often preferred for exothermic neutralization reactions. Fed-batch reactors are commonly used for strongly exothermic reactions (5). As the heat of the reaction can be balanced by the existing cooling of the reactor (6). In fed-batch operating modes, some of the inputs are fed to the reactor before the reaction starts, while the rest is fed to the reactor during the reaction (7). In general, the performance of a batch reactor subjected to an industrial-scale volume change is affected by two important factors, kinetics, and dilution (8).

Despite many years of research and experimental results obtained by chemical engineers in the field of reactor safety, it is known that thermal runaway emergencies still occur in chemical reactors today. In the design and operation of batch and semi-batch reactors, it is necessary to determine the correct and optimum operating conditions and to adapt early warning detection systems to prevent thermal runaways and develop a reliable production process. In the case of homogeneous reactions, a thermal runaway problem may rise faster than for heterogeneous ones due to the lack of interfacial mass transfer resistances (9). A reactor design that provides temperature control is extremely important for such reaction systems. For this reason, tubular (plug) flow reactors (PFR) are recommended. The PFR is characterized by the regularity of the fluid flow in it, without any mixing of the fluid with any other element. In fact, there may be radial mixing of fluid in a PFR; however, there should be no mixing or diffusion along the axial flow. A necessary and sufficient condition for PFR flow is that the residence

time in the reactor is the same for all elements of the liquid (10). The inputs enter the reactor and are consumed while flowing axially and the reaction conversion increases along the length of the reactor (11). This also increases the yield of the product.

In fungicides with fertilizer properties, it should be noted that the final product concentration value should be between 6.2 and 6.7 in the production of monopotassium phosphite ( $\text{KH}_2\text{PO}_3$ ) and dipotassium phosphite ( $\text{K}_2\text{HPO}_3$ ) in order not to harm the soil and the plant as well as showing a nutritive feature (12). Since the pH value of phosphorous acid, the active ingredient in the reaction, is approximately 1.5, it cannot directly contact the plant, in order to prevent it from harming the plant (13). The active substance ( $\text{H}_3\text{PO}_3$ ) reacts with potassium hydroxide (KOH), a strong potassium-containing base, to produce  $\text{KH}_2\text{PO}_3$  and  $\text{K}_2\text{HPO}_3$  in the form of SL (soluble liquid) with fungicidal properties. The pH values of the potassium phosphite salts obtained are approximately 6.5 (3).

Mono and dipotassium phosphide compounds are generally produced by reaction with phosphonic acid ( $\text{H}_3\text{PO}_3$ ) by charging an aqueous solution of potassium hydroxide (KOH) in a batch reactor. Potassium hydroxide (KOH) releases heat during the dissolution process (14), while phosphorous acid ( $\text{H}_3\text{PO}_3$ ) absorbs heat. The neutralization reaction of a weak acid and a strong base is an exothermic reaction that still has unsolved problems in the production, storage, and analysis results. Acid-base foaming, boiling, explosion, and splashes are highly likely to occur in the reaction during the production. Even when the rate of the reaction is slowed, the reaction reaches 94 °C. Phosphine gas (monophosphan,  $\text{PH}_3$ ), is formed at temperatures of 65 °C and above and has an odor reminiscent of garlic and has an extremely toxic feature for humans, plants, and the environment (15). Unless the formation of phosphine gas is prevented or removed from the product, this gas causes serious poisoning as well as reducing the production efficiency rapidly (16). This situation poses a great risk for not only human health but also for the environment and economy. Occupational accidents resulting in many injuries in production with neutralization are recorded: causes temporary or permanent bodily damage, acid-base burns and splashes, environmental residues, and economic damage (17). In order to control splashes and explosions, a reduction in all these risks by adjusting pH values and maintaining acid-base balance is aimed (18).

An economical and safe way for reactor operation and optimization is inevitably required for the production of a potassium polyphosphite composition with enhanced efficacy as an agricultural fungicide (19–21). This study is an experimental study carried out to determine the optimum experimental conditions and the most appropriate operating mode of the neutralization reaction to produce monopotassium phosphite and



dipotassium phosphite salts. For a concentrated fungicide production stoichiometric ratio, operating mode, feed rate, and reactor type are optimized by examining the effects of different operating types (batch, fed-batch and tubular flow operation) on the production process and product yield.

## MATERIALS AND METHODS

The effect of feed order and feed amount on product yield is extremely important in acid-base neutralization reactions. As well as product yield, the feeding sequence ensures a safe production process. For this reason, repeated experiments were carried out in order to determine the optimum input conditions and safe production process of this production reaction, which has significant risks. In the neutralization reaction of a weak acid and strong base, acid was fed to the base. The reaction was observed by recording temperature, pH, and conductivity data at frequent intervals throughout the feeding and product formation.

### Determination of the Optimum Input Concentration in the Batch Reactor

Repeated experiments were carried out with a batch system to develop a safe and sustainable production process of potassium salts of phosphorous acid. The acid/base inlet concentration (mol/L, M) ratios of mono and dipotassium phosphite salts produced in the batch system were determined as 1/1, 1/1.5, 1/2, 1/3, and 1/4. The pH, temperature, and conductivity data of the salts produced with different input concentrations were recorded at regular intervals before feeding, during the reaction, and in the final product. The effects of the input concentration ratio on the reaction conditions and product yield were observed.

### Determination of the Optimum Input Concentration in the Fed-Batch Reactor

In the fed-batch system, repeated experiments were carried out with an acid/base input concentration (M) ratio of 1/1.5. As a result of an exothermic reaction, toxic gas formation is observed due to high temperatures. Phosphine gas ( $\text{PH}_3$ ), which is likely to cause permanent damage to human health, environment, and equipment safety, is an example of these gases. Therefore, it is necessary to keep the temperature under control in order to design a safe production process. Temperature control was achieved by cooling the reactor in a cold-water bath. The initial conditions for pH, water bath, and reactor temperature data for the pilot-scale experiments are shown in Table 1. The production process, which was controlled by a pilot scale, was repeated at the industrial scale and the initial conditions are given in Table 2.

**Table 1:** Initial conditions of the titration experiment performed by adding base to acid in an ice bath in a fed-batch system  $V_{\text{acid}} = 50$  mL,  $V_{\text{base}} = 100$  mL

	pH <sub>acid</sub>	pH <sub>base</sub>	T <sub>acid</sub> °C	T <sub>base</sub> °C
Experiment 1	1.05	15.4	18.3	25.1
Experiment 2	1.2	15.4	15.2	23.5
Experiment 3	1.1	15.5	16.2	22.5

**Table 2:** Initial conditions of the titration experiment performed by adding base to acid in an ice bath in a fed-batch system in industrial scale molarities.

Property	Acid	Base
Molarity, mol/L	7.31	10.96
pH	0.01	15.8
T, °C	20.8	23
Base, mL	50	100

### Determination of the Optimum Input Concentration in the Plug Flow Reactor

It has been observed that the experiments carried out in the fed-batch reactor as an alternative to the batch reactor do not create a safe and sustainable production process according to the temperature increase. Therefore, once the optimum input concentration ratio of 1/1.5 M (A/B) has been determined, an optimum generation system and reactor design are required as the reaction conversion is completed in a short time and the reaction carries significant risks. For a chemical kinetics study, a system should be designed in which samples can be analyzed at certain time intervals. A 12 m long tubular flow reactor with a 10 mm inner and 12 mm outer radii is designed to realize uninterrupted production. There are 5 bases and 1 acid feeding point on the system. Sampling points were made parallel to the feeding points along the reactor. A jacket with a diameter of 14 cm and a length of 120 cm was used to control the high temperature resulting from the reaction around the designed tubular reactor. There is a cooling water inlet at the bottom of the system and a cooling water outlet at the top. The schematic view of the experimental system for tubular flow reactor is given in Figure 1.

The pilot-scale experiments were carried out repetitively with the TFR, which was designed on an industrial scale. As a result of the pilot-scale experiments, the industrial-scale repeated experiments were carried out, as the condition for the sustainability of the system was ensured. In the first stage, 82 g/L acid and base liquid solutions were stored in 5 L volume acid and base tanks for the pilot-scale experiments. Considering the molecular weights of the inputs, it can be calculated that the prepared solutions have 1/1.5 (A/B) molar concentrations. As a result of the flow rate calibration experiments, the optimum flow rate was determined, and the system was expected to come

to a steady state for the first feeding. Acid was fed to the TFR at a flow rate of 370 mL/min. About 12 minutes after the acid was fed, the base was fed from point B1 of the reactor. While the base is fed, the volumetric flow rate of the product, which is formed simultaneously, is recorded and after the feeding, the base flow rate was increased periodically at the 4<sup>th</sup>, 7<sup>th</sup>, and 10<sup>th</sup> minutes. After about 30 minutes, the acid feeding was completed, and the pH data of the product were recorded simultaneously. Industrial-scale experiments were designed, because the experiments completed repeatedly with a pilot scale. 400 g/L acid and base solutions were stored in the 10 L volume acid and base storage tanks. The reactant concentrations were 4.9:7.1 M. In this system, where the optimum input concentration ratio (1/1.5) was provided, repeated experiments were carried out. The base was fed to the designed tubular reactor from point B1 at a flow rate of 150 mL/min and simultaneously from point B2 at a flow rate of 250 mL/min. The acid was fed from point A1 at a flow rate of 400 mL/min. 5 minutes after the system became stable, the base feeding was continued from B1, B2, and B3 points. After 12 minutes, two samples were taken at 15-second intervals, and temperature and pH measurements were made. To control the reaction temperature, cooling water was sent at a flow rate of 17400 mL/min for approximately 18 minutes. After 3 minutes, the volumetric flow rate of the cooling water was set to 22800 mL/min. The base fed from the B3 point at the 22<sup>nd</sup> minute of production continued to be fed from the B4 point until the almost 31<sup>st</sup> minute. The base feeding was completed, and the product pH value was recorded.

### Phosphorus Analysis

Phosphorus analyses were carried out repeatedly to analyze the chemical kinetics and determine the product yield. A calibration graph was created at a wavelength of 460 nm with the reaction input phosphorous acid standard solution, and then the phosphorous acid concentration of the product was determined through the spectrometric method. In the analysis method, nitric acid (29% HNO<sub>3</sub>) solution, 0.25% ammonium vanadate (NH<sub>4</sub>VO<sub>3</sub>) solution, and 5% ammonium molybdate solution ((NH<sub>4</sub>)<sub>6</sub>Mo<sub>7</sub>O<sub>24</sub>.H<sub>2</sub>O) chemicals were used. UV-Vis measurements were obtained with a Shimadzu - UV160 and manual Spectrometer using 1 cm plastic cuvettes (22).

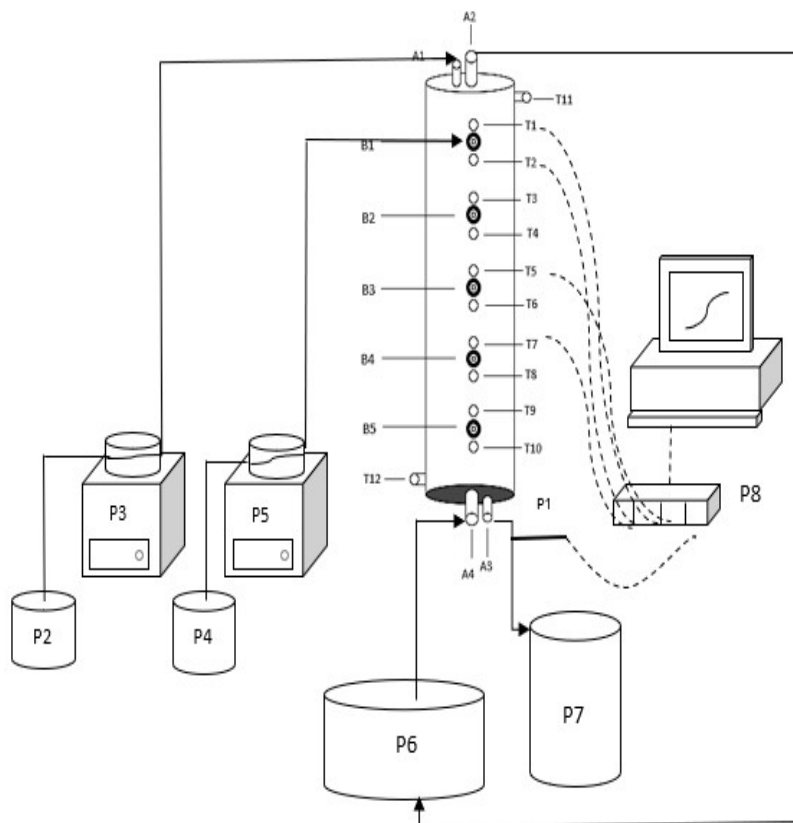
## RESULTS AND DISCUSSION

### Determination of optimum input concentration ratio and reactant feed order

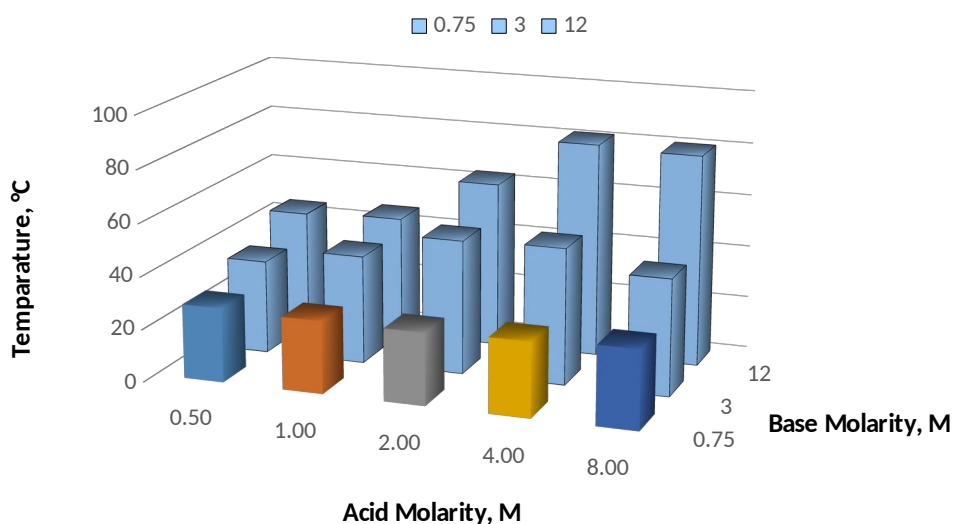
It is known that the pH values of phosphorous acid, potassium hydroxide, and neutralized phosphorous acid (NPA) water solution at different concentrations are ranging from 1.85 to 2.34, 11.98 to 12.88, and 6.26 to 6.96, respectively (12). The repeated experiments on a pilot scale showed that the reaction proceeded efficiently when the reactants were at an equal mass flow rate. It is seen in Figure 2 that the temperature increase reached uncontrollable values as a result of the gradual increase in the acid and base concentrations. It is essential to prevent the formation of toxic phosphine gas and therefore to control the temperature for both product yield and safe process operation. In this case, regardless of the type of production, the optimum input concentration ratio was determined as 1/1.5 (A/ B). When this ratio was maintained, it is seen in Figure 3 that the pH value of the product was recorded in the range of 6.5-7. This value is the common feature of pesticides that have a nutritive effect when applied to the plants. The effects of feed order to the reactor on temperature and pH on diluted and concentrated systems are given in Figure 4. The test results with the pilot scale obtained proved that feeding the reactor at a low flow rate by keeping the input concentration ratio constant would be effective both in terms of occupational health and safety and product yield. When the input conditions for the effective product were provided, it was observed that the acid-base feeding sequence to the reactor did not have a significant effect on the product and the production process.

### Determination of the Type of Reactor and Production

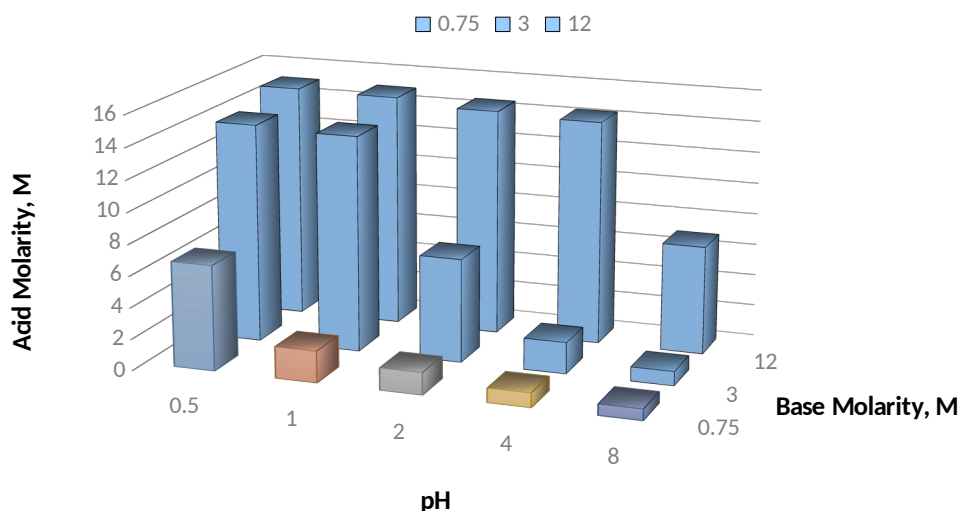
The experiments carried out on a pilot scale and then repeated at an industrial scale, showing that the optimum input concentration ratio should be 1/1.5 for an effective and productive product. After determining the input concentration ratio, the most suitable, reliable, and sustainable reactor type should be determined by considering the production conditions, production time, and product quality of the product. Since the production process of potassium phosphite salts formed by the reaction of a strong base and a weak acid caused acid-base splashes on the pilot scale, it can cause reactor explosion in industrial production. For this reason, errors that might arise were kept under control by conducting repeated experiments with a pilot-scale before designing a safe production process at an industrial scale.



**Figure 1:** Experimental system for tubular flow reactor (A1: acid feeding, A2: cooling water outlet, A3: product outlet, A4: cooling water inlet, B1-B5: base feeding inlets, N1-N5: sampling points, P1:pH meter, P2: Acid feeding tank, P3: Acid pump, P4: Base feeding tank, P5: base pump, P6:cooling water circulator, P7: product tank, P8: online data module (I/O); T1-T10: thermocouples; T11-12: thermometer.



**Figure 2:** Temperature distribution graph as a result of the reactions with different initial concentrations of acid/base with a constant ratio of 1/1.5.

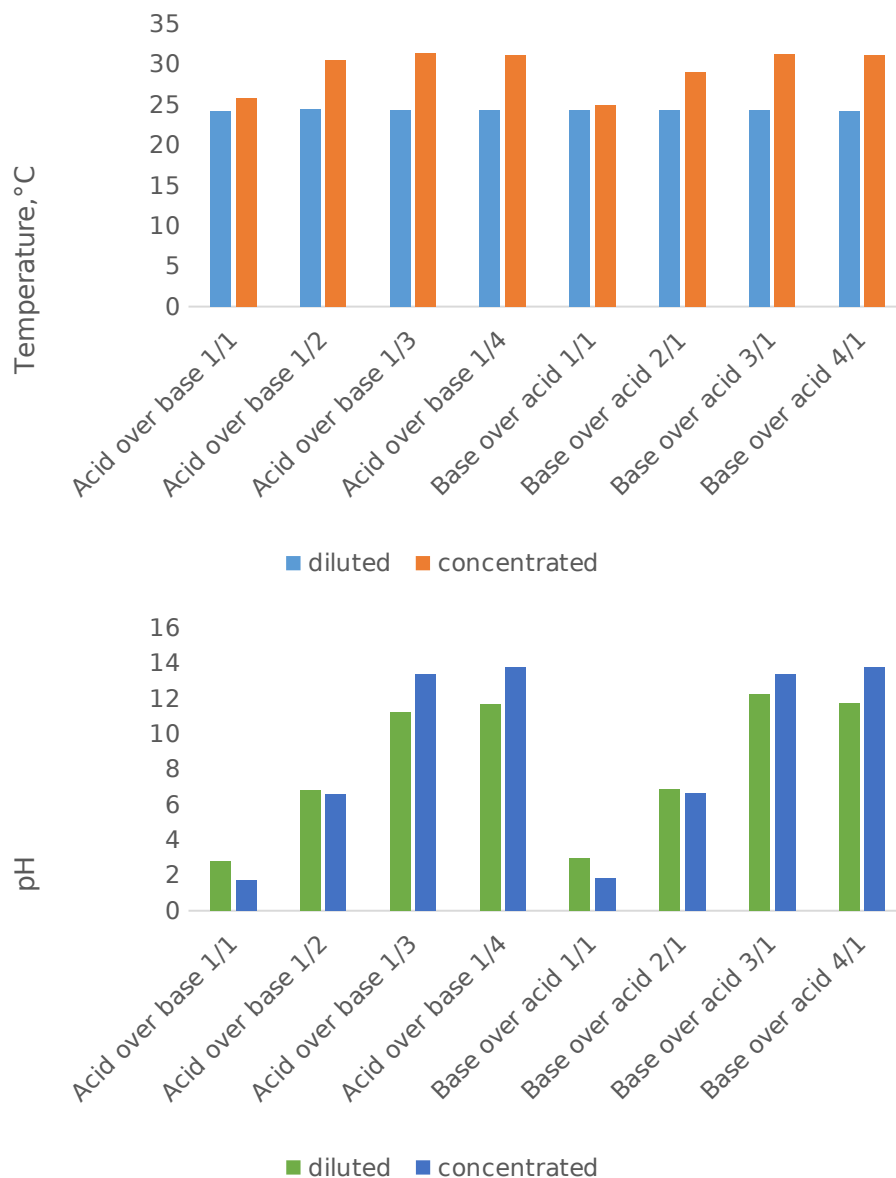


**Figure 3:** The final pH values of the reaction reached at the initial concentrations of Acid and Base (1/1.5 M).

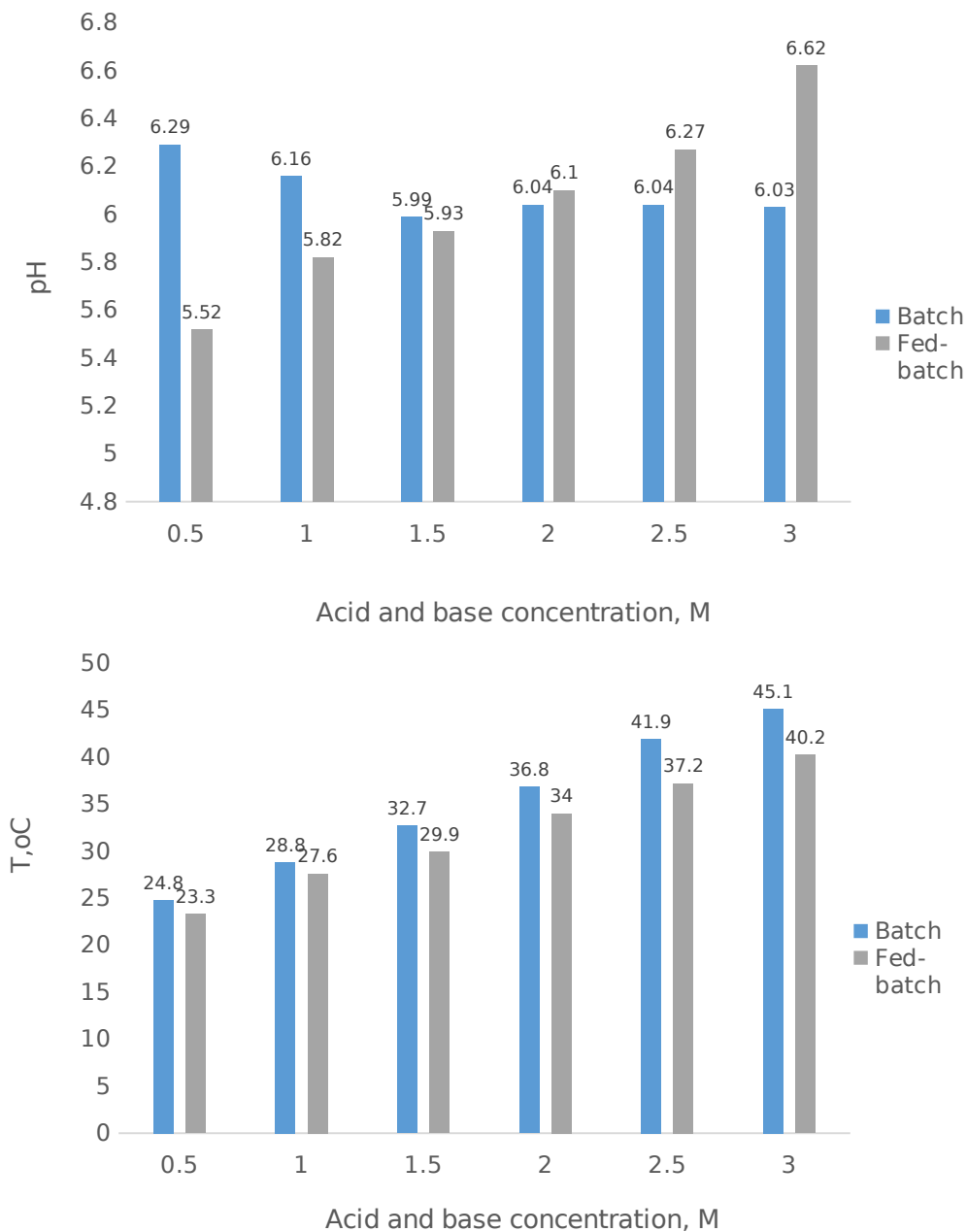
The exothermic nature of the production reaction poses significant risks. As the reactor temperature rises during the reaction, it is expected that phosphine gas, which is poisonous for humans, plants, and the environment, will be formed (15). In cases where phosphine gas is not disposed of, it causes poisoning as well as reducing product yield (16). Toxic and/or undesirable by-products may occur as well as causing acid-base splashes, explosions, and burns. The repeated experiments in the batch reactor caused sudden temperature increases as seen in Figure 5. Because the reaction was very fast and a strong base and a weak acid were used, it was observed that jumps are more likely to occur in batch operation. It was also known that garlic-smelling phosphine gas was formed during the reaction. The sudden temperature that arises in the reactor can be controlled by the design of a jacketed reactor.

Since the reaction that took place was a neutralization reaction, an 'S' curve was expected when the pH values obtained over time were plotted. When fed-batch and batch processes were compared, this result could not be reached because the reaction was very fast in batch processes. As a result of the repeated productions by keeping the 1:1.5 acid: base input concentration constant, the pH values recorded in the batch reactor during production are given in Figure 6.a, while the pH values recorded in the fed-batch reactor are shown in Figure 6.b.

According to Figures 2, 3, and 6, potassium hydroxide solution was added to phosphorous acid slowly with the help of a pump in order to increase the product selectivity and to control the temperature and operate in isotherm in fed-batch operation.

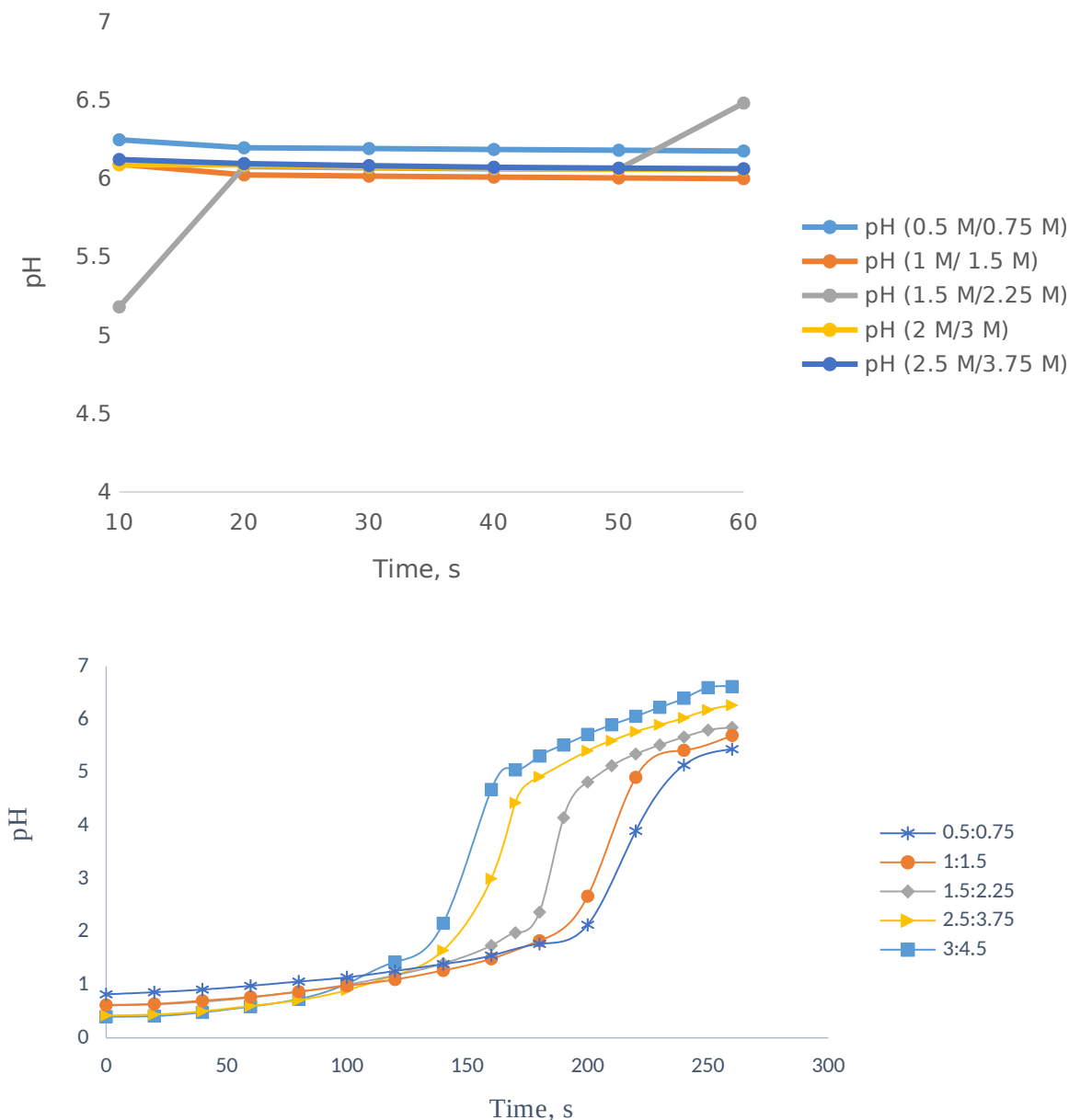


**Figure 4: (Top)** Base over acid and acid over base comparison with temperature on diluted and concentrated system. **(Bottom)** Base over acid and acid over base comparison with pH on diluted and concentrated system.



**Figure 5: (Top)** Comparison of pH values of the product formed in fed-batch and batch operations, **(Bottom)** Comparison of the temperature of the product obtained in fed-batch and batch operations.





**Figure 6: (Top)** Graph of pH change over time at 1/1.5 molarity input ratios in a batch reactor **(Bottom)** Graph of pH change over time at 1/1.5 molarity input ratios in a fed-batch reactor.

### Tubular Flow Reactor Design (TFR)

The production process of the potassium salts of phosphorous acid produced in the batch reactor causes permanent damage to the workplace, employees, and the environment on an industrial scale. In addition, the low yield of the product was analyzed. A fed-batch and jacketed reactor design were found to be more controllable, but it was still difficult to control the temperature. It was necessary to design a system that can be fed continuously for high product yield and a safe and sustainable production process. It is advantageous to be able to take samples at certain time intervals from the reactor, which are fed continuously and slowly from different points, in order to determine the chemical kinetic model.

In this designed tubular reactor system, a recorder was designed to feed the reagents through the reactor at certain intervals and to measure the values such as pH and temperature in line with variation of these points in a controlled manner. In this way, the variation of the values desired to be obtained throughout the reaction with time was easily measured. Even when the desired values such as pH and temperature couldn't be reached, it became easier to intervene in the system.

The experimental data were measured with the analog signal modules throughout the production carried out in the designed TFR. The temperature changes with time recorded at the point T2 given in

Figure 7, the change in the empty jacket temperature with time in Figure 7.b, and the pH change at the reactor outlet over time is given in Figure 7.c.

As seen in Figure 7.a, an instantaneous temperature change occurred when the base was sent to the system; that is, the reaction started quickly, and the temperature increased quickly. As seen in Figure 7.b, no temperature change was observed since no cooling water was sent to the jacket.

When Figure 7.c is examined, it is observed that the pH decreased considerably with the acid being sent to the system at the 380th second. With the addition of the base at 1010 seconds, the pH increased over time, and neutralization was observed. It was observed that the base flow rate should be increased when the pH could not reach the desired range. Thus, it was observed that the flow rate was important and therefore the base flow rate was increased until the desired product pH was reached. When the acid stock finished, the pH value was measured as 5.9. With the end of the acid that was being sent to the system, the pH quickly increased to 13 because only the base remained in the environment, as the base feeding continued. The experimental data were measured with analog signal modules throughout the production carried out in the designed TFR. The temperature changes with time recorded at the point T2 is given in Figure 7, the change in the empty jacket temperature with time in Figure 7.b, and the pH change at the reactor outlet over time is given in Figure 7.c.

In the production reaction, the system was expected to reach steady state after about 12 minutes, the pH value of the samples was measured as 6.5 and the temperature values were measured as approximately 55 °C. At the 30th minute of production, sample pH was recorded as 6.6, and sample temperature was recorded as 26 °C. Approximately 1 minute after this measurement, the base feed was completed, and the pH of the final product was measured as 6.7. In Figure 8, the change in the temperature of the samples taken at the point T2 over time (Figure 8.a), the temperature changes in the jacket over time (Figure 8.b), and the pH change of the product over time (Figure 8.c) are given. The pH is acidic because there is no base

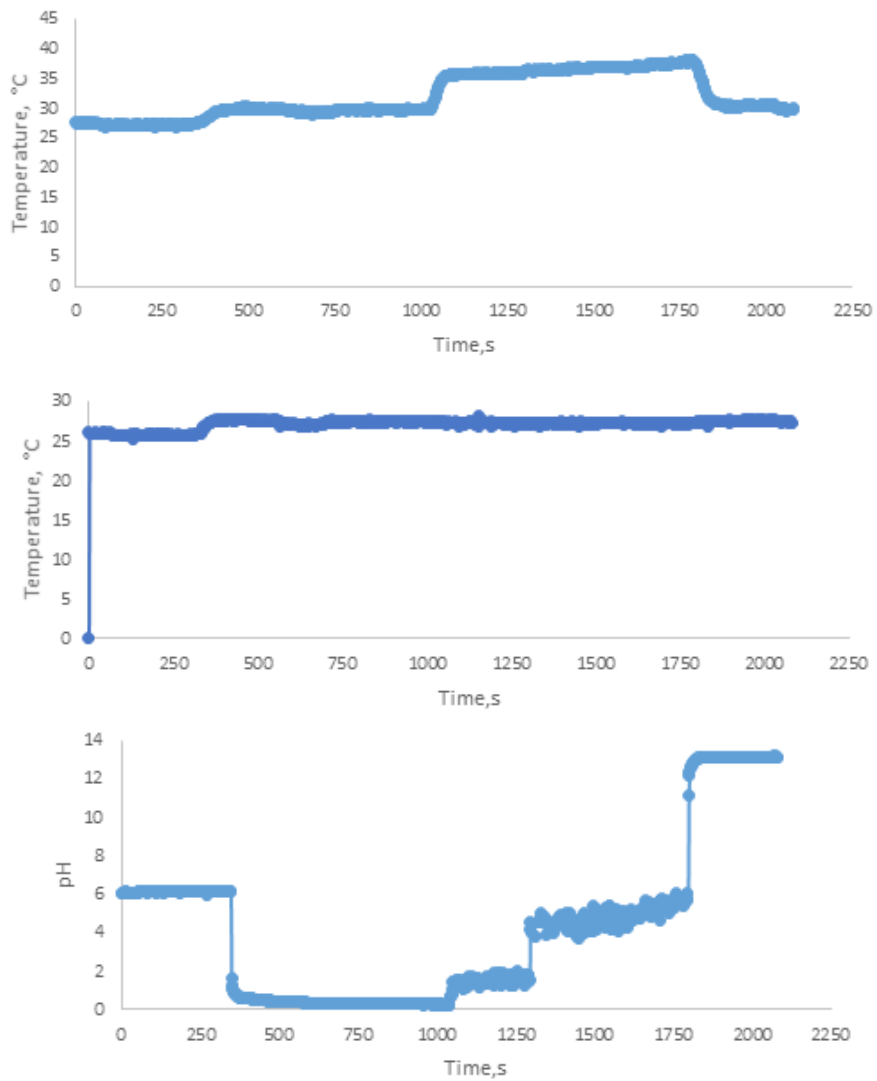
feeding until the 300<sup>th</sup> second. As the reaction started to take place with the feeding, the pH value started to increase. During the reaction, acid feed and base feed from two different points continued. When the reaction was completed, it was observed that the pH value of the desired product was reached. The TFR design was proven to be successfully implemented.

### Results of Phosphorus Acid Analysis

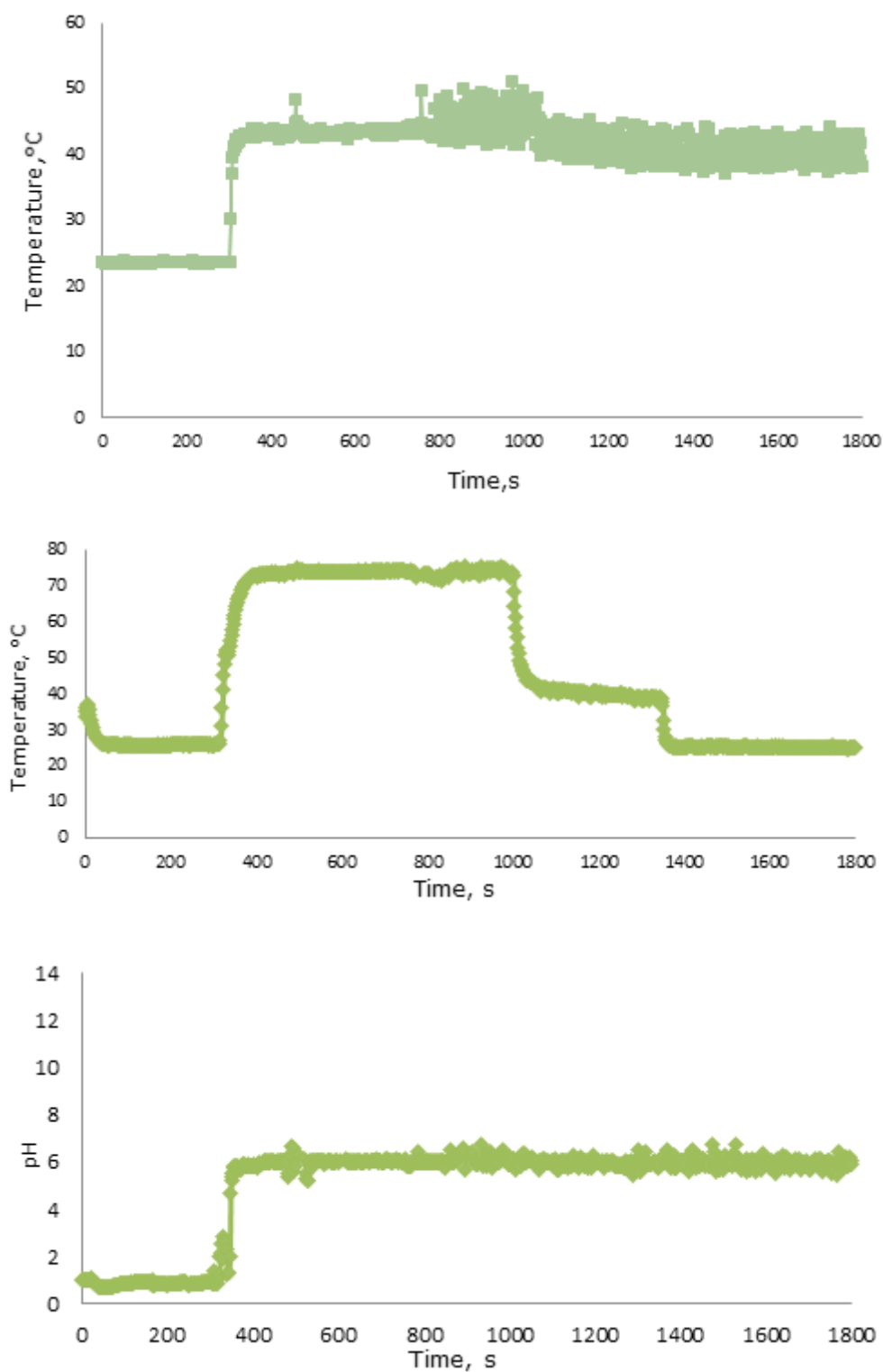
The stock solutions prepared at different concentrations in the range of 0-500 ppm were prepared for analysis with Shimadzu - UV160 and a manual spectrophotometer to form the calibration line of the amount of phosphorous acid contained in the product. It was observed that the maximum pick values of the spectra were read at a wavelength of 350 nm. Separate absorbance values of the solution at each concentration were recorded for the wavelength of 460 nm and the wavelength of 350 nm given in the literature (23). In Figure 9.a, the calibration graph created at a wavelength of 350 nm, and in Figure 9. b, the calibration graph created at a wavelength of 460 nm is given.

The phosphorus acid concentrations of the products obtained in different reactors were analyzed and the percentages of phosphorus content in the products were determined. The conclusive analysis results with the theoretical values with an acceptable margin of error prove the applicability of the analysis method and the high product yield. When the base is fed to the reactor, it is expected that the volume will double and thus the phosphorous acid concentration will be halved. The product analysis results are consistent with the expected theoretical values.

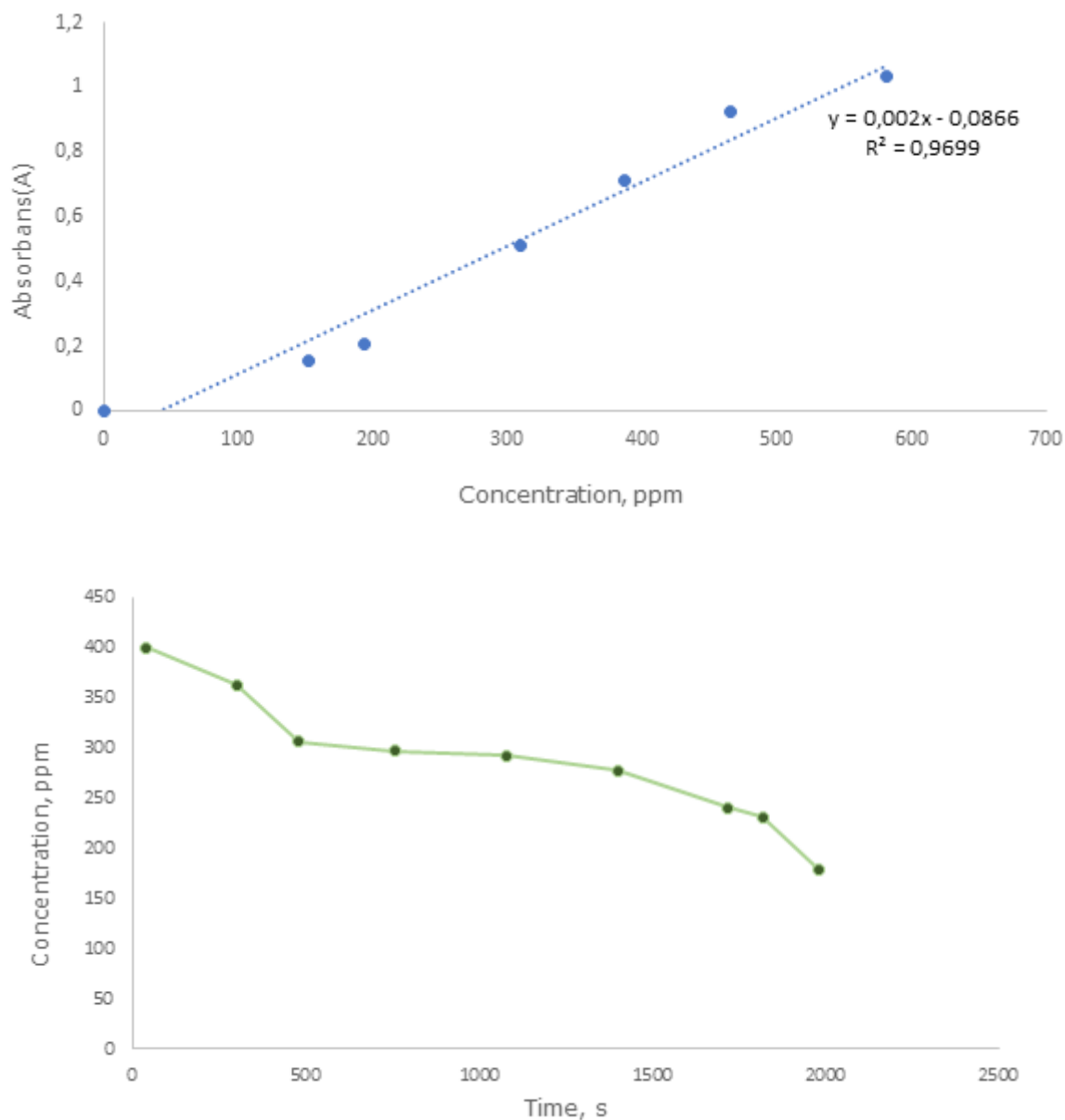
However, in order for the obtained data to be used in determining the chemical kinetic model, it was expected that the amount of 400 g/L  $H_3PO_3$  in the medium was expected to be completely depleted in time, and when the reaction was completed, the 200 g/L  $H_3PO_3$  concentration was calculated in the medium, and it was concluded that the analysis performed not only measured the phosphorus (P%) in the  $H_3PO_3$  but also the total phosphorus amount in the medium. For this reason, it was concluded that the results of the phosphorus analysis could not be used in kinetic analysis calculations.



**Figure 7:** (a) Change of temperature over time at point T2. (b) Change of jacket temperature over time (ambient temperature). (c) pH change in reactor output over time.



**Figure 8: (Top)** Change of temperature at point T2 over time **(Middle)** Change of temperature at point T6 over time **(Bottom)** Change in the pH of the product formed at the reactor output over time.



**Figure 9: (Top)** Calibration graph created at 350 nm wavelength **(Bottom)** Graph of concentration versus time generated at 460 nm wavelength.

In the last decade, usage of continued tubular flow reactors have been seen as promising strategies for industrial production of chemicals. Investigations have been conducted on the various chemical production processes in commercial quantities. Awogbemi et al. studied adaptation of tubular reactor in the production process of biodiesel and found out that using transesterification technique in tubular reactor technologies provide eco-friendly, low-cost, and large-scale production of biodiesel, at a high product yield while generating high-quality biodiesel (24). Burns et al. pointed out the popular usage of tubular flow reactor in the organic chemistry and polymer synthesis and also mentioned advantages of flow techniques including intensified heat transfer, operation under steady state conditions and simplified scale-up with minimal process development (25). Gu et al.

investigated heat transfer and storage performance of steam methane reforming in tubular reactor and achieved 34.8% improvement in thermochemical energy storage efficiency by using insulation and coating (26). Körbahti et al. examined tubular flow reactor for the first time in the electrochemical treatment of water-based paint wastewater system (27). In this study, application of the continuous tubular reactor in phosphorous acid potassium salts production was realized for the first time in literature to ensure concentrated fungicide production.

## CONCLUSION

The results of the experiments showed that the fed-batch reactor was more controllable and sustainable than the batch reactor. However, since it would be

more economical and feasible to provide continuous production on an industrial scale, a tubular flow reactor was designed. The repeated test results conducted to determine the optimum feed flow rates have shown that the safest, most efficient, and sustainable production process is provided by feeding into a tubular flow continuous reactor at a slow flow rate. Considering the temperature and pH data recorded at regular intervals during production, the pH value reached by the final product, and the acid: base feeding sequence did not significantly change the phosphorus concentration of the product because of the analysis. It is necessary to feed slowly the strong base to the reactor from different points of the reactor after feeding the weak acid to the reactor. It is recommended that because it is possible to eliminate possible risks. In future studies, it is suggested that the system will be controlled with advanced control systems to adjust the desired concentration of tubular flow reactors. The temperature inside the reactor was prevented from rising above the desired value with the jacket around the designed tubular reactor and therefore phosphine gas production was prevented. Although it is difficult to control the temperature in the tubular flow reactor, the desired product specifications were obtained are an indication that the reaction can take place in the tubular flow reactor continuously.

#### CONFLICT OF INTEREST

There is no conflict of interest.

#### ACKNOWLEDGMENTS

This study was supported by TUBITAK 2209-B Undergraduate Research Projects Industry-Oriented Support Program with the project number 1139B412001078.

#### REFERENCES

- Kara M, Jannuzzi A, Yön S. In-vitro investigation of the cytotoxic and genotoxic effects of benzimidazole group pesticides benomyl and carbendazim. *J Toxicol Cur Res*. 2019;3(007).
- Milenkovski S, Bååth E, Lindgren PE, Berglund O. Toxicity of fungicides to natural bacterial communities in wetland water and sediment measured using leucine incorporation and potential denitrification. *Ecotoxicology* [Internet]. 2010 Feb [cited 2022 Oct 1];19(2):285-94. Available from: [<URL>](#).
- Lovatt C, Mikkelsen R. Phosphite fertilizers: What are they? Can you use them? What can they do. *Better crops*. 2006;90(4):11-3.
- Liu S. Batch Reactor. In: *Bioprocess Engineering* [Internet]. Elsevier; 2017 [cited 2022 Oct 1]. p. 139-78. Available from: [<URL>](#).
- Bhat J, Madhavan KP, Chidambaram M. Multivariable global input/output linearized internal model control of a semibatch reactor. *Ind Eng Chem Res* [Internet]. 1991 Jul [cited 2022 Oct 1];30(7):1541-7. Available from: [<URL>](#).
- Chang JS, Hsieh WY. Optimization and Control of Semibatch Reactors. *Ind Eng Chem Res* [Internet]. 1995 Feb [cited 2022 Oct 1];34(2):545-56. Available from: [<URL>](#).
- Gooch JW. Semi-Automatic Molding Machine. In: Gooch JW, editor. *Encyclopedic Dictionary of Polymers* [Internet]. New York, NY: Springer New York; 2011 [cited 2022 Oct 1]. p. 654-654. Available from: [<URL>](#).
- Ernst WR. Second-order reaction in a semibatch reactor. *AIChE journal*. 1997;43(4):1114-6.
- Molga EJ, Lewak M, Roel Westerterp K. Runaway prevention in liquid-phase homogeneous semibatch reactors. *Chemical Engineering Science* [Internet]. 2007 Sep [cited 2022 Oct 1];62(18-20):5074-7. Available from: [<URL>](#).
- Levenspiel O. *Chemical Reaction Engineering*. *Ind Eng Chem Res* [Internet]. 1999 Nov 1 [cited 2022 Oct 1];38(11):4140-3. Available from: [<URL>](#).
- Scott HF. *Essentials of Chemical Reaction Engineering*. Prentice Hall; 2017.
- Ann PJ, Tsai JN, Wong IT, Hsieh TF, Lin CY. A Simple Technique, Concentration and Application Schedule for Using Neutralized Phosphorous Acid to Control Phytophthora Diseases. *Plant Pathol Bull* [Internet]. 2009;18(3):155-65. Available from: [<URL>](#).
- Al-Maydama HMA, Gardner PJ. The enthalpy of solution of phosphorous acid (H<sub>3</sub>PO<sub>3</sub>) in water. *Thermochimica Acta* [Internet]. 1990 Apr [cited 2022 Oct 1];161(1):51-4. Available from: [<URL>](#).
- Young JA. Potassium Hydroxide. *J Chem Educ* [Internet]. 2005 Sep [cited 2022 Oct 1];82(9):1304. Available from: <https://pubs.acs.org/doi/abs/10.1021/ed082p1304>
- Chaudhry M. Phosphine resistance. *Pesticide outlook*. 2000;11(3):88-91.
- Hashimoto S, Fujiwara K, Fuwa K. Determination of phosphate ion by gas chromatography with the phosphine generation technique. *Analytical Chemistry*. 1985;57(7):1305-9.
- Lee KW, Han IS. Evaluation of Thermal Hazard in Neutralization Process of Pigment Plant by Multimax Reactor System. *Journal of the Korean Society of Safety*. 2008;23(6):91-9.
- Silva OC, Santos HAA, Dalla Pria M, May-De Mio LL. Potassium phosphite for control of downy mildew of soybean. *Crop Protection* [Internet]. 2011 Jun [cited 2022 Oct 1];30(6):598-604. Available from: [<URL>](#).
- Förster H, Adaskaveg JE, Kim DH, Stanghellini ME. Effect of Phosphite on Tomato and Pepper Plants and on Susceptibility of Pepper to Phytophthora Root and Crown Rot in Hydroponic Culture. *Plant Disease* [Internet]. 1998 Oct [cited 2022 Oct 1];82(10):1165-70. Available from: [<URL>](#).
- McDonald AE, Grant BR, Plaxton WC. Phosphite (phosphorous acid): its relevance in the environment and agriculture and influence on plant phosphate starvation response. *Journal of Plant Nutrition* [Internet]. 2001 Oct 31 [cited 2022 Oct 1];24(10):1505-19. Available from: [<URL>](#).



21. Achary VMM, Ram B, Manna M, Datta D, Bhatt A, Reddy MK, et al. Phosphite: a novel P fertilizer for weed management and pathogen control. *Plant Biotechnol J* [Internet]. 2017 Dec [cited 2022 Oct 1];15(12):1493-508. Available from: [<URL>](#).

22. Gübre analizleri yapma-2 [Internet]. Milli Eğitim Bakanlığı; 2014. Available from: [<URL>](#).

23. Perrin FX, Phan TA, Nguyen DL. Synthesis and characterization of polyaniline nanoparticles in phosphonic acid amphiphile aqueous micellar solutions for waterborne corrosion protection coatings. *J Polym Sci Part A: Polym Chem* [Internet]. 2015 Jul 1 [cited 2022 Oct 1];53(13):1606-16. Available from: [<URL>](#).

24. Awogbemi O, Kallon DVV. Application of Tubular Reactor Technologies for the Acceleration of Biodiesel Production. *Bioengineering* [Internet]. 2022 Jul 27 [cited 2022 Oct 1];9(8):347. Available from: [<URL>](#).

25. Burns JA, Houben C, Anastasaki A, Waldron C, Lapkin AA, Haddleton DM. Poly(acrylates) via SET-LRP in a continuous tubular reactor. *Polym Chem* [Internet]. 2013 [cited 2022 Oct 1];4(17):4809. Available from: [<URL>](#).

26. Gu R, Ding J, Wang Y, Yuan Q, Wang W, Lu J. Heat transfer and storage performance of steam methane reforming in tubular reactor with focused solar simulator. *Applied Energy* [Internet]. 2019 Jan [cited 2022 Oct 1];233-234:789-801. Available from: [<URL>](#).

27. Körbahti BK, Tanyolaç A. Electrochemical treatment of simulated industrial paint wastewater in a continuous tubular reactor. *Chemical Engineering Journal* [Internet]. 2009 May 15 [cited 2022 Oct 1];148(2-3):444-51. Available from: [<URL>](#).





## Preparation and Characterization of Cross-Linked PEI-Lipase Aggregates with Improved Activity and Stability

Nedim ALBAYRAK\*<sup>1</sup>, Mehmet Erhan KANISLI<sup>2</sup>

<sup>(1)</sup> Department of Food Engineering, Faculty of Engineering, Hitit University, 19030 Corum, TURKEY

<sup>(2)</sup> Department of Food Engineering, Faculty of Engineering, Yuzuncu Yil University, 65080 Van, TURKEY

**Abstract:** Using polyethyleneimine (PEI) as the sole precipitation and aggregation agent, PEI-enzyme complexation was investigated with lipases from *Rhizomucor miehei*, *Thermomyces lanuginosus* and *Candida antarctica*. The approach relied on rapid development of PEI-lipase aggregates in a solution and followed by glutaraldehyde cross-linking thus resulting in cross-linked PEI-lipase aggregates. PEI to enzyme mass ratio of a 1/ 20-40 range, alkaline pH and the absence of impurities produced higher coupling yields and activities. The pH affected the precipitability and/or relative activity of the aggregates. Impurities in some lipase preparations may prevent the formation or precipitation of the PEI-lipase aggregates. The aggregates attained higher stabilities especially at high pHs and enhanced thermostability with at least a 20-fold at ambient temperatures. By using *p*-nitrophenyl propionate as a soluble substrate, app.  $V_{max}$  for the immobilized lipase increased by two-fold with only 25% increment in app.  $K_m$  compared with the soluble lipase. Complexation with PEI may have produced favorable interface assisting for conformational change for the lipase activation. Thus, cross-linked PEI-lipase aggregates with ease of recovery and stability can be simple and inexpensive alternative for carrier-free immobilized lipases.

**Keywords:** Polyethyleneimine, Lipase, Glutaraldehyde, Cross-linked PEI-lipase aggregate

**Submitted:** August 26, 2022. **Accepted:** October 06, 2022.

**Cite this:** Albayrak N, Kanisli ME. Preparation and Characterization of Cross-Linked PEI-Lipase Aggregates with Improved Activity and Stability. JOTCSB. 2022;5(2):127-42.

**\*Corresponding author. E-mail:** [nedimalbayrak@hitit.edu.tr](mailto:nedimalbayrak@hitit.edu.tr). Phone: +90(364) 2274533. Fax: +90(364) 2274535.

### INTRODUCTION

Since the start of last century (1), the means of enzyme immobilization have been the subject of numerous investigation yielding various methods (2). Apparently, no method fits all enzymes or all applications of a particular enzyme. Immobilized enzymes are expected to enable reuse of enzyme, provide sufficient stability and thus simplified and efficient product formation (3). In majority of enzyme immobilization procedures, the major focus was devoted to the nature of the support for enzyme to be attached (4-7). Enzyme immobilization on support provides the benefits of ease on handling, better separation and

mechanical stability but the enzyme density in a given area tends to be low (8,9). Also, highly engineered functional particulate type supports tend to be expensive (7,10,11) which is a great burden for industrial scale applications (12). In order to increase volumetric efficiency of an enzyme reactor, the space devoted to carrier should be limited without sacrificing productivity and stability (13).

Our objective is to prepare high-density, carrier-free lipase catalyst with simple and inexpensive means. In recent years, considerable research is directed towards carrier-free enzyme immobilization approaches so that higher catalyst

densities would be achieved by excluding support such as in the concepts of cross-linked enzyme aggregate (3,14). The preparation involves the physical precipitation of the enzyme with the aid of a solvent or salt and further cross-linking generally with glutaraldehyde (GA) to form insoluble cross-linked enzyme aggregates (14–16). The cross-linked enzyme aggregate method shows a significant achievement in the field providing intense form of biocatalyst and turned into a commercial application (17). However, low catalytic efficiencies were reported in a few of the applications due to close confinement (10,18) and diffusion limitations (19). Recently, e.g., a cross-linked aggregate of  $\beta$ -galactosidase from *Aspergillus oryzae* was prepared and used for lactulose/galacto-oligosaccharides (GOS) production (20). It was observed that GOS yield obtained with the immobilized lactase was 25% lower than that of the soluble enzyme. We have previously shown that solo polyethyleneimine (PEI) precipitation of  $\beta$ -galactosidase from *Aspergillus oryzae* and GA cross-linking was able to produce carrier-free aggregates (21). The carrier-free lactase aggregate showed over 95% specific enzyme activity and more importantly was able to carry out lactose conversion as good as the soluble enzyme with no reduction in GOS formation, which suggests PEI-enzyme aggregates are flexible and porous to allow the diffusion of large molecules. However, it remains to be seen the applicability of the PEI - enzyme aggregation approach to other enzymes namely industrially relevant lipases.

Lipases carry out various types of reactions, they hold tremendous potential for clean and ecofriendly transformations in energy, oleo-chemistry and the chemical applications (22–24). It was recognized that lipase applicability in industrial processes was not fully explored due to their low stability or short life-times (7,16,25,26) which make immobilized lipase economically attractive. In essence, success in lipase immobilization relies on delicate balance of various parameters including enzyme flexibility to enable conformational change during interfacial activation as well as solubility for all substrates and the enzyme itself (7,27,28). These challenging aspects should be well considered especially with a carrier-free lipase preparation. Simple and inexpensive confinement of a high number of active and adequately stabilized catalyst in an intense state may be an attractive approach to extend the applicability of lipases(28).-

The goal of the study is to investigate cross-linked PEI- enzyme aggregates with industrially

relevant lipases as a potential carrier-free enzyme preparation. Our previous experience with PEI-enzyme interaction leading to enzyme immobilization and aggregation (21,29–31) may suggest that PEI unforcefully gathers and steers the enzymes yet practically separates one another by cushioning in between, leading to favorable channeling for mass transfer (32). Therefore, we hypothesize that conveniently avoiding the use of organic solvent for precipitation, solely PEI mediated lipase aggregate may lead a novel type of a dense catalyst with desirable attributes of low cost, rapid preparation and high activity and stability. The key factors affecting PEI-enzyme aggregate formation such as PEI to lipase ratio, pH of the aggregation, extent of the GA cross-linking and impurities in enzyme preparations were investigated. Also, carrier-free immobilized lipase characteristics and relevant stabilities were discussed in this study.

## MATERIALS AND METHODS

### Enzyme and Reagents

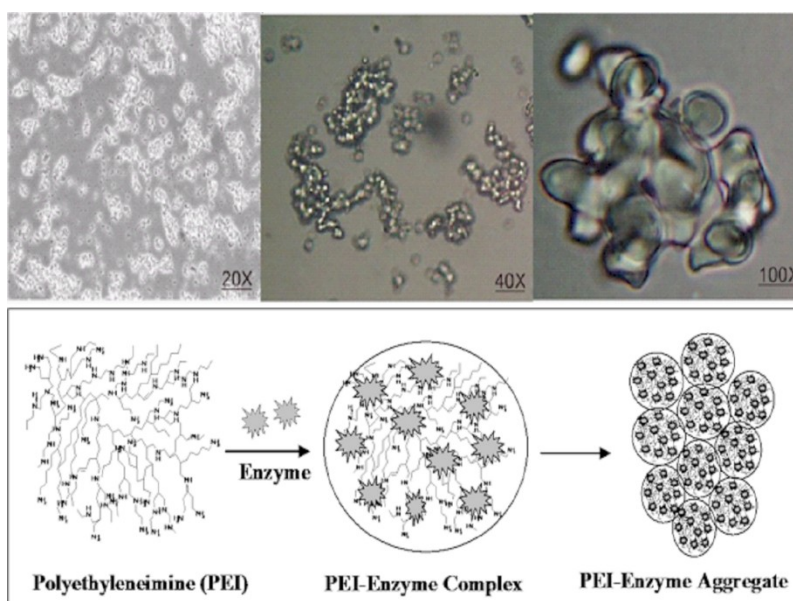
Commercial lipase in liquid forms from *Thermomyces lanuginosus* (Lipozyme TL), and *Rhizomucor miehei* (Novozym 388) were a gift of Novo Nordisk (Bagsvaerd, Denmark). *R. miehei* (ICR-116 Lipase), *Candida antarctica* Cal A (ICR-112) and Cal B (ICR-110) lipases in powder forms were obtained from Codexis (Pasadena, CA, USA). Also, *R. miehei* (Fungal Lipase, 150,000 FIP/g) lipase obtained from Bio-Cat (Troy, VA, USA). *Burkholderia cepacia* (Lipase PS Amano S) was from Amano Inc (Elgin, IL, USA). Branched polyethyleneimine as 50% (w/v) (Number average molecular weight: 60,000; Average molecular weight: 750,000) and glutaraldehyde (GA) as 25% (w/v) aqueous solutions were from Sigma (St. Louis, MO). *para*-Nitrophenyl propionate (*p*-NPP) and *para*-nitrophenol (*p*-NP) (MP Biochemical, France) were used to measure lipase activities. All other reagents were obtained from Merck (Darmstadt, Germany) and they were at least American Chemical Society grade. All solutions used for PEI-lipase aggregate formation including PEI, GA, lipase preparation were made with distilled water and, pH adjustments were made with suitable concentrations of NaOH or HCl.

### Aggregate Preparation

The procedure for formation of cross-linked PEI-lipase aggregates is composed of two main steps as complexation between PEI and the enzyme, and cross-linking of the complexes with GA. PEI-lipase aggregate was prepared by mixing PEI and lipase solutions. After vortexing the turbid

mixture, a GA solution was added to the PEI-lipase slurry and incubated for 5 minutes for cross-linking. PEI solution (0.1 mL) was mixed with a designated lipase solution (0.9 mL) in microcentrifuge tubes. Turbid slurry of PEI-enzyme mixture was centrifuged at 10,000 rpm for 1-2 min (Sigma 1-14, Germany). To evaluate the exclusive effect of PEI on the lipase activity and complex formation, initial lipase activities of PEI-lipase slurry and the supernatant after the centrifugation were determined. The relative lipase activities were compared with respect to

free enzyme (containing neither PEI nor GA). The morphology of PEI-enzyme aggregates in cloudy turbid slurry was analyzed with a phase-contrast microscopy (LEICA DM 2500, Meyer, Texas, USA) (Figure 1). Prior to the GA cross-linking, the effects of PEI to enzyme ratio (1/2.5 - 1/250), pH (6 to 11), mixing (50-200 rpm) and duration (5 to 20 minutes) for effective PEI-lipase complexation were studied. The differences in the activities of the complex solutions and the supernatants can be considered as a degree of the enzyme incorporation into the complexes.



**Figure 1:** Light microscopy images of PEI-lipase aggregates at 20, 40 and 100 magnifications along with the projected mechanism from PEI-enzyme complexation towards aggregation.

Finally, under the optimized conditions for PEI-lipase complexation, the GA solution (0.1 mL) was added to the PEI-lipase mixture and incubated for about 5 min. The effects of the GA concentrations (0.1-10 mg/mL) and the duration (5 to 30 min) for cross-linking were studied. The factors were evaluated according to the outcome of initial lipase activities of the GA cross-linked PEI-lipase complex and the activity remaining in the supernatant. Stability of cross-linked aggregate obtained under the optimized condition was monitored by washing thoroughly with distilled water and buffer (50 mM phosphate buffer pH 7.0). Unless otherwise noted, all the experiments were carried out at room temperature. The experiments were performed in triplicate and the standard deviations were shown in the figures as vertical bars.

### Characterization

Variations in the characteristics of cross-linked PEI-lipase aggregates were investigated by using the *Rhizomucor miehei* lipase (RML) from Novozyme to exemplify the effect of the lipase immobilization procedure obtained under the optimized conditions for the immobilization. After preparation, the precipitates of cross-linked PEI-lipase aggregates in tubes were resuspended to the original volume of the enzyme with 50 mM phosphate buffer (at pH 7) after being washed two times with distilled water. The resuspended aggregates were refrigerated until use and employed for all of the characterization studies including thermal and storage stabilities and the determinations of apparent kinetic constants. For determinations of pH optimum and stability against change in pH, the aggregates resuspended in distilled water were used. All characterization studies for the resuspended aggregates were carried out side-by-side with

free lipase solutions. Examination of the optimum temperature for free and the immobilized enzyme was avoided because of greater interference of autohydrolysis of *p*NPP substrate at higher temperatures (33).

#### *Thermal and Storage Stabilities*

For thermal stability, cross-linked PEI-lipase aggregates were held in a constant-temperature water bath between 35 and 75°C for two hours and then the lipase activities were measured and compared with free enzyme incubated under the same conditions. To determine the storage stability, free and the resuspended aggregates in 50 mM phosphate buffer at pH 7 were kept in refrigeration or at room temperature for nearly one month, and lipase activities were measured from the aliquots taken from samples during incubation. The storage stability of a dry form of cross-linked PEI-lipase aggregates was also included in the study. The aggregate preparation resuspended in distilled water in a glass dish was left to dry and then kept at room temperature for two weeks. After the incubation, the dried aggregates were resuspended in distilled water and rehydrated for 30 min before the measurement of the lipase activities at the end of incubation.

#### *pH Optimum and Stability*

In order to study the effect of pH on the activities of cross-linked PEI-lipase aggregate and soluble lipase, 50 mM acetate (pH 4.0–6.0), phosphate (pH 6.0–7.0), phosphate/carbonate (pH 8.0–10.0) buffers were employed to dissolve or resuspend the enzyme preparation, and also the same buffers were used for diluting the substrate for lipase assays. For the determinations of stability against pH, free lipase and the aggregate preparations dissolved in the same buffer at corresponding pHs were incubated at 25°C for 18 hours. After the incubation, residual lipase activities were measured.

#### *Kinetic Constants*

In order to determine the effect of *p*-nitrophenyl propionate (*p*-NPP) substrate concentrations on the reaction rates for soluble and the aggregated lipases, the concentrations of 0.512–25 mM range were used. The apparent kinetic constants were determined from the data linearized with Lineweaver-Burk plots for approximation of the Michaelis constant ( $K_m$ ) and  $V_{max}$ .

### **Analytical Methods**

#### *Enzyme Assay*

A lipase assay based on the hydrolytic activity of the enzyme from *p*-nitrophenyl propionate (*p*-NPP) substrate was used. The absorbance of *p*-

nitrophenol (*p*-NP) product concentration at 404 nm wavelength was measured spectrophotometrically (Shimadzu UV-1700, Japan). The reaction mixture contained 3 mL of 50 mM phosphate buffer (pH 7.0) and 0.1 mL *p*-NPP solution in acetonitrile (4.1 mM). A 30  $\mu$ L volume of free or immobilized enzyme preparations (resuspensions of PEI-lipase aggregates) was added to the substrate solution and incubated for 5 to 10 minutes at 30°C in a water bath without shaking. The blank composed of the same composition of the reaction mixture but with no enzyme addition and incubated at the same conditions to exclude minor amounts of free or autohydrolyzed *p*-NP product from the amounts catalyzed by the enzyme (33). One International Unit (IU) of lipase activity was defined as the amount (mg) of lipase protein (expressed as Bovine Serum Albumin (BSA)) that liberates one  $\mu$ mol *p*-NP from *p*-NPP under the conditions indicated above. Molar absorptivity of *p*-NP product was experimentally determined ( $\epsilon=8736$  L/M.cm) and used to indicate activity as IU (33).

#### *Protein Assay*

The Coomassie brilliant blue G-250 dye-binding technique was used to determine the protein amounts of the enzyme solutions (34). Relative concentrations of enzyme solutions were indicated as BSA (Acros Organics, Belgium).

#### *Membrane Dialysis*

Regenerated cellulose membranes (Cellu Sep H1, nominal MWCO: 15 kDa) (Membrane Filtration Products, Inc., Texas, USA) were used to dialyze the lipase solutions. Prior to dialysis, lipase solution (0.1 g/mL) in distilled water was centrifuged at 5000 rpm for 5 min. The membranes (holding 0.32 mL/cm) were filled with the centrifuged lipase solution and dialyzed against 1 L phosphate buffer (pH 7, 50 mM). By changing the buffer solution every 12 h, dialysis continued for 36 h at +4 °C under constant stirring.

## **RESULTS AND DISCUSSION**

### **Cross-Linked PEI-Lipase Aggregates**

When a PEI solution was simply mixed with a lipase solution, an instant development of turbid slurry was observed indicating a favorable interaction between molecules of PEI and the enzyme leading to complex formation and aggregation. The colloidal aggregates in a solution were then cross-linked with the GA for permanent fixation. Upon the centrifugation, the aggregates were collected at the bottom leaving clear supernatant solution. Figure 2 shows the

degrees of precipitates obtained at varying PEI concentrations.



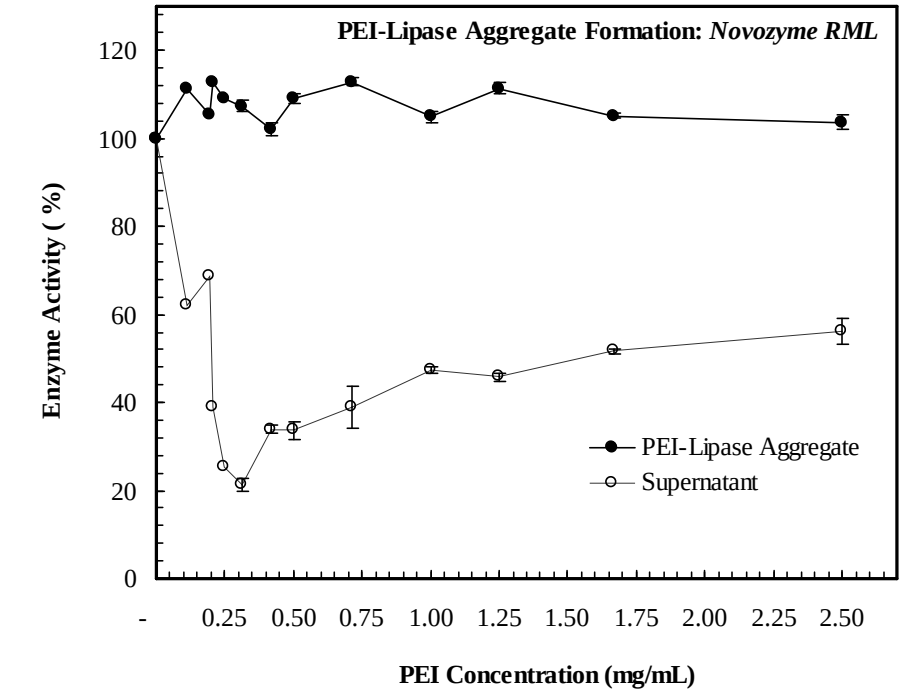
**Figure 2:** Degrees of PEI-lipase precipitates obtained at varying PEI concentrations (different PEI to lipase mass ratio) after centrifugation at 10,000 rpm for 2 min.

#### PEI to Enzyme Ratio

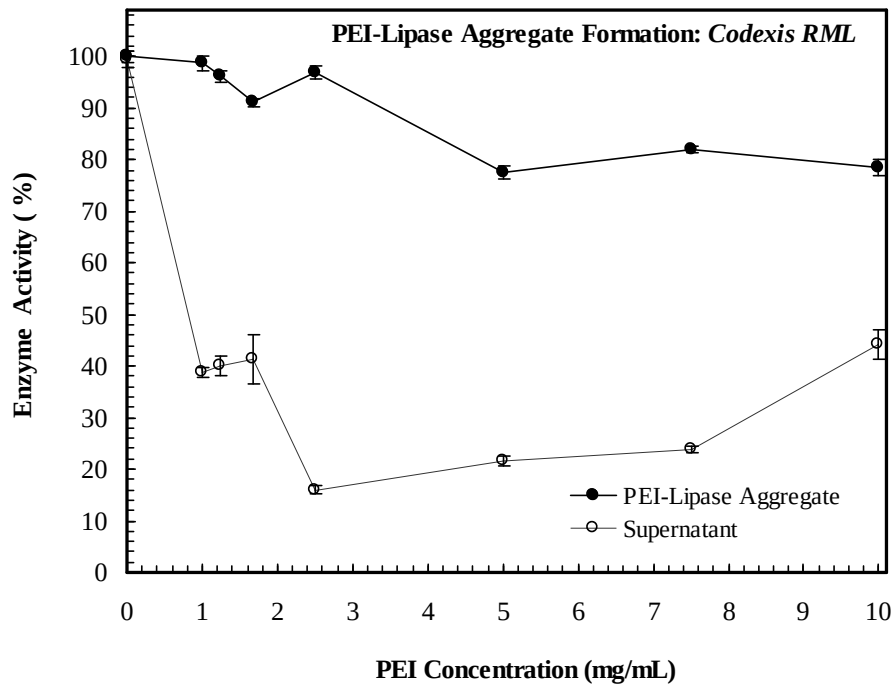
PEI-enzyme complex formation with *Rhizomucor miehei* commercial lipase (RML) preparations from Novozyme or Codexis was investigated at varying PEI to lipase ratios. As seen in Figure 3, increasing concentrations of PEI in the lipase solutions resulted in 110 - 115% lipase activity with Novozyme RML compared to the original free lipase solution with no PEI. Increasing concentrations of PEI lead to a gradual decline in the activity of Codexis RML. As the PEI concentration increased up to 0.3 or 2.5 mg/mL for Novozyme or Codexis RML, the residual lipase activities in supernatant sharply decreased to approximately 15-20% of its initial activity. Further increase in the PEI concentration resulted

in a gradual increase in supernatant activities with both sources of RML. Thus, there appeared to be an optimum PEI to enzyme ratio (or range) associated with not only a highest PEI-lipase aggregate activity in the solution but also a lowest remaining activity in supernatant. The optimal complexation with Novozyme RML or Codexis was attained at the PEI to lipase mass ratio of 1/85 or 1/16 resulting in immobilization yields of 90 or 85%, respectively, based on the lipase activity. Similar to RMLs, as we have previously reported, an optimal PEI-lipase complex formation with lipase A from *C. antarctica* and *T. lanuginosus* (Lipozyme TL) was obtained at a range of PEI to lipase ratio of 1/20 and 1/50 with similar immobilization yields (31).





a



a

**Figure 3:** The effect of PEI concentration on the activity of PEI-lipase complexes in a solution and the remaining activity in supernatant after centrifugation at 10,000 rpm for 2 min by using the *Rhizomucor miehei* commercial lipase preparations from Novozyme and Codexis.

Table 1 compares the levels of protein and Codexis and Novozyme. The Codexis RML in associated specific activities of RMLs from powder form contained nearly 20 times more

protein (expressed as BSA), but only half of the specific activity compared with those of liquid lipase preparation from Novozyme. Apparently, the majority of the protein content of the Codexis RML preparation was proteins without lipase activity. The variation in protein contents of the RMLs could probably be the main reason for the observed difference regarding PEI to lipase mass ratio. Moreover, the gradual decline in the activity

of the PEI-lipase aggregates in Codexis RML may be attributed to the precipitation of a large protein content along with active lipase protein. Nevertheless, lipase contained in the aggregate at the optimum complexation ratio functions as good as free enzyme with a coupling yield of nearly 90% of its initial lipase activity, which may imply porous and the partitioning nature of the PEI complexation.

**Table 1:** Comparisons of protein contents and specific activities for *Rhizomucor miehei* lipases expressed as BSA.

RML Source	RML Protein Conc. ( <sup>a</sup> )	Specific Lipase Activity (IU/mg) ( <sup>b</sup> )	PEI / Lipase (w/w) ( <sup>c</sup> )
Codexis (powder)	43.0% (w/w)	145	1 / 16
Novozyme (liquid)	1.8% (w/v)	299	1 / 85

(<sup>a</sup>) Protein concentration in the enzyme source was expressed as BSA (determined by Bradford method).

(<sup>b</sup>) Experimentally determined specific enzyme activity of the enzyme source based their protein content (expressed as BSA).

(<sup>c</sup>) PEI to lipase mass ratio where the optimal complexation were obtained (see Fig 3).

### The Effect of pH

The effect of pH was investigated for *Thermomyces lanuginosus* (TL) lipase by adjusting the pH of the PEI solution and, the results are displayed in Figure 4. At pH 7, the activity of the PEI-lipase aggregate in solution increased up to 170% (at PEI/lipase ratio 1/50) or even 200% (at PEI - lipase ratio 1/80) and leaving about 20% lipase activity in supernatant, which means that more activity could be precipitated than initially present. At higher pHs between 8 and 10, the PEI-lipase aggregates showed relative activities of 100-120%.

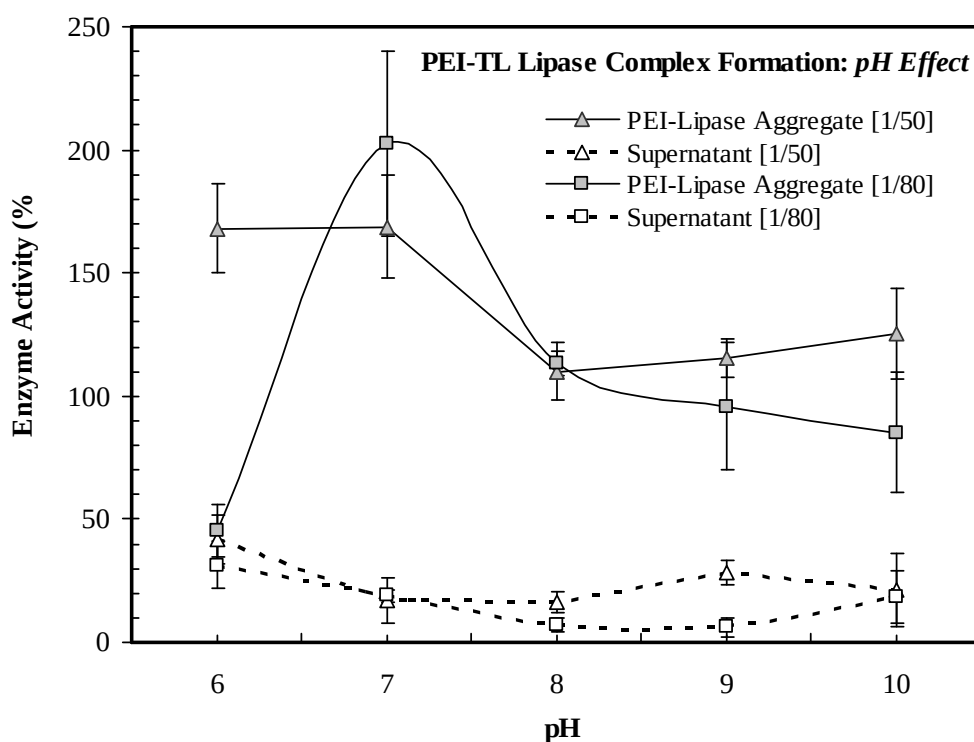
PEI-protein interaction is usually referred to as electrostatic attraction. Considering a high pH of the PEI solution (pH ~ 11.5) used, PEI bearing little or no charge at a dense conformation (35) apparently favors interaction with highly anionic lipases (pI 3.0-5.5) (36,37). Therefore, the probable mechanism for the PEI-enzyme interaction should be dominated by polymer bridging and to lesser extent electrostatic attraction (38). During the previous PEI-lipase complexation experiments, complexation was obtained at natural pH (~ 11.5) set by PEI with no pH adjustment. With the TL lipase, it appeared that more of an electrostatic interaction between pH 7 and 8 might bring about overactivation. Among the lipases studies, TL obviously favored electrostatic interaction toward increased catalytic efficiency.

### Dialyzable Impurities

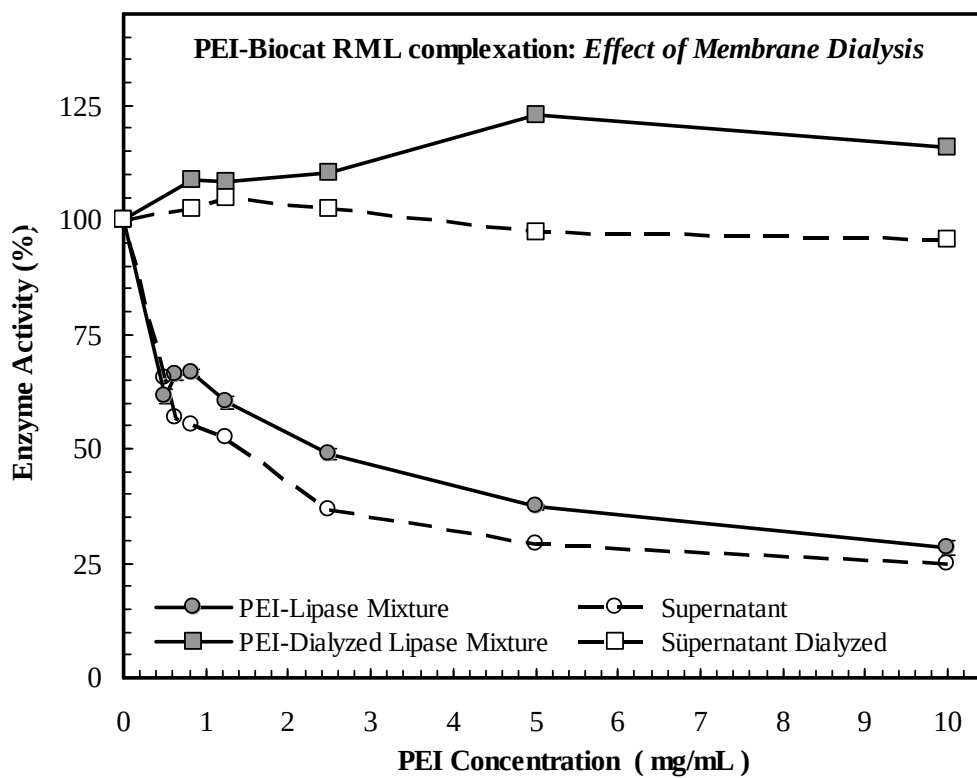
Unlike the other RMLs investigated, with a RML commercial preparation from Bio-Cat, adding PEI to lipase solution failed to produce a turbid mixture or any precipitation after the centrifugation despite variations in the PEI to enzyme ratio. As shown in Figure 5, increasing the PEI concentration was accompanied with a gradual decrease up to 60-70% in the lipase activity of regarding the PEI- lipase mixture or supernatant. When a membrane dialysis (MWCO 15 kDa at 4°C for 36 hours) was performed to remove some of the impurities likely to interfere with enzyme complexation including salts and organic acids, the dialysis had no effect on the protein concentration or lipase activity, but led to a decline in solution pH from 8 to 7 (data was not shown). Also, unlike the effect of PEI on nondialyzed lipase, increasing the PEI concentration did lead to an apparent increase in relative lipase activity of the PEI-lipase mixture up to 120% (Fig 5). However, the interaction of the PEI with dialyzed lipase toward complexation failed to occur again as apparent from either the absence of turbidity or almost no precipitation after centrifugation. Thus, a decrease in the enzyme activity upon PEI-enzyme mixture should not be directly related to sole effect of PEI on enzyme. Similarly, the PEI mixture with lipases from *Candida antarctica* lipase B (Cal B) and *Pseudomonas cepacia* failed to produce precipitable aggregates (data was not shown), although the PEI-lipase aggregates showed a highly turbid slurry and over 100% activity. The Commercial lipase preparation (Cal B) from

Novozyme was reported to contain a substantial amount of sodium benzoate and potassium sorbate and/or nucleic acids (39) and, these are all inhibitory to the PEI enzyme aggregation (21). Assuming that the commercial RMLs had a similar lipase profile, disengagement between the PEI and the lipase could be attributed to other nonproteinaceous constituents such as salts and other anionic compounds (39) which are found in commercial lipase preparations (36). It was determined that a commercial lipase preparation showed 22% protein but of which only 3% corresponded to lipase (40). There is no question

that nonenzymatic proteins and even nonproteinaceous compounds encountered in commercial enzyme powders or solutions interfere with the success of most methods of enzyme immobilization. Similarly in the cross-linked enzyme aggregate formation with lipases, nitrogen containing constituents was found to interfere with the method as well (41). To rule out these factors, a rational strategy to eliminate nonproteinaceous components of a commercial extract can be followed (39) in the case of unsatisfactory precipitation with PEI.



**Figure 4:** The effect of pH on PEI-enzyme aggregate formation with lipase from *Thermomyces lanuginosus* at or near the optimal PEI to lipase mass ratio of 1/50 and 1/80. Lipase activities of the aggregates in solution and the remaining activities in supernatant after centrifugation at 10,000 rpm for 2 min. HCl was used to adjust the pH. The experiments were performed in triplicate and the standard deviation shown as vertical bars.

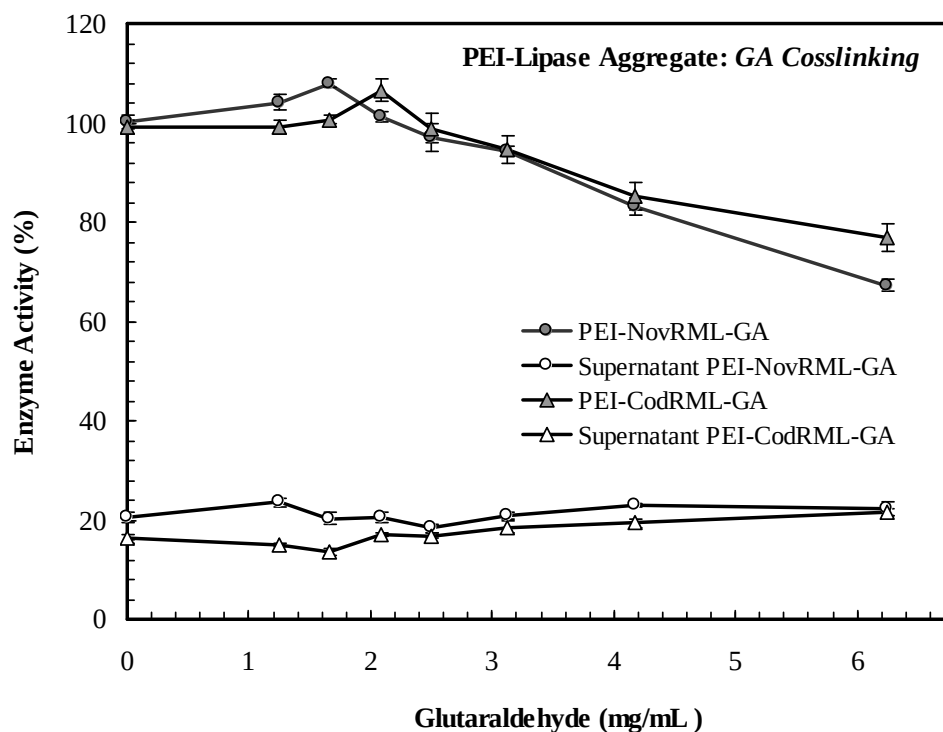


**Figure 5:** The effect of membrane dialysis (with a 15 kDa nominal MWCO regenerated cellulose membrane at 4°C for 36 h) of the lipase solution (0.1 g/mL in distilled water) (dashed lines) compared with normal lipase (straight lines) preparation on the activity of the PEI-lipase complex and precipitability after centrifugation at 10,000 rpm for 2 min by using *the Rhizomucor miehei* commercial lipase preparations from Bio-Cat.

### GA Cross-linking

The aggregates formed by PEI-enzyme interactions are considered as reversible and can be disintegrated to some extent by small anionic species leading to enzyme leach. When the PEI-enzyme aggregates are permanently fixed with a chemical cross-linking, the desired chemical stability against disintegration as well as general physical stability are achieved (42). Since both PEI and enzymes are rich in ammonia, glutaraldehyde (GA) was conveniently employed for permanent fixation of the aggregates. The effect of increasing the GA concentration on the activity of the PEI-lipase aggregate in solution as

well as the efficiency of immobilization was tested for all the lipases at previously optimized PEI to lipase ratios. Figure 6 illustrated the GA effects on RMLs. In general, compared to the absence of GA cross-linking shown in previous experiments, GA cross-linking within a certain range of GA concentration did not change the desirable attributes of the PEI-lipase aggregate formation in all of the lipases studied. It is known that the increase in cross-linking commonly assist greater stabilization against denaturing conditions while often accompanying a reduction in the activity of immobilized enzyme (43).

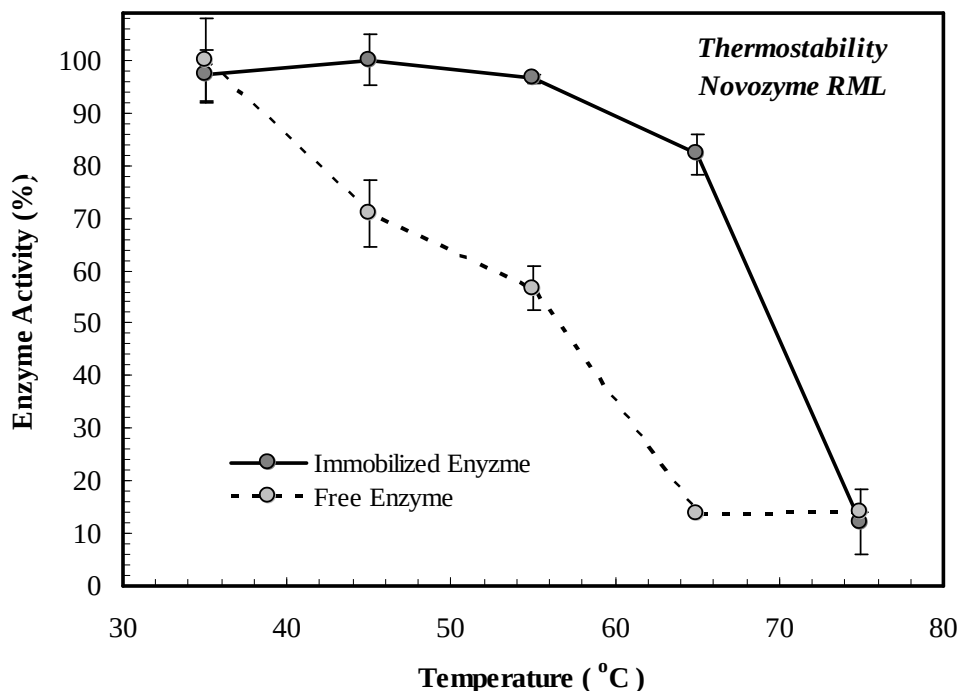


**Figure 6:** The effect of increasing the glutaraldehyde concentration (for 5 min at 20 °C) on the activities of the PEI- *Rhizomucor miehei* lipase aggregates from Novozyme or Codexis in a solution at the PEI to lipase mass ratio of 1/85 or 1/16 and on the levels precipitation after centrifugation (at 10,000 rpm for 2 min), respectively.

The duration for GA cross-linking was found to be an insignificant factor in the activity of aggregates nor the efficiency of precipitation beyond 5 to 10 min of incubation (data not shown). Considering the results for the GA cross-linking, about 2mg/mL GA concentration for 5 to 10 min at room temperature appeared optimum and kept at this level for the rest of the study. It is important to note that the GA cross-linking at this degree provided sufficient stability against leaching of enzyme form the aggregates due to the addition of a salt solution or presence of buffer.

#### Thermal Stability

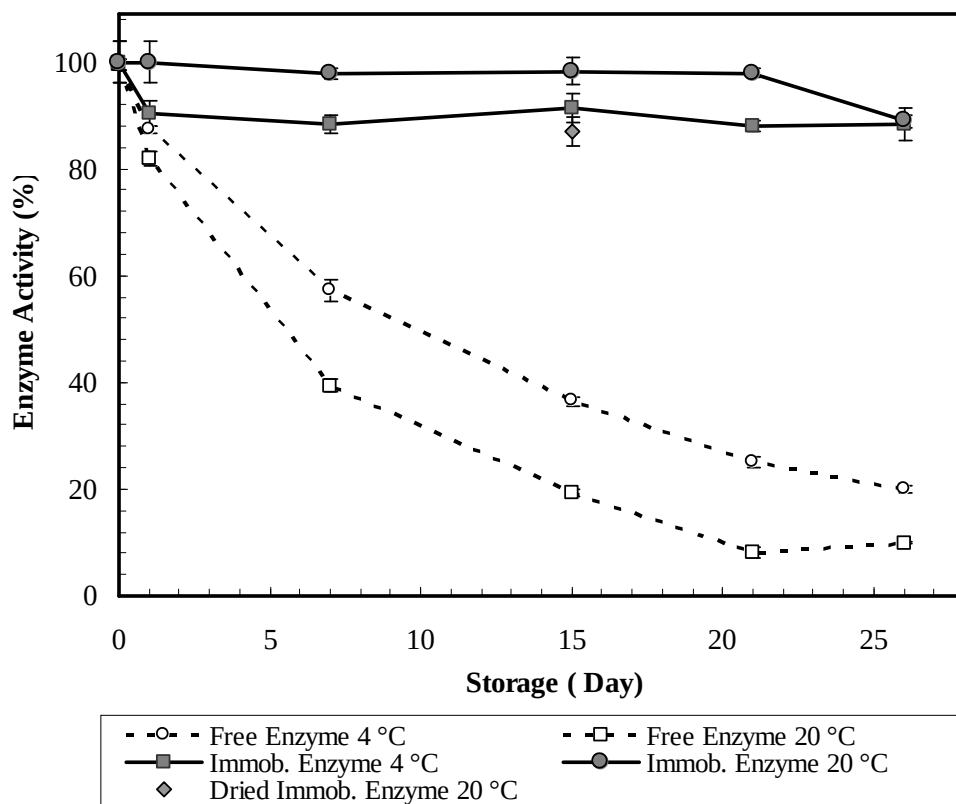
Thermal stability of the GA cross-linked PEI-lipase aggregates from Novozyme RML lipase were shown in Figure 7. The soluble lipase gradually decreased its activity upon increasing temperatures above 35°C and lost 86% at 65°C while the cross-linked aggregates kept full activity up to 55°C and only lost 18% at 65°C. Thus, compared to free lipase, thermal stability of the aggregates in a solution increased substantially.



**Figure 7:** Thermal stabilities soluble and GA cross-linked PEI-lipase aggregates (*Rhizomucor miehei* from Novozyme ) suspended in 50 mM phosphate buffer at pH 7 in a constant-temperature water bath between 35-75 °C. Lipase activities were measured after the incubation for two hours, and the experiments were carried out three parallels at each temperature.

In another set of experiments, the storage stability was evaluated (Figure 8). The soluble RM lipase and the cross-linked aggregates resuspended in phosphate buffer were kept at various conditions for nearly a month. The free enzyme in buffer either refrigerated or stored at room temperature lost nearly 80 or 90 % of its initial activity within three weeks while the aggregates retained nearly full activity. The aggregates had an estimated half-life of 220 at 4°C or 250 days 20°C, which was at least 20-times more stable than that of the soluble enzyme (Table 2). It is interesting to note that the

aggregates stored at 20°C was slightly more stable than that of 4°C while the opposite was observed with the soluble enzyme. Furthermore, the dried form of the aggregates stored at room temperature retained nearly as much activity as the one stored in a buffer. In conclusion, similar to increase in thermal stability, it is clear that the carrier-free preparation approach greatly improved the stability for storage. It was generally observed that PEI is good at preserving native structure at ambient temperatures due to depressing protein denaturation and oxidation during long-term storage (44-46).



**Figure 8:** Storage stabilities for free and GA cross-linked PEI-lipase aggregates (*Rhizomucor miehei* from Novozyme) suspended in 0.1 M phosphate buffer (at pH 7) incubated at 4 or 20 °C for extended period of time. The dried form of immobilized lipase was stored at room temperature for only two weeks. Lipase activities were measured from the aliquots taken from the samples during incubation, and the experiments were carried out three parallels at each temperature.

**Table 2:** Comparison of storage stabilities of free and immobilized lipase from *Rhizomucor miehei* from Novozyme.

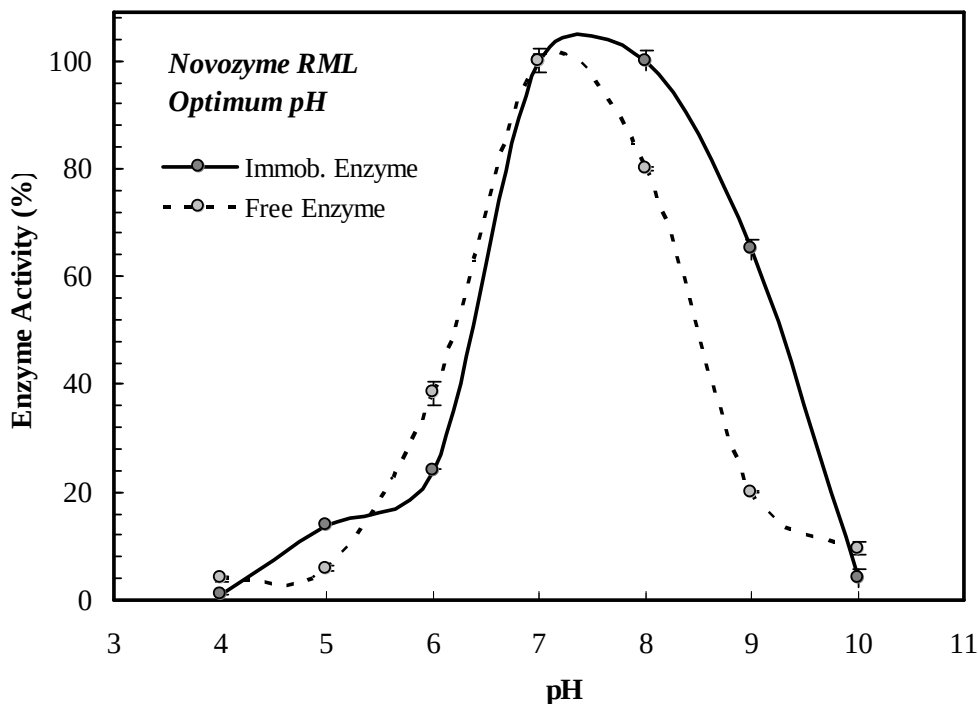
Temperature (°C)	Free Lipase (RML)		Cross-linked Aggregate	PEI-Lipase
	$k_d$ ( $h^{-1}$ )	half life (h)	$k_d$ ( $h^{-1}$ )	half life (h)
4	0.0633	11	0.0028	248
20	0.0967	7	0.0032	217

### pH

The effects of pH on the activities of the free and cross-linked PEI-lipase aggregates were presented in Figure 9. The soluble enzyme showed a narrow optimum at about pH 7 while pH optimum of the aggregates extended one pH unit toward the alkaline range. A change in the optimum pH depends on the charge of the

support and/or enzyme. PEI-enzyme aggregation involves bridging between the negatively charged enzyme and the PEI. Thus, the optimum pH of enzyme is likely to change. It was reported that the pH optima of lipase (47) adsorbed on methacrylate membranes modified with PEI extended towards an alkaline range.

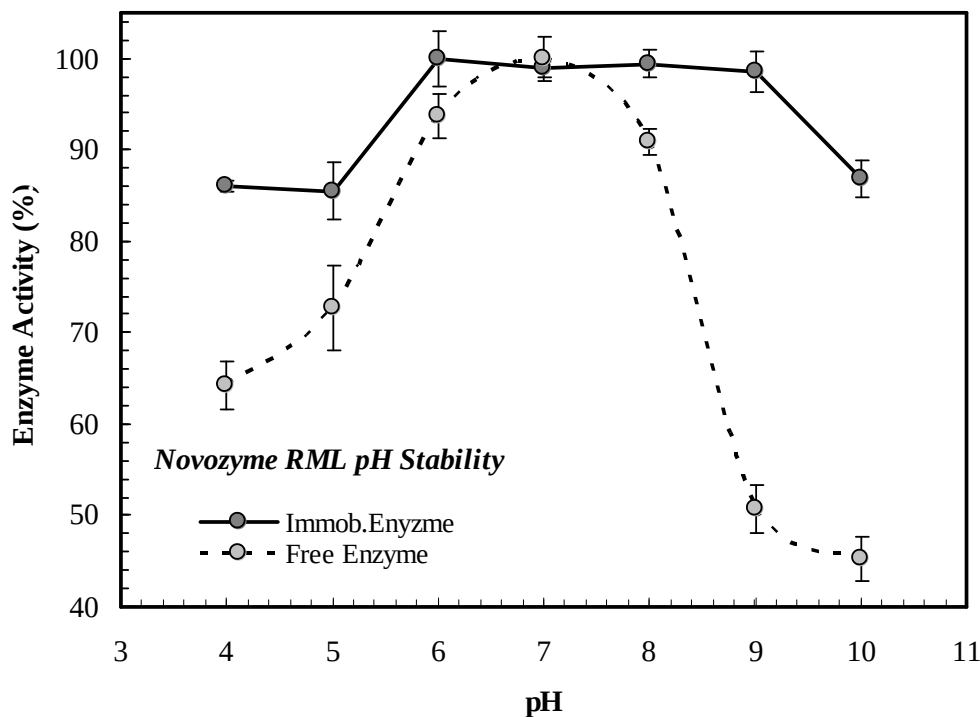




**Figure 9:** The effect of pH on the activities of free and GA cross-linked PEI-lipase aggregates (*Rhizomucor miehei* from Novozyme) suspended in the corresponding buffers of 0.1 M.

The ability to withstand change in the medium pH is an important indication of enzyme stability especially for the immobilization technique initiated with favorable charge interaction. If the bonds between the enzyme and PEI are not sufficiently strong and/or the GA cross-linking was unable to tie the aggregates, then they may disassociate thereby show little or no resistance against the weakening effect of the medium pH. As presented in Figure 10, free lipase kept full activity at its optimum pH 7 and lost nearly 10% of its initial activity at pH 6 or 8. It seems soluble

enzyme was more resistant towards the acidic range where it nearly lost 30% of its activity at pH 5 but lost 50% at pH 9. However, the cross-linked aggregates showed no loss within pH 6 and 9. Also, the aggregates retained complete activity at the pH 9 yet free enzyme lost 50% of its initial activity. Similar to our observations, Cao et al (8) reported that PEI-cross-linked lipase from *Candida rugose* on the surface of magnetic microspheres showed increased alkaline pH and thermal stabilities.



**Figure 10:** pH stabilities of free and GA cross-linked PEI-lipase aggregates (*Rhizomucor miehei* from Novozyme) suspended corresponding buffers. The enzymes were incubated 0.1 M acetate and phosphate buffers at 25 °C for 18 h.

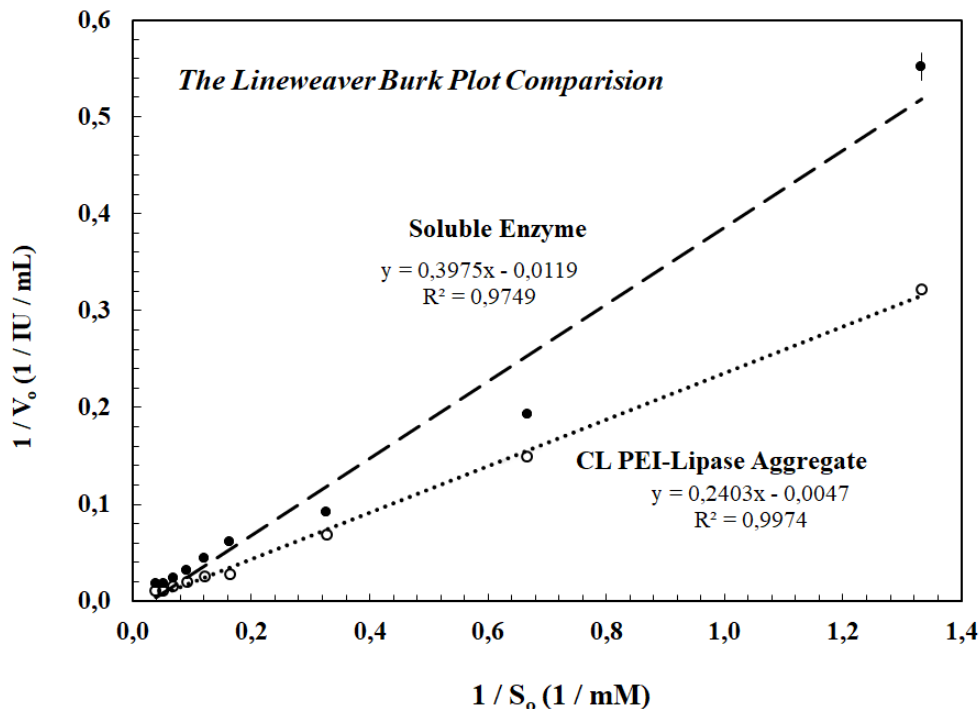
It is important to note that not only PEI interaction but also GA cross-linking of PEI-enzyme aggregate greatly affected overall stability of the immobilized aggregates against pH and heat/duration, indicating minimal distortion of protein structure while retaining catalytic activity (42).

#### **K<sub>m</sub> and V<sub>max</sub>**

In the formation of the macroscopic aggregates between the PEI and the enzyme, a reduction in the enzyme activity due to external and internal diffusion limitation (of substrate/products) imposed by the complexation may be expected. For enzyme immobilization procedures involving intensification of catalyst, it is very much common to observe substantial reduction in

$V_{max_{app}}$  while increase in  $K_{m_{app}}$  due to chemical modification of enzyme as well as steric hindrance (48). Our preparation of PEI-Lipase aggregates containing over 98% enzyme protein can be reversibly precipitated or dispersed in solution yet they display the reaction rates as good as free enzyme with improved stabilities.

Figure 11 presents comparison of the reaction rates for soluble and the aggregated RM lipases on *p*-NPP substrate concentrations within the range of 0.512-25 mM. The apparent kinetic constants were determined from the data linearized with Lineweaver-Burk plots for approximation of the Michaelis constant ( $K_m$ ) and  $V_{max}$  (48), which are presented in Table 3.



**Figure 11:** The effect of *p*-nitrophenyl propionate (*p*-NPP) substrate concentrations on the reaction rates for soluble and GA cross-linked PEI-lipase aggregates (*Rhizomucor miehei* from Novozyme) suspended corresponding buffers. Both reactions were carried out in a water bath without shaking. The apparent kinetic constants were determined from the data linearized with Lineweaver-Burk plots for approximation of the Michaelis constant ( $K_m$ ) and  $V_{max}$ .

**Table 3:** Apparent kinetic constants for free and immobilized *Rhizomucor miehei* lipase from Novozyme.

Parameters <sup>(*)</sup>	Soluble Lipase RML	Cross-linked PEI-Lipase Aggregate
$V_{max}$ (IU/mL)	84	172
$K_m$ (mM)	33	42

(\*) Based on hydrolysis of *p*-nitrophenyl propionate substrate in the range 0.512 - 25 mM in a water bath without shaking.

The approximation derived from Lineweaver-Burk linearized plots in Fig 11.

Compared with the soluble enzyme, the  $V_{max_{app}}$  for PEI-lipase aggregates increased two-fold while the  $K_{m_{app}}$  increased 25%. Representing the highest possible rate when the enzyme is saturated with a substrate,  $V_{max_{app}}$  reveals the intrinsic characteristics of the immobilized enzyme. It was found that the activation step of the lipases (RML or TLL) requires large concerted motions involving the displacement of the helical lid which begins with electrostatic interaction between the lid surface and the adjacent loop resulting in a rollover and the exposure of hydrophobic residues in the active site (49–52). A slightly hydrophobic backbone of the PEI (44) may have stabilized active conformation. Parallel to our observation, nearly two-fold (180%)

increase in relative lipase activity in oppositely charged two polyelectrolyte complex was reported (53). In contrast, compared with free enzyme, 25% increase in  $K_m$  and 40% decrease in  $V_{max}$  was also reported with PEI-cross-linked lipase from *Candida rugosa* on the surface of magnetic microspheres (8). In fact, the aqueous phase which perfectly solubilizes the lipase but energetically puts the enzyme in a difficult state in terms of energy need for conformational change required for lid opening prior to the catalysis (51,52). An increase in  $K_{m_{app}}$  simply means that it takes a little more substrate to saturate the enzyme, which may usually suggest an involvement of diffusion limitations but it may also reflect a weaker bond with the substrate

thus a reflection of the partially open lid of the active site. Thus, better performance of PEI-lipase complex under the unfavorable conditions for reaching the substrate may suggest that the association of lipase with PEI may have produced a favorable interface assisting for conformational change for lipase activation (dislocation of helical lid) through electrostatic interactions resulting in higher rates of catalysis. It is important to note that our assertions about the reaction rates of the PEI-lipase aggregates as well as the values for the kinetic constants were based on *p*-nitrophenyl propionate substrate, which is soluble in water. The characteristics and performance of the immobilized enzyme may vary in various applications with other substrates or in two-phase systems. Nevertheless the present carrier-free lipase aggregates with fully dispersible micron sized particles in aqueous solution as well as organic solvents showing great potential in variety of biocatalytic applications in microemulsion, suspension, dispersion type systems (7,22).

In conclusion, the study presents the preparation and characterization of a carrier-free PEI-enzyme aggregate with several commercially important lipases. The approach relies on PEI as a single aggregating agent. Considering PEI to enzyme mass ratio of 1/20-1/40 for optimal complexation, the PEI-lipase aggregates was mainly composed of enzyme mass with only a few percent of PEI. The cross-linked aggregates at low GA sufficiently provided stability without affecting the aggregate activity. As a simple and inexpensive carrier-free immobilized enzyme, the approach brings about not only enhancing stability and ease of separation but also concentrating the valuable catalyst in volumes or on surfaces without much diffusion resistance.

## ACKNOWLEDGMENTS

This work was supported in part by a grant from the Scientific and Technological Research Council of Turkey (Grant No: 107M487) and the Scientific Research Fund of Yuzuncu Yil University. Appreciation is given to Mehmet Bora Kaydan and Nahit Aktaş for their valuable contributions.

## REFERENCES

- Nelson JM, Griffin EG. Adsorption of invertase. *J Am Chem Soc.* 1916;38(5):1109-15.
- Matijošytė I, Arends IWCE, de Vries S, Sheldon RA. Preparation and use of cross-linked enzyme aggregates (CLEAs) of laccases. *J Mol Catal B Enzym.* 2010;62(2):142-8.
- Cao L, Langen L Van, Sheldon RA. Immobilised enzymes: carrier-bound or carrier-free? *Curr Opin Biotechnol.* 2003;14(4):387-94.
- Liu T, Rao Y, Zhou W, Zhuang W, Ge L, Lin R, et al. Improved adenylate cyclase activity via affinity immobilization onto co-modified GO with bio-inspired adhesive and PEI. *Colloids Surfaces B Biointerfaces.* 2021;205(30):111888.
- Santos JCS dos, Barbosa O, Ortiz C, Berenguer-Murcia A, Rodrigues RC, Fernandez-Lafuente R. Importance of the support properties for immobilization or purification of enzymes. *ChemCatChem.* 2015;7(16):2413-32.
- Misson M, Jin B, Chen B, Zhang H. Enhancing enzyme stability and metabolic functional ability of  $\beta$ -galactosidase through functionalized polymer nanofiber immobilization. *Bioprocess Biosyst Eng.* 2015;38(10):1915-23.
- Cipolatti EP, Manoel EA, Fernandez-Lafuente R, Freire DMG. Support engineering: relation between development of new supports for immobilization of lipases and their applications. *Biotechnol Res Innov.* 2017;1(1):26-34.
- Cao YP, Xia YP, Gu XF, Han L, Chen Q, Zhi GY, et al. PEI-crosslinked lipase on the surface of magnetic microspheres and its characteristics. *Colloids Surfaces B Biointerfaces.* 2020;189:110874.
- Cao L. Immobilised enzymes: science or art? *Curr Opin Chem Biol.* 2005;9(2):217-26.
- Cheng HN, Gross RA. Polymer biocatalysis and biomaterials: Current trends and developments. In: Cheng HN, Gross RA, editors. *Polymer Biocatalysis and Biomaterials II.* Washington, DC: ACS Symposium Series; American Chemical Society; 2008. p. 1-20.
- Roessler U, Nahálka J, Nidetzky B. Carrier-free immobilized enzymes for biocatalysis. *Biotechnol Lett.* 2010;32(3):341-50.
- Würtz Christensen M, Andersen L, Husum TL, Kirk O. Industrial lipase immobilization. *Eur J lipid Sci Technol.* 2003;105(6):318-321.
- Parthasarathy R V, Martin CR. Synthesis of polymeric microcapsule arrays and their use for enzyme immobilization. *Nature.* 1994;369(6478):298-301.
- Cao L, van Rantwijk F, Sheldon RA. Cross-linked enzyme aggregates: a simple and effective method for the immobilization of penicillin acylase. *Org Lett.* 2000;2(10):1361-4.
- Lopez-Serrano P, Cao L, Van Rantwijk F, Sheldon R. Cross-linked enzyme aggregates with enhanced activity: application to lipases. *Biotechnol Lett.* 2002;24(16):1379-1383.
- Velasco-Lozano S, López-Gallego F, Vázquez-Duhalt R, Mateos-Díaz JC, Guisán JM, Favela-Torres E. Carrier-free immobilization of lipase from *Candida*

- rugosa with polyethyleneimines by carboxyl-activated cross-linking. *Biomacromolecules*. 2014;15(5):1896-903.
17. He P, Greenway G, Haswell SJ. Development of a monolith based immobilized lipase micro-reactor for biocatalytic reactions in a biphasic mobile system. *Process Biochem*. 2010;45(4):593-7.
18. Mateo C, Palomo JM, van Langen LM, van Rantwijk F, Sheldon RA. A new, mild cross-linking methodology to prepare cross-linked enzyme aggregates. *Biotechnol Bioeng*. 2004;86(3):273-6.
19. Pchelintsev N a., Youshko MI, Švedas VK. Quantitative characteristic of the catalytic properties and microstructure of cross-linked enzyme aggregates of penicillin acylase. *J Mol Catal B Enzym*. 2009;56(4):202-7.
20. Guerrero C, Vera C, Araya E, Conejeros R, Illanes A. Repeated-batch operation for the synthesis of lactulose with  $\beta$ -galactosidase immobilized by aggregation and crosslinking. *Bioresour Technol*. 2015;190:122-31.
21. Albayrak N, Yang ST. Immobilization of  $\beta$ -galactosidase on fibrous matrix by polyethyleneimine for production of galacto-oligosaccharides from lactose. *Biotechnol Prog*. 2002;18(2):240-251.
22. Taleb MA, Gomaa SK, Wahba MI, Zaki RA, El-Fiky AF, El-Refai HA, et al. Bioscouring of wool fibres using immobilized thermophilic lipase. *Int J Biol Macromol*. 2022;194:800-10.
23. Schmidt M, Bornscheuer UT. High-throughput assays for lipases and esterases. *Biomol Eng*. 2005;22(1-3):51-6.
24. Schmidt-Dannert C, Sztajer H. Screening, purification and properties of a thermophilic lipase from *Bacillus thermocatenuatus*. *Biochem Biophys Acta*. 1994;1214:43-53.
25. Bayramoglu G, Karagoz B, Altintas B, Arica MY, Bicak N. Poly(styrene-divinylbenzene) beads surface functionalized with di-block polymer grafting and multimodal ligand attachment: performance of reversibly immobilized lipase in ester synthesis. *Bioprocess Biosyst Eng*. 2011;34(6):735-46.
26. Prlainović NZ, Knežević-Jugović ZD, Mijin DZ, Bezbradica DI. Immobilization of lipase from *Candida rugosa* on Sepabeads®: the effect of lipase oxidation by periodates. *Bioprocess Biosyst Eng*. 2011;34(7):803-10.
27. Gong MD, Pei XJ, Duan GX, Zhi GY, Liu ZQ, Zhang DH. Molecular cages encapsulating lipase and the effect of cage hydrophobicity and cage size. *Mater Des*. 2022;220:110865.
28. Remonato D, Miotti RH, Monti R, Bassan JC, de Paula AV. Applications of immobilized lipases in enzymatic reactors: A review. *Process Biochem*. 2022;114:1-20.
29. Güleç HA, Gürdaş S, Albayrak N, Mutlu M. Immobilization of *Aspergillus oryzae* beta-galactosidase on low-pressure plasma-modified cellulose acetate membrane using polyethyleneimine for production of galactooligosaccharide. *Biotechnol Bioprocess Eng*. 2010;15(6):1006-1015.
30. Güleç HA. Immobilization of  $\beta$ -galactosidase from *Kluyveromyces lactis* onto polymeric membrane surfaces: effect of surface characteristics. *Colloids Surf B Biointerfaces*. 2013;104:83-90.
31. Ondul E, Dizge N, Albayrak N. Immobilization of *Candida antarctica* A and *Thermomyces lanuginosus* lipases on cotton terry cloth fibrils using polyethyleneimine. *Colloids Surfaces B Biointerfaces*. 2012;95(0):109-14.
32. Bi Y, Zhou H, Jia H, Wei P. A flow-through enzymatic microreactor immobilizing lipase based on layer-by-layer method for biosynthetic process: Catalyzing the transesterification of soybean oil for fatty acid methyl ester production. *Process Biochem*. 2017;54:73-80.
33. Özarslaner E, Albayrak N. Stability of p-nitrophenyl propionate substrate for spectrophotometric measurement of lipase activity. *GIDA*. 2013;38(3):143-9.
34. Bradford M. A rapid and sensitive method for the quantitation of microgram quantities of protein utilizing the principle of protein-dye binding. *Anal Biochem*. 1976;72(1-2):248-54.
35. Borkovec M, Koper GJM. Proton binding characteristics of branched polyelectrolytes. *Macromolecules*. 1997;30(7):2151-8.
36. Bjurlin M, Bloomer S, Haas MJ. Composition and activity of commercial triacylglycerol acylhydrolase preparations. *J Am Oil Chem Soc*. 2001;78(2):153-60.
37. de Fuentes IE, Viseras CA, Ubiali D, Terreni M, Alcántara AR. Different phyllosilicates as supports for lipase immobilisation. *J Mol Catal B Enzym*. 2001;11(4-6):657-663.
38. Lindquist GM, Stratton RA. The role of polyelectrolyte charge density and molecular weight on the adsorption and flocculation of colloidal silica with polyethylenimine. *J Colloid Interface Sci*. 1976;55(1):45-59.
39. Llerena-Suster CR, Briand LE, Morcelle SR. Analytical characterization and purification of a commercial extract of enzymes: A case study. *Colloids Surfaces B Biointerfaces*. 2014;121:11-20.
40. Hernáiz MJ, Rua M, Celda B, Medina P, Sinisterra J V, Sánchez-Montero JM. Contribution to the study of the alteration of lipase activity of *Candida rugosa* by ions and buffers. *Appl Biochem Biotechnol*. 1994;44(3):213-29.

41. Guauque Torres MDP, Foresti ML, Ferreira ML. Cross-linked enzyme aggregates (CLEAs) of selected lipases: a procedure for the proper calculation of their recovered activity. *AMB Express*. 2013;3(1):25.
42. Migneault I, Dartiguenave C, Bertrand MJ, Waldron KC. Glutaraldehyde: behavior in aqueous solution, reaction with proteins, and application to enzyme crosslinking. *Biotechniques*. 2004;37(5):790-802.
43. Pan J, Kong X-D, Li C-X, Ye Q, Xu J-H, Imanaka T. Crosslinking of enzyme coaggregate with polyethyleneimine: A simple and promising method for preparing stable biocatalyst of *Serratia marcescens* lipase. *J Mol Catal B Enzym*. 2011;68(3-4):256-61.
44. Andersson MM, Hatti-Kaul R. Protein stabilising effect of polyethyleneimine. *J Biotechnol*. 1999;72(1-2):21-31.
45. Schwinté P, Ball V, Szalontai B, Haikel Y, Voegel J-C, Schaaf P. Secondary structure of proteins adsorbed onto or embedded in polyelectrolyte multilayers. *Biomacromolecules*. 2002;3(6):1135-43.
46. Herrgård S, Gibas CJ, Subramaniam S. Role of an electrostatic network of residues in the enzymatic action of the *Rhizomucor miehei* lipase family. *Biochemistry*. 2000;39(11):2921-30.
47. Bayramoglu G, Kaya B, Yakup Arica M. Immobilization of *Candida rugosa* lipase onto spacer-arm attached poly(GMA-HEMA-EGDMA) microspheres. *Food Chem*. 2005;92(2):261-8.
48. Hormozi Jangi SR, Akhond M. Introducing a covalent thiol-based protected immobilized acetylcholinesterase with enhanced enzymatic performances for biosynthesis of esters. *Process Biochem*. 2022;120:138-55.
49. Brzozowski AM, Savage H, Verma CS, Turkenburg JP, Lawson DM, Svendsen A, et al. Structural origins of the interfacial activation in *Thermomyces (Humicola) lanuginosa* lipase. *Biochemistry*. 2000;39(49):15071-82.
50. Derewenda Z, Derewenda U, Dodson G. The crystal and molecular structure of the *Rhizomucor miehei* triacylglyceride lipase at 1.9 Å resolution. *J Mol Biol*. 1992;227(3):818-39.
51. Peters GH, Olsen OH, Svendsen a, Wade RC. Theoretical investigation of the dynamics of the active site lid in *Rhizomucor miehei* lipase. *Biophys J*. 1996;71(1):119-29.
52. Rehm S, Trodler P, Pleiss J. Solvent-induced lid opening in lipases: a molecular dynamics study. *Protein Sci*. 2010;19(11):2122-30.
53. Zaitsev SY, Gorokhova I V, Kashtigo T V, Zintchenko A, Dautzenberg H. General approach for lipases immobilization in polyelectrolyte complexes. *Colloids Surfaces A Physicochem Eng Asp*. 2003;221(1-3):209-20.



## Classification of Zinc-Coated Parts in Accordance with their Brightness Degree using Deep Learning Techniques

Ramazan Katırcı<sup>1\*</sup> , Hasan Metehan Akgün<sup>2</sup> , Bilal Tekin<sup>3</sup> ,  
Osman Gökhan Kömürkaya<sup>3</sup> , Metin Zontul<sup>4</sup> , and Oğuz Kaynar<sup>5</sup> .

<sup>1</sup> Metallurgical and Materials Engineering, Sivas University of Science and Technology, Sivas, Turkey

<sup>2</sup> Aircraft Technology, Sivas University of Science and Technology, Sivas, Turkey

<sup>3</sup> Computer Engineering, Sivas University of Science and Technology, Sivas, Turkey

<sup>4</sup> Computer Engineering, Istanbul Ayvansaray University, Istanbul, Turkey

<sup>5</sup> Management Information Systems, Sivas Cumhuriyet University, Sivas, Turkey

**Abstract:** A novel technique was suggested to measure the brightness of the coated parts. The algorithm of Mask RCNN was used to detect the relevant region on the whole image. The pixels of black lines, which are associated with the brightness of the coating and reflected from the foreground, were counted using image processing technique. These pixels were used as the output in the machine learning training to classify the coated parts. The output was binarized to classify the coated plates as "Pass" and "Fail". It was found that the RF model was the best model. The scores of its accuracy, F1, precision, and recall were established to be 0.97, 0.97, 1, and 0.94, respectively. The overlap scores of Mask RCNN were found to be in the range of 0.92-0.97, which proved that Mask RCNN algorithm detected the concerned region with high precision and accuracy.

**Keywords:** Mask RCNN, Deep learning, Machine learning, Zinc electroplating, Brightness measurement, Image processing, Surface detection.

**Submitted:** August 05, 2022. **Accepted:** October 13, 2022.

**Cite this:** Katırcı R, Akgün HM, Tekin B, Kömürkaya OG, Zontul M, Kaynar O. Classification of Zinc-Coated Parts in Accordance with their Brightness Degree using Deep Learning Techniques. JOTCSB. 2022;5(2):145-56.

\*Corresponding author. E-mail: [ramazankatirci@sivas.edu.tr](mailto:ramazankatirci@sivas.edu.tr).

### INTRODUCTION

Engineering components are widely fabricated to meet the expectations in the industrial applications in the world. While these components are produced, some technical requirements such as corrosion, safety, and service lifetime should be considered (1). The surface treatment methods are one of the most important techniques used to enhance the performance and properties of the materials (2). Coating, chemical treatment, painting and anodic oxidation are some of the techniques used widely in the world (3). Coating techniques can be classified as two groups; dry technique and wet technique. As an example to dry technique, thermal spraying, and sputtering methods can be given (4,5). As for the wet technique, electroplating and sol-gel method can be presented (6,7). The electroplating method has many advantages such as running in atmospheric conditions, and not requiring high pressure and temperature (8). The electroplating parameters such as additives, pH, temperature and current

density, influence the coating properties and performance. Especially, organic additives added to the electroplating bath enhance the appearance, throwing power, and covering power of the coating (9). Electroplating is applied for two purposes, decorative and industrial application. While in decorative purpose, the brightness, of the coating (its appearance) is significant, in industrial purpose, hardness, corrosion, and wear resistance are crucial. In order to acquire bright coating, some special organic additives are added to the zinc, copper, nickel, and chromium electroplating bath. These organic additives decrease the crystal size and provide the brightness to the coating (10). Zinc electroplating is commonly implemented for corrosion protection (11).

Zinc electroplating processes are generally applied with three different techniques. These techniques are called acidic, alkaline, and cyanide zinc electroplating processes. Zinc coating acquired from the acidic zinc electroplating bath is very significant because it provides very bright and



flexible coating (12). To measure the brightness of the coating, a glossmeter instrument is generally used. To acquire the brightness of the entire coated surface using glossmeter, many measurements should be taken. It is however very easy to distinguish between a bright and matte surface by human eye. We think that the artificial intelligence methods are promising methods to measure the brightness of the coating using camera-based system. Katirci et al. used the artificial intelligence method to classify the chromium coating in accordance with the appearance of the coating (8). Also, Wang et al. implemented the artificial intelligent method to identify the particle size and shape of granular materials (13).

Many artificial methods are used in engineering applications (14-17). These methods can be divided into two categories, machine learning and deep learning. In recent years, deep learning techniques have been developing at a dizzying speed. Convolutional neural network (CNN) methods such as VGG (18), ResNet (19), Inception (20) and Xception (21) are the most popular methods. Mask RCNN is a technique used for object segmentation. It uses the backbone of ResNet 101. This method detects objects and generates high-quality segmentation mask for each instance (22).

In the industry, many objects next to the coated part may have an interference effect to detect the concerned object. Therefore, Mask RCNN method can be used to extract the irrelevant data from the sample (8). The image processing technique is used to extract the features from the image data.

Various image processing techniques such as thresholding and binarization can be used for this purpose (23).

In our study, to simulate the electroplating bath in the industrial conditions, Hull-cell method developed by R.O.Hull in 1939 was used (24). Hull-cell panels were coated in the acidic zinc electroplating baths prepared using the different composition. Mask RCNN and image processing techniques were used together to extract the relevant data from the images taken from the Hull-cell panels. Machine learning and deep learning technique, including gaussian process (GP), random forest (RF), support vector classifier (SVR), XGBoost (XGB), multilayer perceptron (MLP) were used to classify the appearance (brightness) of coated part in accordance with the zinc electroplating bath. Image processing techniques were used to determine the degree of brightness of the coating by counting the pixels on the black lines.

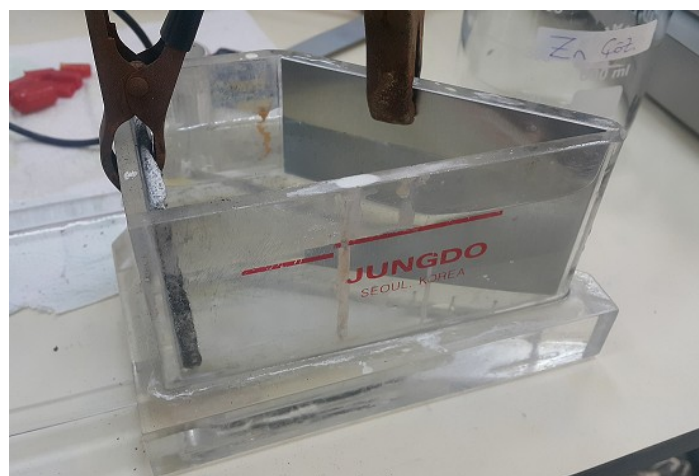
## MATERIALS AND METHODS

The acidic zinc electroplating was carried out using a Thurlby 30V1A-model DC model direct-current generator. The organic additives were added to the acidic zinc electroplating bath at the values in Table 1. The 74 experiments were designed in different concentrations of the additives. The basic zinc electroplating bath consists of 80 g/L  $ZnCl_2$  and 200 g/L  $NH_4Cl$  compounds in water. The overall experimental design was presented in Table S1 (in supplementary material).

**Table 1.** The additive ranges used in the acidic zinc electroplating bath.

Abbreviations	Chemical names	LEVELS						
		1	2	3	4	5	6	7
PA (mL/L)	Propargyl alcohol	5	10	20				
NP10 (mL/L)	Nonylphenol ethoxylate	0.25	1	2	2.75	5.25	10	10.25
BA (g/L)	Benzal acetone	0.2	0.5	1	5			
NA (g/L)	Nicotinic acid	0.2	0.5	1				
SB (g/L)	Sodium benzoate	1	2	4				
EHS (mL/L)	Ethylhexyl sulfate	10	15	25	30	40		
OCB (mL/L)	2-Chlorobenzaldehyde	2	3	5				
TAMOL (g/L)	Naphthalene sulfonate formaldehyde condensate, sodium salt	1	5	10				

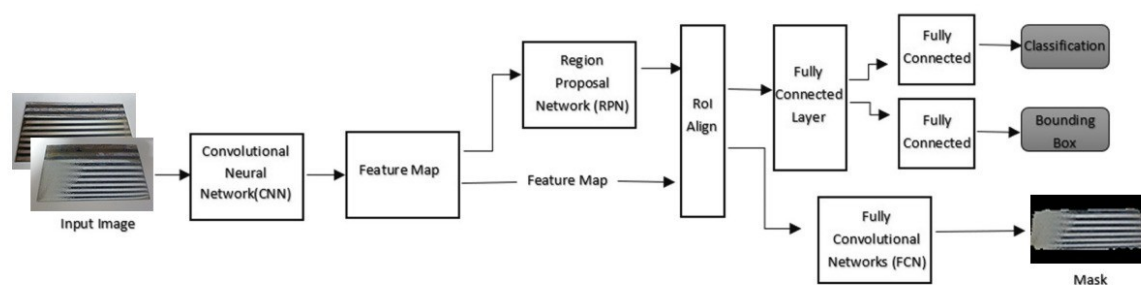
The Hull-cell equipment where the panels were coated using the bath compositions in Table S1 is presented in Figure 1.



**Figure 1:** Hull-cell set-up used in the zinc electroplating.

Mask RCNN algorithm, which uses the backbone of ResNet 101, was used to extract the relevant data from the images. It composes of three steps; 1) extracting the feature map from the input images, 2) sending it to the Region Proposal Network (RPN) for creating region recommendations from the feature maps, 3) transferring the proposed regions

to the fully connected layer for target localization, and obtaining the expected outputs. The architecture of Mask RCNN is presented in Figure 2. Mask RCNN algorithm was downloaded from the github repository: [https://github.com/matterport/Mask\\_RCNN](https://github.com/matterport/Mask_RCNN) and the codes were adapted to our study. All networks were trained in 50 epochs.



**Figure 2:** The architecture of Mask RCNN.

Machine learning algorithms and deep learning technique were performed to classify the quality of the plates depending on their surface brightness. The surface brightness was acquired counting the pixels between 0 and 75 on the black lines in grayscale image (0-255). The image processing technique was used to count the pixels. The pixel count was performed on the extracted data from the image. The number of pixels on the black lines reflected from the foreground were defined as the output for zinc electroplating bath. To classify the quality of the plates according to their brightness, the threshold was specified. The plates above this threshold were coded as 1 (Pass). Those below this threshold were coded as 0 (Fail). OpenCV library was used to count the black pixels. All codings were carried out using python language. Gaussian process (GP), random forest (RF), support vector classifier (SVC), XGBoost (XGB) and multilayer perceptron (MLP) algorithms were used to train the bath composition against the brightness of the coating. The hyperparameters of the models were optimized using gridsearch method. The outputs are presented under the folder of

“HyperparameterOpt” in the supplementary material.

#### **Gaussian Process (GP)**

GP is a supervised learning that can be used for regression and classification based on the Gaussian probability distribution. Gaussian probability distribution functions show the distribution of random variables. GP calculates the probability of the outcome of the input data. And it works well with small datasets, high accuracy rate is achieved (25).

#### **Random Forest (RF)**

RF is a supervised learning method consisting of decision trees designed by Breiman. The decision trees were generated by selecting random samples from the train dataset. When making a prediction with these trees, the predictions of all trees are used. The decision is taken by majority vote. The prediction taking the most votes is selected. RF is used for regression and classification. It has wide usage areas such as ecology, genetics, bioinformatics and medicine (26).

**Support Vector Classifier (SVC)**

SVM is a supervised learning method used for classification, regression, and outlier detection. SVM tries to find the optimal hyperplane that divides the data into two parts. This hyperplane keeps the distance between the two parts at the maximum level. It maximizes the distance between the nearest points in different segments. If the data is not linear and is not divided into two parts, it can be used in nonlinear data by increasing the plane size with the help of kernel functions (27).

**XGBoost (XGB)**

XGBoost is an optimized supervised machine learning algorithm based on the Gradient Boosting algorithm. It became popular with the article written by Tianqi Chen and Carlos Guestrin and its usage has increased. Since it is based on the Gradient Boosting algorithm, it creates weak learning models and combines them into advanced models. With the help of the aim function, it prevents overfitting and increases performance. XGBoost is an ensemble learning based algorithm like RF, but newer than RF. XGBoost creates models quickly because it is suitable for parallelization. It is used for classification and regression and , it is widely used (28).

**Multilayer perception (MLP)**

MLP is a neural network model with input, output and at least one hidden neuron layer. All of these layers are fully interconnected. It was developed by Rumelhart, Hinton, and Williams (4). MLP is a supervised learning algorithm. Input data coming to the input layer is processed and transmitted to the middle layer. The output of each layer becomes the input of the next layer. This process continues until the output layer. When the data is processed, it is multiplied by the weights in the connections. As a result of the operation, the error rate is calculated. The weights are optimized. The weights are recalculated to minimize the error rate (29).

**RESULTS AND DISCUSSION**

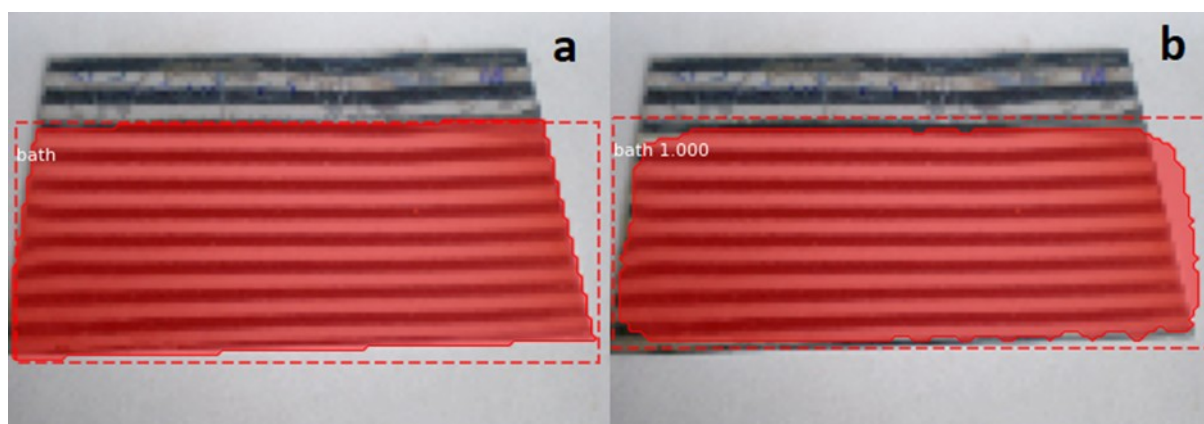
Objects close to the coated parts impair the accuracy of the model, so firstly the data concerned the coated parts should be extracted. Mask RCNN algorithm was trained to detect the concerned region on the image. The validation of the model was tracked computing its loss scores. The loss scores in Table 2 proves that the model was trained with high accuracy.

**Table 2:** The loss scores of train and validation dataset.

	Train	Validation
Loss	0.4250	0.4123
rpn_class_loss	0.0034	0.0038
rpn_bbox_loss	0.0509	0.0243
mrcnn_class_loss	0.0057	0.0061
mrcnn_bbox_loss	0.0405	0.0620
mrcnn_mask_loss	0.3245	0.3161

Figure 3a and b indicate the ground truth and predicted mask respectively. The intersection of over union (IoU) metric was used to determine the accuracy of the masked region on the coated plates. The IoU results are presented in Table 3. As seen in Table, the IoU scores vary between 0.92

and 0.97. These results prove that the reliability of the results is very high and Mask RCNN algorithm detects the region we concern on the plates accurately. Thereafter, the masked region was extracted from the image for the next step. The extracted data are presented in Figure 4.



**Figure 3:** The ground truth (a) and predicted (b) panels as examples.

**Table 3:** The intersection over union (IoU) of validation dataset.

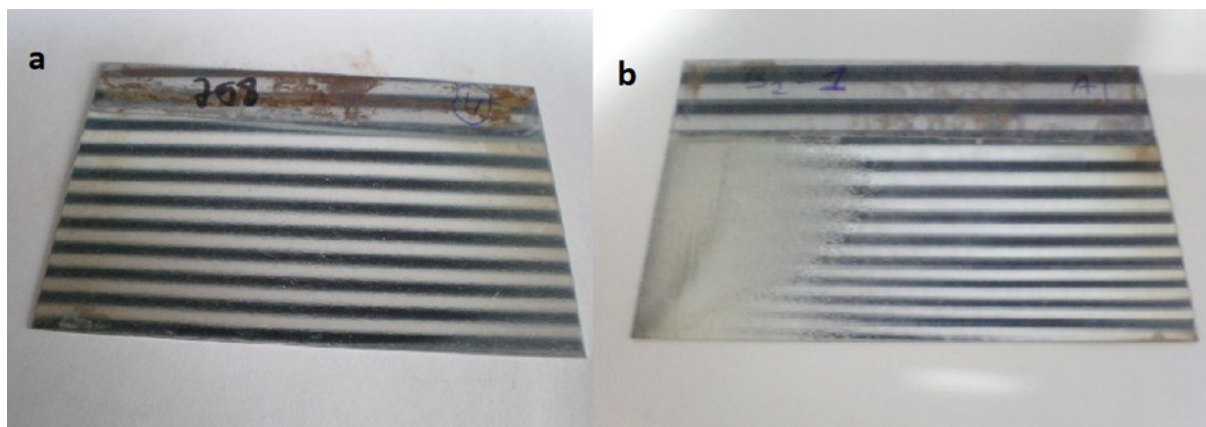
Validation Sample	Intersection Over Union (IoU)
1	0.94
2	0.97
3	0.92
4	0.93
5	0.97
6	0.94
7	0.97
8	0.93
9	0.97
10	0.97

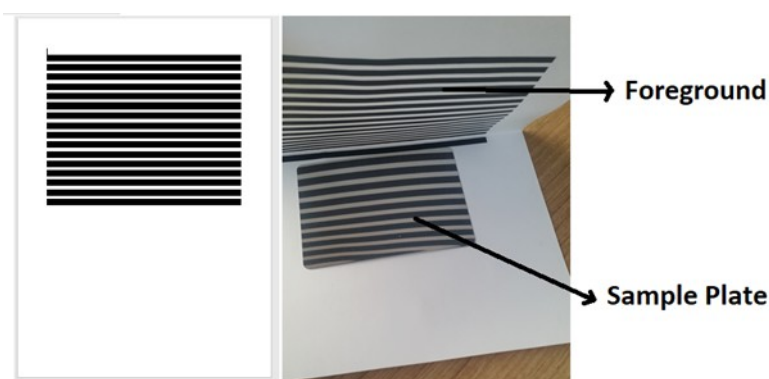
**Figure 4:** The acidic zinc coated plate samples extracted from the redundant data using Mask RCNN algorithm.

As seen in Figure 4, the algorithm has extracted the relevant region from the plate images with high accuracy. This proves that the unnecessary data can be removed from the industrially coated part images.

Figure 5 indicates the zinc coated panels. The black lines on the plates (Figure 5a) are not real, but a reflection. The number of pixels belonging to the black lines is related to the brightness of the surface. Actually, it is not possible to distinguish

bright and smooth matte surfaces from the images. Therefore, to measure the brightness of the surface from the image, the apparatus in Figure 6 was set up and taken the pictures of the coated plates. The clearer the black lines, the brighter the coated surface. The regions where the black lines are interrupted indicate that the surface of the plate is matte (Figure 5b). The black lines on the plates, which indicates the brightness degree, are affected by the bath composition (coating conditions).

**Figure 5:** Two sample panels coated with acidic zinc.

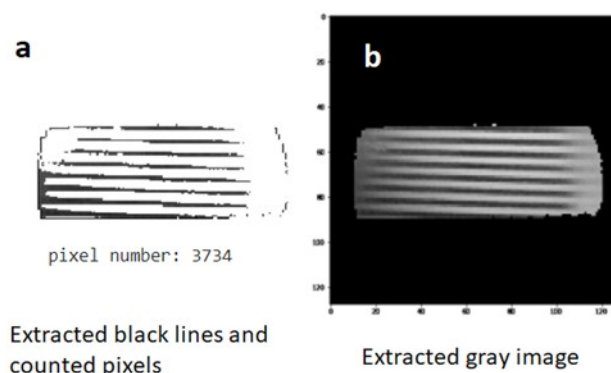


**Figure 6:** The apparatus of taking a picture.

The code and pictures used to count the black lines are presented in Figure 7. The interrupted black lines in Figure 7a depict the matte regions on the plate. When Figure 7a and b are compared, the matte and bright regions on the plates are compatible with one another. These results confirm

that the technique used in this study is an effective tool to define the brightness degree of the plates. The appearance of the plates was also checked by naked eye. It was found that the order of outputs was compatible with the ones checked by naked eye.

```
img_gray_px=np.zeros([height,width,1], dtype=np.uint8)+255
height,width,_=img_r.shape
pix_num=0
for i in range(height):
    for j in range(width):
        if (img_gray[i,j] > 0 and img_gray[i,j] < 75):
            if (i> 50 and j>20) and (i < 220):
                img_gray_px[i,j]=img_gray[i,j]
                pix_num=pix_num+1
horizontalAppendedImg = np.hstack((img_gray_px.reshape(height,width),img_gray))
cv2_imshow(horizontalAppendedImg), print("pixel number:",pix_num)
```



**Figure 7:** The code and pictures used to count the black lines.

The acidic zinc electroplating bath composition was trained in accordance with the brightness (the number of black line pixels). Four machine learning algorithms and one neural network were used to train the models. Threshold value was specified to binarize the outputs. The threshold value was chosen as 3500 pixels. The plates having the pixel number above this threshold was defined as 1 (Pass). The other panels were coded as 0 (Fail).

Accuracy, F1, precision, and recall scores were used to assess the validity of the models. Accuracy shows the ratio of accurately predicted values to the total dataset. This parameter alone is not

sufficient to judge the whole model. Hence, F1 score, precision, and recall metrics were considered. Particularly, F1 score is a very significant metric to select the best model because it indicates the harmonic mean of recall and precision values. These metrics are computed via the confusion matrix. The confusion metrics of the models are demonstrated in Table 6. Accuracy, recall, precision and F1 scores were calculated using Eq. 1-4. The abbreviations of TP, TN, FP and FN are explained in Table 4.

$$\text{Accuracy} = (\text{TP} + \text{TN}) / (\text{TP} + \text{FP} + \text{TN} + \text{FN}) \quad (\text{Eq. 1})$$



F1 score =  $2 * \text{Precision} * \text{Recall} / (\text{Precision} + \text{Recall})$  (Eq. 2)

Precision =  $\text{TP} / (\text{TP} + \text{FP})$  (Eq. 3)

Recall =  $\text{TP} / (\text{TP} + \text{FN})$  (Eq. 4)

Recall refers that what proportion of actual positives (TP) is estimated accurately. Precision depicts what proportion of estimated positives are actually 1. F1 score is the weighted average of recall and precision scores.

**Table 4:** The map of confusion matrix.

		Y-predicted	
		0	1
Y-true	0	True Negative (TN)	False Positive (FP)
	1	False Negative (FN)	True Positive (TP)

Table 5 displays the metric results of the models used. It was found that RF model is the best model to predict the quality of coated plates because its F1 score is higher than the others. The samples coded 0 are totally predicted accurately. Only two samples coded 1 are predicted wrong. The second-best model is MLP (F1 score 0.85). This model

correctly predicted 64 out of 74 samples, but 9 samples were estimated wrong (Table 6). The other models have low accuracies. The success of models (F1 score was considered) was acquired in order of RF > MLP > SVC > GP > XGBoost (Table 5).

**Table 5:** The metrics of the ML and MLP algorithms for brightness.

ML Methods	Accuracy	F1 score	Precision	Recall
MLP	0.88	0.88	0.84	0.91
SVC	0.84	0.83	0.81	0.86
GP	0.68	0.65	0.67	0.63
XGBoost	0.59	0.69	0.54	0.94
RF	0.97	0.97	1	0.94

**Table 6.** The confusion matrix results of brightness.

**MLP**

		Y-predicted	
		0	1
Y-true	0	33	6
	1	3	32

**SVC**

		Y-predicted	
		0	1
Y-true	0	32	7
	1	5	30

**GP**

		Y-predicted	
		0	1
Y-true	0	28	11
	1	13	22

**XGBoost**

		Y-predicted	
		0	1
Y-true	0	11	28
	1	2	33

**RF**

		Y-predicted	
		0	1
Y-true	0	39	0
	1	2	33

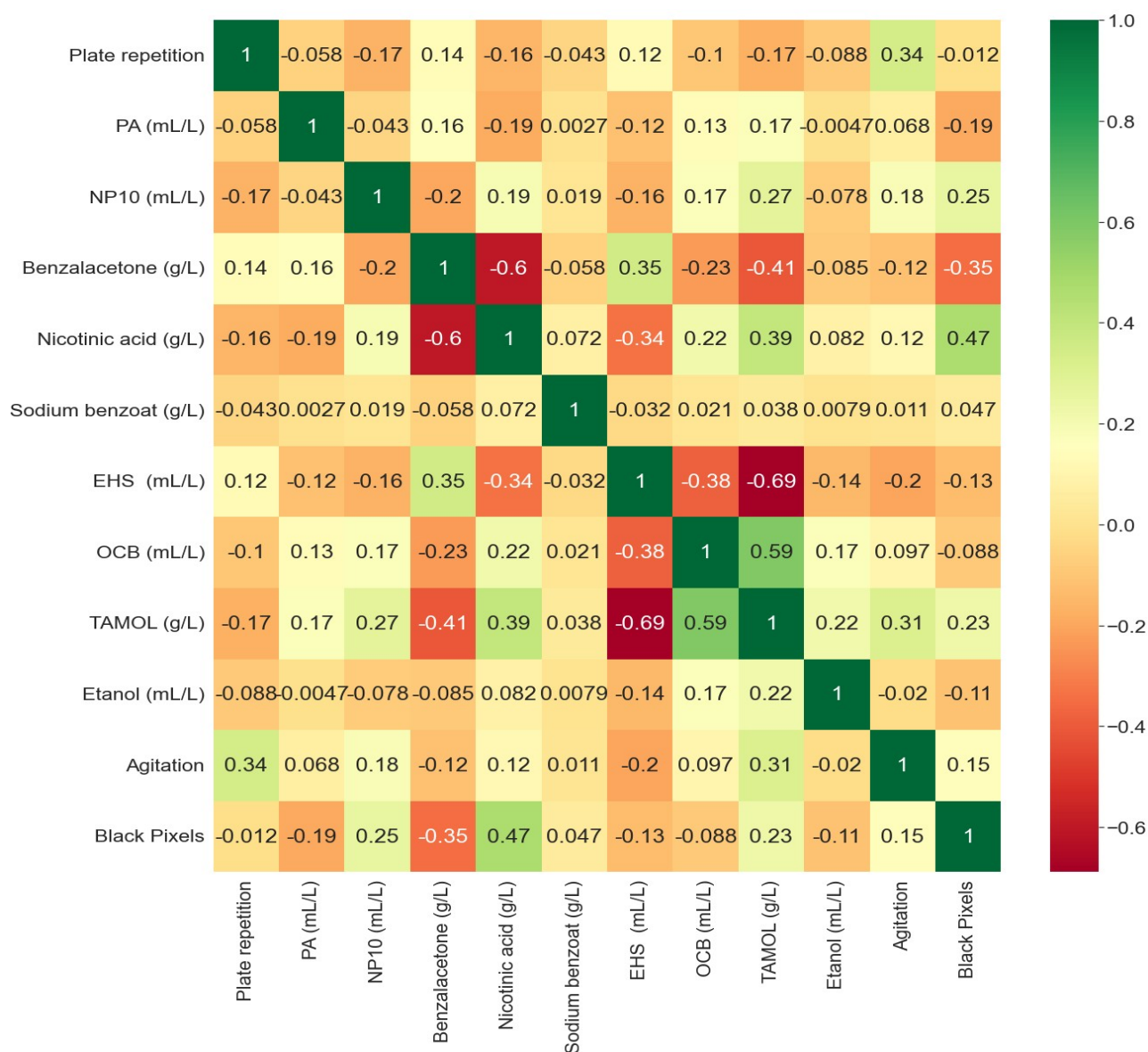


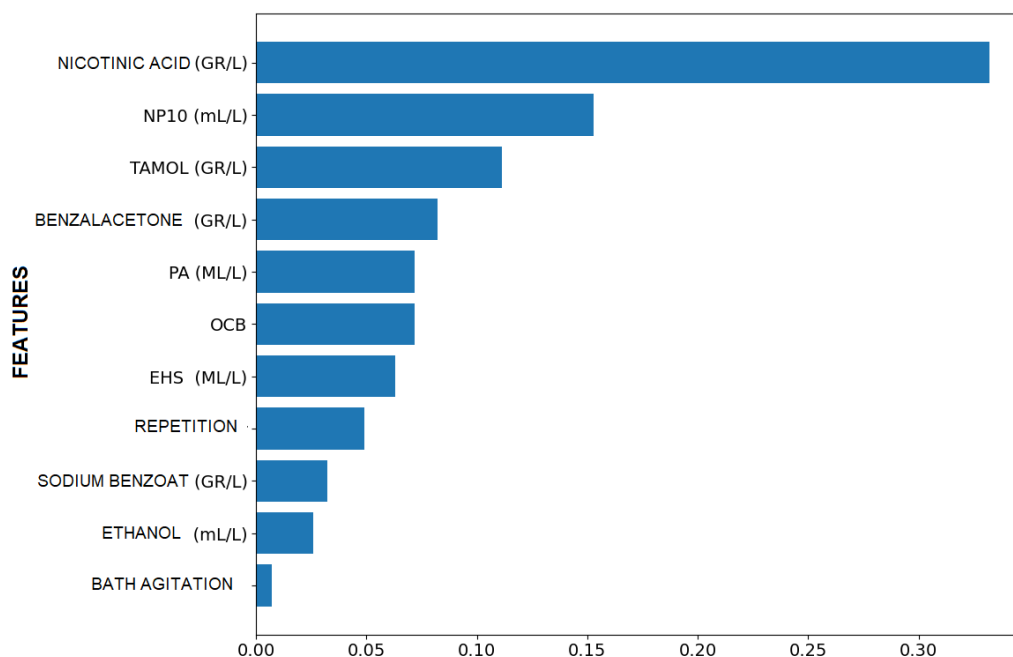
Figure 8: Heatmap of the feature weight matrix.

The heatmap was used to show the relationship between features (inputs) and brightness. Heatmap is a powerful tool to understand the relationship among the parameters at a glance with colors. As seen in Figure 8, the chemical increasing the brightness the most is nicotinic acid. A direct association between nicotinic acid and brightness is 0.47. Benzalacetone indicated the decreasing effect on the brightness (-0.35). Tamol and NP 10 chemicals also showed the brightness enhancing effect. The chemicals enhancing the brightness were acquired in order of nicotinic acid

> NP10 > tamol > agitating > sodium benzoate. The other chemical showed the negative effect on the brightness.

Figure 9 indicates the importance of process parameters and organic chemicals in the electroplating. Random Forest algorithm was utilized to find the importance of the features (input parameters). Nicotinic acid has the most impact on the brightness of the coating. This result is compatible with the results acquired from the heatmap.

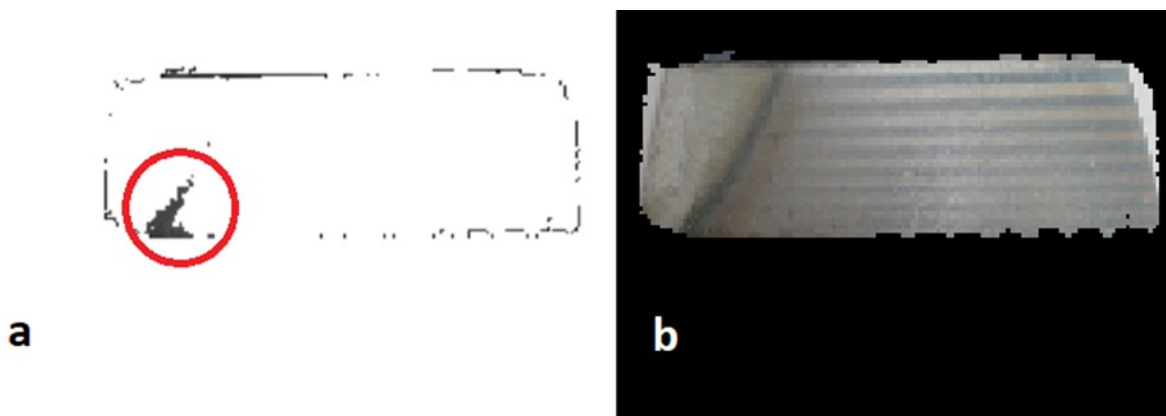




**Figure 9:** The importance of the chemicals in the electroplating bath.

As a result, this study proved that it is possible to measure the brightness of the coated parts using image processing technique. Even though this technique is an effective and strong technique, it has some problems to overcome. The blackness on the plates may sometimes be caused by a coating defect. As seen in Figure 9b, the coated plate is although almost completely matte, the red region on the plate (Figure 9a) is detected as bright by algorithm. In our study, since the error resulting

from coating defects was seldom, the order of brightness and quality of plates did not change. It is possible to overcome this problem using different colors for the reflection lines on the plates. These colors may be fully blue, red or green. In this state, a colored image should be used to count the colored pixels. In our further studies, it is planned to use blue colored lines or circles to measure the brightness of the coating.



**Figure 10:** The image related to the brightness (left) and extracted panel.

**CONCLUSION**

In this study, Mask RCNN algorithm was used to extract the concerned data from the image. Image processing technique was used to count the pixels of the shape reflected from the foreground image. The number of pixels was taken as a measure of brightness. ML algorithms were used to classify the coated parts in accordance with their brightness. Four ML algorithms and one neural network were utilized to train the dataset. It was found that the

RF model was the best model to predict the quality of the coating. Its accuracy, F1, precision and recall scores were found to be 0.97, 0.97, 1, 0.94 respectively.

The chemicals affecting the brightness in the zinc electroplating bath was investigated using heatmap method. The heatmap indicated that nicotinic acid has the most positive impact increasing the brightness of the coating.

This study revealed three important results;

- ✓ Mask RCNN can be used to remove the redundant data from the image.
- ✓ Image processing technique can be used to measure the brightness of the coating.
- ✓ ML algorithms can be used to predict the quality of the coating performed in the zinc electroplatings bath in accordance with their brightness.

In a nutshell, to measure the brightness of the coated parts, a technical set up should be used. In this set up, a suitable reflecting foreground should be chosen. This foreground should contain some colored shapes which will be reflected on the coated parts. The pixels of this shape correspond to the brightness of the coated parts. In the industry, a similar set-up can be used to classify the coated parts as "Fail" and "Pass" on the production line. The object near the coated parts weakens the prediction power of the model. Therefore, the redundant object should be extracted using Mask RCNN algorithm. Image processing technique can be implemented to the extracted data to count the pixels reflected from the foreground. Foreground color and shape is crucial to count the pixels. If the color and shape of the foreground are similar to the defect results from the coating error, the results may be inaccurate. To avoid this problem the different color and shape should be used for the reflection. In our further studies, blue or red colored lines or circles will be utilized to prevent the interference resulting from the coating defect.

#### CONFLICT OF INTEREST

The authors declare that they have no known competing financial interests or personal relationships that could have appeared to influence the work reported in this paper.

#### ACKNOWLEDGMENTS

The experiments reported in this paper were fully performed at TUBITAK ULAKBIM, High Performance and Grid Computing Center (TRUBA resources).

#### REFERENCES

1. Safavi MS, Walsh FC. Electrodeposited Co-P alloy and composite coatings: A review of progress towards replacement of conventional hard chromium deposits. *Surface and Coatings Technology*. 2021 Sep;422:127564. Available from: [<URL>](#),
2. Fotovvati B, Namdari N, Dehghanghadikolaei A. On Coating Techniques for Surface Protection: A Review. *JMMP*. 2019 Mar;3(1):28. Available from: [<URL>](#).
3. Gu Y, Liu J, Qu S, Deng Y, Han X, Hu W, et al. Electrodeposition of alloys and compounds from high-temperature molten salts. *Journal of Alloys and Compounds*. 2017 Jan;690:228-38. Available from: [<URL>](#).

4. Gérard B. Application of thermal spraying in the automobile industry. *Surface and Coatings Technology*. 2006 Oct;201(5):2028-31. Available from: [<URL>](#).

5. Bobzin K, Brögelmann T, Kalscheuer C, Liang T. High-rate deposition of thick (Cr,Al)ON coatings by high speed physical vapor deposition. *Surface and Coatings Technology*. 2017 Aug;322:152-62. Available from: [<URL>](#).

6. Xia F, Xu H, Liu C, Wang J, Ding J, Ma C. Microstructures of Ni-AlN composite coatings prepared by pulse electrodeposition technology. *Applied Surface Science*. 2013 Apr;271:7-11. Available from: [<URL>](#).

7. Safavi MS, Etminkanfar M. A review on the prevalent fabrication methods, microstructural, mechanical properties, and corrosion resistance of nanostructured hydroxyapatite containing bilayer and multilayer coatings used in biomedical applications. *J Ultrafine Grained Nanostruct Mater [Internet]*. 2019 Jun [cited 2022 Oct 17];52(1). Available from: [<URL>](#).

8. Katırcı R, Yılmaz EK, Kaynar O, Zontul M. Automated evaluation of Cr-III coated parts using Mask RCNN and ML methods. *Surface and Coatings Technology*. 2021 Sep;422:127571. Available from: [<URL>](#).

9. Bayati MR, Shariat MH, Janghorban K. Design of chemical composition and optimum working conditions for trivalent black chromium electroplating bath used for solar thermal collectors. *Renewable Energy*. 2005 Nov;30(14):2163-78. Available from: [<URL>](#).

10. Kul M, Oskay K, Erden F, Akça E, Katırcı R, Köksal E, et al. Effect of Process Parameters on the Electrodeposition of Zinc on 1010 Steel: Central Composite Design Optimization. *Int J Electrochem Sci*. 2020 Oct;9779-95. Available from: [<URL>](#).

11. Mirkova L, Maurin G, Krastev I, Tsvetkova C. Hydrogen evolution and permeation into steel during zinc electroplating; effect of organic additives. *Journal of Applied Electrochemistry*. 2001;31(6):647-54. Available from: [<URL>](#).

12. Arnold JO. The Metallurgy of Steel. *Nature*. 1912 May;89(2222):315-6. Available from: [<URL>](#).

13. Yang D, Wang X, Zhang H, Yin Z yu, Su D, Xu J. A Mask R-CNN based particle identification for quantitative shape evaluation of granular materials. *Powder Technology*. 2021 Nov;392:296-305. Available from: [<URL>](#).

14. Kiliçarslan S, Celik M. KAF + RSigELU: A nonlinear and kernel-based activation function for deep neural networks. *Neural Comput & Applic*. 2022 Aug;34(16):13909-23. Available from: [<URL>](#).






15. Kiliçarslan S, Celik M. RSigELU: A nonlinear activation function for deep neural networks.

- Expert Systems with Applications. 2021 Jul;174:114805. Available from: [<URL>](#).
16. Adem K, Kilicarslan S. COVID-19 Diagnosis Prediction in Emergency Care Patients using Convolutional Neural Network. *Akufemubid*. 2021;21(2):300-9. Available from: [<URL>](#).
17. Adem K. Impact of activation functions and number of layers on detection of exudates using circular Hough transform and convolutional neural networks. *Expert Systems with Applications*. 2022 Oct;203:117583. Available from: [<URL>](#).
18. Simonyan K, Zisserman A. Very Deep Convolutional Networks for Large-Scale Image Recognition. 2014 [cited 2022 Oct 17]; Available from: [<URL>](#).
19. He K, Zhang X, Ren S, Sun J. Deep Residual Learning for Image Recognition. In: 2016 IEEE Conference on Computer Vision and Pattern Recognition (CVPR) [Internet]. Las Vegas, NV, USA: IEEE; 2016 [cited 2022 Oct 17]. p. 770-8. Available from: [<URL>](#).
20. Szegedy C, Vanhoucke V, Ioffe S, Shlens J, Wojna Z. Rethinking the Inception Architecture for Computer Vision. In: 2016 IEEE Conference on Computer Vision and Pattern Recognition (CVPR) [Internet]. Las Vegas, NV, USA: IEEE; 2016 [cited 2022 Oct 17]. p. 2818-26. Available from: [<URL>](#)
21. Chollet F. Xception: Deep Learning with Depthwise Separable Convolutions. In: 2017 IEEE Conference on Computer Vision and Pattern Recognition (CVPR) [Internet]. Honolulu, HI: IEEE; 2017 [cited 2022 Oct 17]. p. 1800-7. Available from: [<URL>](#).
22. Yu Y, Zhang K, Yang L, Zhang D. Fruit detection for strawberry harvesting robot in non-structural environment based on Mask-RCNN. *Computers and Electronics in Agriculture*. 2019 Aug;163:104846. Available from: [<URL>](#).
23. Kumar G, Bhatia PK. A Detailed Review of Feature Extraction in Image Processing Systems. In: 2014 Fourth International Conference on Advanced Computing & Communication Technologies [Internet]. Rohtak, India: IEEE; 2014 [cited 2022 Oct 17]. p. 5-12. Available from: [<URL>](#).
24. Hull R. Current Density Range Characteristics, Their Determination and Application. *Proc Am Electroplaters Soc*. 1939;27:52.
25. Hu J, Sun Y, Li G, Jiang G, Tao B. Probability analysis for grasp planning facing the field of medical robotics. *Measurement*. 2019 Jul;141:227-34. Available from: [<URL>](#).
26. Reza M, Miri S, Javidan R. A Hybrid Data Mining Approach for Intrusion Detection on Imbalanced NSL-KDD Dataset. *ijacsa* [Internet]. 2016 [cited 2022 Oct 17];7(6). Available from: [<URL>](#).
27. Vapnik VN. *The Nature of Statistical Learning Theory* [Internet]. New York, NY: Springer New York; 2000 [cited 2022 Oct 17]. Available from: [<URL>](#).
28. Chen T, Guestrin C. XGBoost: A Scalable Tree Boosting System. In: *Proceedings of the 22nd ACM SIGKDD International Conference on Knowledge Discovery and Data Mining* [Internet]. San Francisco California USA: ACM; 2016 [cited 2022 Oct 17]. p. 785-94. Available from: [<URL>](#).
29. Rumelhart DE, Hinton GE, Williams RJ. Learning Internal Representations by Error Propagation. In: *Readings in Cognitive Science* [Internet]. Elsevier; 1988 [cited 2022 Oct 17]. p. 399-421. Available from: [<URL>](#).





## The Isolation of *Streptomyces* species in Different Soil Sources from Middle Anatolian Regions of Turkey

Zeynep Yilmazer Hitit<sup>1\*</sup> , Sila Eldemir<sup>2</sup> , Harun Buyukegen<sup>2</sup> ,  
Kemal Kesenci<sup>2</sup> , Suna Ertunc<sup>1</sup>  and Bulent Akay<sup>1</sup> 

<sup>1</sup>Ankara University, Department of Chemical Engineering, 06100, Ankara, Turkey.

<sup>2</sup>Safa Tarim AS, Konya, Turkey.

**Abstract:** *Streptomyces* is the largest species of the *actinomycetes* group, with more than 500 defined species, aerobic, gram-positive, and phylogenetic class filamentous (thin protruding in thread form). It is a large group that is mostly found in the soil and as a secondary metabolite of its fermentation, it enables the production of various and important components (antibiotics, chemotherapeutics, fungicides, herbicides, and immunosuppressants) in the field of industry and medicine. In this study, six bacterial isolates were isolated from soil samples in different regions of Turkey. Morphological characteristics, gram staining, and PCR test were applied for identification. Six isolates, *Streptomyces mutabilis*, *S. collinus*, *S. peucetius*, *S. cyaneofuscatus*, *S. albogriseolus* and, *S. griseoflavus*, were compared with the general characteristics of the *Streptomyces* species in International *Streptomyces* Project. Air and reverse side mycelium color were determined, and all were confirmed by the gram-positive test. Studies have shown that the regions of Ankara and Konya are rich in *Streptomyces* species.

**Keywords:** *Actinomycetes*; *Streptomyces* *sp.*; Isolation; Antibiotic; Secondary metabolite.

**Submitted:** June 24, 2022. **Accepted:** October 30, 2022.

**Cite this:** Hitit ZY, Eldemir S, Buyukegen H, Kesenci K, Ertunc S, Akay B. The Isolation of *Streptomyces* species in Different Soil Sources from Middle Anatolian Regions of Turkey. JOTCSB. 2022;5(2):157-66.

**\*Corresponding author. E-mail:** [zyilmazer@ankara.edu.tr](mailto:zyilmazer@ankara.edu.tr).

### INTRODUCTION

*Actinomycetes* are bacteria belonging to the *Actinomycetales* group known as *actinobacteria*. They are spore-forming gram-positive bacteria and are characterized by the formation of mycelium, which protrudes on the medium and produces asexual spores (1). Compared to yeast and other microorganisms, they contain high amounts of guanine and cytosine in their DNA structure (2). Within 24 hours, colonies that can only be seen under a microscope are formed. Colony formation is very slow. It takes 3-4 days to be seen with the naked eye. It takes 7-14 days of incubation to see mature mycelium. *Streptomyces avermitilis* is a spore-forming, aerobic gram-positive bacteria belonging to the mesophilic actinomycete group. Spores are spherical or oval and usually occur in chains. Albumin, glycerol-asparagine, inorganic salt, starch, and oatmeal agar media are required for

sporulation to occur. Gray spores form on light brown agar and the colony reverses from dark brown to tan. Culture grows best between 27-37 °C. This group has a strong tendency to produce antibiotics with different chemical structures and biological activities (3).

The presence and distribution of *Streptomyces* species belonging to *actinomycetes*, the most abundant group in soil, are highly affected by the physical and chemical conditions of the soil such as temperature, pH, types of organic materials, and moisture content. Acidic-resistant groups are the most abundant *actinomycetes* in acidic soil, while they are less abundant in soils with alkaline pH (4). They are widely recognized for their ability to produce industrially important enzymes, and secondary metabolites during fermentation, and, in addition, to cover about 80% of antibiotic products (5). The identification and isolation of

microorganisms producing secondary metabolites have been the focus of research for several years (6).

Chemical, molecular and taxonomic properties of the genus *Streptomyces* have been revealed by several studies (7–12). According to this, non-acidic, rarely fragmented submerged hyphae (0.5-2 µm) are organisms in which reproduction occurs by dormant spores at the ends of the aerial hyphae (13). A few exceptional species form short spore chains in submerged mycelium; *sclerotium*, *pycnidium*, *sporangium*, and synnemata-like structures can be formed (14). Colonies at the beginning of growth are smooth and soft, then hard-tight, cottony, granular, powdery, or velvety. Most strains can produce species-specific antibiotics (3). A large number of pigments responsible for the color of the submerged micelle can be self-produced, as well as secreted pigments.

The cell wall contains large amounts of L-Diaminopimelic acid (L-DAP) in its peptidoglycan structure. It contains no mycolic acid and saturated iso and anteiso fatty acids, hexa and octa dehydrogenated menaquinone with nine isoprene units as the predominant isoprenoid. It also contains complex polar oil containing phosphatidylinositol, phosphatidylglycerol, phosphatidylinositol, and phosphatidylinositol with these oil characteristics, it belongs to the phospholipid type 2 group. The Guanine+Cytosine ratio of its DNA varies between 69-78%. It is mostly rotten; a few species are rarely pathogenic in humans and animals, some in plants. The number of species in the genus *Streptomyces* is increasing (15).

More than 650 species were reported in the German Collection of Microorganisms and Cell Cultures (DSMZ). Thus, this genus became a member of the genus *Actinobacteria* with the highest number of species in the order *Actinomycetales* (16). Based on all these classifications, *Streptomyces* has been divided into 20 major, 41 minor, and 22 single-member groups. Large classes are considered to be the groups of species consisting of six or more types of strains, while small classes are considered to be a single species consisting of 2-5 types of strains (16–20).

Contents of the medium affect *Streptomyces* isolation (5). It has been observed that the best isolation occurs in media containing glycerol or starch as a carbon source, and arginine, casein, or nitrate as a nitrogen source. Different antifungal agents called nystatin, cycloheximide, and pimaric are generally used during isolation to obtain pure bacterial isolates. *Streptomyces* are identified by their spore size, morphology, chains, pigmentation, physiological and biochemical properties, and resistance to antibiotic resistance (21).

Standard microbiological methods, biochemical analysis, and DNA sequencing are used to selectively identify the genus and species of isolated microorganisms. *Streptomyces* forms stable filaments and can produce long-chain spores that grow in aerobic conditions. Direct and indirect screening methods to determine antibiotic producers have often been used to isolate a particular microorganism. While direct screening of strains includes bioassay or chemical methods, indirect screening includes the correlation of antibiotic production with strain characteristics (11). *Streptomyces* members are very important due to their ability to produce various types of secondary metabolites such as Valinomycin, Neomycin B, Avermectin, Neomycin C, Bicosamycin, Colabomycin A, Colabomycin C, Germakradionel, Hormaomycin, etc. (5).

Isolation and identification of *Streptomyces cp.* were carried out by three basic methods in the literature (22–24). Siddique et al (2014) performed isolation by using different types of media such as *Actinomyce*te isolation medium (AC) and Kuster's isolation medium (KU) for the single colony, Yeast Extract Malt Extract Glucose Medium (YMG) and *Streptomyces* isolation medium (SC) for preculture and culture growths (22). Ariffuzzaman et al (2010) tested Glycerolarginine isolation medium (GAM) for the single colony, Modified starch casein agar medium (MSCAM), Tryptone-soybean agar medium (TSA) and Yeast Extract Malt Extract Glucose Medium (YMG) for the preculture and culture growths (23). Kumar et al (2010) determined the isolation of *Streptomyces cp.* by starch casein agar (SCAM) for a single colony and Yeast Extract Malt Extract Glucose Medium (YMG) for the preculture and culture growths (24).

In this study, *Streptomyces* antibiotic-producing bacteria were isolated from soil samples from Ankara and Konya regions. Different media were used to screen pure *Streptomyces* strains. The antibacterial activities of various isolates were evaluated, and their morphological structures were determined.

## MATERIALS AND METHODS

### Isolation and Identification of *Streptomyces* from Soil

The soil suspended in sterile water is diluted and spread on selective agar medium and then subjected to aerobic incubation at 25-28 °C.

### Collection and Preparation of Soil Samples

Soil samples were taken from Ankara and Konya regions. The methods used in sampling and preparation are given below.

#### Method 1 (22)

Soil samples are taken with a sterile spatula by digging 3 cm from the soil surface and stored in

clean, dry and sterilized polyethylene bags at 40 °C until pre-treatment. Each 1-g soil sample is suspended in 100 mL of sterile 0.9% NaCl solution and incubated at 28°C for 30 min at 180 rpm in an orbital shaker. Samples are spread on petri dishes containing *Actinomyccete* isolation medium (AC), (pH=7, 5 g/L glycerol, 2 g/L KH<sub>2</sub>PO<sub>4</sub>, 0.1 g/L asparagine, 0.1 g/L MgSO<sub>4</sub>.7H<sub>2</sub>O, 1 mg/L FeSO<sub>4</sub>.7H<sub>2</sub>O, and 15 g/L agar) and Kuster's isolation medium (KU), (pH=7.1, 10 g/L soluble starch, 2 g/L KNO<sub>3</sub>, 2 g/L K<sub>2</sub>HPO<sub>4</sub>, 2 g/L NaCl, 0.05 g/L MgSO<sub>4</sub>.7H<sub>2</sub>O, 0.02 g/L CaCO<sub>3</sub>, 0.01 g/L FeSO<sub>4</sub>.7H<sub>2</sub>O, and 18 g/L agar) and incubated for 7-10 days at 28 °C.

Samples grown on *Actinomyccete* isolation (AC) and Kuster's agar media (KU) were incubated while the ones that could be *Streptomyces* were labeled, and single colony screenings were made on Yeast Extract Malt Extract Glucose Medium (YMG) (pH=7.3, 4 g/L yeast extract, 10 g/L malt extract, 4 g/L glucose, 20 g/L agar) containing 0.05 mg/mL nystatin and incubated at 28 °C for 7-10 days for colony formation.

Single colonies are transferred to *Streptomyces* isolation medium (SC) (pH= 7.0) consists of 5 g/L glucose, 4 g/L L-glutamic, 19 g/L K<sub>2</sub>HPO<sub>4</sub>, 0.7 g/L MgSO<sub>4</sub>.7H<sub>2</sub>O, 1 g/L NaCl, 3 mg/L FeSO<sub>4</sub>.7H<sub>2</sub>O, 25 g/L agar, and 0.05 mg/L nystatin.

#### Method 2 (23)

Soil samples are taken with a sterile spatula by digging 4 cm from the soil surface and stored in clean, dry and sterilized polyethylene bags at 40 °C. Each 1-g soil sample is diluted 1:10 and 1:100 with sterile water or 0.9% NaCl solution, and the soil suspensions are heated in a water bath at 50 °C for 10 minutes. Samples are spread on petri dishes containing Glycerolarginine (GAM) isolation medium (pH 7.4) consists of 1 g/L L-Asparagine, 1 g/L Dipotassium phosphate, 0.01 g/L FeSO<sub>4</sub>.7H<sub>2</sub>O, 0.001 g/L MgCl<sub>2</sub>.4H<sub>2</sub>O, 0.001 g/L ZnSO<sub>4</sub>. 7H<sub>2</sub>O, 20 g/L Agar, and 0.05 mg/L Nystatin and incubated at 25 °C for 7-10 days.

While the soil samples growing in GAM medium are in the incubation stage, colonies that could be *Streptomyces* are marked. Single colony was cultivated on modified starch casein agar medium and incubated for colony formation at 28 °C for 7-10 days. Modified starch casein agar medium (MSCAM) (pH=7.2) consists of 10 g/L soluble starch, 15 g/L agar, 50% sea water, and 0.05 mg/mL nystatin. Cultures taken from this isolation medium are plated on Modified starch-casein agar medium to which cyclohexamide and nystatin (0.05 mg/mL) have been added. The formed colonies are transferred back to Tryptone-soybean agar medium. Colonies are observed on this medium by incubating at 25 °C for 2-7 days. Tryptone-soybean agar medium (TSA) (pH=7): 15 g/L peptone from casein,

5 g/L peptone from soybean meal, 5 g/L NaCl, and 15 g/L Agar.

Cultures showing growth in TSA medium are transferred to YMG medium, and the strains are maintained at 4 °C for 2-month periods and serially maintained for a longer period. It is considered a *Streptomyces* culture if it grows in a YMG medium.

#### Method 3 (24)

Soil samples are taken from a depth of 10-15 cm. The samples are air-dried for 1 week, crushed, and sieved. Each 1-g soil sample is suspended in 100 mL of sterile 0.9% NaCl and incubated at 28 °C in an orbital shaker for 30 minutes at 180 rpm. Samples are spread by taking 0.1 mL into petri dishes containing starch casein agar (SCAM) isolation medium and incubated at 28-30 °C and monitored for 48, 72, and 96 hours. SCAM (pH 7.2) consists of 10 g/L soluble starch, 1 g/L casein powder 50% seawater, and 15 g/L agar. While the soil samples grown in the SCAM medium are in the incubation stage, bacteria that may be *Streptomyces* species are marked and a single colony is cultivated in the SCAM medium and colony formation is observed at 28 °C for 7-10 days. Repetitive transfers of cultures from SCAM isolation media are performed on YMG media. Maintained at 4 °C after repeated transfers. Selected samples are cultivated in a single colony in YMG medium.

#### Morphological Characterization

The morphology of *Streptomyces* colonies after colony proliferation was characterized based on air mycelial morphology, and reverse side color principles. Microscopic slides were prepared for all isolates and examined under the microscope.

#### Gram Stain

Gram-positive responses were investigated for *Streptomyces* isolates. A small amount of distilled water is dripped onto the coverslip in the sterile cabinet, and a single colony is taken from the petri dish with the help of a loop and spread homogeneously on the coverslip. The water in the lamella is evaporated on the burner flame. Crystal violet solution is dripped onto the coverslip and left for 1 minute. After a 1-minute period, the excess crystal violet solution is disposed of. Lugol solution is dripped and left for 1 minute. The preparation is washed with distilled water. Excess water on the lamella is disposed of. It is washed with a decolorizing solution and then washed with distilled water. It is dyed with saffron, left for 1 minute. The preparation is washed with plenty of distilled water and dried. Some immersion oil is poured onto the dried preparation. It is examined under a microscope.

Microorganisms seen in purple are marked as gram (+), and those seen in pink-red color are marked as grams (-).



### DNA Isolation, Polymerase Chain Reaction (PCR), and Sequence Analysis

YMG liquid nutrient medium is prepared; the selected samples are mixed with the aid of the loop and microorganism proliferation is observed. At the end of the process, 2 mL of the sample taken from the YMG liquid medium was used for DNA isolation. For isolation GeneJET Genomic DNA Purification Kit (Thermo Cat No: K0721) was used and the following steps are applied in order. 2 mL of liquid YMG medium with microorganisms is taken into Eppendorf tubes with the help of a micropipette then sample is centrifuged at 5000 g for 10 min. The supernatant is disposed of, and the precipitate is centrifuged once again under the same conditions. The supernatant is disposed of without disturbing the pellet. In order to lyse the cells, 200 µL of Lysis Buffer (20 mM Tris-HCl, pH:8, 2 mM EDTA, 1.2% TritonX-100, and 20 mg/mL lysozyme) is added and incubated for 45 min at 37 °C. 10 µL of Lysozyme enzyme is added and waited for a minute. At the end of the incubation, 200 µL of lysis solution and 100 µL of Proteinase K are added and mixed thoroughly and incubated for 30 min at 56 °C. 20 µL of RNase A is added to the solution and incubated for 10 min at room temperature. 400 µL of 50% ethanol is added to the solution and the suspension is transferred to the column with mixing. After spinning down at 6000 g for a minute, the bottom part is discarded, and the column is transferred to new tubes. 500 µL of Washing Solution I is added and centrifuged at 8000 g for a minute. The bottom liquid is discarded, and 500 µL of Washing Solution II is added to the column and centrifuged at maximum speed for 3 minutes. The bottom liquid is discarded, and the column is centrifuged again for 1 min at maximum speed. After centrifugation, the column is transferred to a new 1.5 mL microcentrifuge tube and 50 µL of elution buffer is added. DNA samples are stored at -20 °C after centrifugation at 8000 g for a minute. The primers, which came in lyophilized form, were first diluted with ultrapure water to 100 µmol per microliter. The stock is diluted to 10 µmol per microliter for later use in PCR. PCR is performed using DreamTaq DNA Polymerase (Cat: EP0703). Standard 3-step PCR Cycling is as follows, initial denaturation for a cycle for 5 min at 95 °C, denaturation for 35 cycles for 30 sec at 95 °C, 30 sec at 58 °C and a min at 72 °C, final extension for a cycle for 10 min at 72 °C.

~920 base pair PCR amplicons are submitted for Forward-Reverse DNA sequencing specific to the 16S rDNA gene. The nucleotide sequences resulting from the sequencing reaction are aligned to the NCBI database with the "Basic Local Alignment Search Tool (BLAST)" algorithm.

The obtained genomic DNA is tested in RAPD reactions to show the suitability of the isolated DNA

for PCR reactions. Electrophoresis of DNA samples is performed on gels containing 1% agarose. After PCR, 5 µL of the obtained products are taken, mixed with 1 µL of 6X loading paint and run under 100-Volt electric current. The 1 kb DNA Marker (Fermentas, Finland) is used to determine the size of the approximately 920 bp long amplicon. After electrophoresis, the gels are stained in 0.2 µg/mL ethidium bromide (Biotium, Cat: 40042) solution for 20 minutes and visualized and photographed under UV light at 366 nm wavelength using a transilluminator.

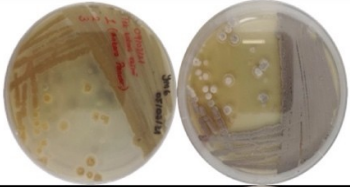
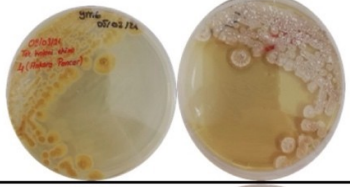
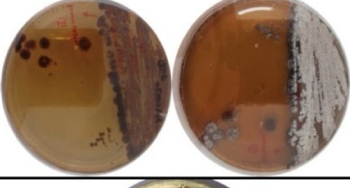

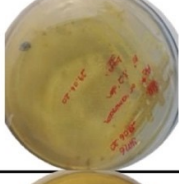
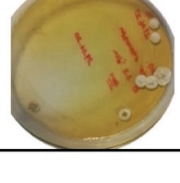
### Antimicrobial Activity with Well Management

An antimicrobial activity study was planned on the determined species, and according to this study, *Escherichia coli* (*E. coli*) and *Staphylococcus* (*Staph*) pathogenic microorganisms were selected and the effectiveness of antibiotic production of microorganisms on these pathogens was examined. Lysogeny broth (LB) solid, LB liquid and LB soft media were prepared and sterilized. 5 µL of *E. coli* and *Staph* were separately inoculated in 5 mL of LB liquid medium. Pathogens were activated by incubation at 37 °C at 180 rpm for 18 hours. LB solid medium was prepared in glass tubes as 5 mL and LB solid medium was prepared in petri dishes as 10 mL. At the end of 18 hours, 1 µL of activated pathogens was taken and inoculated into 5-mL LB soft tubes after the media was melted at 95 °C and mixed well, then poured onto LB solid petri dishes. After media solidifies, wells were drilled in the divided areas of the petri dish with the well drilling apparatus. Two of the wells were filled directly by taking samples from the liquid fermentation media of isolated microorganisms, and two of them were filled with centrifugated sample. One well was filled with physiological saline for negative control purposes. After 10-15 minutes of waiting period, petri dish was left to incubate for 18 hours, and at the end of the incubation antimicrobial activity was observed.

### RESULTS AND DISCUSSION

The isolation of *Streptomyces* type antibiotic-producing bacteria was carried out from six soil samples in Ankara and Konya regions by using 3 different nutrient media. After 5-7 days of incubation in aerobic conditions, characteristic colonies of *Streptomyces* are observed, and pure culture is obtained by plating a single colony on selective media.

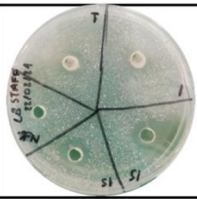
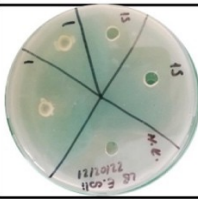
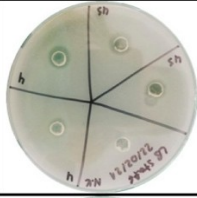
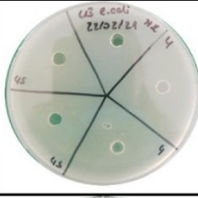
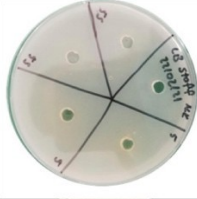
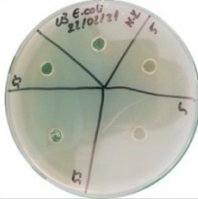
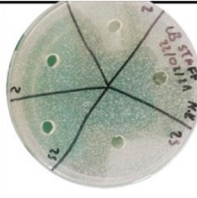
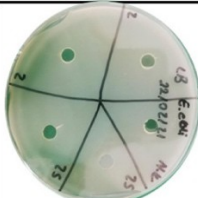
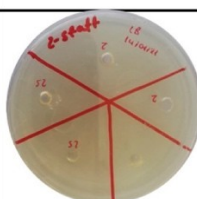
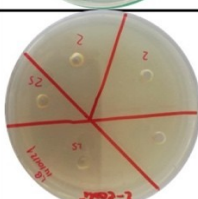
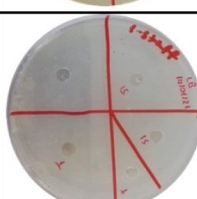
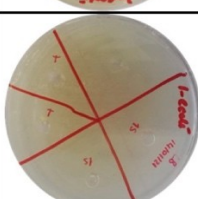
First, morphological characterization was performed based on the morphology of *Streptomyces* colonies, air mycelium morphology, reverse side color principles after colony proliferation. Their isolation methods and the back and front mycelial images are given in Figure 1.

Soil Sample Area	Isolated microorganism type	Gram Staining (+/-)	Isolation pathway	Back/front mycelial images
Ankara	<i>Streptomyces mutabilis</i>	+	<b>Method 1 ve 3</b> First inoculation from KU medium to SC medium at a dilution of 10 <sup>0</sup> , black hairy microorganism	
	<i>Streptomyces collinus</i>	+	<b>Method 3</b> First inoculation, white hairy microorganism from SC medium at 10 <sup>2</sup> dilution ratio (inoculation from SC to SC)	
	<i>Streptomyces peucetius</i>	+	<b>Method 2</b> Black hairy microorganism by inoculation a single colony from GAM medium to MSCAM medium at a dilution ratio of 10 <sup>2</sup> .	
Konya	<i>Streptomyces cyaneofuscatus</i>	+	<b>Method 3</b> First sowing at 10 <sup>2</sup> dilution ratio, black microorganism (inoculation from SCAM to SCAM)	
	<i>Streptomyces albogriseolus</i>	+	<b>Method 1</b> First inoculation from AC medium at a dilution of 10 <sup>0</sup> , white microorganism (inoculation from AC to YMG inoculation)	
	<i>Streptomyces griseoflavus</i>	+	<b>Method 1</b> First inoculation from KU at a dilution of 10 <sup>0</sup> , yellow microorganism (inoculation from KU to YMG)	

**Figure 1:** The isolated microorganism species and the isolation pathway.

*S. mutabilis*, *S. albogriseolus* and *S. griseoflavus* are isolated with KU and AC agar medium with Method 1. Although they are isolated with the same method, they have different aerial and reverse side mycelia color. The only *Streptomyces* species that is formed in the GAM medium with Method 2 is *S.*

*peucetius* which is unlike the others in terms of aerial and reverse side mycelia color and soluble pigment color. *S. mutabilis*, *S. collinus* and *S. cyaneofuscatus* are the *Streptomyces* species that are isolated with Method 3.

Soil Sample Area	Isolated microorganism type	Well Diffusion Method (for <i>Staph</i> and <i>E.coli</i> )	<i>Staph</i>	<i>E. coli</i>
Ankara	<i>Streptomyces mutabilis</i>	Effective on <i>Staph</i>		
	<i>Streptomyces collinus</i>	Effective on <i>Staph</i>		
	<i>Streptomyces peucetius</i>	Not effective		
Konya	<i>Streptomyces cyaneofuscatus</i>	Not effective		
	<i>Streptomyces albogriseolus</i>	Not effective		
	<i>Streptomyces griseoflavus</i>	Not effective		

**Figure 2:** Antimicrobial activity of isolated microorganism species on two different pathogenic microorganisms.

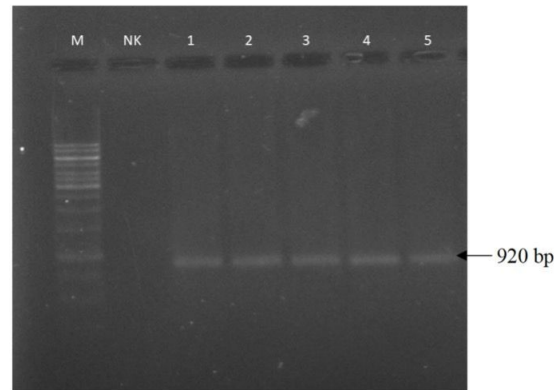
In Figure 2, the activities of *Streptomyces* species isolated from soils in Ankara and Konya regions on *Staph* and *E. coli* pathogens by well diffusion method are given. It was concluded that none of the microorganisms were effective on *E. coli* for Ankara soil. However, *S. mutabilis* shows the most prominent activity for the *Staph* pathogen, as well as *S. collinus*. As can be seen from the petri images

of Konya soil, it was concluded that none of the microorganisms were effective on *E. coli* and *Staph*.

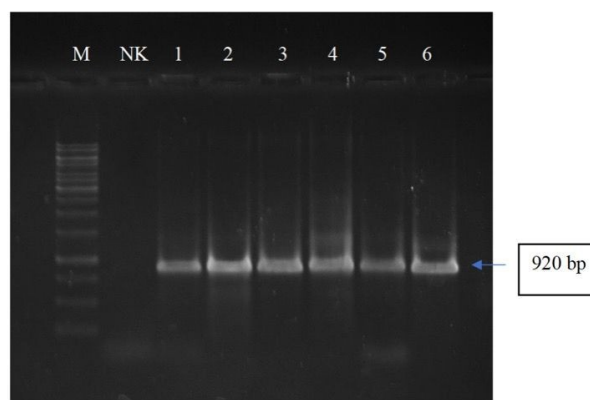
DNA sequence analysis results and DNA sequences are given in Figure 3 and PCR gel image of microorganisms isolated from the regions Ankara and Konya are given in Figures 4 and 5.

Soil Sample Area	Isolated species	Ratio	DNA sequence
Ankara	<i>Streptomyces mutabilis</i>	99.88%	TAAGGCGCGGGGCTTACCATGCAAGTCGAACGATGAACCACCTTCGGGTGGGGATTAGTGGCGAAC GGGTGAGTAGCACGTGGGCAATCTGCCCTGCACCTTGGGACAAGCCCTGGAAACGGGGTCTAATACGG GATACTGACCCCTCGAGGCAATCTGCGAGGTTGCGAAAGTCCCGCGGTGACAGGATGAGCCCGGGCTA TCAGCTAGTTGGTAGAGCCTAATGGCTACCAAGGCGACGACGGGTAGCCGGCTGAGAGGGCGACC GGCCACACTGGGACTGAGACACGACCCANNNTCTAATACGGGAGGAGCAGTGGGGAATATTGCACA ATGGGCGAAAGCTGATGCAGCGACGCCGCGTGGGGATGACGGCCCTTCGGGTGTAAACCTCTTTCA GCAGGGAAGAAGCGAAAGTGACGGTACCTGCAGAAGAAGCGCCGGTAACTACGTGCCAGAGCCG GGTAATACGTAGGGCGCAAGCGTTGTCGGGAATTATTGGCGTAAAGAGCTCGTAGCCGGCTTGTAC GTCGGTTGTGAAAGCCGGGGCTTAACCCCGGGTCTGCAGTCGATACGGGACGGCTAGAGTTCGGTAG GGGAGATCGAAATTCCTGGTGTAGCGGTGAAATGCGCAGATATCAGGAGGAACACCGGTGGCGAAGG CGGATCTCTGGGGCAAACTGACCCTGAAGAGCAAAANCCTGGGGAAACGAGGATTTAAATCCCC TGGAGCCCCCCCCNAAACGGGGGGGCCAAGGGTGGGGGACATTTTCCANTTTCCCGGGCCCC CTAACCTTTAAATGCCCCCCCGGGGAGACNCCCCAGGGTAAAACCTCAAGGAATNTGGGGA
	<i>Streptomyces collinus</i>	99.42%	AAATTANNTGGGACTTCCAGGGCGGGGCACTTAAATGCGTTAGCTCGGCACGGACAACGTGGAAAT GTTGCCACACACTAGTGCCACCGTTTACGGCGTGGACTACCAGGGTATCTAATCTCTTTCCTCCCCA CGCTTTCGCTCCTCAGCGTCACTATCGGCCAGAGATCCGCTTCGCCACCGGTGTTCTCCTGATATC TGCGCATTTACCGCTACACAGGAATTCGATCTCCCTACCGAATCTAGCTCGCCGTATCGACTG CAGACCCGGGTTAAGCCCGGGCTTTCACAACCGACGTGACAAGCCGCTACGAGCTCTTTACGCC AATAATTCGGCAACCGCTCGCGCCCTACGTAATACCGCGGTGCTGGCAGTGTAGCCGGCCTTTC TTCTGACGGTACCGTCACTTTCGCTTCTCCCTGCTGAAAGAGGTTTACAACCCGAAAGCCGCTATCCC TCACGGCGCTCGTGCATCAGGCTTTCGCCATTTGTCAATATTCCTCCACTGCTGCCCTCCGATAGGAG TCTGGGCGGTGCTCAGTCCAGTGTGGCCGCTGCCCTCTCAGGGCCGCTACCCGTCGTGCGCTTGTG GAGCCACTACCTACCAACAAGTGTATAGCCCGGGCTCATCTGCACCCGCGAGCTTTCGAACCG TCTGGATGCCAGCGGATCAGTATCCGGTATTAGACCCGTTTCCAGGGTGTTCACAGATGACGAG GCAGATTGCCACGTTTACTACCCGTTCCGCACTAATCCCCACCGAAGTGTTCATCGTTCGACTTG CATGTGTTAAGCACCGCCGACGGTTCGCTGAGCCAGGATCCAACTCTAAAAA
	<i>Streptomyces peucetius</i>	99.65%	TACCGGGCGGCTTCCAAAGGGCGGGGACTTAAATGCGTTAGCTCGGCACCGACGAGTGGAAATGTCG CCAACACCTAGTCCCAAGTTCACGGCGTGGACTACCAGGGTATCTAATCTCTGCTCCTCCACGCT TTCGCTCCTCAGCGTCACTAATGGCCAGAGATCCGCTTCGCCACCGGTGTTCTCCTGATATCTGCG CATTTACCGCTACACAGGAATTCGATCTCCCTACCACTTAGCTGCCCCGATCGAATTCGAGA CCCGGGTTAAGCCCGGGCTTTCACATCCGACGGGACAAGCCGCTACGAGCTCTTACGCCAATA ATTCCGGACAACGCTTTCGCCCTACGTAATACCGCGGTGCTGGCAGTGTAGCCGGCCTTCTTCT GCAGGTACCGTCACTTTCGCTTCTCCCTGCTGAAAGAGGTTTACAACCCGAAAGCCGCTATCCCTCAC GCGCGTGCATCAGGCTTTCGCCATTTGCAATATTCCTCCACTGCTGCCCTCCCGTAGGATCTG GGCGGTCTCAGTCCAGTGTGGCCGCTGCCCTCTCAGGCGG CTACCCGTCGTCGCTTGGTAGGCCATCACCACCAACAAGCTGATAGCCCGGGCTCATCTTCAC CGCCGAGCTTTCAACCGCAGACCATGCGATCCGAGTGTATCCGGTATTAGACCCGTTTCCAGGGC TTGTCCAGAGTGAAGGGAGATGTCACCGTGTACTACCCGTTGCCACTAATCCCTCCCGAAGG AGGTTTCATCGTTCGACTTGTGTTAAGCACCGCCGACGGTTCGCTGACGCTGACCTCAAACTCT AAA
Konya	<i>Streptomyces cyaneofuscatus</i>	99.76%	CCAGGGCGGGCTTAAACNATGCAAGTCGAACGATGAAGCCTTTCGGGGTGGATTAGTGGCGAACGGGT GAGTAACACGTGGGCAATCTGCCCTTCACTCTGGGACAAGCCCTGGAAACGGGGTCTAATACCGGATA ACACTCTGTCCCGCATGGGACGGGGTAAAAGCTCCGGCGGTGAAGGATGAGCCCGGGCTATCAGC TTGTTGGTGGGTAATGGCTACCAAGGCGACGACGGGTAGCCGGCTGAGAGGGGACCCGGCA CTGGGACTGAGACACGGCCAGACTCCTACGGGAGGACGAGTGGGGAATATTGCACAATGGGCGAA AGCCTGATGCAGCGACGCCGCTGAGGGATGACGGCTTCGGGTTGTAAACCTCTTTCAGCAGGGAAG AAGCGAAAGTGACGGTACCTGCAGAAGAAGCGCCGGTAACTACGTGCCAGCAGCCGGGTAATACG TAGGGCGCAAGCGTTTCCGGAATTATTGGGCGTAAAGAGCTCGTAGCCGGCTTGTACGTCGGATGT GAAAGCCCGGGCTTAAACCCGGGTGCTGATTCGATACCGGCTAGTAGAGTGTGGTAGGGAGATCG GAATTCCTGGTGTAGCGGTGAAATGCGCAGATATCAGGAGGAACACCGGTGGCGAAGCCGGATCTCT GGGCCATTAAGTACGCTGAGGAGCGAAAGCGTGGGGAGCGAAGGATAGATACCCTGGTGTAGTCCA CGCGTAAACGTTGGGAAGTGGTGTGGCGACATTCACGTCGTCGGTCCGCGACTAACGCATTA GTTCCCGCTGGGGAGTACGGCCGAAGGCTAAAACCTCAAGGAAATTTGACG
	<i>Streptomyces albogriseolus</i>	99.88%	ACCGGGGGGGCTTACCATGCAAGTGCAGACGATGAACCACCTTCGGTGGGGATTAGTGGCGAACGGGT GAGTAACACGTGGGCAATCTGCCCTTCACTCTGGGACAAGCCCTGGAAACGGGGTCTAATACCGGATA CTGACCCGCTTGGGCTACCAAGCGGTTGAAAGCTCCGGCGGTGACAGGATGAGCCCGGGCTATCAG CTTGTGGTGGGTAATGGCTACCAAGGCGACGACGGGTAGCCGGCTGAGAGGGCGACCGGCCAC ACTGGGACTGAGACACGGCCAGACTCCTACGGGAGGACGAGTGGGGAATATTGCACAATGGGCGA AAGCCTGATGCAGCGACGCCGCTGAGGGATGACGGCTTCGGGTTGTAAACCTCTTTCAGCAGGGAA GAAGCGAAAGTGACGGTACCTGCAGAAGAAGCGCCGGTAACTACGTGCCAGCAGCCGGTAAATAC GTAGGGCGGAGCGTGTCCGGAATTATTGGGCGTAAAGAGCTCGTAGGCGGCTTGTACGTCGGTTG TGAAAGCCCGGGCTTAAACCCGGGTGCTGAGTTCGATACGGGACGGCTAGAGTTCGGTAGGGGAGATC GGAATTCCTGGTGTAGCGGTGAAATGCGCAGATATCAGGAGGAACACCGGTGGCGAAGCCGGATCTC TGGCCGATACTGACGCTGAGGAGCGAAAGCGTGGGGAGCGAACAGGATAGATACCCTGGTGTAGTCC ACGCCGTAACCGGTGGGCACTAGGTGTGGGGGACATTCACGTCGTCGGTCCGCGAGCTAACGCATTA AGTCCCCGCTGGGGAGTACGGCCGAAGGCTAAAACCTCAAGGAAATTTGACG
	<i>Streptomyces griseoflavus</i>	98.95%	CCCCGGGGGCTTACACATGCAAGTGCAGACGATGAACCACCTTCGGTGGGGATTAGTGGCGAACGGGT GAGTAACACGTGGGCAATCTGCCCTGCACTCTGGGACAAGCCCTGGAAACGGGGTCTAATACCGGATA CTGATCCGCTGGGATCTCGCGGTTTCGAAAGCTCCGGCGGTGACAGGATGAGCCCGGGCTATCAG CTTGTGGTGGGTAATGGCTACCAAGGCGACGACGGGTAGCCGGCTGAGAGGGCGACCGGCCAC ACTGGGACTGAGACACGGCCAGACTCCTACGGGAGGACGAGTGGGGAATATTGCACAATGGGCGA AAGCCTGATGCAGCGACGCCGCTGAGGGATGACGGCTTCGGGTTGTAAACCTCTTTCAGCAGGGAA GAAGCGAAAGTGACGGTACCTGCAGAAGAAGCGCCGGTAACTACGTGCCAGCAGCCGGTAAATAC GTAGGGCGGAGCGTGTCCGGAATTATTGGGCGTAAAGAGCTCGTAGGCGGCTTGTACGTCGGTTG TGAAAGCCCGGGCTTAAACCCGGGTGCTGAGTTCGATACGGGACGGCTAGAGTTCGGTAGGGGAGATC GTAGGGCGGAGCGTGTCCGGAATTATTGGGCGTAAAGAGCTCGTAGGCGGCTTGTCCGCTCGGATG TGAAAGCCCGGGCTTAAACCCGGGTGCTGATTCGATACGGGACGGCTAGAGTTCGGTAGGGGAGATC GGAATTCCTGGTGTAGCGGTGAAATGCGCAGATATCAGGAGGAACACCGGTGGCGAAGCCGGATCTC TGGCCGATACTGACGCTGAGGAGCGAAAGCGTGGGGAGCGAACAGGATAGATACCCTGGTGTAGTCC ACGCCGTAACCGGTGGGCACTAGGTGTGGGGGACATTCACGTCGTCGGTCCGCGAGCTAACGCATTA AGTCCCCGCTGGGGAGTACGGCCGAAGGCTAAAACCTCAAGGAAATTTGACG

Figure 3: DNA sequence analysis results of isolated microorganism species.



**Figure 4.** PCR gel image of microorganisms isolated from Ankara soil. M: 1 kb Marker. NK: Negative control, 1- *S. mutabilis*, 4- *S. collinus*, 5- *S. peucetius*.



**Figure 5.** PCR gel image of microorganisms isolated from Konya soil. M: 1kb Marker. NK: Negative control, 1-*S. cyaneofuscatius*, 2- *S. albogriseolus*, 6- *S. griseoflavus*

Chemical, molecular, and taxonomic properties of the genus *Streptomyces* have been revealed by several studies. Siddique et al. studied *S. avermitilis* isolation from different soil samples of Pakistan. Different media compositions were applied for the screening of pure *Streptomyces* species and antibacterial and antifungal activities of various isolates were studied (22). Arifuzzaman et al. investigated screening *Actinomycetes* from Sundarbans soil for antibacterial compounds against some gram-negative pathogenic bacteria. For this purpose, a GAM isolation medium was used and it was concluded that Karanjal region of Sundarbans is rich in *Actinomycetes* (23). Kumar et al. studied the isolation of *Actinomycetes* from the soil samples of the wasteland and garden of Ghaziabad and assessed their anti-bacterial properties. The SCAM medium was used according to that purpose and fifteen isolates of *Actinomycetes* showed activity against bacteria (24). In the present study six isolates, *S. mutabilis*, *S. collinus*, *S. peucetius*, *S. cyaneofuscatius*, *S. albogriseolus* and *S. griseoflavus*, are compared with the general characteristics of the *Streptomyces* species with 3 different methods specific to *Streptomyces* species.

Air, reverse side mycelium colors, and antimicrobial activities are determined.

## CONCLUSION

In this study, six *Streptomyces* species are isolated from soil samples collected randomly from Ankara and Konya regions. Studies showed that the regions of Ankara and Konya are rich in *Streptomyces* species and Methods 1-3 can be used for the isolation of *Streptomyces* species. If the specific *Streptomyces* species are to be isolated from soil, then the isolation medium in Method 1-3 must be chosen carefully to reach that specific *Streptomyces* species. Further study is in progress to see and improve antibiotics production of isolated *Streptomyces* species with fermentation using optimization methods.

## CONFLICT OF INTEREST

There is no conflict of interest.



## REFERENCES

1. Kodzius R, Gojobori T. Marine metagenomics as a source for bioprospecting. *Mar Genomics* [Internet]. 2015;24:21–30. Available from: [<URL>](#).
2. Takahashi Y, Nakashima T. Actinomycetes, an Inexhaustible Source of Naturally Occurring Antibiotics. *Antibiot (Basel, Switzerland)* [Internet]. 2018 May 24;7(2):45. Available from: [<URL>](#).
3. de Lima Procópio RE, da Silva IR, Martins MK, de Azevedo JL, de Araújo JM. Antibiotics produced by Streptomyces. *Brazilian J Infect Dis* [Internet]. 2012;16(5):466–71. Available from: [<URL>](#).
4. Poomthongdee N, Duangmal K, Pathom-aree W. Acidophilic actinomycetes from rhizosphere soil: diversity and properties beneficial to plants. *J Antibiot (Tokyo)* [Internet]. 2015;68(2):106–14. Available from: [<URL>](#).
5. De Simeis D, Serra S. Actinomycetes: A Never-Ending Source of Bioactive Compounds—An Overview on Antibiotics Production. Vol. 10, *Antibiotics*. 2021. Available from: [<URL>](#).
6. Hug JJ, Bader CD, Remškar M, Cirnski K, Müller R. Concepts and Methods to Access Novel Antibiotics from Actinomycetes. *Antibiot (Basel, Switzerland)* [Internet]. 2018 May 22;7(2):44. Available from: [<URL>](#).
7. Chater KF. Recent advances in understanding Streptomyces. *F1000Research* [Internet]. 2016 Nov 30;5:2795. Available from: [<URL>](#).
8. Barka EA, Vatsa P, Sanchez L, Gaveau-Vaillant N, Jacquard C, Klenk H-P, et al. Taxonomy, physiology, and natural products of Actinobacteria. *Microbiol Mol Biol Rev*. 2016;80(1):1–43. Available from: [<URL>](#).
9. Tchinda RAM, Boudjeko T, Simao-Beanoir A-M, Lerat S, Tsala É, Monga E, et al. Morphological, physiological, and taxonomic characterization of actinobacterial isolates living as endophytes of cacao pods and cacao seeds. *Microbes Environ*. 2016;ME15146. Available from: [<URL>](#).
10. Book AJ, Lewin GR, McDonald BR, Takasuka TE, Wendt-Pienkowski E, Doering DT, et al. Evolution of high cellulolytic activity in symbiotic Streptomyces through selection of expanded gene content and coordinated gene expression. *PLoS Biol*. 2016;14(6):e1002475. Available from: [<URL>](#).
11. Anderson AS, Wellington EM. The taxonomy of Streptomyces and related genera. *Int J Syst Evol Microbiol*. 2001 May;51(Pt 3):797–814. Available from: [<URL>](#).
12. Williams ST. Genus Streptomyces waksman and henrici 1943. *Bergey's Man Syst Bacteriol*. 1989;4:2452–92. Available from: [<URL>](#).
13. Sharma A, Gautam S, Saxena S. Streptomyces. In: Batt CA, Tortorello MLBT-E of FM (Second E, editors. Oxford: Academic Press; 2014. p. 560–6. Available from: [<URL>](#).
14. Ogata S. Morphological and physiological differentiation in Streptomyces. *J Agric Chem Soc Japan*. 1991. Available from: [<URL>](#).
15. Hain T, Ward-Rainey N, Kroppenstedt RM, Stackebrandt E, Rainey FA. Discrimination of Streptomyces albidoflavus Strains Based on the Size and Number of 16S-23S Ribosomal DNA Intergenic Spacers. *Int J Syst Evol Microbiol* [Internet]. 1997;47(1):202–6. Available from: [<URL>](#).
16. Stackebrandt E, Rainey FA, Ward-Rainey NL. Proposal for a new hierarchic classification system, Actinobacteria classis nov. *Int J Syst Bacteriol*. 1997;47(2):479–91. Available from: [<URL>](#).
17. Kim B, Sahin N, Minnikin DE, Zakrzewska-Czerwinska J, Mordarski M, Goodfellow M. Classification of thermophilic streptomycetes, including the description of Streptomyces thermoalcalitolerans sp. nov. *Int J Syst Bacteriol*. 1999 Jan;49 Pt 1:7–17. Available from: [<URL>](#).
18. Labeda DP. DNA relatedness among strains of the Streptomyces lavendulae phenotypic cluster group. *Int J Syst Bacteriol* [Internet]. 1993;43(4):822–5. Available from: [<URL>](#).
19. Labeda DP, Lyons AJ. Deoxyribonucleic Acid Relatedness Among Species of the “Streptomyces cyaneus” Cluster. *Syst Appl Microbiol* [Internet]. 1991;14(2):158–64. Available from: [<URL>](#).
20. Williams ST, Goodfellow M, Wellington EM, Vickers JC, Alderson G, Sneath PH, et al. A probability matrix for identification of some Streptomyces. *J Gen Microbiol*. 1983 Jun;129(6):1815–30. Available from: [<URL>](#).
21. Rashad FM, Fathy HM, El-Zayat AS, Elghonaimy AM. Isolation and characterization of multifunctional Streptomyces species with antimicrobial, nematicidal and phytohormone activities from marine environments in Egypt. *Microbiol Res* [Internet]. 2015;175:34–47. Available from: [<URL>](#).
22. Siddique S, Syed Q, Adnan A, Qureshi FA. Isolation, Characterization and Selection of Avermectin-Producing Streptomyces avermitilis Strains From Soil Samples. *Jundishapur J Microbiol* [Internet]. 2014/06/01. 2014 Jun;7(6):e10366–e10366. Available from: [<URL>](#).
23. Arifuzzaman M, Khatun M, Rahman H. Isolation and screening of actinomycetes from Sundarbans soil for antibacterial activity. *African J Biotechnol*. 2010;9:4615–9. Available from: [<URL>](#).
24. Kumar N, Singh R, Mishra S, Singh A, Pachouri UC. Isolation and screening of soil Actinomycetes as source of antibiotics active against bacteria. *Int J Microbiol Res*. 2010 May 10;2:12–6. Available from: [<URL>](#).







## A Study on Drying of Thin-Layer Pepino by Infrared and Microwave Methods and Their Color Analysis\*

Zehra Ozden OZYALCIN<sup>1</sup> , Azmi Seyhun KIPCAK <sup>1\*</sup>

<sup>1</sup>Department of Chemical Engineering, Yildiz Technical University, Istanbul, 34220, Turkey.

**Abstract:** Pepino is an exotic fruit that contains high vitamin C and is known to have many beneficial effects on health. In this study, thin layer drying and color changes of pepino fruit by infrared (IR) and microwave (MW) methods were investigated. Effective moisture diffusions and activation energy were calculated from the drying data. Uniformly sliced pepino fruit was processed without peeling. While IR drying processes were performed at 60, 70, and 80 °C temperatures in 210, 165, and 120 minutes, respectively, MW drying processes were completed at 25, 16, and 6 minutes at 140, 210, and 350 W power levels. While the initial average moisture content was 18.5702 kg water/kg dry, the lowest moisture content was determined as 0.3250 at 80 °C in IR and 0.1263 water/kg dry matter×min at 350 W at MW. Effective moisture diffusions ( $D_{eff}$ ) for IR were calculated between  $6.69 \times 10^{-10}$  -  $1.23 \times 10^{-9}$  m<sup>2</sup>/s, while for MW it was found between  $8.75 \times 10^{-9}$  -  $3.75 \times 10^{-8}$  m<sup>2</sup>/s. The activation energy ( $E_a$ ) was 29.80 kJ/mol for IR and 33.30 kW/kg for MW. In addition, it was determined that color preservation was better in the IR method, and local burns were observed in the samples in the microwave method.

**Keywords:** Activation Energy, Drying Rate, Effective Moisture Diffusivity, Exotic Fruit, *Solanum maricatum*.

**Submitted:** October 03, 2022. **Accepted:** November 01, 2022.

**Cite this:** Ozyalcin ZO, Kipcak AS. A Study on Drying of Thin-Layer Pepino by Infrared and Microwave Methods and Their Color Analysis. JOTCSB. 2022;5(2):167-72.

\*Corresponding author. E-mail: [skipcak@yildiz.edu.tr](mailto:skipcak@yildiz.edu.tr).

### INTRODUCTION

Pepino (*Solanum maricatum*) is a thin-skinned and juicy tropical, semi-tropical fruit of the nightshades family. Pepino, whose taste is often likened to melon and cucumber, can also be called pepino melon, melon pear, or tree melon. It is produced in South America, Australia, New Zealand, and the USA. Studies have shown that pepino has protective effects against many health problems thanks to its high vitamin C content (1).

Preservation of foodstuffs and especially fruits are generally provided by drying processes. While thermal-based traditional methods have been used for years, numerous drying techniques have been developed as a result of the need for lower costs and higher final product quality. Microwave drying is a technique based on electromagnetic waves, independent of the product's thermal properties to be dried. The main benefit of choosing it is that it offers instant drying, which saves time and energy

(2 - 4). In addition, infrared drying takes place by absorbing the energy provided by the source by the product to be dried without heating the air in the environment and drying the product by turning it into thermal energy. This method, which has a high-end product quality, is gaining popularity due to energy savings (4, 5).

Although there are studies on drying exotic fruits, there are relatively few studies on pepino, and those that exist are often based on conventional techniques. A few examples of studies on exotic fruits can be given as follows; Raaf et al. studied oven and sun drying kinetics and mathematical modelling of amla fruit (6), Ozgen and Celik evaluated the design parameters on convective dryer of kiwi slices (7), Raj and Dash investigated the microwave vacuum drying kinetics of dragon fruit slice (8). Izli et al. studied mango drying with freeze dryer, microwave, and hot air drying techniques (9), Luelue et al. investigated microwave vacuum drying of lychee fruit and the

microstructure change due to drying (10). As an example of the few pepino drying studies, Uribe et al. examined the conventional drying and mathematical modeling of pepino at different temperatures (11). Di Scala et al. examined the traditional drying of pepino and the examination of its physicochemical properties (12). According to Izli et al. examined pepino drying using a combination of conventional methods and microwaves at different temperatures and power levels (13). Ozcan et al. studied the effect of microwave and oven drying on the bioactive compounds of pepino (14).

In this study, the behavior of Pepino fruit in thin layer drying with infrared and microwave processes was investigated and effective moisture diffusion, activation energy, and color changes were calculated.

## MATERIALS AND METHODS

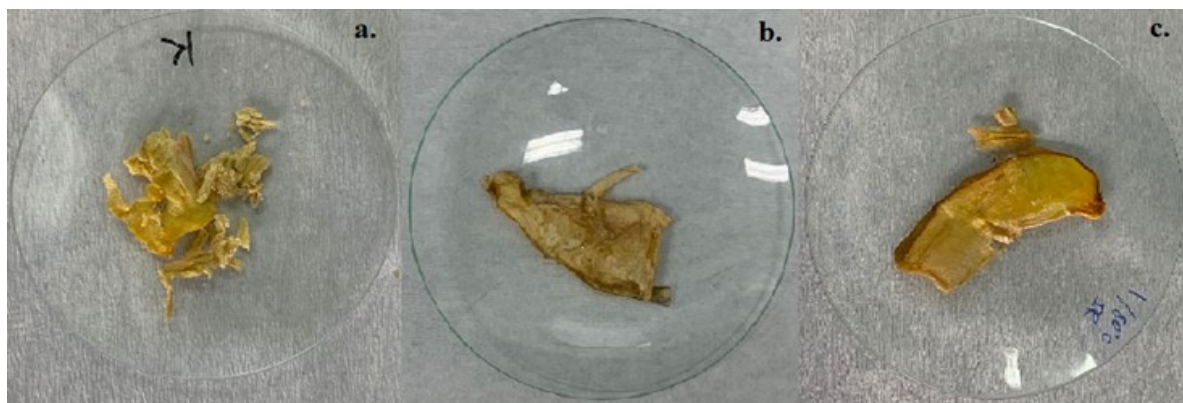
### Apparatus

Pepinos purchased from a local grocery chain in Istanbul, Turkey in April 2021 were sliced unpeeled with a thickness of  $5 \pm 0.01$  mm and weight of  $10 \pm 0.15$  grams. Dimensions were measured with manual calipers and weights were measured with a Radwag AS 220.R2 digital balance (Radwag

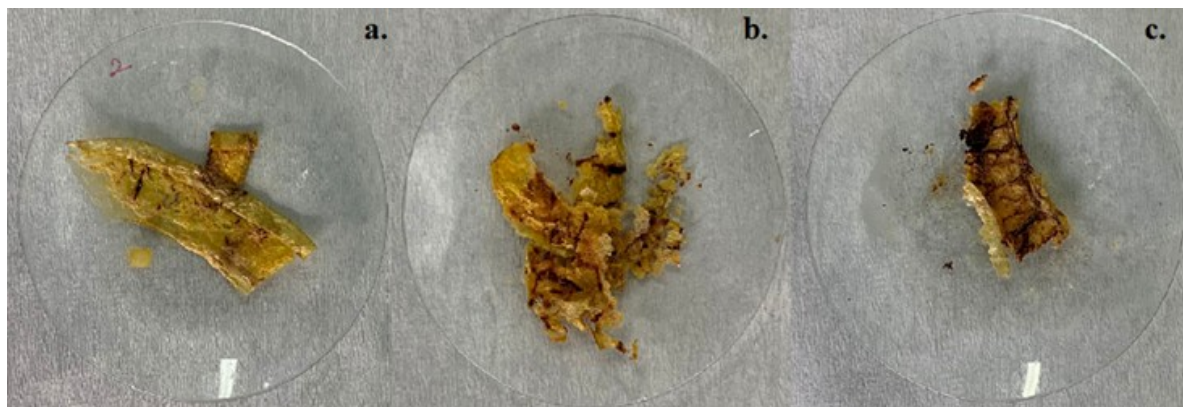
Balances and Scales, Radom, Poland). The sliced samples were processed in the oven Nüve EV-018 (Nüve, Ankara, Turkey) for 3 hours at  $105 \text{ }^\circ\text{C}$  to determine the moisture content according to the Association of Official Analytical Chemists (AOAC, 2005) procedure (15). In drying processes using unpeeled pepinos with a thickness of  $5 \pm 0.01$  mm and  $10 \pm 0.15$  grams, MA 50.R model infrared moisture analyzer (Radwag Balances and Scales, Radom, Poland) at 60, 70 and  $80 \text{ }^\circ\text{C}$  and Delonghi MW205S microwave dryer (Delonghi, Treviso, Italy) at power levels of 140, 210 and 350 W were used. Color changes of the samples before and after drying were determined with a PCE-CSM 1 model (PCE Instruments UK Ltd., Southampton Hampshire, UK) color analyzer.

### Drying Kinetics Calculations

The moisture content was calculated to be 94.89% on a wet basis and 18.5702 kg water/kg dry matter by moisture determination. During the drying process, weight measurements were made at intervals of 15 minutes for IR and 1 minute for MW, and drying was continued until the moisture content of the samples fell below 10%. After drying, the samples are shown in Figures 1 and 2 for IR and MW, respectively.



**Figure 1:** IR dried samples at a. 60 °C, b. 70 °C, and c. 80 °C.



**Figure 2:** MW dried samples at a. 140 W, b. 210 W, and c. 350 W.

During the falling rate period, in which the drying occurs substantially, moisture is transported from the center to the surface by diffusion. It then evaporates into the surrounding environment of the product, resulting in the mass transfer of moisture. The diffusion mechanism of drying is explained by Fick's second law equation. Moisture content (M) and moisture ratio (MR) required for the application of this law are calculated by Equations 1 and 2 (16):

$$M = \frac{m_w}{m_d} \quad (\text{Eq. 1})$$

$$MR = \frac{M_t - M_e}{M_0 - M_e} \quad (\text{Eq. 2})$$

where M is the moisture content (kg water/kg dry matter),  $m_w$  is the water content (kg) and,  $m_d$  is the dry matter content (kg). MR stands for the moisture ratio,  $M_0$ ,  $M_t$ , and  $M_e$  are moisture content at initial, at any time, and at equilibrium in kg water/kg dry matter. Effective moisture diffusivity can be calculated using MR value as in Equation 3, by taking its logarithm as in Equation 4 to linearize the equation;

$$MR = \frac{8}{\pi^2} \exp\left(-\frac{\pi^2 D_{eff} t}{4L^2}\right) \quad (\text{Eq. 3})$$

$$\ln(MR) = \ln\left(\frac{8}{\pi^2}\right) - \left(\frac{\pi^2 D_{eff}}{4L^2} t\right) \quad (\text{Eq. 4})$$

The activation energy was calculated based on the temperature and power provided by the drying devices. Arrhenius-type equations for temperature-based IR and power-based MW operations are given in Equations 5 and 6 (17):

$$D_{eff} = D_0 \exp\left(\frac{E_a}{RT}\right) \quad (\text{Eq. 5})$$

$$D_{eff} = D_0 \exp\left(-\frac{E_a m}{P}\right) \quad (\text{Eq. 6})$$

where  $E_a$  is the activation energy value (kJ/mol),  $D_0$  is the pre-exponential factor of the Arrhenius equation ( $m^2/s$ ),  $R$  is the universal gas constant (8.314 kJ/mol.K),  $P$  is the microwave power (W) and  $m$  is the sample weight (kg). When the graph of  $\ln(D_{eff})$  versus  $1/T$  for IR and  $\ln(D_{eff})$  versus  $m/P$  for MW is plotted. For MW the activation energy is the slope of its graph, for IR  $E_a$  can be calculated as shown in Equation 7:

$$E_a = -\text{slope} \times R \quad (\text{Eq. 7})$$

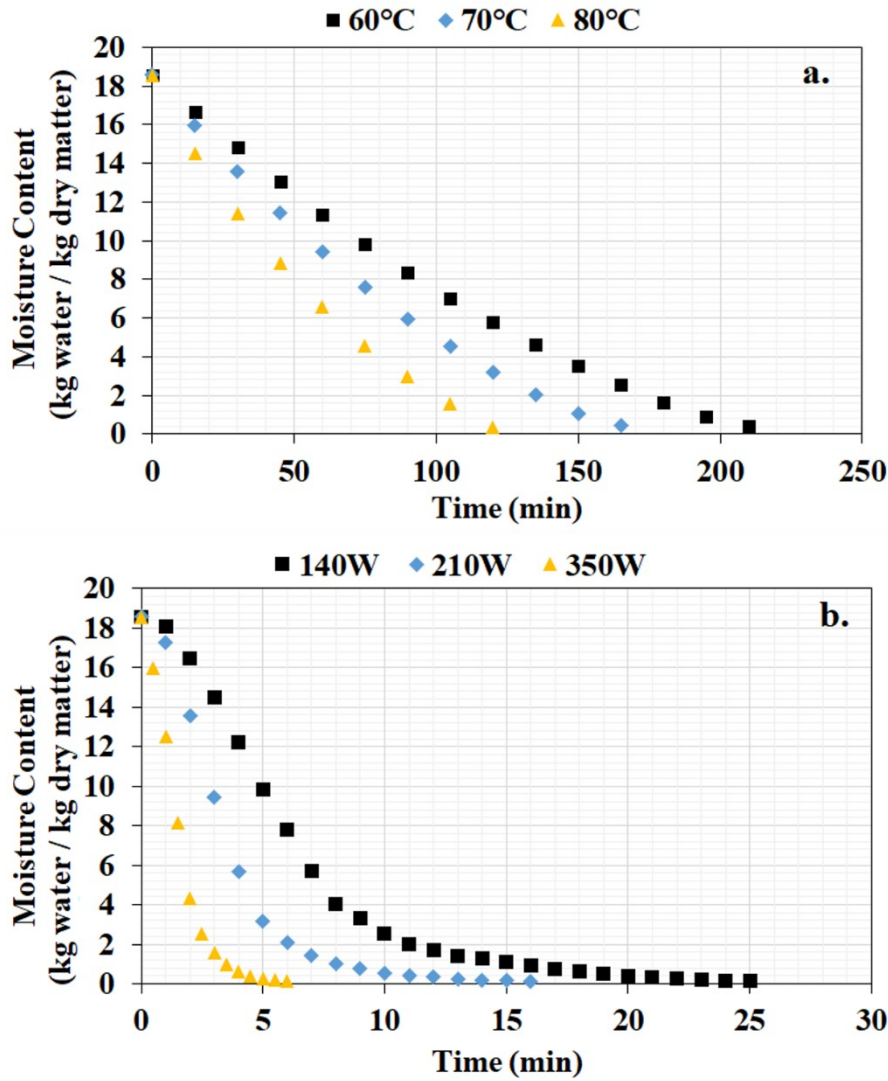
To audit the quality standards of the dried products, color analysis was performed on each sample from 5 different regions, before and after the experiment. In the color analysis, the lightness/darkness value  $L^*$ , the redness/greenness value  $a^*$ , and the yellowness/blueness value  $b^*$  were measured and the  $\Delta E$  (color change) values of the dried samples, which were the difference with the untreated sample, were calculated by Equation 8 (16):

$$\Delta E = \sqrt{(L_0 - L)^* + (a_0 - a)^* + (b_0 - b)^*} \quad (\text{Eq. 8})$$

where,  $L_0^*$ ,  $a_0^*$ , and  $b_0^*$  values are the  $L^*$ ,  $a^*$ , and  $b^*$  values of the raw samples, respectively.

## RESULTS AND DISCUSSION

The drying curves of the samples whose initial average moisture content was determined as 18.5702 kg water/kg dry matter are given in Figure 3. The final moisture values of the samples dried at IR 60, 70, and 80 °C for 210, 165, and 120 minutes, respectively, were found as 0.4306, 0.4218, and 0.3250 kg water/kg dry matter. In addition, the final moisture values of the samples dried for 25, 16, and 6 minutes at MW 140, 210, and 350 W, respectively, were found to be 0.1322, 0.1286, and 0.1263 kg water/kg dry matter. These results indicate that a decrease in drying times and final moisture contents is brought about by an increase in temperature and power levels. Comparing MW and IR techniques, it can be said that MW offers instant drying.



**Figure 3:** Drying curves for a. IR- and b. MW-dried pepino.

Effective moisture diffusion values were calculated using the slope from the logarithmic moisture content-time plot shown in Figure 4. The slope values for IR at 60, 70 and 80 °C can be read in the graphs as -0.000264, -0.000343, and -0.000486 and as -0.003454, -0.005561, and -0.014812 for MW. The effective moisture diffusion values calculated from here are;  $6.69 \times 10^{-10}$ ,  $8.69 \times 10^{-10}$ , and  $1.23 \times 10^{-9} \text{ m}^2/\text{s}$  for IR at 60, 70 and 80 °C, respectively,  $8.75 \times 10^{-9}$ ,  $1.41 \times 10^{-8}$ , and  $3.75 \times 10^{-8} \text{ m}^2/\text{s}$  for MW at 140, 210 and 350 W.

The results show that effective moisture diffusion increases with increasing temperature levels and

energy levels. This situation can be interpreted as the increase in diffusion as a result of the acceleration of the molecules with the increase in the energy taken by the unit cell.

Activation energies calculated using Figure 4 and equations 5 and 6 are 29.80 kJ/mol for IR and 33.30 kW/kg for MW. Using data from the color analysis, total color change values were calculated and were found as 9.89, 10.67, and 12.43 for IR at 60, 70, and 80 °C, respectively, and as 11.14, 12.36, and 19.91 for MW at 140, 210 and 350 W, respectively.

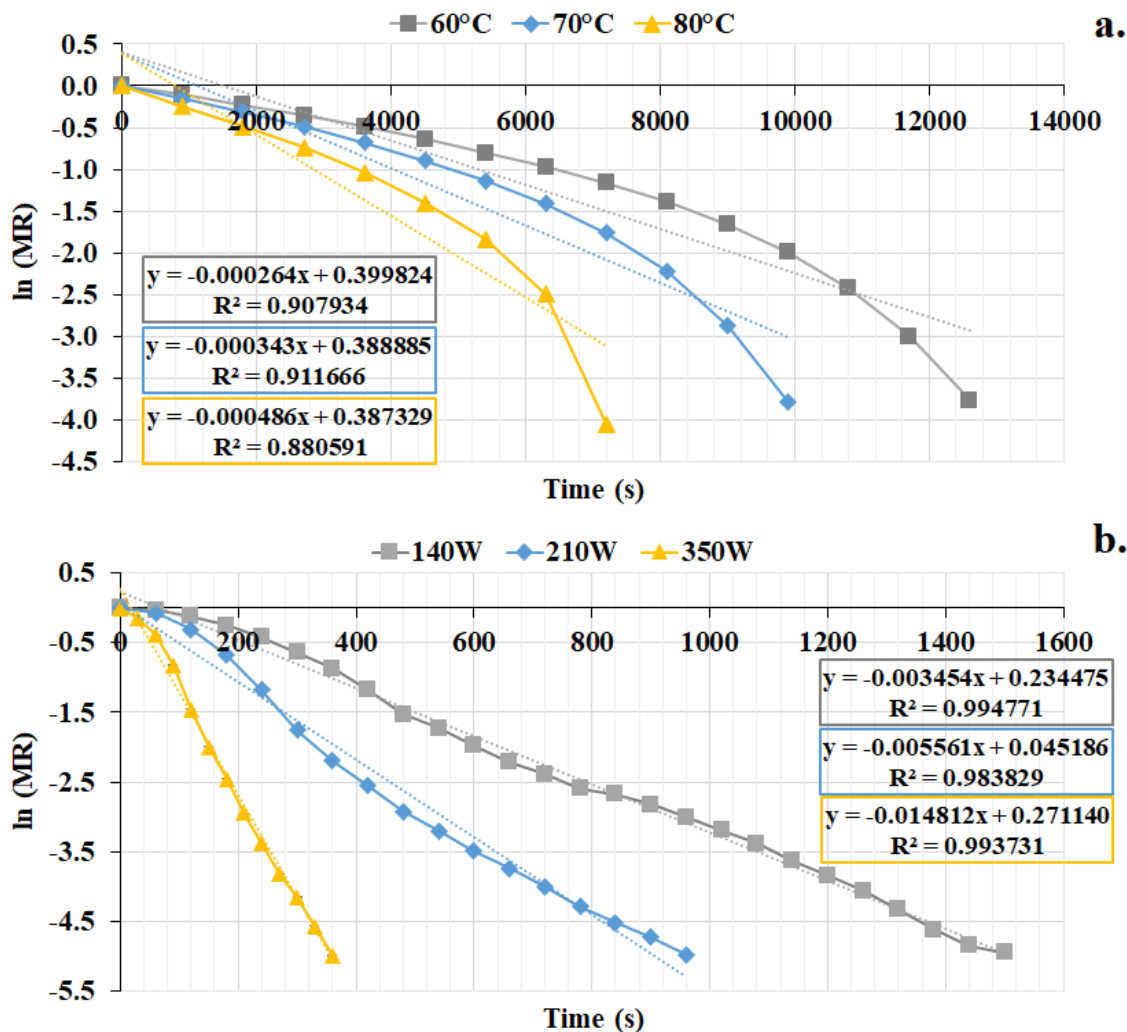


Figure 4: In(MR) vs time graph for a. IR and b. MW.

All drying results are summarized in Table 1. As can be seen from Figures 1 and 2, and the color values in the table, local burns have occurred in the MW due to instantaneous high power levels and the

quality of the final product has deteriorated considerably. In addition, it was determined that the lowest change was achieved in 80 °C products, which have the fastest drying time in IR.

Table 1: Data for thin-layer drying of pepino.

Drying method	Drying time (min)	Final moisture content (kg water/kg dry matter)	Effective moisture diffusivity (m <sup>2</sup> /s)	Color change (ΔE)
IR - 60 °C	210	0.4306	$6.69 \times 10^{-10}$	9.89
IR - 70 °C	165	0.4218	$8.69 \times 10^{-10}$	10.67
IR - 80 °C	120	0.3250	$1.23 \times 10^{-9}$	12.43
MW - 140 W	25	0.1322	$8.75 \times 10^{-9}$	11.14
MW - 210 W	16	0.1286	$1.41 \times 10^{-8}$	12.36
MW - 350 W	6	0.1263	$3.75 \times 10^{-8}$	19.91

**CONCLUSION**

In this study, infrared and microwave drying properties of thin-layer sliced pepino fruit were investigated. Effective moisture diffusivity values, activation energies, and drying rates were

calculated and color changes of dried fruits as a quality parameter were investigated. As a result of the experimental studies, it has been determined that the sample final moisture contents and drying times in MW drying are much less than IR. In addition, local burns occurred due to rapid drying in



MW, but no burnt areas were found in the samples dried with IR. The color analysis supported visual examinations and the least color change was observed with IR. Accordingly, it can be said that IR drying is more effective when the quality of the final product is ahead of the drying time.

## ACKNOWLEDGMENTS

The authors received no financial support for the research, authorship, and/or publication of this article.

## REFERENCES

- Gurung S, Chakravarty S, Chhetri B, Khawas T. An introduction to Pepino (*Solanum muricatum Aiton*): Review. International Journal of Environment, Agriculture and Biotechnology. 2016;1(2):143-8. Available from: [<URL>](#).
- Lenaerts S, Van Der Borght M, Callens A, Van Campenhout L. Suitability of microwave drying for mealworms (*Tenebrio molitor*) as alternative to freeze drying: Impact on nutritional quality and colour. Food Chemistry. 15 July 2018;254:129-36. Available from: [<URL>](#).
- Radoiu M. Microwave drying process scale-up. Chemical Engineering and Processing - Process Intensification. Sep;2020;155:108088. Available from: [<URL>](#).
- Ozyalcin ZO, Kipcak AS. The Effect of Ultrasonic Pre-Treatment on the Temperature Controlled Infrared Drying of *Loligo Vulgaris* and Comparison with the Microwave Drying. Turkish Journal of Fisheries and Aquatic Sciences. 29 Dec;2020;21(03):135-45. Available from: [<URL>](#).
- Delfiya DSA, Prashob K, Murali S, Alfiya PV, Samuel MP, Pandiselvam R. Drying kinetics of food materials in infrared radiation drying: A review. Journal of Food Process Engineering. 2022;45(6):e13810. Available from: [<URL>](#).
- Raaf A, Putra TW, Mulana F, Syamsuddin Y, Supardan MD. Investigation of kinetics of amla (*Emblica officinalis*) fruit drying process. South African Journal of Chemical Engineering, 2022;41, 10-16. Available from: [<URL>](#).
- Ozgen F, Celik N. Evaluation of Design Parameters on Drying of Kiwi Fruit. Applied Sciences. 2019; 9(1):10. Available from: [<URL>](#).
- Raj Bhagya, Dash Kshirod. Microwave vacuum drying of dragon fruit slice: Artificial neural network modelling, genetic algorithm optimization, and kinetics study. Computers and Electronics in Agriculture. 2020; 178, 105814. Available from: [<URL>](#).
- Izli N, Izli G, Taşkın O. Influence of different drying techniques on drying parameters of mango. Ciência e Tecnologia de Alimentos. 2017; 37. Available from: [<URL>](#).
- Luelue H, Qiao F, Fan D. Microstructure changing and moisture removing of lychee during microwave vacuum drying. International Journal of Agricultural and Biological Engineering 9.3 2016; 162-169. Available from: [<URL>](#).
- Uribe E, Vega-Galvez A, Di Scala K, Oyanadel R, Saavedra Torrico J, Miranda M. Characteristics of Convective Drying of Pepino Fruit (*Solanum muricatum Ait.*): Application of Weibull Distribution. Food and Bioprocess Technology. 01 Nov;2009;4:1349-56. Available from: [<URL>](#).
- Di Scala K, Vega-Galvez A, Uribe E, Oyanadel R, Miranda M, Vergara J, vd. Changes of quality characteristics of pepino fruit (*Solanum muricatum Ait*) during convective drying. International Journal of Food Science & Technology. 14 Feb;2011;46:746-53. Available from: [<URL>](#).
- Izli G, Taskin O, Izli N. Convective, Microwave and Combined Microwave-Convective Drying of Pepino. Erwerbs-Obstbau. 01 June;2021;63(2):175-84. Available from: [<URL>](#).
- Ozcan MM, Al Juhaimi F, Ahmed IAM. et al. Effect of microwave and oven drying processes on antioxidant activity, total phenol and phenolic compounds of kiwi and pepino fruits. J Food Sci Technol; 2020;57, 233-242. Available from: [<URL>](#).
- AOAC. Official method of Analysis. 18th Edition. Washington DC. USA: 2005. Association of Officiating Analytical Chemists.
- Ozyalcin ZO, Kipcak AS. The Ultrasound Effect on the Drying Characteristics of *Loligo vulgaris* by the Methods of Oven and Vacuum-oven. Journal of Aquatic Food Product Technology. 07 Feb;2022;31(2):187-99. Available from: [<URL>](#).
- Doymaz I, Kipcak AS, Piskin S. Microwave drying of green bean slices: drying kinetics and physical quality. Czech Journal of Food Sciences. 21 July;2015;33 (2015) (No. 4):367-76. Available from: [<URL>](#).



## Evaluation of the Removal Efficiency of Diclofenac in the Aquatic Environment by Combined Coagulation and Adsorption Processes

Kadir Özdemir<sup>1\*</sup> , Esin Aras<sup>1</sup> 

<sup>1</sup>Zonguldak Bülent Ecevit University, Faculty of Engineering, Department of Environmental Engineering, 67100 Zonguldak, Turkey.

**Abstract:** In decades, the presence of anti-inflammatory drugs diclofenac (DCF) in water resources has become an extremely threatening factor in terms of environmental protection and pollution. In this study, the removal efficiencies of DCF in aqueous sources were studied by adsorption, conventional coagulation, and combined coagulation methods using carbon nanotubes (CNTs). Experimental studies were carried out by adding certain doses of 1 g/L stock DCF solution prepared in the laboratory to water samples. In order to determine the adsorbing capacity of DCF, three different adsorbents as single-walled CNT (SWCNT), multi-walled CNT (MWCNT), and powdered activated carbon (PAC) were used as a function of pH and ionic strength. As a result of batch adsorption experiments performed in both ULW and UDWTP samples, the highest DCF sorption capacity was observed in SWCNT at pH =3 as 4.82 mg.g<sup>-1</sup> and 3.82 mg.g<sup>-1</sup>, respectively, and also DCF adsorption capacity increased when the ionic strength was increased from 6.0×10<sup>-1</sup> to 1.0 M. Furthermore, the experimental results showed that the Freundlich equation about correlation coefficient ( $R^2=0.99$ ) is the best isotherm model to describe the adsorption process in all water sources. On the other hand, results in coagulation experiments demonstrated that the maximum removal percentages of DCF in ULW (94.81%) and UDWTP (91.97%) occurred with combined SWCNT with Alum compared to only Alum coagulation. Experimental data obtained in this study reveal that combined coagulation with CNTs is more appropriate to minimize the pollution caused by DCF, especially in the aquatic environment, rather than adsorption and coagulation processes.

**Keywords:** Diclofenac, environmental protection, adsorption, combined coagulation.

**Submitted:** September 21, 2022. **Accepted:** November 07, 2022.

**Cite this:** Özdemir K, Aras E. Evaluation of the Removal Efficiency of Diclofenac in the Aquatic Environment by Combined Coagulation and Adsorption Processes. JOTCSB. 2022;5(2):173-82.

**\*Corresponding author. E-mail:** [kadir.ozdemir@beun.edu.tr](mailto:kadir.ozdemir@beun.edu.tr)

### INTRODUCTION

The scarcity of natural water resources potential and water pollution are among the leading global problems that should be emphasized (1). Wastewater discharged from various sources to the environment constitutes an important part of water pollution. Further, the structure and composition of the pollutants in the water vary depending on the result of houses, agricultural areas, hospitals, human activities, and different industrial processes (2). These new generation pollutants, called micropollutants, which are found in water from nanograms to micrograms, are resistant compounds that are difficult to remove with conventional treatment methods. (3). They can also occur as

perfluorinated compounds, dioxins, aromatic hydrocarbons, and by-products of primary pollutants, as well as carbon-based compounds as solvents, pesticides, industrial chemicals, and by-products in the environmental environment (4). Micropollutants cause short and long-term toxicological effects such as antibiotic resistance and hormonal disorders in terms of human health (5). Currently, there is no regulated standard for important micropollutants such as pharmaceutical compounds, EDC, and PPCPs. In our country, "Environmental Quality Standard" values have been determined for micropollutants in order to protect and improve the quality of water resources within the scope of the "Regulation on Surface Water Quality" (6).



Pharmaceutical compounds (Pharmaceuticals), personal care products (PPCPs), and endocrine disrupting chemicals (EDCs) are among the most common types of micropollutants in aquatic environments such as surface waters, groundwater, drinking water, and wastewater treatment plants (7).

DCF, 2-[(2,6-dichlorophenyl)amino]phenylacetic acid, is a water-soluble (polar) non-steroidal anti-inflammatory drug with a permanent structure (8). It is often used to treat inflammation and pain in pathologies such as rheumatoid arthritis (9). After DCF is taken into the body, it is excreted in the urine with the resulting metabolites and less than 1% unchanged molecule as a result of biotransformation (10). DCF is of great importance in terms of environmental risk, as it has the highest acute effect among chemicals with an anti-inflammatory nature. In the studies, the lowest effect concentration (LOEC) value was observed in fish; changes in the liver, kidney, and gill cells have been reported at a DCF concentration of 1 µg/L, and deterioration in the renal tissue and changes in gill structures at a LOEC of 5 µg/L (11). Depending on its common use, DCF residues have often been detected in surface water sources, rivers, and water treatment plants. Many studies in the literature have revealed that conventional treatment processes such as coagulation and filtration, and adsorption, especially used in drinking water treatment plants, are ineffective in the removal of DCF (12). There are many studies on the removal of diclofenac in the literature (13-15). Suarez et al. investigated the removal efficiencies of pharmaceuticals such as DCF, naproxen, ibuprofen, and carbamazepine with conventional treatment processes (coagulation-flocculation + filtration) in their study on hospital wastewater (16). As a result of conventional treatment, they observed that the removal efficiencies of DCF, naproxen, ibuprofen, and carbamazepine were 22%, 31%, 12%, and 6%, respectively. Marcela et al. observed that the removal efficiencies of DCF vary between 5% and 40% in their studies using conventional treatment processes (17). Kennedy et al. observed a removal efficiency between 20% and 50% in the adsorption studies of 30 drug-based micropollutants, including DCF, with granular activated carbon at a pilot scale in drinking water treatment plants (18). In adsorption experiments using laboratory-scale powdered activated carbon, it was determined that micropollutants were removed at a higher efficiency when the activated carbon dose was increased (19). In the literature research on DCF removal, when carried out with advanced oxidation processes such as UV+H<sub>2</sub>O<sub>2</sub>, Fenton process (Fe<sup>2+</sup> + H<sub>2</sub>O<sub>2</sub> → Fe<sup>3+</sup> + OH• + OH<sup>-</sup>), ozonation, UV+ ozonation, ozonation + peroxane (O<sub>3</sub> + H<sub>2</sub>O<sub>2</sub>), ozonation + UV+H<sub>2</sub>O<sub>2</sub> and photocatalytic processes, the removal efficiencies found to be higher (21). On the other hand, carbon nanotubes (CNTs) have large surface areas and they

are extraordinary properties with their porous and layered structures, generally, single-walled carbon nanotubes (SWCNTs) and multi-walled carbon nanotubes (MWCNTs) are used in water treatment (20). Due to their adjustable physical, chemical, and electrical structures, they are often used in water treatment technology as organic and inorganic substances, heavy metals, volatile organics, personal care products, pharmacological products, and endocrine disruptors. It is widely used as an effective adsorbent in the removal of micropollutants such as chemicals (21, 22). Further, since some of the CNTs are hydrophilic, they can easily remove most of the micropollutants thanks to their high solubility in water and high adsorption properties. In this study, considering these disadvantages of the treatment processes used to date for the removal of micropollutants, the use of carbon nanotube materials, which have become very attractive, as a coagulant material has been considered as an alternative. There is a few number of studies in the literature comparing the removal efficiency of DCF compounds using adsorption and combined coagulation processes. Therefore, the original value of this study is that it will be one of the first studies in which it is planned to remove micropollutants that cannot be removed by conventional treatment methods such as coagulation and adsorption in drinking water sources, using CNT materials as coagulants, with high efficiency by combined coagulation method.

## EXPERIMENTAL

### Water source and sampling

The water samples used in the experimental studies were taken from Ulutan Dam (ULW), which provides drinking water to Zonguldak in Turkey, and from the Ulutan drinking water treatment plant outlet (UDWTP). Water quality parameter values related to water samples are given in Table 1.

The samples were taken as single samples in 5 L glass containers and quickly delivered to the laboratory. The water samples were kept in the refrigerator at +4 °C against any microbial activity until they were used in experimental studies.

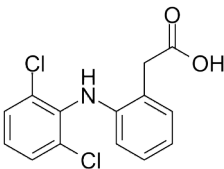
### Chemicals and Reagents

DCF was supplied by Sigma Aldrich (Germany). Table 2 displays the chemical structure and physical properties of DCF. The stock solution of DCF was prepared by weighing 0.1 g with an analytical balance and dissolved completely in 1 L of distilled water.

**Table 1:** Physicochemical characteristics of water sources.

Parameter s	Unit	Ulutan Dam (ULW)		Ulutan Drinking Water Treatment Plant (UDWTP)	
		Min-Max.	Average	Min-Max.	Average
pH	°	7.07-7.42	7.21	7.68-8.16	7.88
Turbidity	NTU	3.1-8.6	4.2	0.3-0.9	0.6
Conductivity	µS/cm	385-696	543	211-487	328
Alkalinity	mg/L	88-132	118	104-139	130
T. Hardness	CaCO <sub>3</sub>	123-171	135	132-194	149
Chloride	mg/L	41-75	54	63-125	79
TOC	mg/L	4.15-6.27	5.47	3.81-6.32	4.85
UV <sub>254</sub>	cm <sup>-1</sup>	0.07-0.12	0.85	0.08-0.14	0.11
SUVA	L/mg.m	2.17-2.61	2.35	2.58-3.02	2.75

**Table 2.** Physical and chemical properties of DCF.

CAS Number	15307-86-5
Molecular formula	C <sub>14</sub> H <sub>11</sub> Cl <sub>2</sub> NO <sub>2</sub>
Molecular structure	
Molecular weight	296.16 g/mol
Log Kow	4.5
pKa	4.15
Solubility in water	2.37 mg/L (25 °C)

SWCNTs (1–2-nm diameter, 5–30-mm length) were obtained from Cheap Tubes, Inc. (Brattleboro, Vermont, USA). MWCNTs (50–80-nm diameter, 5–9-mm length) were purchased from Sigma Aldrich (St. Louis, Missouri, USA). Aluminum sulfate (Al<sub>2</sub>SO<sub>4</sub>.18H<sub>2</sub>O) and iron(III) chloride (FeCl<sub>3</sub>) were purchased from Fisher Scientific (Fair Lawn, New Jersey, USA). Stock solutions of 10 g/L for both coagulants were prepared by adding 10 g of each chemical to 1 L of ultrapure deionized water and stirring overnight. NaCl was used to make solutions of various ionic strengths. Powdered active carbon (PAC) was purchased from Norit.

#### Purified CNTs

We followed the previous procedure for the purification of CNTs (23).

#### Coagulation Experiments

We followed the previous procedure for Coagulation Experiments (23).

#### Batch Adsorption Experiments

Stock suspensions of the adsorbents (MWCNTs, SWCNTs, and PAC) were prepared by adding 1 g of the adsorbents to 200 mL of distilled water and stirring the solution with a magnetic stirrer at 600 rpm. All the experiments were performed in the dark in a thermostat-controlled shaker, maintained at 25 °C and 200 rpm. Based on the results from preliminary kinetic studies, a stirring time of 6 h was selected as the equilibrium time for activated carbon. The amount of adsorbed DCF was calculated according to the following Equation (1);

$$Q_e = (C_0 - C_e) \times V/M \quad (\text{Eq. 1})$$

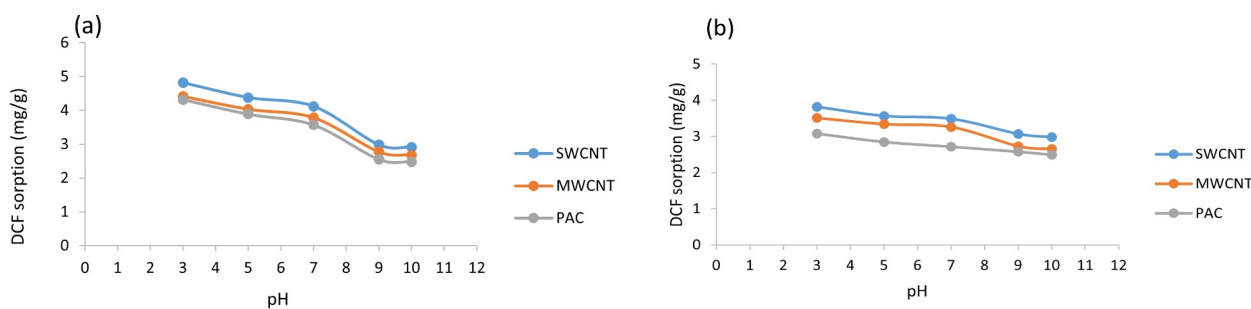
where  $Q_e$  is the adsorption capacity (mg. g<sup>-1</sup>),  $C_0$  and  $C_e$  are the initial and equilibrium concentrations in the solution (mg L<sup>-1</sup>), respectively,  $V$  is the volume of the solution (L) and  $M$  is the mass of adsorbents (g).

#### Analytical Methods

DCF analyses were performed using a UV spectrophotometer (UV-Shimadzu-1800) device at a

wavelength of 276 nm. All water samples were analyzed based on the procedures described in the Standard Methods (24). Before analysis, water samples were passed through 0.45  $\mu\text{m}$  membrane filter paper. TOC analysis (Shimadzu-5000A TOC analyzer) was conducted by the high-temperature combustion method (24).

## RESULTS AND DISCUSSION



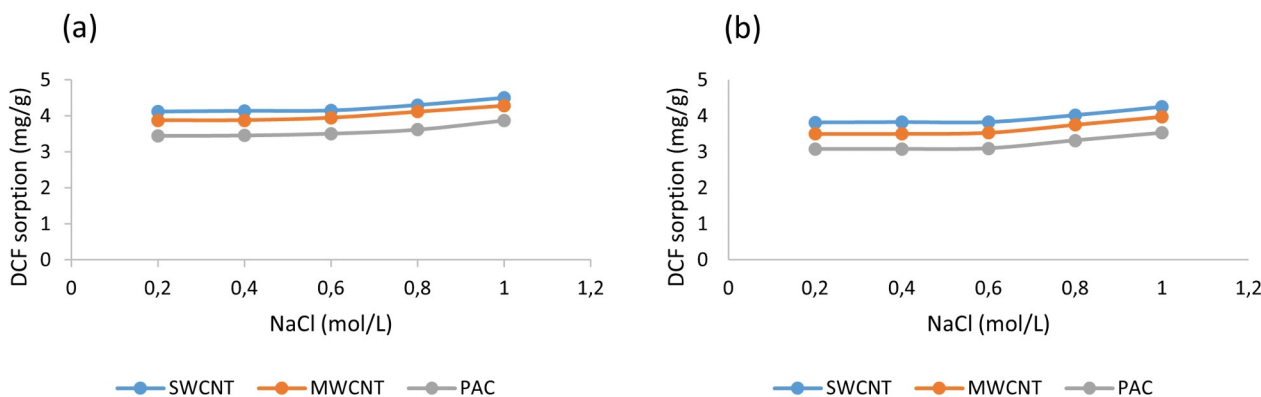
**Figure 1:** Effect of pH on DCF adsorption onto three adsorbents (a) ULW, and (b) UDWTP.

On the other hand, the sorption capacity of MWCNT and PAC was The DCF absorption capacities of MWNT and PAC at acidic pH values in Ulutan dam raw water samples varied between 4.40 and 3.90  $\text{mg.g}^{-1}$ , respectively (Fig. 1a). It is between 3.5 and 2.85  $\text{mg.g}^{-1}$  in the examples of the UDWPT (Fig. 1b). One of the important results obtained in this study is that the absorption capacity of DCF decreases significantly as the pH increases. As seen in Figure 1a, in DCF removal with SWNT, MWNT, and PAC adsorbents at pH 10, it was determined that the adsorption capacities decreased to 2.92, 2.68, and 2.48  $\text{mg.g}^{-1}$ , respectively. Similarly, DCF removal performed with all three adsorbents in the water samples taken from UDWPT is between 70% and 90% at pH 3 and decreases to 20% at pH 10 (Fig. 1b). For example; the  $Q_e$  values of ULW samples were 4.41 and 4.03  $\text{mg.g}^{-1}$  in adsorption with MWNT at pH 3 and pH 5, they decreased to 2.77 and 2.68  $\text{mg.g}^{-1}$  at pH 10, respectively. Similar results have been obtained in studies on the subject

### Impact of pH and Ionic strength on DCF Adsorption

Figure 1 presents the adsorption capacity values of DCF on SWCNT, MWCNT, and PAC adsorbents at different pH values are shown. As seen in Figure 1, in both water samples, the highest adsorption capacity of DCF ( $Q_e = 4.82 \text{ mg.g}^{-1}$ ) was observed in the adsorption processes performed with SWCNT at pH 3.

in the literature (25, 26). In other words, the increase in pH will cause the dispersion of positively charged functional groups on the surface and the formation of new negatively charged groups. At high pH ( $\text{pH} = 10$ ), due to deprotonation of the phenolic groups presented on the sorbent surface, the adsorption capacity is greatly reduced as the repulsion between the adsorbate and adsorbent negative charges increases. Moreover, electrostatic interactions are extremely important for the sorption mechanisms (11). Adsorption studies with SWCNT showed higher DCF removal compared to MWCNT and PAC. This result is probably related to the larger surface area and smaller diameter of SWCNT compared to others (27, 28). Figure 2 shows the effect of ionic strength on DCF adsorption in samples from both sources. In this study, to demonstrate the effect of ionic strength, NaCl was used to adjust the ionic strength, and five different concentrations of 0.2, 0.4, 0.6, 0.8, and 1.0 mol/L were applied to adjust the ionic strength.



**Figure 2:** Effect of ionic strength on DCF adsorption onto three adsorbents (a) ULW and (b) UDWTP.

No significant change occurs in the adsorption of DCF on SWCNT, MWCNT, and PAC up to an ionic strength of 0.6 M. When the ionic strength increased from 0.6 to 1 M, the adsorption of DCF also increased from 4.15 to 4.5 for SWCNT, from 3.95 to 4.29 mg.g<sup>-1</sup> for MWCNT, and from 3.51 to 3.87 mg.g<sup>-1</sup> for PAC at ULW samples (Figure 2a). Similarly, in the samples taken from the treatment plant, the adsorption capacity increased from 3.82 to 4.25 mg.g<sup>-1</sup> for SWCNT, from 3.51 to 3.98 mg.g<sup>-1</sup> for MWCNT, and from 3.08 to 3.53 mg.g<sup>-1</sup> for PAC (Figure 2b). This situation can be explained that sorbent particles and DCF molecules are both surrounded by an electric double layer due to electrostatic interactions. Based on the Gouy-Chapman theory of the diffuse double layer, the thickness of the double layer is compressed by an increase in the ionic strength of the solution (29). Further, the increase in ionic strength could enhance the uptake of ionic compounds such as DCF by CNTs because of a screening effect of the surface charge produced by the added salt (30, 31).

**Adsorption Isotherms**

In this study, Langmuir and Freundlich isotherm models were used to determine the adsorption capacity of DCF in both the raw water samples of the ULW and UDWTP samples. The linearized Langmuir isotherm model is expressed by the following Equation (2);

$$1/Q_e = (1/K_L * Q_o * 1/C_e) + 1/Q_o \quad (\text{Eq. 2})$$

Where  $Q_e$  (mg.g<sup>-1</sup>) is the amount of DCF in equilibrium held on the adsorbent,  $Q_o$  (mg.g<sup>-1</sup>) is the maximum amount of DCF adsorbed,  $C_e$  (mg.L<sup>-1</sup>) is the liquid phase concentration at equilibrium, and  $K_L$

(L.mg<sup>-1</sup>) is the relationship between DCF and adsorbent.

On the other hand, the linearized Freundlich isotherm expression is shown by Equation (3).

$$\text{Log}Q_e = \text{Log}K_F + 1/n(\text{Log}C_e) \quad (\text{Eq. 3})$$

Where,  $K_F$  ((mg/g)(L/mg)<sup>1/n</sup>) and  $n$  (dimensionless) are constants, including factors affecting the adsorption process such as adsorption capacity and intensity,  $Q_e$  (mg.g<sup>-1</sup>) adsorption capacity, and  $C_e$  (mg.L<sup>-1</sup>) showing the equilibrium concentration, respectively.

In Figures 3 and 4, the sorption capacity of DCF by SWCNT, MWCNT, and PAC adsorbents in both water sources, respectively, is illustrated by Langmuir and Freundlich isotherm plots.

The experimental  $Q_e$  versus  $C_e$  data have been fit to Langmuir and Freundlich models and the isotherm parameters were determined. As shown in Figures 3 and 4, the Freundlich model fits the best for the experimental data for three adsorbents according to the  $R^2$  value ( $R^2 = 0.99$ ), as compared to the Langmuir model ( $R^2=0.97$ ). Also, the Freundlich model is applied to adsorption in heterogeneous systems. Isothermal points showed an increase in adsorption capacity with DCF concentration increasing. In other words, plots display that the sorption did not achieve a limit value or the adsorbent saturation, indicating a multilayer adsorption process (32) Langmuir and Freundlich isotherm parameters, constants, and correlation coefficient  $R^2$  and values showing the sorption potential of DCF on three different adsorbents in both water sources are given in Table 3.

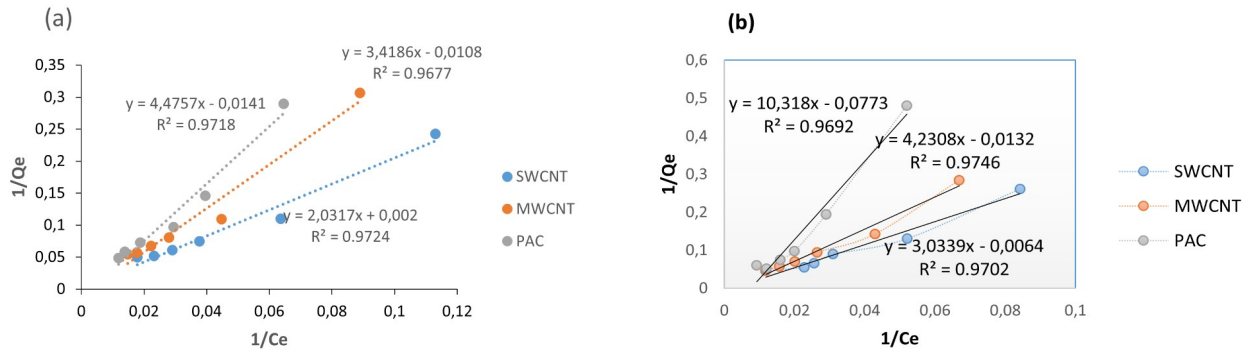


Figure 3. Langmuir isotherms of DCF sorption (a) ULW and (b) UDWTP.

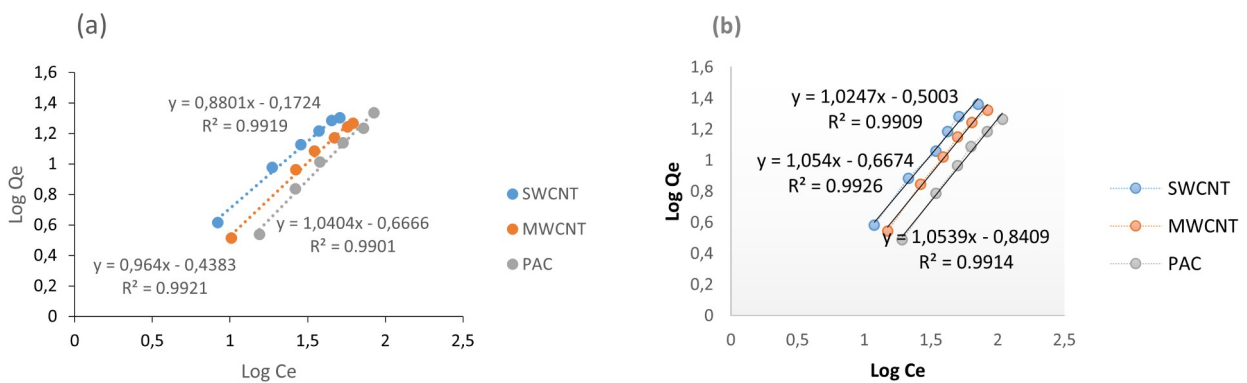


Figure 4. Freundlich isotherms of DCF sorption (a) ULW and (b) UDWTP.

Table 3. Isotherm parameters of Langmuir and Freundlich models for the sorption of DCF.

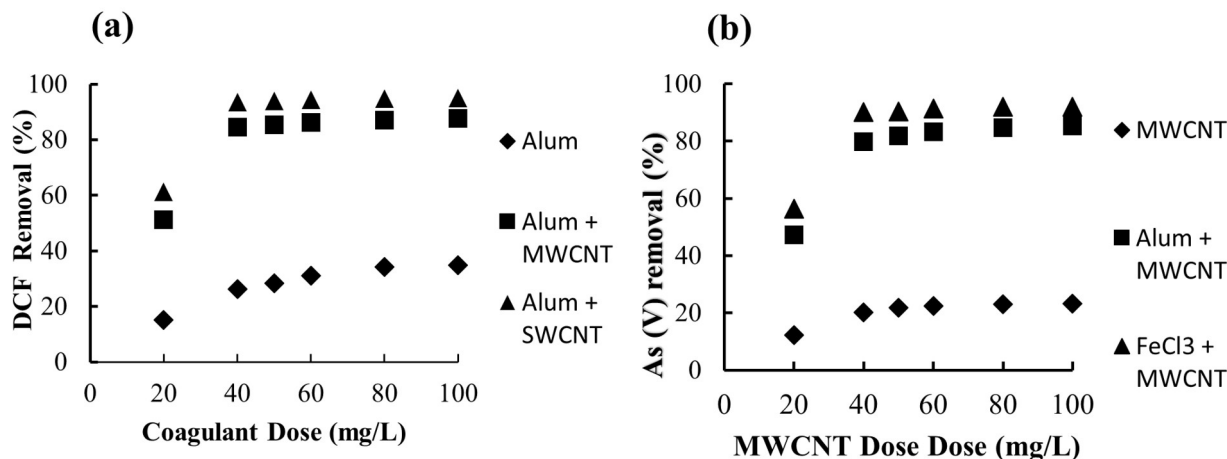
Source	Adsorbents	Langmuir			Freundlich		
		Q <sub>0</sub> (mg/g)	K <sub>L</sub> (L/mg)	R <sup>2</sup>	K <sub>F</sub>	n	R <sup>2</sup>
ULW	SWCNT	500	0.0007	0.9718	1.668	1.498	0.9919
	MWCNT	92.59	0.0302	0.9677	0.999	1.9686	0.9921
	PAC	70.92	0.003	0.9724	0.725	2.213	0.9901
UDWT	SWCNT	156.25	0.002	0.9687	1.005	1.845	0.9909
	MWCNT	75.76	0.003	0.9635	1.003	2.15	0.9926
UDWT	PAC	12.94	0.008	0.9548	1.002	2.6272	0.9914

In the meantime, as a result of the DCF adsorption onto three adsorbents, the highest removals DCF (84.23% and 79.5%) was observed onto SWCNT in ULW and UDWTP, respectively, followed by MWCNT (77.25% and 71,56%) and PAC (68.4% and 61,27%). This result can probably be evaluated that the SWCNTs have a small diameter and large surface compared to MWCNTs and PAC (Figs. 3 and 4). On the other hand, the DCF percentage of DCF removal in ULW is slightly higher than in UDWTP.

This finding shows that pH and ionic strength has an important impact on the adsorption process. In this study, while pH and conductivity values in ULW were 7.24 and 543 μS/cm respectively, these were measured as 7.88 and 384 μS/cm in UDWTP (Table 1). This can be also interpreted that two parameters can change the adsorbent surface charge and also pH may affect adsorbate solubility and dissociation of surface functional groups of adsorbent. Similar

results were performed in some literature research (33-36).

### DCF Removal by Conventional and Combined Coagulation



**Figure 5:** DCF removal with conventional and combined coagulation (a) ULW and (b) UDWTP.

The lowest DCF removal (12.3%) was observed as a result of coagulation with alum in UDWT. The maximum DCF removal in ULW detected when using only alum was recorded as 34.27%. The maximum removal percentages were achieved by combining coagulation with SWCNT+ Alum in ULW and UDWTP samples as 94.81% and 91.97%, respectively. On the other hand, the removal percentages of DCF were slightly lower in ULW (87.11%) and UDWT (84.6 %) samples using MWCNT+ Alum than using SWCNT + Alum. In this study, coagulation removal of DCF in ULW and UDWTP samples is also closely related to the nature of the natural organic matter in water resources and other inorganic and organic pollutants.

### CONCLUSION

In this study, the removal efficiency of DCF in experimental studies carried out in the laboratory was investigated in batch adsorption, coagulation, and combined coagulation processes using CNTs. In experimental studies related to adsorption, it has been determined that the DCF sorption capacity of SWCNT, MWCNT, and PAC adsorbents is higher at acidic pH values rather than alkaline pH values. Meanwhile, it was reported that the adsorption process of DCF on SWCNT, MWCNT, and PAC was defined by the Freundlich isotherm model rather than that by Langmuir. In other words, the values of fitting parameters related to isotherms in all pH represent a multi-layer adsorption process. On the other hand, experimental studies were carried out to display the effect of ionic strength using NaCl. There was no change in DCF adsorption capacity up to 0.6 M concentration, while there was a significant increase in DCF adsorption capacity as the ionic

strength increased at concentrations greater than 0.6 M. In addition, it was observed that much higher amounts of DCF removal were achieved in coagulation studies using CNTs. Compared with adsorption and conventional coagulation, the highest DCF removal was obtained as a result of combined coagulation experiments with SWCNT + Alum (93.1%). Therefore, the results of this study also revealed that the combined coagulation process with CNTs used as an aid coagulant instead of coagulation and adsorption may be more effective in the removal of micropollutants such as DCF in water resources.

### CONFLICT OF INTEREST

There is no conflict of interest between the authors.

### ACKNOWLEDGMENTS

The authors are indebted to the Zonguldak Bülent Ecevit University, Scientific Research Projects Commission (Project Number: 2021-77047330-02).

### REFERENCES

- Jain SN, Tamboli SR, Sutar DS, Jadhav SR, Marathe JV, Shaikh AA, et al. Batch and continuous studies for adsorption of anionic dye onto waste tea residue: Kinetic, equilibrium, breakthrough and reusability studies. *Journal of Cleaner Production*. 2020 Apr;252:119778. [<URL>](#).
- Shahedi A, Darban AK, Taghipour F, Jamshidi-Zanjani A. A review on industrial wastewater treatment via electrocoagulation processes. *Current Opinion in Electrochemistry*. 2020 Aug;22:154-69. [<URL>](#).

3. Trojanowicz M. Removal of persistent organic pollutants (POPs) from waters and wastewaters by the use of ionizing radiation. *Science of The Total Environment*. 2020 May;718:134425. [<URL>](#).
4. Huerta-Fontela M, Galceran MT, Ventura F. Occurrence and removal of pharmaceuticals and hormones through drinking water treatment. *Water Research*. 2011 Jan;45(3):1432-42. [<URL>](#).
5. Li Y, Zhu G, Ng WJ, Tan SK. A review on removing pharmaceutical contaminants from wastewater by constructed wetlands: Design, performance and mechanism. *Science of The Total Environment*. 2014 Jan;468-469:908-32. [<URL>](#).
6. Anonymous. Water framework directive 2008/105/EC. European parliament and of the council [Internet]. European Union; 2008. Available from: [<URL>](#).
7. Kostich MS, Batt AL, Lazorchak JM. Concentrations of prioritized pharmaceuticals in effluents from 50 large wastewater treatment plants in the US and implications for risk estimation. *Environmental Pollution*. 2014 Jan;184:354-9. [<URL>](#).
8. Bartels P, Vontumplingjr W. Solar radiation influence on the decomposition process of diclofenac in surface waters. *Science of The Total Environment*. 2007 Mar 1;374(1):143-55. [<URL>](#).
9. Álvarez S, Ribeiro RS, Gomes HT, Sotelo JL, García J. Synthesis of carbon xerogels and their application in adsorption studies of caffeine and diclofenac as emerging contaminants. *Chemical Engineering Research and Design*. 2015 Mar;95:229-38. [<URL>](#).
10. Acuña V, Ginebreda A, Mor JR, Petrovic M, Sabater S, Sumpter J, et al. Balancing the health benefits and environmental risks of pharmaceuticals: Diclofenac as an example. *Environment International*. 2015 Dec;85:327-33. [<URL>](#).
11. Bhadra BN, Ahmed I, Kim S, Jung SH. Adsorptive removal of ibuprofen and diclofenac from water using metal-organic framework-derived porous carbon. *Chemical Engineering Journal*. 2017 Apr;314:50-8. [<URL>](#).
12. Margot J, Kienle C, Magnet A, Weil M, Rossi L, de Alencastro LF, et al. Treatment of micropollutants in municipal wastewater: Ozone or powdered activated carbon? *Science of The Total Environment*. 2013 Sep;461-462:480-98. [<URL>](#).
13. Huang Z, Gong B, Huang CP, Pan SY, Wu P, Dang Z, et al. Performance evaluation of integrated adsorption-nanofiltration system for emerging compounds removal: Exemplified by caffeine, diclofenac and octylphenol. *Journal of Environmental Management*. 2019 Feb;231:121-8. [<URL>](#).
14. Lima FS, de Barros Neto EL, Melo RPF, da Silva Neto JM, Bezerra Lopes FW, de Jesus Nogueira Duarte L. Removal of diclofenac sodium from aqueous solution using ionic micellar flocculation-assisted adsorption. *Separation Science and Technology*. 2022 Dec 12;57(18):2997-3011. [<URL>](#).
15. Rigobello ES, Dantas ADB, Di Bernardo L, Vieira EM. Removal of diclofenac by conventional drinking water treatment processes and granular activated carbon filtration. *Chemosphere*. 2013 Jun;92(2):184-91. [<URL>](#).
16. Suarez S, Lema JM, Omil F. Pre-treatment of hospital wastewater by coagulation-flocculation and flotation. *Bioresource Technology*. 2009 Apr;100(7):2138-46. [<URL>](#).
17. de Franco MAE, de Carvalho CB, Bonetto MM, de Pelegrini Soares R, Féris LA. Diclofenac removal from water by adsorption using activated carbon in batch mode and fixed-bed column: Isotherms, thermodynamic study and breakthrough curves modeling. *Journal of Cleaner Production*. 2018 Apr;181:145-54. [<URL>](#).
18. Kennedy AM, Reinert AM, Knappe DRU, Ferrer I, Summers RS. Full- and pilot-scale GAC adsorption of organic micropollutants. *Water Research*. 2015 Jan;68:238-48. [<URL>](#).
19. Moreira NFF, Orge CA, Ribeiro AR, Faria JL, Nunes OC, Pereira MFR, et al. Fast mineralization and detoxification of amoxicillin and diclofenac by photocatalytic ozonation and application to an urban wastewater. *Water Research*. 2015 Dec;87:87-96. [<URL>](#).
20. Phattarapattamawong S, Kaiser AM, Saracevic E, Schaar HP, Krampe J. Optimization of ozonation and peroxone process for simultaneous control of micropollutants and bromate in wastewater. *Water Science and Technology*. 2018 May 31;2017(2):404-11. [<URL>](#).
21. Özdemir K. The use of carbon nanomaterials for removing natural organic matter in drinking water sources by a combined coagulation process. *Nanomaterials and Nanotechnology*. 2016 Jan;6:184798041666368. [<URL>](#).
22. Wang X, Lu J, Xing B. Sorption of Organic Contaminants by Carbon Nanotubes: Influence of Adsorbed Organic Matter. *Environ Sci Technol*. 2008 May 1;42(9):3207-12. [<URL>](#).
23. Özdemir K. Removal of Arsenate in drinking water sources by combined coagulation process. *Journal of the Turkish Chemical Society Section A: Chemistry*. 2022 Feb 8;247-54. [<URL>](#).
24. APHA. Standard methods for the examination of water and wastewater. American Public Health Association (APHA): Washington, DC, USA. 2005;21.
25. Zhao J, Xu L, Su Y, Yu H, Liu H, Qian S, et al. Zr-MOFs loaded on polyurethane foam by polydopamine for enhanced dye adsorption. *Journal of Environmental Sciences*. 2021 Mar;101:177-88. [<URL>](#).
26. Titchou FE, Zazou H, Afanga H, El Gaayda J, Akbour RA, Hamdani M. Removal of Persistent Organic Pollutants (POPs) from water and wastewater by adsorption and electrocoagulation process. *Groundwater for Sustainable Development*. 2021 May;13:100575. [<URL>](#).
27. Humbert H, Gallard H, Suty H, Croué JP. Natural organic matter (NOM) and pesticides removal using a combination of ion exchange resin and powdered activated carbon (PAC). *Water Research*. 2008 Mar;42(6-7):1635-43. [<URL>](#).



28. Bolto B, Dixon D, Eldridge R, King S, Linge K. Removal of natural organic matter by ion exchange. *Water Research*. 2002 Dec;36(20):5057–65. [<URL>](#).
29. Rashid MA, Buckley DE, Robertson KR. Interactions of a marine humic acid with clay minerals and a natural sediment. *Geoderma*. 1972 Aug;8(1):11–27. [<URL>](#).
30. Fontecha-Cámara MA, López-Ramón MV, Álvarez-Merino MA, Moreno-Castilla C. Effect of Surface Chemistry, Solution pH, and Ionic Strength on the Removal of Herbicides Diuron and Amitrole from Water by an Activated Carbon Fiber. *Langmuir*. 2007 Jan 1;23(3):1242–7. [<URL>](#).
31. Vinu A, Hossain KZ, Satish Kumar G, Ariga K. Adsorption of l-histidine over mesoporous carbon molecular sieves. *Carbon*. 2006 Mar;44(3):530–6. [<URL>](#).
32. Yousef RI, El-Eswed B, Al-Muhtaseb AH. Adsorption characteristics of natural zeolites as solid adsorbents for phenol removal from aqueous solutions: Kinetics, mechanism, and thermodynamics studies. *Chemical Engineering Journal*. 2011 Jul;171(3):1143–9. [<URL>](#).
33. Pezoti O, Cazetta AL, Bedin KC, Souza LS, Martins AC, Silva TL, et al. NaOH-activated carbon of high surface area produced from guava seeds as a high-efficiency adsorbent for amoxicillin removal: Kinetic, isotherm and thermodynamic studies. *Chemical Engineering Journal*. 2016 Mar;288:778–88. [<URL>](#).
34. Jodeh S, Abdelwahab F, Jaradat N, Warad I, Jodeh W. Adsorption of diclofenac from aqueous solution using Cyclamen persicum tubers based activated carbon (CTAC). *Journal of the Association of Arab Universities for Basic and Applied Sciences*. 2016 Jun;20(1):32–8. [<URL>](#).
35. Sotelo JL, Ovejero G, Rodríguez A, Álvarez S, Galán J, García J. Competitive adsorption studies of caffeine and diclofenac aqueous solutions by activated carbon. *Chemical Engineering Journal*. 2014 Mar;240:443–53. [<URL>](#).
36. Zhao Y, Liu F, Qin X. Adsorption of diclofenac onto goethite: Adsorption kinetics and effects of pH. *Chemosphere*. 2017 Aug;180:373–8. [<URL>](#).





## Life Cycle Assessment and Characterization of Tincal Ore Reinforced Polyester and Vinylester Composites

Emrah Yilmaz<sup>1\*</sup> , Ercan Aydoğmuş<sup>2</sup> , Ahmet Demir<sup>3</sup> 

<sup>1</sup>Düzce University, Faculty of Engineering, Department of Civil Engineering, Düzce, Türkiye

<sup>2</sup>Firat University, Faculty of Engineering, Department of Chemical Engineering, Elazığ, Türkiye

<sup>3</sup>Düzce University, Faculty of Arts and Sciences, Department of Physics, Düzce, Türkiye

**Abstract:** In this study, the quality performance, compressive strength, surface hardness, electrical conductivity, and life cycle assessment (LCA) of the composites produced by reinforcing tincal ( $\text{Na}_2\text{B}_4\text{O}_7 \cdot 10\text{H}_2\text{O}$ ) into polyester and vinylester resins at different rates have been determined. Tincal ore, which is ground with a particle size of 74-149 microns, is dried in an oven at 105 °C for 2 hours and then added to the resins at the ratios of 0 wt.%, 1 wt.%, 2 wt.%, and 3 wt.%. According to the results obtained, it has been determined that the compressive strength and Shore D hardness of the composite raises as the tincal mass ratio increases up to certain amounts. According to the mechanical test results, it is found that 3 wt.% tincal reinforcement maximized the compressive strength of the polyester composite, and 2 wt.% tincal reinforcement maximized the compressive strength of the vinylester composite. In the electrical conductivity test results, it is seen that the first relaxation time of the polyester composite is  $2.14 \cdot 10^{-4}$  s and the relaxation times of vinylester composite vary between  $10^{-4}$  and  $10^{-6}$  seconds. LCA results showed that vinylester composite had more environmental effects than polyester composite except for ozone layer depletion (ODP) effect. Although there is a partial increase (<0.5%) in the environmental impact of composites with tincal reinforcement, it is thought that the increase in the technical performance of the composites will tolerate this partial increase.

**Keywords:** Polyester, vinylester, tincal, hardness, compressive strength, dielectric properties, life cycle assessment.

**Submitted:** July 20, 2022. **Accepted:** November 07, 2022.

**Cite this:** Yilmaz E, Aydoğmuş E, Demir A. Life Cycle Assessment and Characterization of Tincal Ore Reinforced Polyester and Vinylester Composites. JOTCSB. 2022;5(2):183-94.

**\*Corresponding author. E-mail:** [emrahyilmaz@duzce.edu.tr](mailto:emrahyilmaz@duzce.edu.tr) .

### INTRODUCTION

Resins are widely used in many different sectors as the basic raw material in the production of high-performance composite materials. Some of the resins commonly used in the production of fiber-reinforced composite materials are polyester, vinylester, polyurethane, and epoxy resins (1-8). Many natural and synthetic fillers are preferred to increase the technical properties of materials obtained from resins and to reduce the amount of petrochemicals used. With the help of these additives and fillers, some physical and chemical

properties of the synthesized products can be improved (9-15). Besides, there are improvements in the mechanical and thermal properties of composite materials produced from resins reinforced with various additives and fillers (16).

In a study in the literature, it has been determined that the fire safety performance of the composites obtained by adding boron nitride to the epoxy resin increases. It has been observed that the composite materials produced by reinforcing different proportions of boron nitride (filler) into vinylester

resin have improvements in impact, hardness, and abrasion resistance (17,18).

In another study, composite samples are obtained by reinforcing unsaturated polyester with borax at different mass ratios. It has been observed that the addition of certain amounts of borax increases the mechanical strength, Shore D hardness, and thermal conductivity coefficient of polyester composites (19). There is also a need to make environmental assessments in studies to increase the performance of such resin composites. For example, the life cycle assessment (LCA) method is used in environmental sustainability studies of composite materials (20-22). In the literature, there are studies for the production of composite materials and determining the environmental performance of these materials by LCA method (23-25). With LCA studies, environmental effects of composite materials such as climate change impact, acidification, and eutrophication potentials are shared transparently (26,27).

In this research, composite materials have been produced by reinforcing tincal at different rates into orthophthalic-based unsaturated polyester and bisphenol-A epoxy-based vinylester resins. It was determined that certain amounts of tincal reinforcement increase the compressive strength and surface hardness of polyester and vinylester composites. In addition, the dielectric properties of the produced composites and by LCA method their environmental effects were investigated.

## MATERIALS AND METHODS

Unsaturated polyester (UP), methyl ethyl ketone peroxide (MEKP), and cobalt octoate (Co Oc) components were supplied from Turkuaz Polyester. Vinylester resin and its components were purchased from Poliya Company (Turkey). Besides, tincal used in this study was supplied from the Eti Maden (Eskişehir Kirka Boron) factory.

Tincal was added to the UP at different rates (0 wt.%, 1 wt.%, 2 wt.%, and 3 wt.%) and mixed at 1000 rpm for 4 minutes. After adding 0.5 wt.% Co Oc and 1.5 wt.% MEKP, respectively, at room temperature at a mixing speed of 750 rpm for 90 seconds, they were poured into standard molds. After waiting 24 hours for the curing of the obtained samples, necessary tests and analyses were carried out (28-35).

Also, tincal was added to the bisphenol-A epoxy-based vinylester resin. After providing a homogeneous mixture of vinylester resin and tincal, certain amounts of the hardener were added and the mixture was mixed and heated (600 rpm, 2 min, and 45 °C). After the mixture obtained was poured into standard molds and waited for one day for curing, necessary tests and analyses were carried out.

Ultrasonic water bath was used to prevent air bubbles that may occur in the prepared mixtures. Besides, mold release agents are applied to standard steel cylindrical molds, allowing the samples to come out easily. In Figure 1, the mixtures prepared under laboratory conditions and the samples obtained are shown.



**Figure 1:** Preparation of tincal-reinforced vinylester and polyester composites.

As seen in Figure 2, the samples are produced in a cylindrical shape with a diameter/length ratio of  $\frac{1}{2}$  (40 mm/80 mm). Compressive strength is performed by ASTM C 579-01. In the experimental

study, a loading rate of 41MPa/min is applied for all samples. Three samples are produced from each mixture to perform the compressive strength.



**Figure 2:** Tincal-reinforced composite samples before and after compressive strength test.

Shore D hardness tests were carried out by ISO 868 (ASTM D 2240) standard. As seen in Figure 3, cylindrical samples with a diameter of 4 cm are used to determine the hardness values of polyester

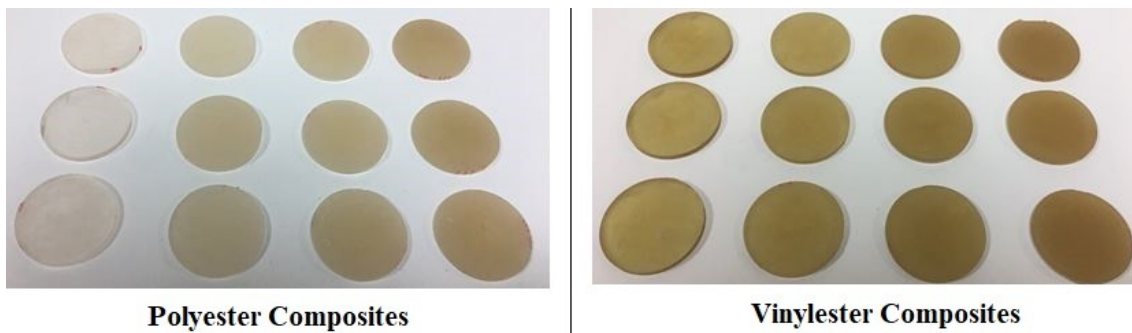
and vinylester composites. Hardness measurements have been made from 5 different points on 3 different samples and calculated by averaging.



**Figure 3:** Shore D hardness testing of polyester and vinylester composites.

Samples with a diameter of 4 cm were used to determine the dielectric properties of the composites (Figure 4). The dielectric properties

have been measured with the Novacontrol Alpha-A impedance analyzer at a temperature of 300 K in the frequency range of 10 Hz and 10 MHz.



**Figure 4:** Cylindrical samples cut for determination of dielectric properties of composites.

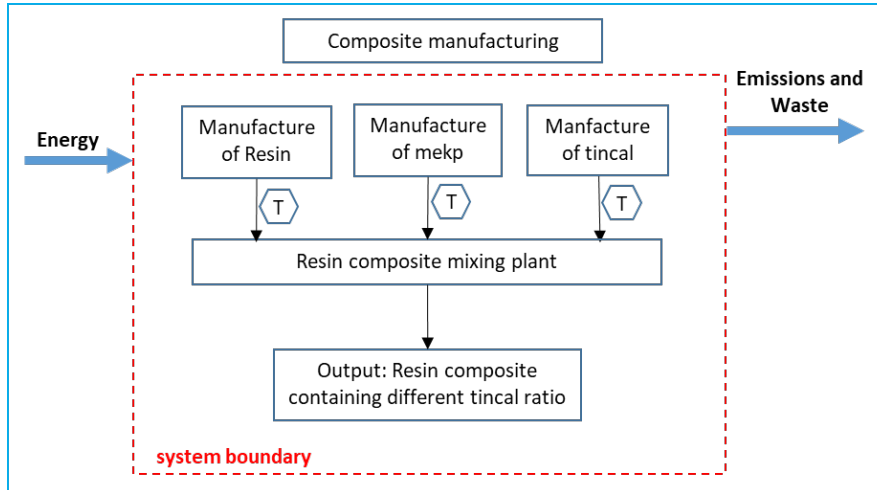
### Life Cycle Assessment

In this study, ISO 14040 and ISO 14044 standards were used to evaluate the environmental impact of the composite materials produced (36).

### Purpose and Scope

The aim of the study is to estimate the main environmental effects of polyester and vinylester composites produced with tincal reinforcement at different rates. The system boundaries of the

presented composites follow a cradle-to-gate approach and include manufacturing steps of polyester and vinylester composites. The functional basis chosen for this study is the production of 1 kg of tincal reinforced resin composites. In the life cycle analysis shown in Figure 5, raw material procurement (1), transportation of raw materials to the mixing laboratory (2), and composite products in the laboratory (3) stages.



**Figure 5:** The system boundary of tincal reinforced resin composite production (T: transport).

**Inventory Analysis**

The production process of the examined composites is explained in detail in the sections above. The inventory data presented in Table 1 were obtained from laboratory measurements as part of the experimental work conducted in this study and converted to the functional unit “1 kg of tincal-reinforced resin composite”. It is assumed

that all transportation is done by road using diesel fuel. A distance of 100 km is assumed to transport all raw materials to the mixing plant. The mixers and ultrasonic baths used in the preparation process of resin composites are low voltage and 0.022 kWh energy is used to produce 1 kg of resin composite. Life cycle inventory data is taken from the Ecoinvent V3.5 database.

**Table 1:** Inventory for the production of 1 kg of tincal-reinforced resin composites.

Materials	Resins (g) (polyester and vinylester)	Co Oc (g)	MEKP (g)
0 wt.%	980	4.90	14.70
1 wt.%	971	4.86	14.57
3 wt.%	952	4.76	14.28

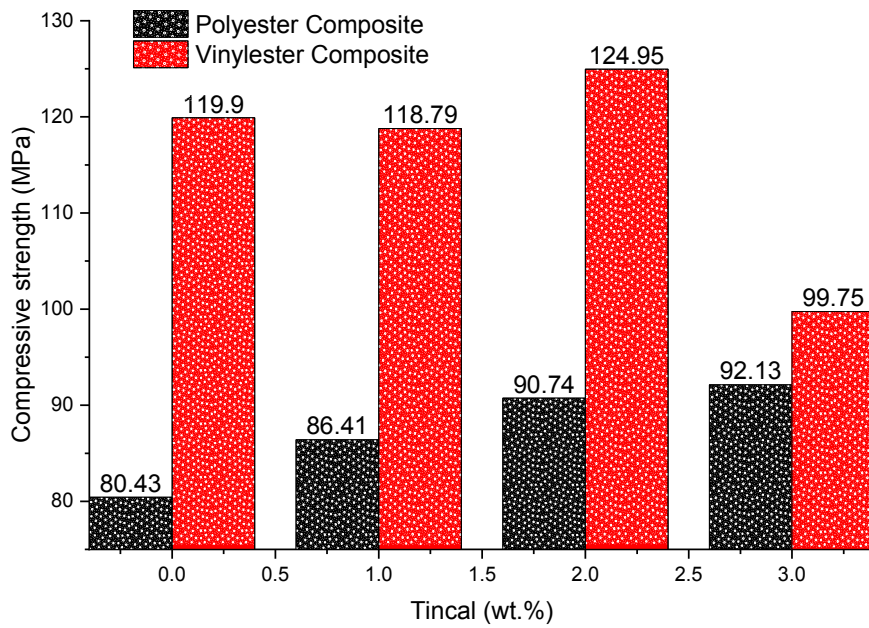
**Impact Assessment**

LCA modeling was performed in SimaPro 9.1.1.1. As in similar studies (37), CML-IA baseline method created by Center for Environmental Sciences (Leiden University) has been chosen for life cycle impact assessment. Six environmental impact categories are considered in the analysis, including climate change, acidification, eutrophication, fossil fuel, photochemical oxidation, and ozone depletion.

**RESULTS AND DISCUSSIONS**

In Figure 6, the compressive strength values of tincal reinforced polyester and vinylester composite samples are seen comparatively. When the graph is examined, it is seen that the highest compressive strength value (124.95 MPa) is reached when 2 wt.% tincal is added to the vinylester resin. When 2 wt.% tincal is added to the vinylester resin, the compressive strength increases by 4.2%. It has been determined that the compressive strength increases with the increase in the amount of tincal in the polyester resin. When 3 wt.% tincal is added to the polyester resin, the compressive strength raises by 14.6%.

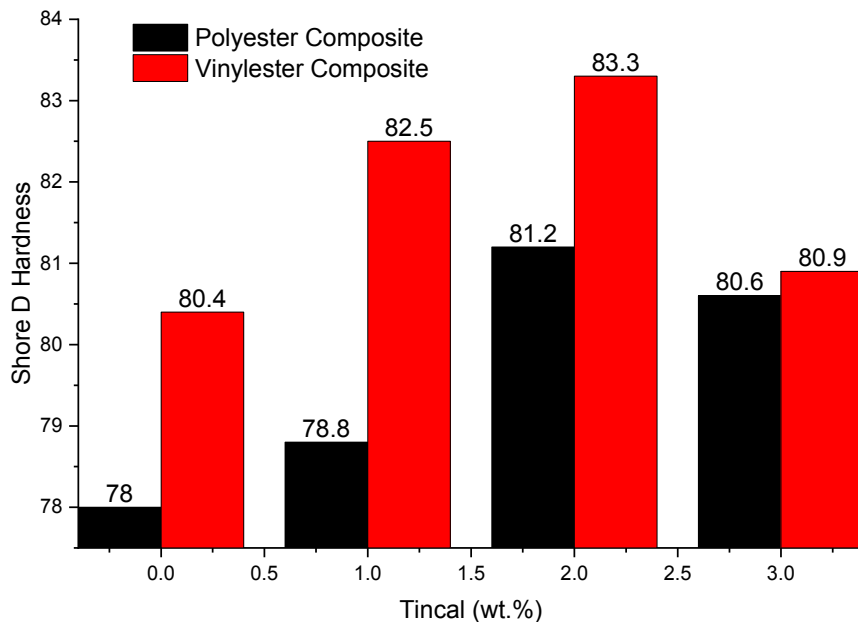




**Figure 6:** Compressive strength values of tincal reinforced resin composites.

In Figure 7, Shore D hardness of tincal reinforced resin composites is compared. The addition of tincal up to 2 wt.% to the vinylester resin increased the surface hardness (3.6%) of the composite. However, the addition of tincal up to 3 wt.% decreases both Shore D hardness of the

vinylester composite. The addition of tincal up to 2 wt.% to the orthophthalic-based polyester resin increases the surface hardness (4.1%) of the composite. However, up to 3%, tincal reinforcement slightly decreases Shore D hardness of the polyester composite.



**Figure 7:** Shore D hardness values of tincal reinforced resin composites.

The images of tincal reinforced resin composites after compression tests are given in Figure 8. The vinylester composite samples do not disperse after the compression test and the experiments are

completed with a shortening in height. It is in the form of deformation that occurs with an overlapping agglomeration in the middle regions of the samples. However, the lengths of the polyester



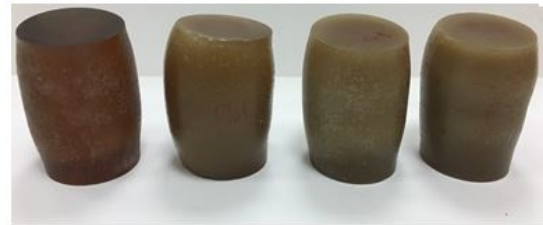
composites are shortened and the samples are deformed vertically. It has been observed that the shortening in length decreases as the amount of

tincal increases. In contrast to the vinylester samples, cracking occur in the polyester composites.



**Tincal Reinforced Polyester Composites**

**Tincal Reinforced Vinylester Composites**



**Figure 8:** Tincal-reinforced composite specimens after compression strength test.

### Dielectric Polarization and Relaxation Mechanisms of Tincal-Reinforced Resin Composites

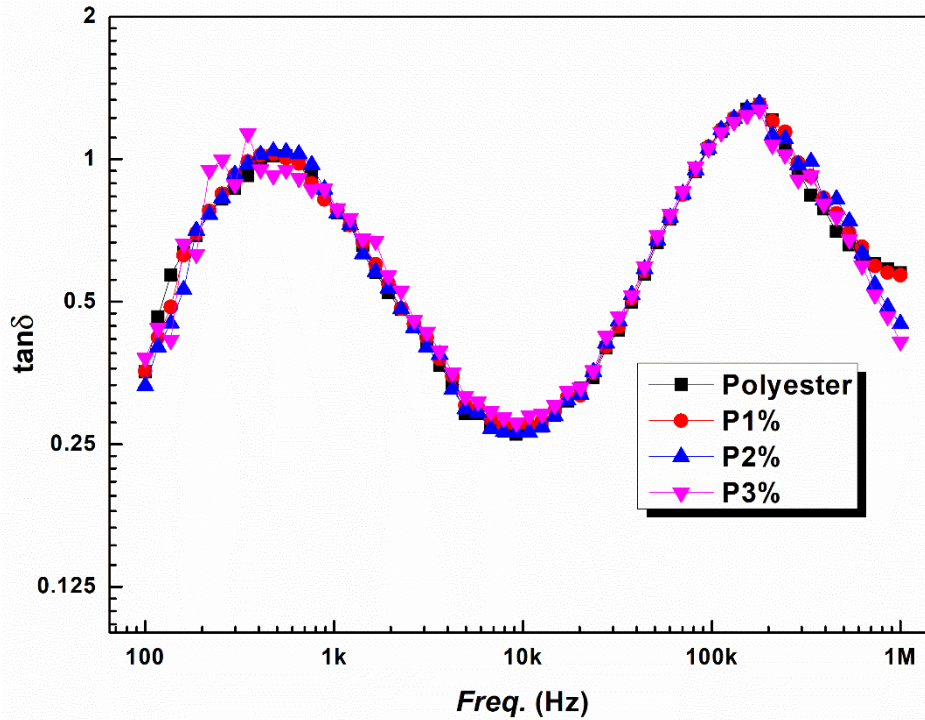
It provides information about the dielectric properties of materials, and their mechanisms such as conduction, and polarization/relaxation. Many parameters such as thickness, structure, and surface area of the material are effective when examining dielectric properties. With the help of these parameters, real and imaginary dielectric constants are obtained from the capacitance and conductance value of the material. While the real dielectric constant ( $\epsilon'$ ) is a measure of the resistance of the material against charge transmission in its internal structure, the imaginary dielectric constant ( $\epsilon''$ ) is a measure of the energy lost during the charge transition in response to the

material to the electric field. Since these two parameters do not react to the electric field at the same time, a phase difference occurs between them. However, to obtain comprehensive information about the conduction and polarization/relaxation mechanisms in the material, it is necessary to look at the loss tangent, which is defined as the ratio of energy loss to resistance and is a measure of the phase difference angle.

$$\epsilon^* = \epsilon' - j \times \epsilon'' \quad (\text{Eq. 1})$$

$$\tan(\delta) = \frac{\epsilon''}{\epsilon'} \quad (\text{Eq. 2})$$

In Figure 9, the dielectric properties of the tincal-reinforced polyester composite are shown.

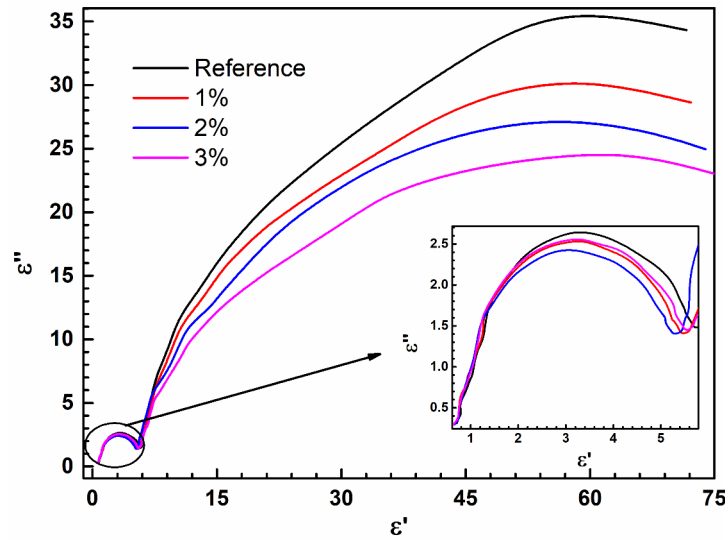


**Figure 9:** Dielectric properties of tincal-reinforced polyester composites.

When Figure 8 is examined, it is seen that there is no change in the  $\tan(\delta)$  or dielectric properties of the materials with doping, but two spot frequencies (475 Hz and 175 kHz) with full polarization is provided for each material. Alternating current at frequencies ranging from 100 Hz to 1 MHz is applied to these materials and they are exposed to an electric field. From 100 Hz, positive charges and negative charges start to polarize in the direction of the field by forming dipoles, and after this frequency, all polarized dipoles start the relaxation process. The relaxation process can be roughly described by the following spot frequency-period relationship.

$$\omega \times \tau = 1 \quad (\text{Eq. 3})$$

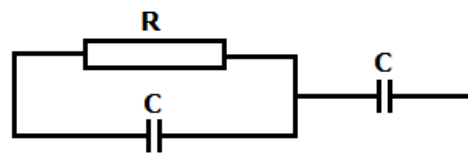
According to this relationship, the first relaxation time for all the materials is obtained as  $2.14 \cdot 10^{-4}$  s. The polarization type that completes the relaxation in this time interval is dipole or Maxwell-Wagner polarization. In other words, dipole or Maxwell-Wagner type polarization takes place around 475 Hz in all materials. This relaxation process continues up to about 10 kHz according to Figure 8. After 10 kHz, all of the dipoles begin to polarize again in the direction of the applied AC (alternating current) field, and full polarization is achieved a second time around 175 kHz. According to Equation 3, the relaxation process here is obtained as  $9 \cdot 10^{-7}$  s. The relaxation time at this spot frequency indicates that the polarization mechanism shifts from dipole or Maxwell-Wagner type polarization to ionic polarization.



**Figure 10:** Cole-Cole diagram of tincal reinforced vinylester composites.

It contains at least one semicircle for materials that operate as a mechanism of characteristics, polarization, and relaxation of dielectric properties as a smooth behavior and is known as Cole-Cole Diagram. The completion of a semicircle can be depicted with an RC circuit in the material. If an unfinished semicircle reveals that the polarization is realized, but the relaxation does not occur, such behavior means that there is no resistance to polarization. Thus, the depicted circuit can be expressed as a single capacitor in this case. In Figure 10, it is seen that a semicircle is completed in all of the vinylester composites with tincal reinforced vinylester and the continuation of a quarter circle. In this form, the materials can be expressed by a capacitor depiction in the series with an RC circuit consisting of an electrically

connected resistance (R) and a capacitor (C) in parallel with each other in the internal structure. This depicted circuit is called an equivalent circuit and its diagram is as in Figure 11. Equality is used on the top of the semicircle to calculate relaxation times from Cole-Cole diagrams. According to Figure 10 is examined, the relaxation times of vinylester and tincal reinforced vinylester composites vary between  $10^{-4}$  and  $10^{-6}$  seconds. Also, it is seen that their amplitude increases with reinforcement rates in the first and second semicircles. We can say that the increase in amplitude reduces relaxation times. Finally, polarization and relaxation mechanisms of tincal reinforced vinylester composite composites can be attributed to the dipole type relaxation, which we call Maxwell Wagner or orientation.



**Figure 11:** Tincal reinforced resin composites equivalent circuit diagram.

**Environmental Sustainability Assessment**

The environmental impact results for the production of 1 kg of tincal reinforced polyester and vinylester resin composites are presented in table 2. The total CC effect of polyester composite (P (3 wt.%) and vinylester composite (V (3 wt.

%) with the best compressive strength performance was estimated to be 3.77 kg CO<sub>2</sub>/kg and 4.29 kg CO<sub>2</sub>/kg, respectively. In both composite materials, the resin is the main hotspot, contributing 97%.

**Table 2:** Environmental impacts on the production of tincal reinforced resin composites.

Composite	CC (kg CO <sub>2</sub> )	ADF (MJ)	ODP x 10 <sup>3</sup> (g CFC-11) eq)	POP x 10 <sup>3</sup> (kg C <sub>2</sub> H <sub>4</sub> ) eq)	AP x 10 <sup>3</sup> (kg SO <sub>2</sub> eq)	EP (kg PO <sub>4</sub> eq)
P (0 wt.%)	3.7627	82.2068	0.5829	7.1465	15.6830	6.3685
P (1 wt.%)	3.7642	82.2261	0.5831	7.1470	15.7006	6.3717
P (2 wt.%)	3.7656	82.2454	0.5833	7.1476	15.7183	6.3749
P (3 wt.%)	3.7671	82.2647	0.5835	7.1481	15.7359	6.3781
V (0 wt.%)	4.2895	87.3614	0.3272	8.1065	17.9749	6.8149
V (1 wt.%)	4.2910	87.3806	0.3274	8.1071	17.9925	6.8181
V (2 wt.%)	4.2924	87.3999	0.3276	8.1076	18.0102	6.8213
V (3 wt.%)	4.2939	87.4192	0.3278	8.1082	18.0278	6.8245

CC: Climate change, ADF: Abiotic depletion (fossil fuels), ODP: Ozone layer depletion, POP: Photochemical oxidant potential, AP: Acidification potential, EP: Eutrophication potential, P: Polyester, V: Vinylester, 0-3 wt.%: resin tincal ratio.

When Table 2 is examined, it is seen that the environmental impacts of vinylester resin composites, except for ODP, are higher than the environmental impacts of polyester resin composites. It is seen that the contribution of accelerators, electricity, transportation, and tincal used in composite production to environmental effects is quite low. In this case, the environmental effects of bisphenol A epoxy-based vinylester resin (except for ODP) are observed to be higher than those of orthophthalic acid-based unsaturated polyester resin.

It was calculated that there is an increase in environmental effects with the increase of tincal ratio in polyester and vinylester resins, but this increase contributes less than 1% to the total effect. When Figure 5 and Table 2 are evaluated together, the compressive strength increases with the increase of tincal in the polyester resin and when 3 wt.% tincal is added to the resin. It has been determined that there is an increase of 0.12% in the climate change category, 0.07% in fossil resource consumption, 0.11% in ozone depletion, 0.02% in photochemical oxidation, 0.34% in acidification and 0.15% in eutrophication. The highest compressive strength and surface hardness values are obtained when 2 wt.% tincal is added to the vinylester resin. When this 2% change is examined in terms of environment, it was found that there is an increase of 0.10% in the climate change category, 0.07% in fossil resource consumption, 0.19% in ozone depletion, 0.02% in photochemical oxidation, 0.29% in acidification, and 0.14% in eutrophication.

## CONCLUSIONS

Increasing the tincal content in the polyester resin increases the compressive strength of the polyester composite. When 3 wt.% tincal is added to the polyester resin, the compressive strength increases by 14.6%. The highest compressive

strength is obtained when 2 wt.% tincal is added to the vinylester resin. When tincal has been evaluated according to the sample that is not reinforced, there is an increase of 4.2% depending on the change in the tincal reinforcement ratio. Depending on the tincal addition rate, the highest surface hardness increase is obtained when 2 wt.% tincal is added to the resins. While the surface hardness increase rate in the polyester composite is 4.1%, it is found at 3.6% in the vinylester sample. Tincal ore reinforcement increases Shore D hardness and density of the polyester composite (38). For all polyester composites, the first relaxation time is  $2.14 \cdot 10^{-4}$  s and the relaxation time is  $9 \cdot 10^{-7}$  s. It has been observed that the relaxation times of vinylester composites vary between  $10^{-4}$  and  $10^{-6}$  seconds. LCA results showed that the environmental impact of vinylester resin composites is higher than that of polyester resin composites, and there is a partial increase in the environmental impact of composites with tincal reinforcement. It is thought that the performance of the composites increases with the addition of tincal to the polyester and vinylester resin and this increase will tolerate the partial increase in the environmental effects of the composites caused by tincal.

## ACKNOWLEDGMENT

The authors thank the managers and employees of Kirka Boron Operations Directorate of Eti Maden Company, who provided the supply of tincal ore used in the study.

## REFERENCES

- Bai T, Wang D, Yan J, Cheng W, Cheng H, Shi SQ, et al. Wetting mechanism and interfacial bonding performance of bamboo fiber reinforced epoxy resin composites. *Composites Science and Technology* [Internet]. 2021 Sep [cited 2022 Nov 8];213:108951. Available from: <URL>.

2. Chen YH, Wu CH, Chen YC. Optimized condition for eco-friendly wood composites manufactured from castor oil-based polyurethane. *Construction and Building Materials* [Internet]. 2021 Nov [cited 2022 Nov 8];306:124789. Available from: [<URL>](#).
3. Teng K, Ni Y, Wang W, Wang H, Xu Z, Chen L, et al. Adjustable micro-structure, higher-level mechanical behavior and conductivities of preformed graphene architecture/epoxy composites via RTM route. *Composites Part A: Applied Science and Manufacturing* [Internet]. 2017 Mar [cited 2022 Nov 8];94:178–88. Available from: [<URL>](#).
4. Lin W, Shi QQ, Chen H, Wang JN. Mechanical properties of carbon nanotube fibers reinforced epoxy resin composite films prepared by wet winding. *Carbon* [Internet]. 2019 Nov [cited 2022 Nov 8];153:308–14. Available from: [<URL>](#).
5. Wang H, Yuan J, Zhu Z, Yin X, Weng Y, Wang Z, et al. High performance epoxy resin composites modified with multifunctional thiophene/ phosphaphenanthrene-based flame retardant: Excellent flame retardance, strong mechanical property and high transparency. *Composites Part B: Engineering* [Internet]. 2021 Dec [cited 2022 Nov 8];227:109392. Available from: [<URL>](#).
6. Petraşcu OL, Manole R, Pascu AM. The behavior of composite materials based on polyurethan resin subjected to uniaxial tensile test. *Materials Today: Proceedings* [Internet]. 2022 [cited 2022 Nov 8];62:2673–8. Available from: [<URL>](#).
7. Erturk AT, Yarar E, Vatanserver F, Sahin AE, Kilingel M, Alpay YO. A comparative study of mechanical and machining performance of polymer hybrid and carbon fiber epoxy composite materials. *Polymers and Polymer Composites* [Internet]. 2021 Nov [cited 2022 Nov 8];29(9\_suppl):S655–66. Available from: [<URL>](#).
8. Alpay Y, Uygur I, Kilincel M. On the optimum process parameters of infrared curing of carbon fiber-reinforced plastics. *Polymers and Polymer Composites* [Internet]. 2020 Jul [cited 2022 Nov 8];28(6):433–9. Available from: [<URL>](#).
9. Xu W, Wu X, Shi B. Toughening agent for melamine formaldehyde resin: A new method for recycling chrome shavings. *Polymer* [Internet]. 2022 Jun [cited 2022 Nov 8];253:124979. Available from: [<URL>](#).
10. Lakhari MT, Bai Y, Wong LS, Paul SC, Anggraini V, Kong SY. Mechanical and durability properties of epoxy mortar incorporating coal bottom ash as filler. *Construction and Building Materials* [Internet]. 2022 Jan [cited 2022 Nov 8];315:125677. Available from: [<URL>](#).
11. Luo C, Li J, Chen Z, Lin J, Chen L, He S. Improving the charge dissipating performance and breakdown strength of epoxy resin by incorporating polydopamine-coated barium titanate. *Materials Today Communications* [Internet]. 2022 Jun [cited 2022 Nov 8];31:103619. Available from: [<URL>](#).
12. Jia F, Fagbohun EO, Wang Q, Zhu D, Zhang J, Gong B, et al. Improved thermal conductivity of styrene acrylic resin with carbon nanotubes, graphene and boron nitride hybrid fillers. *Carbon Resources Conversion* [Internet]. 2021 [cited 2022 Nov 8];4:190–6. Available from: [<URL>](#).
13. Halim ZAA, Yajid MAM, Nurhadi FA, Ahmad N, Hamdan H. Effect of silica aerogel – Aluminium trihydroxide hybrid filler on the physio-mechanical and thermal decomposition behaviour of unsaturated polyester resin composite. *Polymer Degradation and Stability* [Internet]. 2020 Dec [cited 2022 Nov 8];182:109377. Available from: [<URL>](#).
14. Reuter J, Greiner L, Kukla P, Döring M. Efficient flame retardant interplay of unsaturated polyester resin formulations based on ammonium polyphosphate. *Polymer Degradation and Stability* [Internet]. 2020 Aug [cited 2022 Nov 8];178:109134. Available from: [<URL>](#).
15. Na T, Liu X, Jiang H, Zhao L, Zhao C. Enhanced thermal conductivity of fluorinated epoxy resins by incorporating inorganic filler. *Reactive and Functional Polymers* [Internet]. 2018 Jul [cited 2022 Nov 8];128:84–90. Available from: [<URL>](#).
16. Gangil B, Ranakoti L, Verma SK, Singh T. Utilization of waste dolomite dust in carbon fiber reinforced vinylester composites. *Journal of Materials Research and Technology* [Internet]. 2022 May [cited 2022 Nov 8];18:3291–301. Available from: [<URL>](#).
17. Feng T, Wang Y, Dong H, Piao J, Wang Y, Ren J, et al. Ionic liquid modified boron nitride nanosheets for interface engineering of epoxy resin nanocomposites: Improving thermal stability, flame retardancy, and smoke suppression. *Polymer Degradation and Stability* [Internet]. 2022 May [cited 2022 Nov 8];199:109899. Available from: [<URL>](#).
18. Boztoprak Y, Kartal İ. Bor Nitrür Partikülleriyle Takviyelendirilmiş Vinil Ester Matrisli Kompozitlerin Mekanik Özelliklerinin İncelenmesi. *El-Cezeri Fen ve Mühendislik Dergisi* [Internet]. 2019 Jan 31 [cited 2022 Nov 8]; Available from: [<URL>](#).
19. Orhan R, Aydoğmuş E, Topuz S, Arslanoğlu H. Investigation of thermo-mechanical characteristics of borax reinforced polyester composites. *Journal of Building Engineering* [Internet]. 2021 Oct [cited 2022 Nov 8];42:103051. Available from: [<URL>](#).
20. Yılmaz E, Arslan H, Subaşı S, Uğur LO, Bideci A. Geri Dönüştürülmüş Lastik Atık İkameli Poliüretan Dolgulu Kompozit Panellerin Yaşam Döngüsü Değerlendirmesi. *Düzce Üniversitesi Bilim ve Teknoloji Dergisi* [Internet]. 2018 Aug 1 [cited 2022 Nov 8];6(4):1224–33. Available from: [<URL>](#).
21. Yılmaz E, Aykanat B, Çomak B. Environmental life cycle assessment of rockwool filled aluminum sandwich facade panels in Turkey. *Journal of Building Engineering* [Internet]. 2022 Jun [cited 2022 Nov 8];50:104234. Available from: [<URL>](#).
22. Benli Yıldız N, Arslan H, Yılmaz E. Life Cycle Assessment of Building Materials: Literature Review. *JOR*. 2020;8(1):210–9.
23. La Rosa AD, Greco S, Tosto C, Cicala G. LCA and LCC of a chemical recycling process of waste CF-thermoset composites for the production of novel CF-thermoplastic



composites. Open loop and closed loop scenarios. *Journal of Cleaner Production* [Internet]. 2021 Jul [cited 2022 Nov 12];304:127158. Available from: [<URL>](#).

24. La Rosa AD, Banatao DR, Pastine SJ, Latteri A, Cicala G. Recycling treatment of carbon fibre/epoxy composites: Materials recovery and characterization and environmental impacts through life cycle assessment. *Composites Part B: Engineering* [Internet]. 2016 Nov [cited 2022 Nov 12];104:17–25. Available from: [<URL>](#).

25. Li X, Lv X, Zhou X, Meng W, Bao Y. Upcycling of waste concrete in eco-friendly strain-hardening cementitious composites: Mixture design, structural performance, and life-cycle assessment. *Journal of Cleaner Production* [Internet]. 2022 Jan [cited 2022 Nov 12];330:129911. Available from: [<URL>](#).

26. Kousis I, Fabiani C, Pisello AL. Could a bio-resin and transparent pavement improve the urban environment? An in field thermo-optical investigation and life-cycle assessment. *Sustainable Cities and Society* [Internet]. 2022 Apr [cited 2022 Nov 12];79:103597. Available from: [<URL>](#).

27. Forcellese A, Marconi M, Simoncini M, Vita A. Life cycle impact assessment of different manufacturing technologies for automotive CFRP components. *Journal of Cleaner Production* [Internet]. 2020 Oct [cited 2022 Nov 12];271:122677. Available from: [<URL>](#).

28. Aydoğmuş E, Arslanoğlu H, Dağ M. Production of waste polyethylene terephthalate reinforced biocomposite with RSM design and evaluation of thermophysical properties by ANN. *Journal of Building Engineering* [Internet]. 2021 Dec [cited 2022 Nov 12];44:103337. Available from: [<URL>](#).

29. Aydoğmuş E, Arslanoğlu H. Kinetics of thermal decomposition of the polyester nanocomposites. *Petroleum Science and Technology* [Internet]. 2021 Jul 18 [cited 2022 Nov 12];39(13–14):484–500. Available from: [<URL>](#).

30. Aydoğmuş E. Biohybrid nanocomposite production and characterization by RSM investigation of thermal decomposition kinetics with ANN. *Biomass Conv Bioref* [Internet]. 2022 Oct [cited 2022 Nov 12];12(10):4799–816. Available from: [<URL>](#).

31. Aydoğmuş E, Dağ M, Yalçın ZG, Arslanoğlu H. Synthesis and characterization of waste polyethylene reinforced modified castor oil-based polyester biocomposite. *J of Applied Polymer Sci* [Internet]. 2022 Jul 15 [cited 2022 Nov 12];139(27). Available from: [<URL>](#).

32. Şahal H, Aydoğmuş E, Arslanoğlu H. Investigation of thermophysical properties of synthesized SA and nano-alumina reinforced polyester composites. *Petroleum Science and Technology* [Internet]. 2022 Aug 8 [cited 2022 Nov 12];1–17. Available from: [<URL>](#).

33. Demirel MH, Aydoğmuş E. Atik maske takviyeli polyester kompozit üretimi ve karakterizasyonu. İnönü Üniversitesi Sağlık Hizmetleri Meslek Yüksek Okulu Dergisi [Internet]. 2022 Jan 17 [cited 2022 Nov 12]; Available from: [<URL>](#).

34. Demirel MH, Aydoğmuş E. Waste Polyurethane Reinforced Polyester Composite, Production, and Characterization. *Journal of the Turkish Chemical Society Section A: Chemistry* [Internet]. 2022 Mar 26 [cited 2022 Nov 12];443–52. Available from: [<URL>](#).

35. Yanen C, Aydoğmuş E. Characterization of Thermo-Physical Properties of Nanoparticle Reinforced the Polyester Nanocomposite. *DÜFED*. 2021;10(2):121–32.

36. Finkbeiner M, Inaba A, Tan R, Christiansen K, Klüppel HJ. The New International Standards for Life Cycle Assessment: ISO 14040 and ISO 14044. *Int J Life Cycle Assessment* [Internet]. 2006 Mar [cited 2022 Nov 12];11(2):80–5. Available from: [<URL>](#).

37. Chard J, Basson L, Creech G, Jesson D, Smith P. Shades of Green: Life Cycle Assessment of a Urethane Methacrylate/Unsaturated Polyester Resin System for Composite Materials. *Sustainability* [Internet]. 2019 Feb 15 [cited 2022 Nov 12];11(4):1001. Available from: [<URL>](#).

38. Yanen C, Dağ M, Aydoğmuş E. Investigation of Thermophysical Properties of Colemanite, Ulexite, and Tincal Reinforced Polyester Composites. *European Journal of Science and Technology* [Internet]. 2022 May 3 [cited 2022 Nov 12]; Available from: [<URL>](#).







## An Investigation on Fatty Acid Compositions of Three-Generation Biodiesel Fuels

Huseyin Sanli<sup>1\*</sup> , Fevzi Yasar<sup>2</sup> 

<sup>1</sup>Tekirdag Namik Kemal University, Corlu Vocational School, Department of Automotive Technology, Tekirdag, 59860, Turkey

<sup>2</sup>Batman University, Vocational School of Technical Sciences, Department of Refinery and Petro-chemistry, Batman, 72060, Turkey

**Abstract:** Biodiesel's fuel properties affecting engine performance, combustion and emission characteristics significantly depend on the feedstock from which it is produced. The most important parameter which influences the feedstock properties is its fatty acid composition. Fatty acid chain length, unsaturation level, and the type of unsaturated bonds have significant impacts on the feedstock and therefore on biodiesel fuel properties. Biodiesel is generally divided into three generations, depending on its feedstock. In this experimental study, twelve different biodiesel fuels covering three generations were produced, their fatty acid distributions were determined and compared with each other. It has been determined that the biodiesel obtained from coconut oil had quite different fatty acid distribution compared to other biodiesel fuels. Coconut biodiesel, palm biodiesel and cottonseed oil biodiesel fuels were in the first three order in terms of saturated fatty acid content, while algal oil biodiesel had the lowest saturation level.

**Keywords:** Biodiesel, Feedstock, Fatty acid composition, Fuel property.

**Submitted:** October 20, 2022. **Accepted:** November 10, 2022.

**Cite this:** Sanli H, Yasar F. An Investigation on Fatty Acid Compositions of Three-Generation Biodiesel Fuels. JOTCSB. 2022;5(2):195-202.

**\*Corresponding author. E-mail:** [hsanli@nku.edu.tr](mailto:hsanli@nku.edu.tr).

### INTRODUCTION

Together with industry and households, transportation sector is one of the main factors causing very high energy consumption and environmental pollution. Despite many economic and geopolitical problems in the world, energy demand of transportation sector has been increasing each year. Meeting this energy need is crucial for the continuity of the global supply chain. The current problems in reaching fossil energy sources has revealed the vital significance of sustainable and domestically producible alternative energy resources much more clearly. The use of alternative energy in the transportation sector is an issue that should be strongly emphasized in terms of sustainable and environmentally friendly transportation. Nowadays, electrification in the

automotive industry is a very popular issue and is expanding rapidly. However, there are many technical problems that should be solved, especially in medium-heavy duty vehicles and working machines. In addition, the unit price of electricity to be consumed in these vehicles and the regulations on taxation are not clear yet. Biodiesel is a very important alternative energy source since it can be used in all areas of transportation sector including sea and airway. It is compatible with the existing fuel distribution and station network, and does not require a significant change in the fuel and injection systems of the vehicles. Infrastructure investment can be made with smaller budgets compared to other alternative energy sources. As biodiesel can be produced from domestic feedstocks, it can alleviate the dependence on the import energy sources causing

current account deficit problem. Moreover, compared to petroleum-based diesel fuel, biodiesel has more environmentally friendly exhaust emissions (excluding NO<sub>x</sub>) and superior lubricity property. (1-5).

### BIODIESEL FEEDSTOCKS

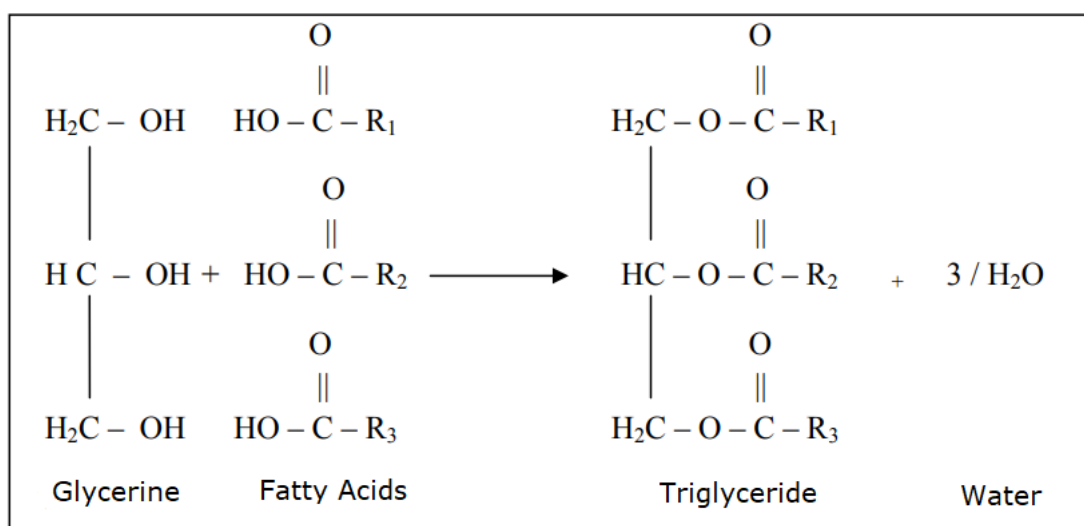
When the related literature is examined, it is seen that the use of vegetable oils in diesel engines as fuel started with the invention of the diesel engine (6). Vegetable oils' unacceptably high viscosities which prevent their direct usage in diesel engines are significantly reduced by a chemical reaction called transesterification. Biodiesel which is an alternative diesel fuel can be produced from lots of different feedstocks. However, when today's industrial scale biodiesel production is examined globally, it is seen that edible vegetable oils such as soybean oil, rapeseed oil, palm oil, etc. are still the main feedstock of this industry. Edible vegetable oils are classified as the first generation biodiesel feedstock. Waste frying oils, waste animal fats and inedible oils can also be used as feedstock in biodiesel production. A biodiesel fuel produced from waste feedstocks or inedible vegetable oils is defined as the second-generation biodiesel fuel. Another biodiesel feedstock that is more recent than other feedstocks is algae. A biodiesel fuel of algal oil origin is called as the third-generation biodiesel (7).

The feedstock type from which biodiesel is produced has the determinant impact on the sustainability of the biodiesel industry and on the cost of biodiesel as well as on the obtained

biodiesel's physico-chemical fuel properties. During transesterification reaction, the fatty acid distribution of the biodiesel feedstock remains almost constant. In other words, the fatty acid composition of the biodiesel fuel reflects the fatty acid structure of the feedstock from which it is produced, and consequently the fuel properties of different origin biodiesels show significant differences. For example, cetane number, viscosity, calorific value, and lubricity increase with increasing fatty acid chain length. Moreover, as the fatty acid saturation level increases, oxidative stability improves, whereas cold flow properties are adversely affected (8-10). In order to better understand a biodiesel fuel chemically, it is critical to understand the chemical structure of the feedstock from which biodiesel fuel is produced.

### The Chemical Structure of Biodiesel Feedstocks

Biodiesel feedstocks (oils and fats) are formed as a result of the bonding (esterification) of three moles of fatty acids to one mole of glycerine with ester bonds (the bond between hydroxyl and carboxyl groups). They are also called glycerides, since there is glycerine in the formation of oil and fat. During the formation of an oil or fat molecule, three ester bonds are formed and three moles of water are released. The resulting structure is defined as triglyceride (triacylglycerol). The main chemical constituent of vegetable oils and animal fats are triglycerides. Oils and fats are composed of about 90-98% triglycerides and limited number of di- and monoglycerides (11). Triglyceride formation mechanism is shown in Figure 1.



**Figure 1:** Triglyceride formation mechanism.

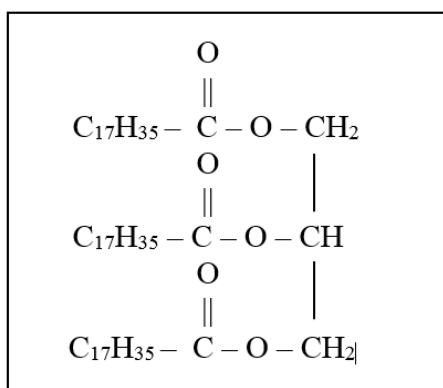
R<sub>1</sub>, R<sub>2</sub> and R<sub>3</sub> in the figure stand for the fatty acid molecules. When the fatty acids in a triglyceride molecule are the same it is called as a simple

triglyceride. They are rarely seen in the nature. If two or more different fatty acids are combined with glycerine, it is termed a mixed triglyceride (12).

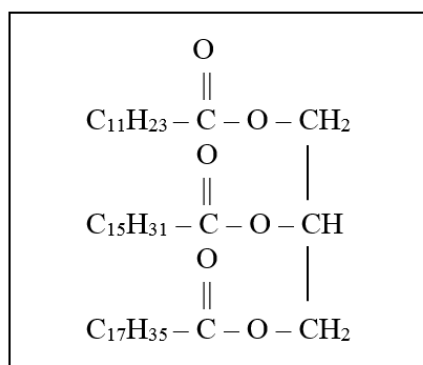
Figures 2 and 3 show an example of simple triglyceride and mixed triglyceride, respectively.

In a triglyceride molecule, the mass of glycerol is about 41 grams, whereas the mass of fatty acid radicals is about 650-790 grams. These amounts show us that fatty acid radicals constitute a very big portion of the reactive groups and so they greatly affect the physico-chemical characteristics.

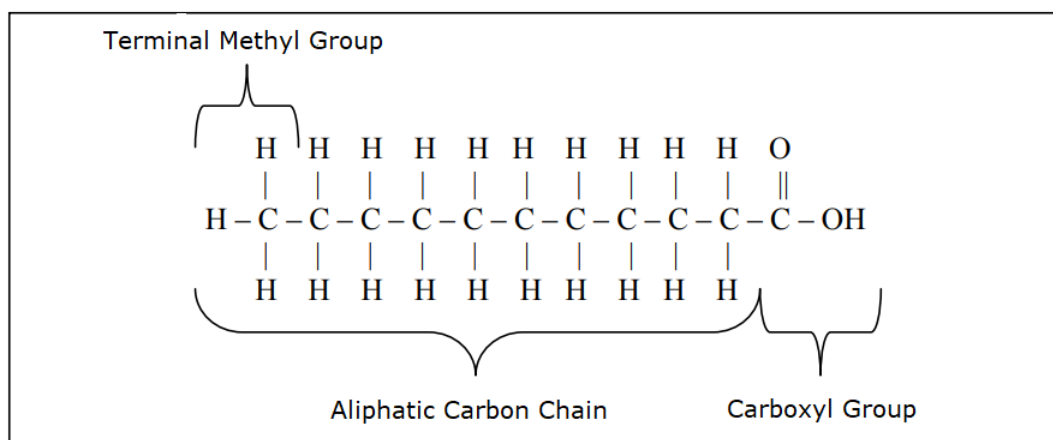
The importance of comprehensive analysis of fatty acids, which comprise about 96% of a triglyceride molecule, is clearly seen. Fatty acids can be defined as organic acids consisting of a carboxyl group and a straight carbon atom chain (13). The chemical structure of a fatty acid can be seen in Figure 4 at which the structural formula of undecanoic acid is illustrated.



**Figure 2:** Simple triglyceride (tristearin).



**Figure 3:** Mixed triglyceride (lauropalmitostearin).



**Figure 4:** The chemical structure of a fatty acid.

Fatty acids differ from each other in their carbon chain length, the number and the position of double bonds. Fatty acids can be saturated at which all carbon atoms bonding each other with single bonds or unsaturated containing one or more double bonds. A fatty acid is shown by two numbers. The first number indicates the number of

carbon atoms in the fatty acid chain while the second number shows the number of double bonds. For instance, C 18:2 (linoleic acid) indicates that this fatty acid has totally 18 carbon atoms and contains 2 double bonds. The some common fatty acids found in oils and fats can be seen in Table 1.

**Table 1:** Some common fatty acids and their chemical structures.

Fatty Acid Name	Carbon Atom :Double Bond (C:D)	Chemical Structure
Butyric Acid	C 4:0	CH <sub>3</sub> (CH <sub>2</sub> ) <sub>2</sub> COOH
Caproic Acid	C 6:0	CH <sub>3</sub> (CH <sub>2</sub> ) <sub>4</sub> COOH
Caprylic Acid	C 8:0	CH <sub>3</sub> (CH <sub>2</sub> ) <sub>6</sub> COOH
Capric Acid	C 10:0	CH <sub>3</sub> (CH <sub>2</sub> ) <sub>8</sub> COOH
Lauric Acid	C 12:0	CH <sub>3</sub> (CH <sub>2</sub> ) <sub>10</sub> COOH
Myristic Acid	C 14:0	CH <sub>3</sub> (CH <sub>2</sub> ) <sub>12</sub> COOH
Myristoleic Acid	C 14:1	CH <sub>3</sub> (CH <sub>2</sub> ) <sub>3</sub> CH=CH(CH <sub>2</sub> ) <sub>7</sub> COOH
Palmitic Acid	C 16:0	CH <sub>3</sub> (CH <sub>2</sub> ) <sub>14</sub> COOH
Palmitoleic Acid	C 16:1	CH <sub>3</sub> (CH <sub>2</sub> ) <sub>5</sub> CH=CH(CH <sub>2</sub> ) <sub>7</sub> COOH
Stearic Acid	C 18:0	CH <sub>3</sub> (CH <sub>2</sub> ) <sub>16</sub> COOH
Oleic Acid	C 18:1	CH <sub>3</sub> (CH <sub>2</sub> ) <sub>7</sub> CH=CH(CH <sub>2</sub> ) <sub>7</sub> COOH
Linoleic Acid	C 18:2	CH <sub>3</sub> (CH <sub>2</sub> ) <sub>4</sub> CH=CHCH <sub>2</sub> CH=CH(CH <sub>2</sub> ) <sub>7</sub> COOH
Linolenic Acid	C 18:3	CH <sub>3</sub> CH <sub>2</sub> CH=CHCH <sub>2</sub> CH=CHCH <sub>2</sub> CH=CH(CH <sub>2</sub> ) <sub>7</sub> COOH
Arachidic Acid	C 20:0	CH <sub>3</sub> (CH <sub>2</sub> ) <sub>18</sub> COOH
Gadoleic Acid	C 20:1	CH <sub>3</sub> (CH <sub>2</sub> ) <sub>7</sub> CH=CH(CH <sub>2</sub> ) <sub>9</sub> COOH
Behenic Acid	C 22:0	CH <sub>3</sub> (CH <sub>2</sub> ) <sub>20</sub> COOH
Erucic Acid	C 22:1	CH <sub>3</sub> (CH <sub>2</sub> ) <sub>7</sub> CH=CH(CH <sub>2</sub> ) <sub>11</sub> COOH
Lignoceric Acid	C 24:0	CH <sub>3</sub> (CH <sub>2</sub> ) <sub>22</sub> COOH

If unsaturated fatty acids are examined in more detail, it will be seen that the position of double bonds can also be different. Double bond position, just like the number of double bonds, has a significant influence on the chemical reactivity. There are two different position possibilities for double bonds: in the conjugated double bond position there is no methylene (CH<sub>2</sub>) group between the double bonds. The double bonds in the carbon chain are separated by a single bond. In the isolated double bond position, there are one or more methylene groups between the double bonds in the carbon chain. Conjugated fatty acids show quite different physico-chemical properties from isolated fatty acids having the similar closed chemical formula. Conjugated fatty acids react more easily than isolated fatty acids (14).

Another important issue that needs to be emphasized in terms of double bond configuration is the "cis" and "trans" configurations. These double bond configurations also significantly affect the properties of a vegetable oil or an animal fat. In the "cis" configuration, the carbon chains on either side of the double bonds tend towards each other and the hydrogen atoms in the double bond are on the same side. There is a slight bend in the double bond location. Most of the unsaturated fatty acids have "cis" double bonds. In the "trans"

configuration, hydrogen atoms in the double bond are on the opposite side. "Trans" carbon chain is almost straight. "Cis" and "trans" configuration show different properties. For example; "trans" fatty acids have higher melting point than "cis" fatty acids. The melting point of oleic acid (C18:1 cis) having "cis" double bond is 18.9 °C, while the melting point of elaidic acid (C18:1 trans) with a double bond in the "trans" configuration is 43 °C (15).

As mentioned in the previous sections, feedstock type used in biodiesel production affects not only the break-even price of the obtained fuel but also the sustainability of the biodiesel industry. Moreover, biodiesel's fuel properties are highly dependent on the feedstock from which it is produced. Fatty acid composition significantly affects the characteristics of vegetable oils and animal fats and inevitably the physico-chemical fuel properties of the biodiesel fuel produced from these feedstocks. For this reason, it is very important to determine the fatty acid composition of biodiesel fuels obtained from different feedstocks. However, the number of studies in which wide range of biodiesel fuels' fatty acid distributions are determined, comprehensively analysed and compared with each other is very

limited. In this experimental study, it was aimed to partially fill this gap in the literature.

## MATERIALS AND METHODS

The main goal of this experimental study was to determine the different origin biodiesel fuels' fatty acid structures on which biodiesel fuel properties are largely dependent. To make a comprehensive study, 12 different biodiesel fuels (covering three biodiesel generations) were produced from various feedstocks. Soybean oil, corn oil, safflower oil, olive oil, sunflower oil, palm oil, rapeseed oil, algae oil, cottonseed oil, hazelnut oil, waste frying oil and coconut oil were used as feedstock for biodiesel production. Transesterification reaction conditions were 6:1 molar ratio of methanol:feedstock, 1% KOH (w/w), reaction temperature of 60 °C and 1 hour reaction duration. After the reaction was finished, the mixture was transferred into a separatory funnel and left overnight for complete glycerol phase separation. The glycerol phase was drained and the methyl ester was washed four times with distilled water at 50 °C. After the washing process, biodiesel fuel was dried at 101 °C for 1 hour. The dried fuel was filtered and then stored in the refrigerator at 4 °C. All biodiesels were observed for one week and no phase separation or bottom sedimentation problems were detected. Fatty acid distributions of all produced biodiesel fuels were determined by using IUPAC 2.301 method.

## RESULTS AND DISCUSSION

Biodiesel fuels were coded as following: Safflower biodiesel fuel (SfB), waste frying oil biodiesel fuel (WFB), sunflower oil biodiesel fuel (SB), hazelnut oil biodiesel fuel (HB), rapeseed oil biodiesel fuel (RB), corn oil biodiesel fuel (CB), palm oil biodiesel fuel (PaB), cotton seed oil biodiesel fuel (CtB), soybean oil biodiesel fuel (SoB), olive oil biodiesel fuel (OB), coconut oil biodiesel fuel (CcB), and algal oil biodiesel fuel (AIB). Fatty acid distributions of all biodiesel fuels produced in this study were given in Table 2.

As seen in Table 2, biodiesel fuels produced from different feedstocks contain varying percentages of different fatty acids. Stearic acid (C 18:0), oleic acid (C 18:1), linoleic acid (C 18:2) and linolenic acid (C 18:3) were detected in all biodiesel fuels. Palmitic acid (C 16:0) was found in all biodiesel fuels except SB whereas myristic acid (C 14:0) was detected in all biodiesel fuels apart from AIB. When the table is examined, it is seen that oleic acid and linoleic acid were the most dominant fatty acids in almost all biodiesel fuels examined. The most dominant fatty acids in SfB were linoleic acid (75.59%), oleic acid (12.91%) and palmitic acid (6.65%), respectively. WFB's oleic acid (45.15%)

and linoleic acid (39.74%) contents were close to each other. As saturated fatty acids, the content of palmitic acid (8.80%) was almost twice the stearic acid amount (4.20%). It also contained trace amounts of myristic acid (0.13%). Linoleic acid (54.83%) and oleic acid (33.43%) were the two most prominent fatty acids in SB. In addition, this should be underlined that, among all tested biodiesel fuels, pentadecenoic acid (C 15:1) was only detected in SB (6.46%). HB differed from all other biodiesel fuels with its octadecenoic fatty acid content of 74.24%. It was seen that the oleic acid (2.22%) and stearic acid (2.14%) contents of HB were almost the same. The most dominant fatty acids of the biodiesel fuel (RB) produced from rapeseed oil, which is the basic feedstock of the EU biodiesel industry, were oleic acid (62.13%) and linoleic acid (21.71%). Linoleic acid (52.58%), oleic acid (31.69%), palmitic acid (11.34%) and stearic acid (2.13%) were the basic fatty acids that constitute CB. The saturation level of PaB was relatively higher than other biodiesel fuels apart from CcB. The first three fatty acids of PaB were oleic acid (42.53%), palmitic acid (39.38%) and linoleic acid (10.69%). Stearic acid content of PaB (4.25) was close to those of WFB (4.20%) and SoB (4.19%). Almost all the fatty acid composition of CtB was composed of linoleic acid (56.17%), palmitic acid (21.79%), oleic acid (17.26%) and stearic acid (2.60%). Linolenic acid content (43.23%) of SoB produced from soybean oil, which is the main feedstock of the US biodiesel industry, was quite remarkable and was much higher than those of all other biodiesel fuels. The oleic acid (24.53%) and linoleic acid (21.25%) contents and also palmitic acid (6.25%) and stearic acid (4.19%) contents of SoB were quite close to each other. OB's oleic acid content (70.23%) was in the first order among all biodiesel fuels. In addition to oleic acid, OB consisted of palmitic acid (13.03%), linoleic acid (9.51%), and stearic acid (3.66%). It should be especially expressed that CcB was quite different from other biodiesel fuels terms of its fatty acid composition. It contained significant amounts of fatty acids that other biodiesels did not have. CcB's lauric acid (48.89%), caprylic acid (8.49%) and capric acid (5.85%) contents distinguished it from other biodiesels. In addition to these fatty acids, CcB contained myristic acid (19.67%), palmitic acid (7.49%), oleic acid (4.66%), and stearic acid (3.32%). It should be strongly underlined that CcB, with its saturation level of 94.42%, was by far in the first order among the 12 different biodiesel fuels examined in this study. The saturation level of PaB (45.59%), which was the second in terms of saturated fatty acid content, was almost half of CcB. As can be understood from the Table 2, the fatty acid diversity of AIB, which is classified as 3rd generation biodiesel, was more limited than other biodiesel fuels. It was determined that AIB

composed of 62.09% oleic acid, 21.22% linoleic acid, 9.54% linolenic acid and 1.70% stearic acid. In addition, another issue that should be

emphasized is that AIB fuel (total saturation rate of 6.41%) had the lowest saturation level among the tested biodiesel fuels.

**Table 2:** Fatty acid compositions of biodiesel fuels (% w/w).

C:D	SfB	WfB	SB	HB	RB	CB	PaB	CtB	SoB	OB	CcB	AIB
C 5:0	-	-	-	-	-	-	0.04	-	-	-	0.70	-
C 8:0	-	-	-	-	-	-	-	0.01	-	-	8.49	-
C 10:0	-	-	-	-	-	-	0.05	0.01	-	-	5.85	-
C 11:0	-	-	0.10	-	-	-	-	-	-	-	-	-
C 12:0	-	-	-	-	-	-	0.49	0.07	-	-	48.89	-
C 13:0	-	-	-	-	-	-	-	-	-	-	0.01	-
C 14:0	0.09	0.13	0.09	0.04	0.06	0.04	1.04	0.60	0.05	0.02	19.67	-
C 14:1	-	-	0.02	-	-	-	-	-	-	-	-	-
C 15:0	0.02	-	-	-	0.03	-	0.05	0.02	0.02	-	-	-
C 15:1	-	-	6.46	-	-	-	-	-	-	-	-	-
C 16:0	6.65	8.80	-	5.20	5.54	11.34	39.58	21.79	6.25	13.03	7.49	4.71
C 16:1	0.07	-	0.10	0.32	0.20	0.10	0.18	0.47	0.08	0.97	-	0.20
C 17:0	0.04	-	-	0.03	-	0.07	0.09	0.07	0.06	0.14	-	-
C 17:1	-	-	-	0.08	0.07	-	0.03	0.03	0.03	0.22	-	0.06
C 18:0	3.29	4.20	3.55	2.14	1.70	2.13	4.25	2.60	4.19	3.66	3.32	1.70
C18:1 <sup>a</sup>	0.02	-	0.02	74.24	0.04	-	0.05	0.15	0.03	-	-	-
C18:1 <sup>b</sup>	12.91	45.15	33.43	2.22	62.13	31.69	42.53	17.26	24.53	70.23	4.66	62.09
C 18:2	75.59	39.74	54.83	14.36	21.71	52.58	10.69	56.17	21.25	9.51	0.70	21.22
C 18:3	0.12	0.20	0.05	0.11	6.65	0.92	0.24	0.14	43.23	0.54	0.05	9.54
C 18:5	-	-	-	-	-	-	-	-	0.02	-	-	-
C 20:3	-	-	-	-	0.03	-	-	-	0.24	-	-	-
C 20:4	0.02	-	0.03	-	0.02	0.02	0.01	0.02	0.02	0.02	-	0.02

a: Octadecenoic acid, b: Oleic Acid.

## CONCLUSION

The physico-chemical fuel properties of a biodiesel fuel are largely dependent on the feedstock type from which it is produced. At this point, the most important parameter is the fatty acid configuration of the feedstock and so the biodiesel. Biodiesel fuels are divided into three generations according to the feedstock from which they are produced. In addition to the differences between different origin biodiesel fuels in terms of economy and sustainability issues, biodiesels of different generations will have different fatty acid contents and will inevitably and significantly show different physico-chemical fuel properties affecting engine characteristics. In this experimental study, it was aimed to compare the fatty acid distributions of various biodiesel fuels from different generations. For this purpose, 12 different biodiesel fuels (covering three generations) were produced and their fatty acid structures were determined and compared with each other. It has been observed that the investigated biodiesel fuels contained different percentages of different fatty acids in accordance with their different natures. However, it has been observed that all biodiesel fuels contained palmitic acid, stearic acid, oleic acid, linoleic acid and linolenic acid (in different percentages). CcB differed from other biodiesel fuels in terms of fatty acid diversity. The biodiesel with the highest saturation rate was CcB. The high saturation value of this fuel improves its some

features such as cetane number, oxidative stability, lubricity, heating value whereas leads to high viscosity deteriorating the atomization quality. Among the 12 biodiesel fuels examined in this study, AIB had the lowest saturation ratio. Since the high unsaturation level of AIB will improve the cold flow properties of this fuel compared to the other biodiesel fuels, it offers an important potential to AIB as an aviation fuel.

## CONFLICT OF INTEREST

The authors declare that they have no known competing financial interests or personal relationships that could have appeared to influence the work reported in this paper.

## REFERENCES

1. Keven A, Karaali R. Investigation of an Alternative Fuel for Diesel Engines. Acta Phys Pol A [Internet]. 2015 Aug [cited 2022 Nov 19];128(2B):B-282-B-286. Available from: <URL>.
2. Yaşar F. Comparison of fuel properties of biodiesel fuels produced from different oils to determine the most suitable feedstock type. Fuel [Internet]. 2020 Mar [cited 2022 Nov 19];264:116817. Available from: <URL>.
3. Alptekin E, Sanli H, Canakci M. Combustion and performance evaluation of a common rail DI diesel engine fueled with ethyl and methyl esters. Applied Thermal Engineering [Internet]. 2019 Feb [cited 2022 Nov 19];149:180-91. Available from: <URL>.

4. Hu J, Du Z, Li C, Min E. Study on the lubrication properties of biodiesel as fuel lubricity enhancers. Fuel [Internet]. 2005 Mar 17 [cited 2022 Nov 19];S0016236105000700. Available from: <URL>.
5. Hoekman SK, Robbins C. Review of the effects of biodiesel on NOx emissions. Fuel Processing Technology [Internet]. 2012 Apr [cited 2022 Nov 19];96:237-49. Available from: <URL>.
6. Sanli H. An experimental investigation on the usage of waste frying oil-diesel fuel blends with low viscosity in a Common Rail DI-diesel engine. Fuel [Internet]. 2018 Jun [cited 2022 Nov 19];222:434-43. Available from: <URL>.
7. Ahmad AL, Yasin NHM, Derek CJC, Lim JK. Microalgae as a sustainable energy source for biodiesel production: A review. Renewable and Sustainable Energy Reviews [Internet]. 2011 Jan [cited 2022 Nov 19];15(1):584-93. Available from: <URL>.
8. Sharma V, Hossain AK, Griffiths G, Duraisamy G, Jacob Thomas J. Investigation on yield, fuel properties, ageing and low temperature flow of fish oil esters. Energy Conversion and Management: X [Internet]. 2022 May [cited 2022 Nov 19];14:100217. Available from: <URL>.
9. Sanli H, Canakci M, Alptekin E. Predicting the higher heating values of waste frying oils as potential biodiesel feedstock. Fuel [Internet]. 2014 Jan [cited 2022 Nov 19];115:850-4. Available from: <URL>.
10. Mishra S, Anand K, Mehta PS. Predicting the Cetane Number of Biodiesel Fuels from Their Fatty Acid Methyl Ester Composition. Energy Fuels [Internet]. 2016 Dec 15 [cited 2022 Nov 19];30(12):10425-34. Available from: <URL>.
11. Marchetti JM. Biodiesel production technologies. New York: Nova, Nova Science Publishers, Inc; 2010. 166 p. ISBN: 978-1-61668-963-6.
12. Barut Gök S, Pehlivan EC, Aydın M, Erdoğan Y. Silybum marianum L. TOHURLARININ YAĞ ASİDİ KOMPOZİSYONU İLE TOHUM YAĞI VE SİLYMARİN EKSTRAKTİNİN ANTİMİKROBİYAL ETKİSİ. GIDA / THE JOURNAL OF FOOD [Internet]. 2020 Dec 30 [cited 2022 Nov 19];110-8. Available from: <URL>.
13. Behr A, Gomes JP. The refinement of renewable resources: New important derivatives of fatty acids and glycerol. Eur J Lipid Sci Technol [Internet]. 2010 Jan [cited 2022 Nov 19];112(1):31-50. Available from: <URL>.
14. Graboski MS, McCormick RL. Combustion of fat and vegetable oil derived fuels in diesel engines. Progress in Energy and Combustion Science [Internet]. 1998 Jan [cited 2022 Nov 19];24(2):125-64. Available from: <URL>.
15. Canakci M, Sanli H. Biodiesel production from various feedstocks and their effects on the fuel properties. J Ind Microbiol Biotechnol [Internet]. 2008 May [cited 2022 Nov 19];35(5):431-41. Available from: <URL>.







## The Effects of the Addition of Dill Oil (*Anethum graveolens*) into Biodiesel-Diesel Blends

Onur Alp DİKİYOL<sup>1</sup> , Berna KABADAYI<sup>1</sup> , Elif İŞLER<sup>1</sup> , İrem CİNGÖZ<sup>1</sup> ,  
Carlos da Silva BENTO<sup>1</sup> , Nalan TÜRKÖZ KARAKULLUKÇU<sup>2</sup> , Gediz UĞUZ<sup>1\*</sup> 

<sup>1</sup>Ondokuz Mayıs University, Department of Chemical Engineering, Samsun, 55200, Turkey

<sup>2</sup>Ondokuz Mayıs University, Blacksea Advanced Technology Research and Application Center, Samsun, 55200, Turkey

**Abstract:** The effects of dill oil extract as an antioxidant on the crystallization properties of colza biodiesel were investigated. 3000 ppm dill oil (*Anethum graveolens*) was blended with colza biodiesel-diesel mixtures at certain rates. The chemical antioxidant butylated hydroxytoluene (BHT) was used to compare the effects. For this reason, the samples were prepared and called D100, B20D80, B20D80D, and B20D80BHT. The crystallization temperatures ( $T_{cr}$ ) of the samples were determined by using a Differential Scanning Calorimetry (DSC) technique. The values of samples with antioxidants were decreased compared to the non-antioxidant biodiesel sample (B100). The order of antioxidant power was  $D100 < B20D80 < B20D80BHT < B20D80D$ . DSC results showed that the crystallization onset temperatures for D100, B20D80, B20D80BHT and B20D80D were  $-11.37$  °C,  $-13.42$  °C,  $-14.94$  °C, and  $-15.65$  °C, respectively. The addition of dill oil extract as a natural antioxidant had a positive effect on biodiesel oxidative stability for 3000 ppm concentration. Natural dill oil showed a similar efficiency with BHT that the synthetic chemical antioxidant. The dill oil can be used as an antioxidant after the complete standard fuel tests.

**Keywords:** Anethum graveolens oil, Biodiesel, Colza biodiesel, Dill oil, Natural antioxidant, Oxidative stability.

**Submitted:** October 31, 2022. **Accepted:** November 22, 2022.

**Cite this:** Dikyol OA, Kabadayı B, İşler E, Cingöz İ, Bento, da Silva C, Türköz Karakullukçu N, et al. The Effects of the Addition of Dill Oil (*Anethum graveolens*) into Biodiesel-Diesel Blends. JOTCSB. 2022;5(2):203-12.

**\*Corresponding author. E-mail:** [gediz.uguz@omu.edu.tr](mailto:gediz.uguz@omu.edu.tr).

### INTRODUCTION

Energy resources are a crucial factor in the economies of many countries as they are used in many areas. Fossil fuels (such as oil, coal, and natural gas) have been used as the main energy sources around the world for a long time. (Atabani et al., 2019). The high consumption of fossil fuels has increased carbon emissions, which has accelerated the global warming. The CO<sub>2</sub> gas released because of the combustion fossil fuels has a negative impact on the environment. The frequent occurrence of these climate problems encourages countries to develop renewable energy sources (1, 2). Due to the negative effects of fossil fuels on the

environment and the decrease in their reserves, environmentally friendly and sustainable alternative fuels are being researched instead of fossil fuels (3).

In new-renewable energy sources, biomass energy such as biofuel has the greatest technical potential. Biodiesel is obtained by esterification reaction of oils/animal fats (4) or waste cooking oils (5,6) with alcohols, and constitutes an alternative to conventional diesel (7). Biodiesel contains various saturated/unsaturated fatty acid esters, mainly fatty acid methyl esters (FAMES) (Boulal et al., 2019). Biodiesel has some advantages such as being biodegradable, having fast dissolution in nature, having an absence of toxic waste, being non-

explosive, and has supply security because of the wide raw material resources available. Since biodiesel is a better lubricant compared to petroleum diesel, it prolongs the life of the engine. Due to the fact that production can be completely domestic, eliminates foreign dependence (8). Besides the advantages, there are also disadvantages in the use of biodiesel, such as high production cost, the tendency to oxidation, and high NO<sub>x</sub> exhaust emissions. These disadvantages might prevent the frequent use of biodiesel. NO<sub>x</sub> emissions

are 10% higher than conventional diesel, but as there is no sulfur in its composition, NO<sub>x</sub> emission can be reduced by using a catalytic converter. Compared to diesel biodiesel cold flow properties are worse, and cold weather may cause problems during the first start-up. Biodiesel can be applied as a substitute for conventional diesel, or biodiesel can be blended with diesel (Jain & Sharma, 2011a) or alcohols (Maleki & Ashraf Talesh, 2022) instead of diesel fuels. Biodiesel is generally named as in Table 1.

**Table 1.** Biodiesel codes and the content of the code (9)

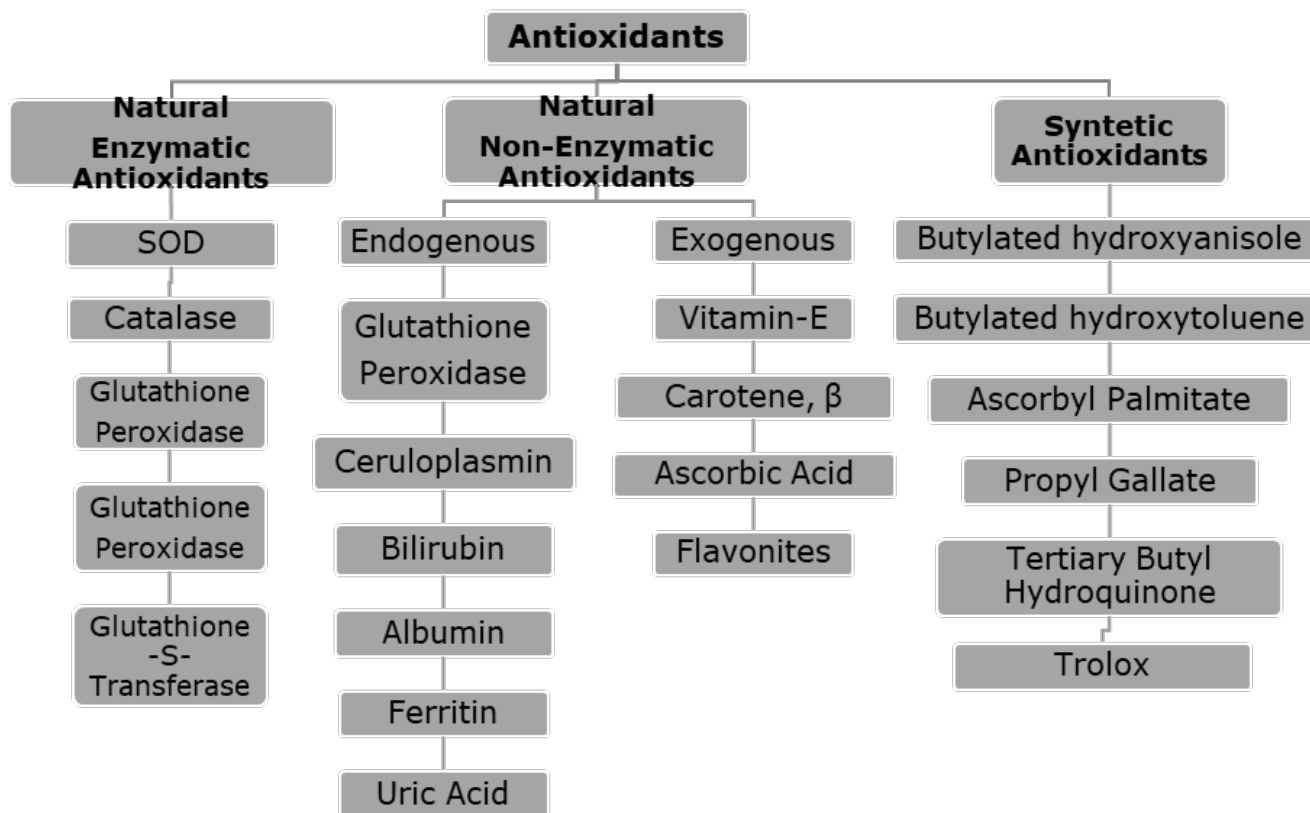
<b>Standard Code</b>	<b>Biodiesel Content (%)</b>	<b>Diesel Content (%)</b>
B5	5	95
B20	20	80
B50	50	50
B100	100	-

There are three different types of biodiesel. These are; FAME (Fatty Acids Methyl Ester), HVO (Hydroprocessed Vegetable Oil), and BTL (Biomass to Liquids). In Europe and America, biodiesel produced in certain proportions can be added to diesel fuel. As fuel stability of the fuel depends on the climatic conditions, oxidation may occur in the fuel due to heat changes and as a result of this oxidation, deposits may occur in the fuel, and this

situation can cause storage stability issues. Antioxidants are added to the biodiesel-diesel blend to improve some properties like oxidation stability as well as cold flow, to prevent or delay the oxidation in the fuel (10). The types of antioxidants involved are divided into *Natural and Synthetic* (11). The antioxidant types were classified in Figure 1. The studies about natural antioxidants from plants were represented in Table 2.

**Table 2:** Presented studies about natural oil as an antioxidant in the literature.

<b>Antioxidant</b>	<b>Biodiesel</b>	<b>Report</b>
Tert-Butylhydroquinone	Soybean	Longer induction period (12)
Butylated hydroxyanisole Butylated hydroxytoluene	Palm oil	Reduced emissions (13)
Butylated hydroxyanisole	Calophyllum inophyllum	Reduced nitrogen oxide (14)



**Figure 1:** Classification of antioxidants (15).

Dill, which was found suitable to be used in the study, is generally preferred as a sedative, antispasmodic, diuretic, and gas blocker in babies, which contains essential oil, fixed oil, and phenolic components. The well-being of dill essential oil is proportional to the percentages of carvon and α-phellandrene in it. Carvone and limonene are the main mixtures in dill essential oil. Dill is preferred in foods as an antioxidant due to its intense taste and essential oil (16).

The data obtained because of the experiment were compared with BHT, a synthetic antioxidant. BHT, or by its chemical name 2,6-di-tert-butyl-p-cresol

(DBPC), is a synthetic phenolic antioxidant widely used as a food additive. BHT, due to its phenolic structure, gives hydrogen from phenolic hydroxide groups and prevents the emergence of free fatty acid radicals in the head part of the fatty acid. It has a high antioxidant character. It activates the quality of the oils and prevents the formation of deposits. BTH is used in the food and rubber sectors, metallurgy, cosmetics, pharmaceuticals, embalming liquids, antifreeze, and auto chemistry liquids, and it is also widely used in the fuel industry. The properties of BHT is depicted in Table 3.

**Table 3:** The properties of BHT.

Chemical structure	Molecular weight (g/mol)	Chemical formula
	220.35	C <sub>15</sub> H <sub>24</sub> O

Dill (*Anethum graveolens* L.) is an annual or biennial herb belonging to the Apiaceae family. Dill essential oil is used for the treatment of gastrointestinal disorders such as abdominal [distension](#), gastritis, intestinal spasm, and flatulence. The leaf, seed, and essential oil of dill shows good antioxidant activities (17).

Dill was preferred for this study because of the natural antioxidant properties it contains. The essential oil was obtained using soxhlet extraction. The extracted oil was added to 3000 ppm into various prepared biodiesel-diesel fuel mixtures. Biodiesel-diesel fuel mixture containing extract was subjected to various characterization tests. FT-IR is a highly preferred type of characterization test due to its characteristics such as being cheap and giving fast results, so it was preferred for this study. At the stage of determining the crystallization point of the resulting fuel mixture, DSC was used. Because of the tests carried out and the data obtained, improvements in the crystallization point occurred with the addition of dill extract to biodiesel-diesel fuel mixtures. Such a study could open up new directions for the field of biodiesel research in the future (18–20). In this study, the effects of *Anethum graveolens* oil addition to biodiesel-diesel blends. FT-IR and DSC analyses were performed and the obtained data were evaluated.

## EXPERIMENTAL SECTION

### Materials and Methods

n-Hexane (97%) was purchased from Sigma-Aldrich. Colza biodiesel (B100) and diesel fuel were provided commercially by Biodiesel Company (TBE) and fuel company (OPET) in Turkey, respectively. *Anethum graveolens* were collected manually in the region of Samsun, Turkey. It was cleaned with distilled water to remove surface impurities. Then it was dried in the oven at 70 °C for 48 hours to yield a fine powder. After drying, samples were crushed and sieved by a grinder. This was preserved by storage at the temperature of 4 °C against both light and humidity, until following extractions.

### Soxhlet Extraction

*Anethum graveolens* powder (20 g) was firstly put in a filter paper cellulose cartridge and then extracted for 8 h on a soxhlet apparatus using 300 mL of analytical grade n-hexane as a solvent. After the extraction, the residual solvent was separated from the solid with a rotary evaporator. The remaining substance was kept in a drying oven at 40 °C for 48 hours. Finally, the glass round-bottomed flask containing the substance was sealed and stored at the temperature of 4 °C until following process (21).

### Preparations of Biodiesel-Diesel Blends

Standard biodiesel-diesel blends were prepared with 20% biodiesel and 80% diesel. The mixture was called as B20D80. The plant extracts were added into the blends at 3000 ppm level.

### Fourier Transform Infrared Spectroscopy (FT-IR)

The possible chemical functional groups present in *Anethum graveolens* were investigated with FT-IR (Perkin Elmer, Spectrum-Two, USA). The sample surface was scanned in the 650–4000 cm<sup>-1</sup> range. The ATR FT-IR spectra were recorded at room temperature. The background subtraction, baseline, and data tune-up correction were done.

### Differential Scanning Calorimetry (DSC)

To determine the crystallization temperatures of D100, B20D80, B20D80D, B20D803000, and BHT were analyzed by DSC Q-2000 (TA Instrument-Waters, USA). Dynamic DSC measurements were carried out in an aluminum crucible with a small variation in sample mass of approximately 5±0.5 mg and placed in the DSC module with a similar empty pan as reference. The rate of cooling was 10 °C/min between -90 °C and 25 °C with a flow rate of 50 mL/min. The instrument was flushed with nitrogen. Each DSC test took about 16.5 minutes to complete a single sample. The summary of the DSC method is given in Table 4 (18).

**Table 4:** Summary of DSC method by TA Q-2000 DSC (18).

Instrument	TA Q-2000 DSC
Sample amount	5±0.5 mg
Gas	Nitrogen
Flow rate	50 mL/min
Temperature range	-90 °C-25 °C
Ramp rate	10 °C/min

## RESULTS AND DISCUSSIONS

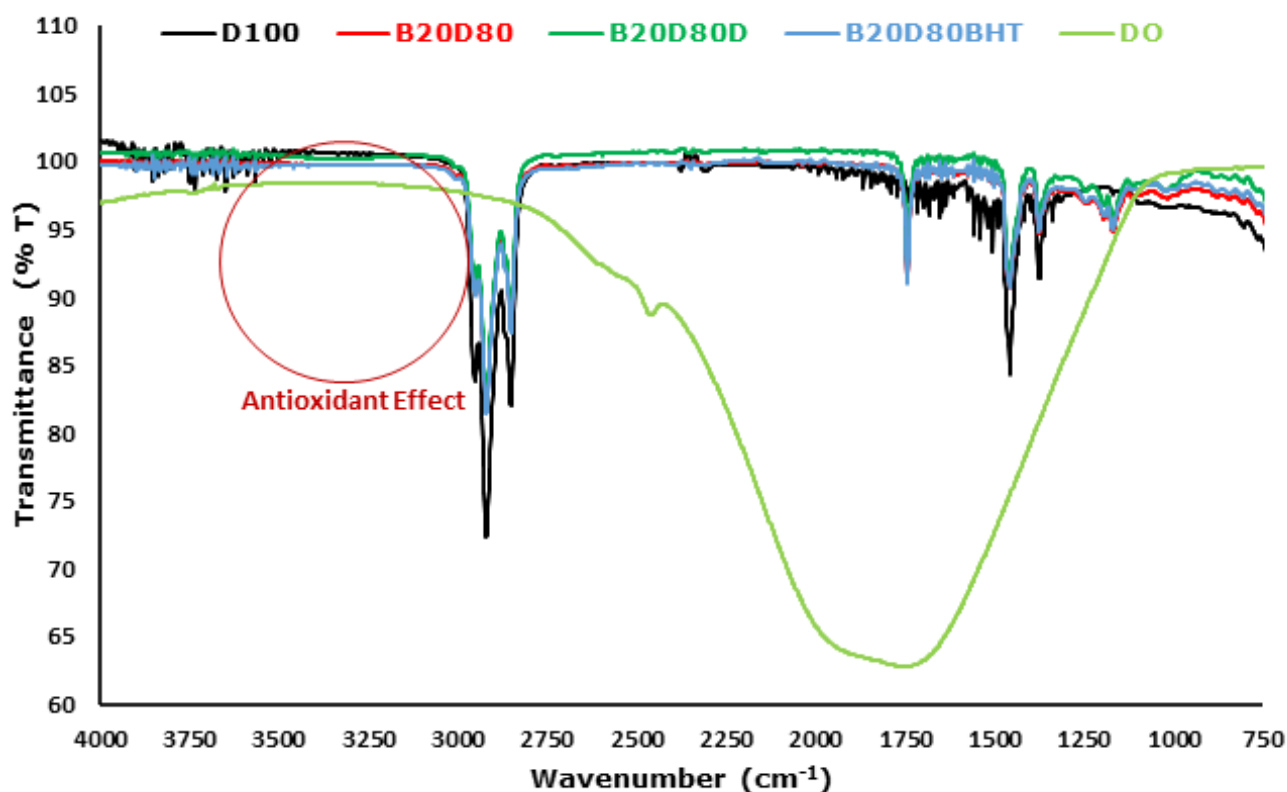
### FT-IR

In the FTIR spectra, the spectrum placed between wavenumber (cm<sup>-1</sup>) vs. transmittance percentage (T %) shows the regions of the spectrum that specific molecular vibrations containing in the D100,

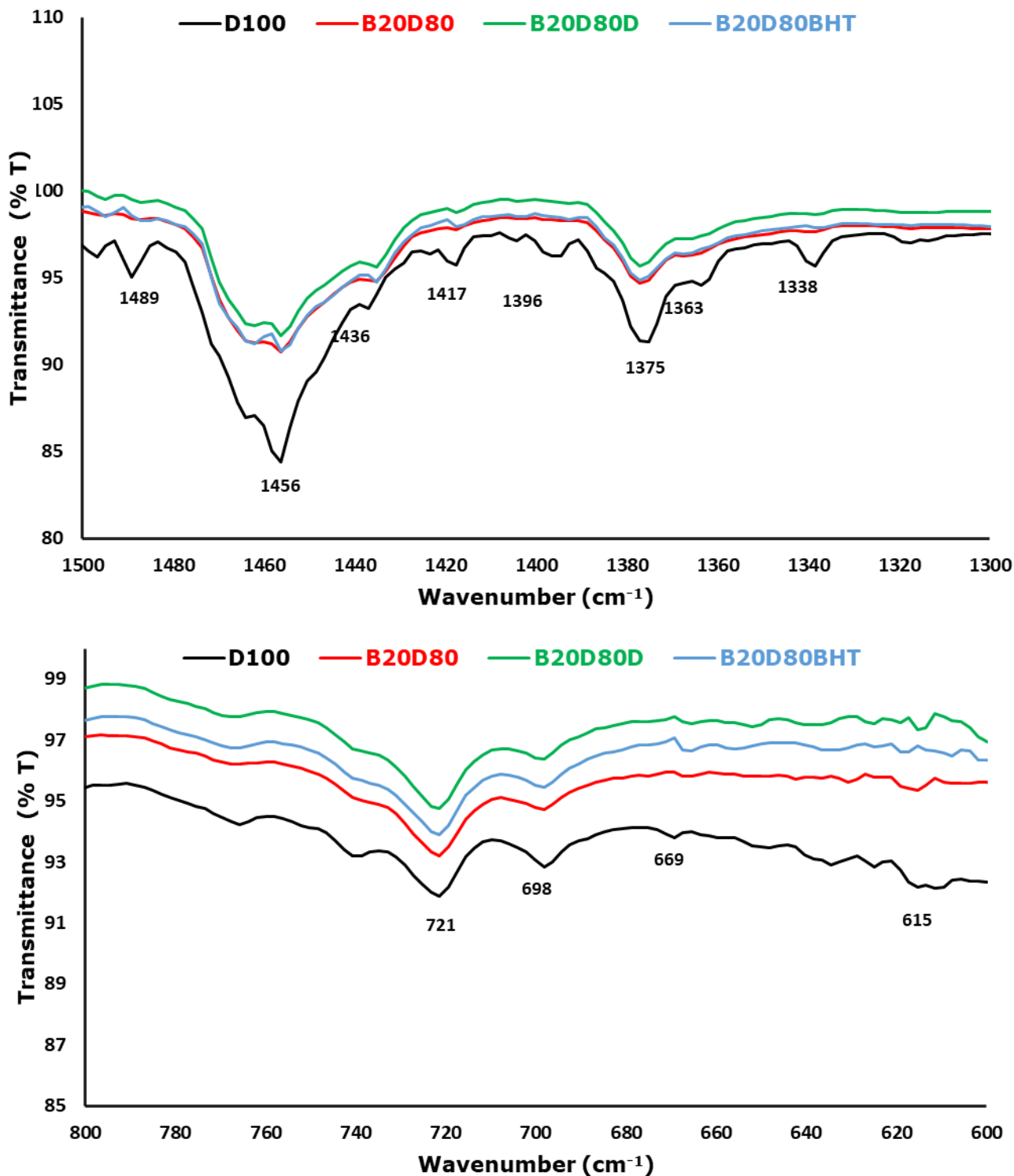
B20D80, B20D80D, B20D803000, and BHT. Generally, wavenumber and transmittance percentage were obtained for  $\nu(\text{O-H})$  (3000–3700 cm<sup>-1</sup>),  $\nu(\text{C-H})$  (2700–3000 cm<sup>-1</sup>),  $\nu(\text{C=O})$  (1500–1800 cm<sup>-1</sup>), and  $\nu(\text{C-O})$  (600–1400 cm<sup>-1</sup>) vibrations. Oxidation stability is shown by  $\nu(\text{O-H})$  and  $\nu(\text{CH})$  vibrations of samples because of the

substitution by alkyl functionals in ortho- and para position to develop the electron density around the -OH group. In the FTIR spectra,  $\nu(\text{C-O})$  and  $\nu(\text{C=O})$  vibrations represent in the presence of ether or ester functional groups in a sample (22). The effect of adding natural and synthetic antioxidants to biodiesel samples at 3000 ppm concentration.  $\nu(\text{O-H})$  valence-stretching vibration of an unbounded hydroxyl group is usually quoted as being  $3700\text{--}3500\text{ cm}^{-1}$ . In addition, IR spectra of function biodiesel samples indicate a decrease in the intensity of the vibrations at  $\nu(\text{C-H})$  ( $2700\text{--}3000$

$\text{cm}^{-1}$ ). Because of increase in saturation represents that there is a lack of possibility in favor oxidative polymerization reaction. Antioxidant activity as  $\text{D100} < \text{B20D80} < \text{B20D80D} < \text{B20D80BHT} < \text{B20D80D}$  because phenolic antioxidants can be positioned in the same order (23). Consequently, the increases in the transmittance in the antioxidant effect regions of the FTIR spectrum with the addition of antioxidants are evidence of the effectiveness of the added antioxidant which has carvone and limonene groups. The lists of functional groups identified were shown in Table 5 (24).



**Figure 2:** FT-IR spectra of D100, B20D80, B20D80D, DO, and B20D80BHT between  $750\text{--}4000\text{ cm}^{-1}$  range.



**Figure 3:** FT-IR spectra of D100, B20D80, B20D80D, and B20D80BHT between 600-800 cm<sup>-1</sup> range



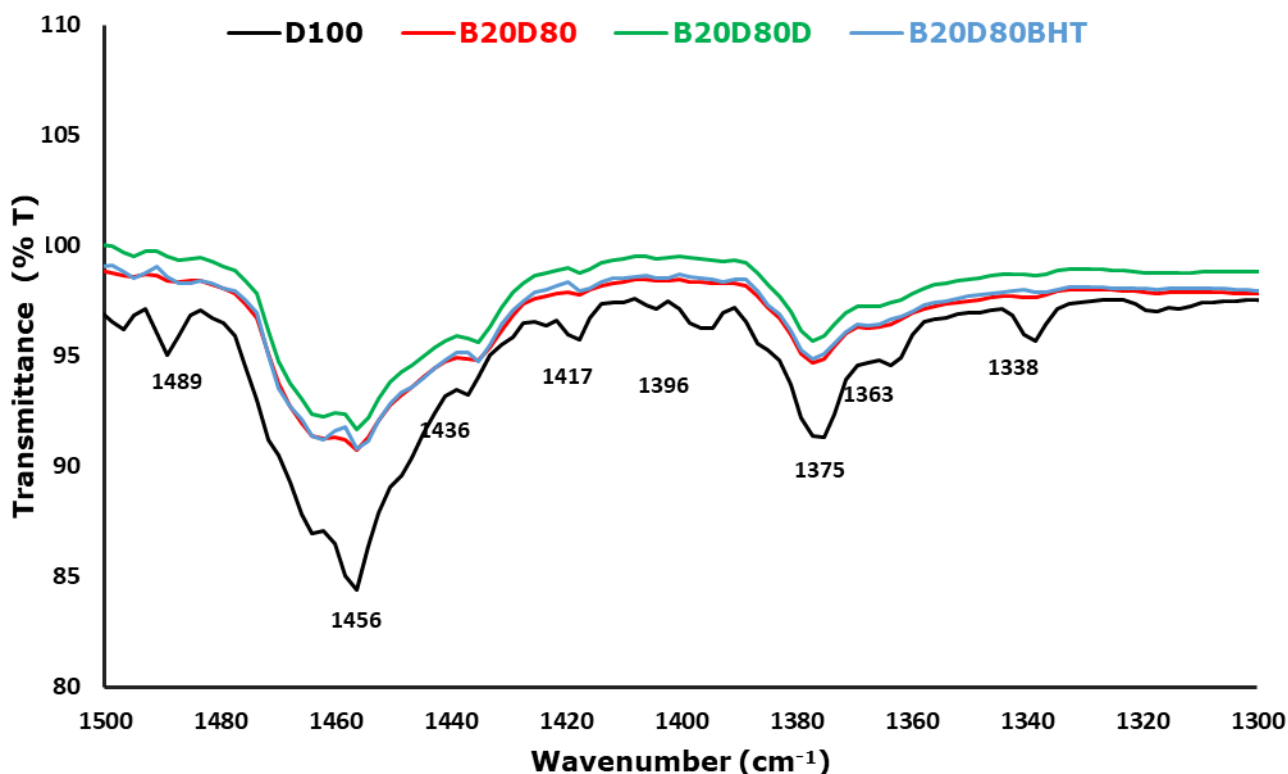


Figure 4: FT-IR spectra of D100, B20D80, B20D80D, and B20D80BHT between 1300-1500 cm<sup>-1</sup> range.

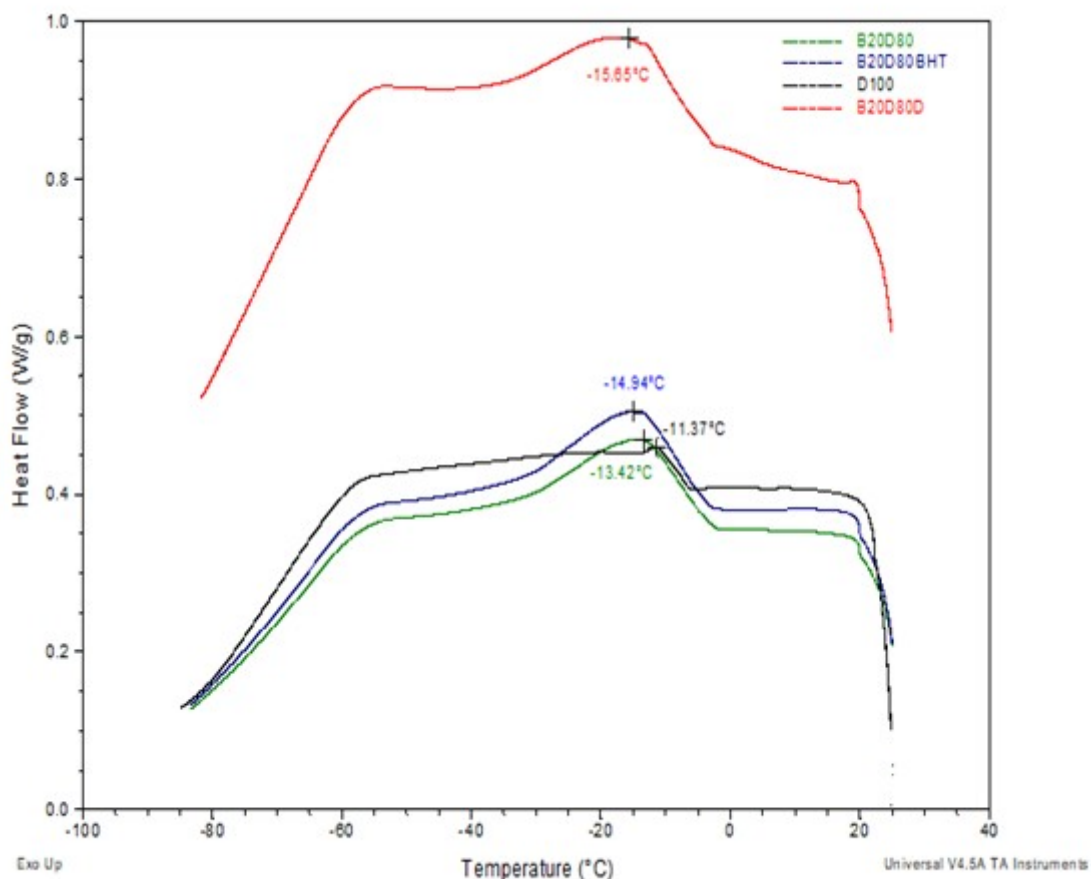
Table 5: Functional group frequencies of the fuel samples (24).

Wavenumber cm <sup>-1</sup>	Types of vibration	Functional Groups
3300-3750	Stretching 1	O-H of alcohols
2950	Asymmetrical stretching 2	=C-H of alkenes
2930	Asymmetrical stretching 3	C-H of alkanes
2860	Symmetrical stretching 4	C-H of methylene
1755	Stretching 5	C=O of ester carbonyl functional group
1240-1030	Stretching	C-O of alkoxy esters, ethers, and C-O-C
710	Bending of alkenes and overlapping of rocking vibration of methylene 7	=C-H and -(CH <sub>2</sub> ) <sub>n</sub> methylene groups of cis-disubstituted alkenes and aromatic
690	Out of plane bending 8	=C-H of cis-disubstituted alkene and aromatics

**DSC**

This study increased the crystallization temperature of the natural antioxidant blend fuel from -11.37 °C to -15.65 °C as a consequence of comparing three

distinct samples and DSC measurements of natural, synthetic antioxidant blended fuel, and diesel fuel (Table 6).



**Figure 5:** DSC thermograms of B20D80, B20D80D, B20D80BHT, and D100.

**Table 6.** The crystallization temperature of B20D80, B20D80D, B20D80BHT, and D100.

<b>Sample code</b>	<b>Crystallization temperature (°C)</b>
<b>D100</b>	-11.37
<b>B20D80</b>	-13.42
<b>B20D80D</b>	-15.65
<b>B20D80BHT</b>	-14.94

As a result of the study, the crystallization points of the biodiesel-diesel mixture, in which dill extract was added as a natural antioxidant were determined. Crystallization points of biodiesel-diesel fuel with natural and synthetic antioxidant mixture were determined by the DSC device. As a result, it was found that dill extract increased the crystallization point in the fuel by about 17% better

than other samples. When the FT-IR results were examined for biodiesel-diesel fuel mixtures, it was seen that the % permeability values increased with the antioxidant effect.

**Recommendation:** Dill extract has shown improvement in the fuel mixture as an antioxidant,

but other standard tests of the fuel should also be performed.

## CONCLUSIONS

This work was intended to examine how natural antioxidants (dill oil extract) affected the performance of biodiesel and biodiesel-diesel blends. It examined the impact of dill oil extract on oxidative stability as well as the temperature at which colza biodiesel crystallizes. The crystallization point is a crucial characteristic of biodiesel and diesel fuels because, at low temperatures, the saturated chemicals that are present in these solutions start to crystallize and produce wax, which can clog filters and pipes and cause engine malfunction. In this study, dill oil extract was used as a natural antioxidant, and for comparative purposes, BHT was used as the synthetic antioxidant.

To carry out this study, four samples were prepared, which are, D100, B20D80, B20D80D, and B20D80BHT. FT-IR, and DSC techniques were used to characterize the samples. The presence of possible functional groups in the samples were determined using FT-IR, and the crystallization temperatures of the samples determined by using DSC. According to the FT-IR graphics, the biodiesel-diesel blend with 3000 ppm of dill oil extract, designated B20D80D, has fewer functional groups than other samples, such as B20D80BHT, which indicates that the dill oil extract increased the oxidative stability of the mixture. On the other hand, from the DSC results, it was found that the dill extract increased the crystallization point in the fuel by 17% better than other samples.

Although dill oil extract has shown excellent results as an antioxidant for biodiesel-diesel blends, more studies and tests should be conducted to determine what its other effects are in biodiesel-diesel blends and whether or not it can be used on a large scale by the fuel industry.

## CONFLICT OF INTEREST

Not applicable.

## ACKNOWLEDGMENTS

The authors would like to thank KİTAM, Ondokuz Mayıs University, Samsun, Turkey, for the FT-IR and DSC analysis. The authors would like to thank İbrahim Ethem OLUKÇUOĞLU (Head of the Library Department of Ondokuz Mayıs University) for literature research.

## REFERENCES

1. Mohamed H, Ben Jebli M, Ben Youssef S. Renewable and fossil energy, terrorism, economic growth, and trade: Evidence from France. *Renewable Energy* [Internet]. 2019

Aug [cited 2022 Nov 22];139:459–67. Available from: [<URL>](#)

2. Abbasi KR, Shahbaz M, Zhang J, Irfan M, Alvarado R. Analyze the environmental sustainability factors of China: The role of fossil fuel energy and renewable energy. *Renewable Energy* [Internet]. 2022 Mar [cited 2022 Nov 22];187:390–402. Available from: [<URL>](#)

3. Atabani A, Mekaoussi M, Uguz G, Arpa O, Ayanoglu A, Shobana S. Evaluation, characterization, and engine performance of complementary fuel blends of butanol-biodiesel-diesel from Aleurites moluccanus as potential alternative fuels for CI engines. *Energy & Environment* [Internet]. 2020 Aug [cited 2022 Nov 22];31(5):755–84. Available from: [<URL>](#)

4. Helmi F, Helmi M, Hemmati A. Phosphomolybdic acid/chitosan as acid solid catalyst using for biodiesel production from pomegranate seed oil via microwave heating system: RSM optimization and kinetic study. *Renewable Energy* [Internet]. 2022 Apr [cited 2022 Nov 22];189:881–98. Available from: [<URL>](#)

5. Malhotra R, Ali A. 5-Na/ZnO doped mesoporous silica as reusable solid catalyst for biodiesel production via transesterification of virgin cottonseed oil. *Renewable Energy* [Internet]. 2019 Apr [cited 2022 Nov 22];133:606–19. Available from: [<URL>](#)

6. Bencheikh K, Atabani AE, Shobana S, Mohammed MN, Uğuz G, Arpa O, et al. Fuels properties, characterizations and engine and emission performance analyses of ternary waste cooking oil biodiesel-diesel-propanol blends. *Sustainable Energy Technologies and Assessments* [Internet]. 2019 Oct [cited 2022 Nov 22];35:321–34. Available from: [<URL>](#)

7. Aghbashlo M, Peng W, Tabatabaei M, Kalogirou SA, Soltanian S, Hosseinzadeh-Bandbafha H, et al. Machine learning technology in biodiesel research: A review. *Progress in Energy and Combustion Science* [Internet]. 2021 Jul [cited 2022 Nov 22];85:100904. Available from: [<URL>](#)

8. Kant Bhatia S, Kant Bhatia R, Jeon JM, Pugazhendhi A, Kumar Awasthi M, Kumar D, et al. An overview on advancements in biobased transesterification methods for biodiesel production: Oil resources, extraction, biocatalysts, and process intensification technologies. *Fuel* [Internet]. 2021 Feb [cited 2022 Nov 22];285:119117. Available from: [<URL>](#)

9. Jain S, Sharma MP. Oxidation stability of blends of Jatropha biodiesel with diesel. *Fuel* [Internet]. 2011 Oct [cited 2022 Nov 22];90(10):3014–20. Available from: [<URL>](#)

10. Uguz G. Inhibitory effect of thyme oil as an antioxidant for waste cooking oil biodiesel crystallization. *Energy & Environment* [Internet]. 2021 Nov 20 [cited 2022 Nov 22];0958305X2110613. Available from: [<URL>](#)

11. Uğuz G, Atabani AE, Mohammed MN, Shobana S, Uğuz S, Kumar G, et al. Fuel stability of biodiesel from waste cooking oil: A comparative evaluation with various antioxidants using FT-IR and DSC techniques. *Biocatalysis and Agricultural Biotechnology* [Internet]. 2019 Sep [cited 2022 Nov 22];21:101283. Available from: [<URL>](#)

12. Dunn RO. Effect of oxidation under accelerated conditions on fuel properties of methyl soyate (biodiesel). *J Amer Oil Chem Soc* [Internet]. 2002 Sep [cited 2022 Nov 22];79(9):915–20. Available from: [<URL>](#)
13. Rizwanul Fattah IM, Masjuki HH, Kalam MA, Mofijur M, Abedin MJ. Effect of antioxidant on the performance and emission characteristics of a diesel engine fueled with palm biodiesel blends. *Energy Conversion and Management* [Internet]. 2014 Mar [cited 2022 Nov 22];79:265–72. Available from: [<URL>](#)
14. Nanthagopal K, Ashok B, Saravanan B, Patel D, Sudarshan B, Aaditya Ramasamy R. An assessment on the effects of 1-pentanol and 1-butanol as additives with Calophyllum Inophyllum biodiesel. *Energy Conversion and Management* [Internet]. 2018 Feb [cited 2022 Nov 22];158:70–80. Available from: [<URL>](#)
15. Bunaciu A, Fleschin S, Aboul-Enein H. FTIR spectroscopy used for study the thermal degradation of lard. *Egypt Pharmaceut J* [Internet]. 2021 [cited 2022 Nov 22];20(2):166. Available from: [<URL>](#)
16. Decker EA, Alamed J, Castro IA. Interaction Between Polar Components and the Degree of Unsaturation of Fatty Acids on the Oxidative Stability of Emulsions. *J Americ Oil Chem Soc* [Internet]. 2010 Jul [cited 2022 Nov 22];87(7):771–80. Available from: [<URL>](#)
17. Rostaie M, Fallah S, Lorigooini Z, Abbasi Surki A. The effect of organic manure and chemical fertilizer on essential oil, chemical compositions and antioxidant activity of dill (*Anethum graveolens*) in sole and intercropped with soybean (*Glycine max*). *Journal of Cleaner Production* [Internet]. 2018 Oct [cited 2022 Nov 22];199:18–26. Available from: [<URL>](#)
18. Mohammed MN, Atabani AE, Uguz G, Lay CH, Kumar G, Al-Samarrae RR. Characterization of Hemp (*Cannabis sativa* L.) Biodiesel Blends with Euro Diesel, Butanol and Diethyl Ether Using FT-IR, UV-Vis, TGA and DSC Techniques. *Waste Biomass Valor* [Internet]. 2020 Mar [cited 2022 Nov 22];11(3):1097–113. Available from: [<URL>](#)
19. Uğuz G, Ayanoğlu A. Characterization of Waste Tire Pyrolysis Products by GC, ICP-MS, TGA and DSC. *Bitlis Eren Üniversitesi Fen Bilimleri Dergisi* [Internet]. 2021 Sep 1 [cited 2022 Nov 22];10(3):930–42. Available from: [<URL>](#)
20. Uğuz G, Ayanoğlu A. Chemical characterization of waste tire pyrolysis products. *International Advanced Researches and Engineering Journal* [Internet]. 2021 Aug 15 [cited 2022 Nov 22];5(2):163–70. Available from: [<URL>](#)
21. Marsoul A, Ijjaali M, Elhajjaji F, Taleb M, Salim R, Boukir A. Phytochemical screening, total phenolic and flavonoid methanolic extract of pomegranate bark (*Punica granatum* L): Evaluation of the inhibitory effect in acidic medium 1 M HCl. *Materials Today: Proceedings* [Internet]. 2020 [cited 2022 Nov 22];27:3193–8. Available from: [<URL>](#)
22. Yakan H, Çakmak Ş, Buruk O, Veyisoğlu A, Muğlu H, Türköz Karakullukçu N. New 5-methylisatin including thiocarbohydrazones: preparation, structure elucidation and antimicrobial activity. *Res Chem Intermed* [Internet]. 2022 Oct [cited 2022 Nov 22];48(10):4331–45. Available from: [<URL>](#)
23. Uğuz G. Antioxidant effect of clove oil on biodiesel produced from waste cooking oil. *Biomass Conv Bioref* [Internet]. 2021 Jun 30 [cited 2022 Nov 22]; Available from: [<URL>](#)
24. Berthomieu C, Hienerwadel R. Fourier transform infrared (FTIR) spectroscopy. *Photosynth Res* [Internet]. 2009 Sep [cited 2022 Nov 22];101(2–3):157–70. Available from: [<URL>](#)



## Application of Factorial Design in Adsorption Studies of Silver Ions with Multi-Walled Carbon Nanotubes

Feza Geyikçi 

*Ondokuz Mayıs University, Department of Chemical Engineering, 55139, Samsun, TURKEY*

**Abstract:** The adsorption-related applications of CNTs to solve environmental pollution problems have received considerable attention in recent years. Carbon nanotubes are strong materials with the capacity to form covalent bonds. These features can be improved with various modifications. The use of CNTs in the adsorption of heavy metals has become widespread. MWCNT-Metal pairs can be important for many different applications. The aim of this study is to investigate the Ag(I) ions adsorption capacity of MWCNTs from aqueous solutions using the experimental design method. A full factorial design was employed to optimize the adsorption of Ag(I) ions onto multi-walled carbon nanotubes (MWCNT). The effects of process parameters such as the initial Ag(I) concentrations (10 and 100 mg/L), pH (2 and 8) and multi-walled carbon nanotubes dosage (0.1 and 1.0 g/L) on Ag(I) adsorption were investigated on the adsorption process. Under acidic conditions, the removal efficiency of silver ions was found to be high by using MWCNTs. According to the results of factorial design calculations, the maximum adsorption capacity was found as 0.998 mg/g.

**Keywords:** Multi-walled carbon nanotubes, full factorial design, Ag(I) adsorption.

**Submitted:** November 12, 2022. **Accepted:** November 28, 2022.

**Cite this:** Geyikçi F. Application of Factorial Design in Adsorption Studies of Silver Ions with Multi-Walled Carbon Nanotubes. JOTCSB. 2022;5(2):213-20.

**Corresponding author. E-mail:** [fezag@omu.edu.tr](mailto:fezag@omu.edu.tr), Tel: +90 (362) 312 1919-1343

### INTRODUCTION

Heavy metals are among the most common pollutants found in industrial effluents. The presence of excess amounts of these metals in the environment is of great concern due to their accumulated toxicity in living organisms and threatening human life and the environment. Among the heavy metals such as lead, copper, cadmium, zinc, silver, and nickel, the least harmful metal is silver. Silver is one of the transition metals found in nature in the form of compounds. It is often found combined in copper or lead mineralization (1-3). Its main industrial use is as a silver halide compound in the production of photographic film. Other industrial uses include electrical conductivity, thermal conductivities, photosensitivity, battery catalysts, and mirrors. Silver (Ag) as one of the precious metals has prominent ductility and antibacterial properties, and the free silver ion is dangerous for sensitive aquatic plants and representative species of invertebrates (4-6).

While the adsorption method is used for the recovery or uptake of silver from aqueous media, methods such as precipitation, ion exchange, membrane processes, solvent extraction, electro coagulation, coagulation-flocculation, adsorption, reductive exchange and electrolytic recovery are also applied. Adsorption is known as a method used in the recovery process and synthesis of new material types. Adsorption processes using activated carbon and carbon nanotubes have been widely proposed and used for the removal of different (organic and inorganic) pollutants from waters. This process is generally applied method to protect water resources (7). Apart from the purification method, this method can be applied for the synthesis of materials with many different properties. Cost-effective materials that have been investigated for their potential use as adsorbents for heavy metal uptake include agricultural waste, food organic waste, algae, fungi, bacteria, fly ash, red mud, industry waste, fly ash, phosphogypsum bentonite

limestone waste materials as refuse concrete, zeolite and others (8–11).

In recent years, adsorption studies with different carbon nanotubes have attracted attention. Carbon nanotubes (CNTs) are one of the most commonly used building blocks of nanotechnology. CNTs had been discovered by Iijima, and has led research to new area in many interdisciplinary investigations as the advantages of CNTs are unique structural, electronic, optoelectronic, semiconductor, mechanical, thermal, chemical, and physical properties. CNTs are new generation materials with the potential to be used in water pollution control. The USEPA has identified CNTs as a key material to be used in environmental applications such as treatment and remediation. In a previous study, CNTs were oxidized with nitric acid and then treated as adsorbent for various heavy metal ions including  $\text{Cu}^{2+}$ ,  $\text{Zn}^{2+}$ ,  $\text{Pb}^{2+}$ ,  $\text{Cd}^{2+}$ ,  $\text{Co}^{2+}$  from wastewater (12). Since then CNTs have been gaining increasing recognition for their adsorption capabilities. This is mainly due to their extremely small size, uniform pore distribution and large specific surface area (13–15). CNTs can be classified into two main types: single wall carbon nanotubes (SWCNT) and multi-wall carbon nanotubes (MWCNT). MWCNTs provide high electrical conductivity. There are two main methods to modify MWCNTs for further adsorption applications, including noncovalent modification and covalent modification (12). MWCNTs have high electrical conductivity, a large specific area, and exceptional chemical inertness, also making them ideal for use in energy storage devices (16). MWCNT/Metal nanohybrids can be used in the synthesis of polyalcohols. The PtCoNi/MWCNTs nanocatalyst was used for the hydrogenation of furfural (17). Due to their large specific surface area, small size, and hollow and layered structures, MWCNTs have been proven to possess great potential as superior adsorbents for removing many kinds of organic and inorganic contaminants including 1,2-dichlorobenzene, trihalomethanes, microcystins, fluoride, lead, arsenate, cationic dyes, and ureamic toxins (18,19). In another study, ZIF-8/MWCNTs-COOH was synthesized as a nanoadsorbent in the removal of

dyestuff (Congo Red) and antibiotic (tetracycline) wastes (20). Because of their accessible availability and inexpensiveness, MWCNTs have been widely used in many studies. They have excellent advantages such as distinctive hollow structure, chemical stability, and large specific surface area. MWCNTs were modified with carboxyl and  $\text{MoS}_2$  and used for adsorption of Ag(I) ions. The maximum adsorption capacity of the  $\text{MoS}_2$ /MWCNTs nanohybrid for Ag(I) was 601.97 mg/g. This result was obtained with the activated MWCNTs and no other study related to Ag(I) adsorption of MWCNTs was found in the literature. However, the studies on the adsorption of heavy metals with MWCNTs are still very limited in the literature. In this study, the evaluation of the best adsorption conditions of Ag (I) ions onto MWCNTs has been made using a  $2^3$  factorial design method. The main objectives of this research are as follows: (1) To analyze the effect of controllable factors in the adsorption process with experimental data; (2) To determine the changing experimental conditions for the adsorption of Ag(I) onto MWCNTs; (3) To create a model equation for adsorption efficiency using the MiniTab 20 Software. Experiments were performed as a function of pH, adsorbent dosage and initial Ag(I) ions concentration of the solution.

## MATERIAL AND METHODS

### Materials and Reagents

MWCNTs synthesized by the catalytic vapor decomposition method were purchased from Chengdu Organic Chemicals Co. Ltd. The specific properties of MWCNTs are presented in Table 1. The morphology of MWCNTs are given by scanning electron microscopy (SEM, Zeiss Supra 50VP). SEM images (Figure. 1) show that carbon materials have very distinct morphological features. In Figure 1, the presence of characteristic helical MWCNTs were observed. The micrographs of MWCNTs are evidence of the adsorption process of MWCNTs with Ag(I). The pure MWCNTs were given in Figure 1 and have their outer diameter in the between 8 and 15 nm with tubular structures.

**Table 1:** The specific properties of MWCNTs.

Outer Diameter (nm)	8-15
Length	50 $\mu\text{m}$
Specific Surface Area	>233 $\text{m}^2/\text{g}$
Ash	<1.5 wt%
EC	> $10^2$ s/cm
Purity	>95 wt %

All chemicals were purchased in analytical purity and were used without further purification. All the plastic and glassware were cleaned by soaking in dilute  $\text{HNO}_3$  (1:9 v/v) and were rinsed with distilled water prior to use. To determine the effect of pH, adsorbent dosage and initial metal concentration on

Ag(I) ions adsorption efficiency, batch experiments were conducted. A stock solution that consisted of 1000 mg/L of the Ag(I) ions was prepared and diluted according to initial concentrations. The pH of the solutions was adjusted with  $\text{HNO}_3$  (Merck) or NaOH (Merck) solutions by using WTW 330 pH-



meter with a combined pH electrode. The samples were continuously agitated with a speed of 175 rpm at a room temperature for 1 h.

The maximum adsorption capacity at equilibrium  $q_e$  (mg/g), was calculated by (Eq.1):

$$q_e = \frac{(C_o - C_e)V}{m} \tag{1}$$

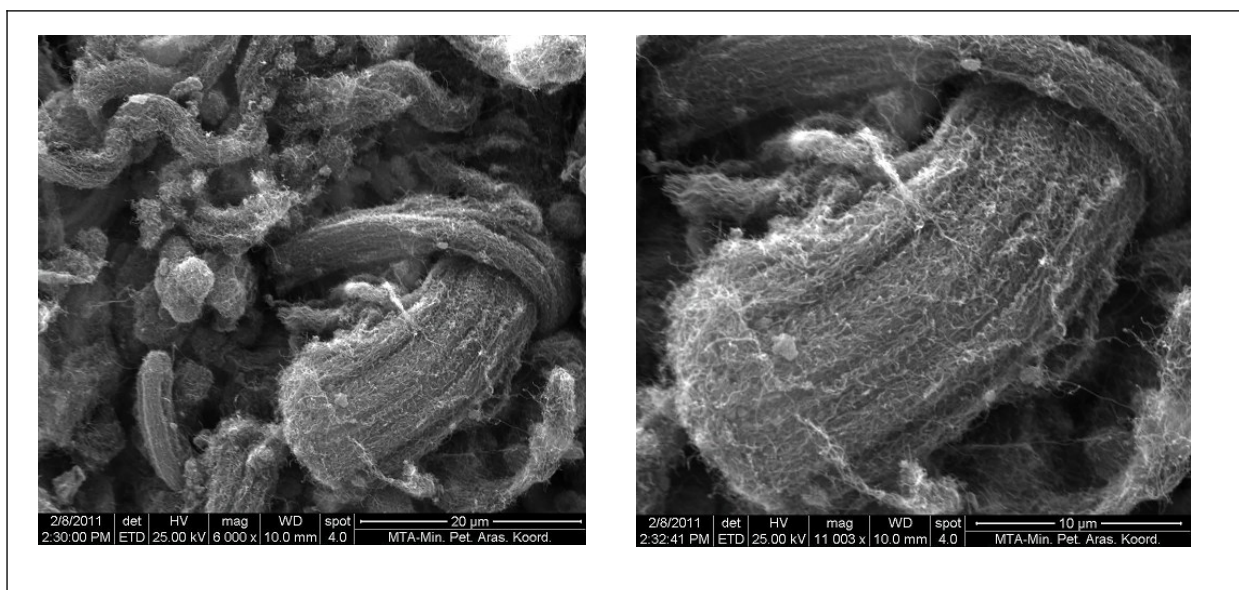
where  $C_o$  is the initial concentration of silver solution (mg/L),  $C_e$  is the equilibrium concentration of silver

solution (mg/L),  $V$  is volume of silver solution (mL), and  $m$  is the adsorbent weight (g).

The adsorption percentage of silver was calculated by the difference of initial concentration using the equation (Equation 2) expressed as follows:

$$R = \frac{C_o - C_e}{C_o} \times 100 \tag{2}$$

where  $C_o$  is the initial concentration of silver solution (mg/L),  $C_e$  is the equilibrium concentration of silver solution (mg/L), and  $R$  is the retention of Ag(I) ions in % of the added amount.



**Figure 1:** (Left) and (right) Some SEM images of helical multi-walled carbon nanotubes.

**Factorial Experimental Design**

Experimental factorial design is employed, to reduce, the number of experiment cost, time, to find best overall optimization of the experimental conditions. The design determines that factors have important effects on a response as well as how the effect of one factor varies with the level of the other factors. The number of experimental runs at  $b$  levels is  $b^k$ , where  $k$  is the number of factors and have successfully applied by many researchers. Today, the most widely used kind of experimental design, to estimate main effects as well as interaction effects, is the  $2^p$  factorial design in which each variable is investigated at two levels (21,22).

The  $2^3$  factorial experiments were applied in two levels high and low. The low and high levels of the factors were listed in the Table 2. These levels of the factors were determined by considering some preliminary experiments. The experiments were carried out two parallel and adsorption efficiencies (%) was determined as average of experiments. The order in which the experiments were made was randomized to avoid systematic errors. The results of experiments data were analyzed with the Minitab 16 software, and the main effects and interactions between factors were determined. The cubic diagram levels for high and low of three factors, pH, adsorbent dosage, and initial concentration, is given in Figure 2.

**Table 2:** Factors and levels used in the factorial design.

Factor	Coded Symbol	Low Level (-1)	High Level (+1)
pH	A	2.0	8.0
Adsorbent Dosage (g/L)	B	0.1	1.0
Initial Concentration (mg/L)	C	10	100



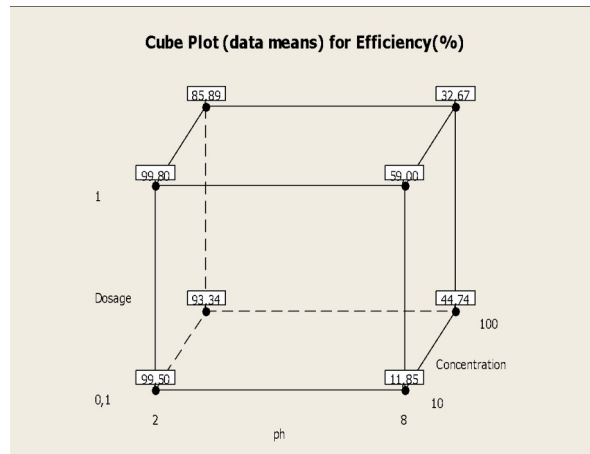


Figure 2: Cubic plots for efficiency (%).

RESULTS AND DISCUSSION

The SEM images of the MWCNTs and Ag(I) ions after adsorption were presented in Figure 3. The factorial design matrix and efficiency calculated in each factorial experiment is shown in Table 3, with the low (-1) and high (+1) levels as specified in Table 2. Figure 2 illustrates the mean of the experimental results for the respective low and high levels of pH, adsorbent dosage, and initial

concentration. Factors that influence the adsorbed quantity of Ag(I) ions adsorbed onto MWCNTs were evaluated by using factorial plots: main effect and interaction effect. The SEM images of MWCNTs/Ag(I) given in Figure 3 were taken under acidic conditions (pH 2). After adsorption, it was seen that Ag(I) uptake in macrostructure of MWCNTs. This heterogeneous structure is characteristic and contains plenty of micropores and cavities where adsorption of Ag(I) occurs.

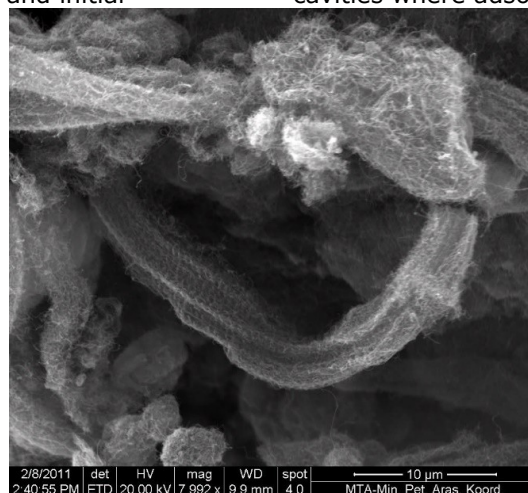


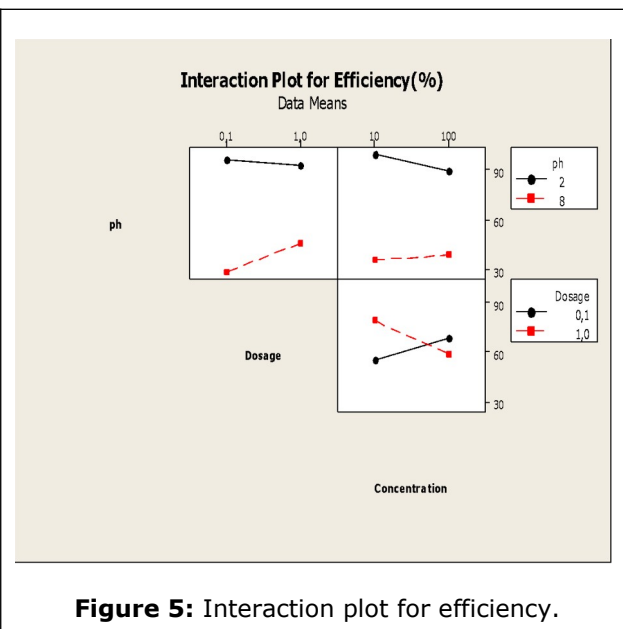
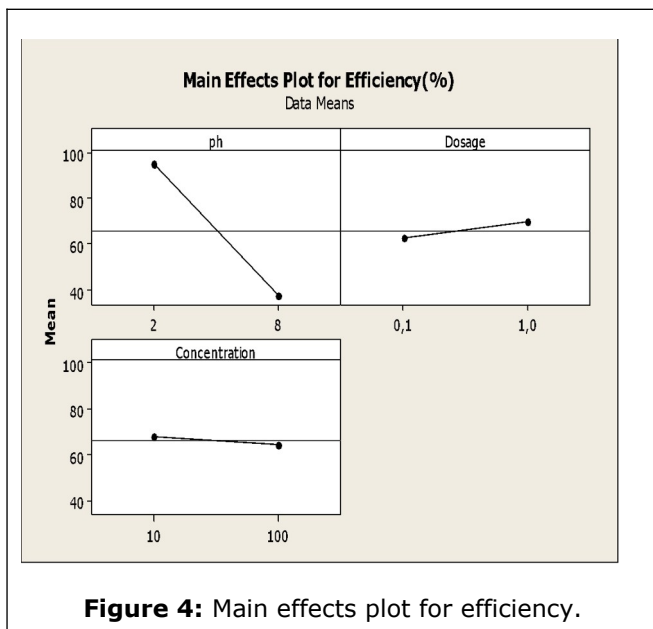
Figure 3: Scanning electron microscope (SEM) images of Multi-walled Carbon Nanotubes/Ag(I).

Table 3: Design matrix and the results of the 2<sup>3</sup> full factorial design.

Run No.	Factor			Efficiency (%)		Average
	A	B	C	Replicate		
				I	II	
1	-1	-1	-1	99.50	99.50	99.50
2	+1	-1	-1	11.90	11.80	11.85
3	-1	+1	-1	99.80	99.80	99.80
4	+1	+1	-1	59.60	58.40	59.00
5	-1	-1	+1	93.23	93.45	93.34
6	+1	-1	+1	44.80	44.68	44.74
7	-1	+1	+1	85.90	85.88	85.89
8	+1	+1	+1	32.70	32.64	32.67

The results of main effect and interaction effect were given as graphs in Figure 4 and 5. The main effects of each parameter on the silver adsorption are shown in Figure 4. The main effects plots were generated to represent the results of regression

analysis. It shows only the factors that were significant at the 95% confidence interval. The interaction effects of each parameter on the silver adsorption are shown in Figure 5.



The graphs of interaction effects explain the interaction effects between experimental parameters. According to the Figure 5, the strongest interaction is between adsorbent dosage and initial concentration. Because the lines are not parallel to each other, there is little interaction between pH and adsorbent dosage, and pH and initial concentration. But these interactions are not strong. Under acidic conditions, the Ag(I) uptake efficiency onto MWCNTs was found high due to favorable electrostatic interactions (23).

Significant levels of ANOVA and P-value were used to check the significance of the effect on % efficiency. The significance of the regression coefficients was determined by applying a Student's t-test. All effects were significant with 95% confidence level. The adequacy of model was evaluated in terms of the analysis of variance (ANOVA) (24). Coefficients of the model, standard deviation of each coefficient were presented for the full 2<sup>3</sup> factorial designs in Table 4. In addition, the model presented an adjusted square correlation coefficient R<sup>2</sup> (adj) of 99.98%, fitting the statistical model quite well. In this way, the Ag(I) ions uptake by MWCNTs could be expressed using the following equation:

$$R (\%) = 65.85 - 28.78 \times \text{pH} + 3.49 \text{ Dosage} - 1.69 \text{ Concentration} + 5.28 \text{ pH} \times \text{Dosage} + 3.3 \text{ pH} \times \text{Concentration} - 8.37 \text{ Dosage} \times \text{Concentration} - 6.43 \text{ pH} \times \text{Dosage} \times \text{Concentration}$$

Table 5 shows the sum of squares being used to estimate the factors effect and the *F*-ratios, which are defined as the ratio of respective mean-square-effect to the mean-square-error. The significance of these effects was evaluated using the t-test, and had a significance level of 5%; i.e., with a confidence level of 95%. The *R*-squared statistic indicated that the first-order model explained 99.99% of *R*'s variability to the rejection of null hypothesis, it appears that the main effect of each factor and the interaction effects were statistically significant: *P*<0.05. The results revealed that the studied factors (A, B and C), their 2-way interaction (AB, AC and BC) and 3-way interaction (ABC) were statistically significant to *R* (%).

It was found that experimental design approach can predict equilibrium adsorption behavior for MWCNT and Ag(I). The adsorption capacity determined from the 2<sup>3</sup> factorial design onto MWCNT was compared with uptake different heavy metal ions and results was given in the Table 6. The performance of MWCNTs for the removal of miscellaneous heavy metal has been demonstrated, and varying values of the adsorption efficiency (%) have been reported in the literature. In this work, Ag(I) uptake by MWCNT was the greatest with a maximum value of 0.998 mg/g, while maximum Ag(I) uptake capacity of MoS<sub>2</sub>/MWCNTs was 601.97 mg/g.

**Table 4:** Estimated Effects and Coefficients.

Estimated Effects and Coefficients for Efficiency(%) (coded units)						
Term	Effect	Coef	SE	Coef	T	P
Constant	65.85	0.07697	855.47	0.000		
pH	-57.57	-28.78	0.07697	-373.94	0.000	
Dosage	6.98	3.49	0.07697	45.36	0.000	
Concentration	-3.38	-1.69	0.07697	-21.94	0.000	
pH*Dosage	10.56	5.28	0.07697	68.58	0.000	
pH*Concentration	6.66	3.33	0.07697	43.25	0.000	
Dosage*Concentration	-16.74	-8.37	0.07697	-108.75	0.000	
pH*Dosage*Concentration	-12.87	-6.43	0.07697	-83.58	0.000	

S = 0,307896 PRESS = 3,0336

R-Sq = 100,00% R-Sq(pred) = 99,98% R-Sq(adj) = 99,99%

**Table 5:** Analysis of Variance.

Analysis of Variance for Efficiency(%) (coded units)									
Source	DF	Seq	SS	Adj	SS	Adj	MS	F	P
Main	Effects	3	13496.7	13496.7	4498.9	47456.82	0.000		
	pH	1	13256.1	13256.1	13256.1	139831.94	0.000		
	Dosage	1	195.0	195.0	195.0	2057.19	0.000		
	Concentration	1	45.6	45.6	45.6	481.33	0.000		
2-Way	Interactions	3	1744.4	1744.4	581.5	6133.54	0.000		
	pH*Dosage	1	445.8	445.8	445.8	4702.99	0.000		
	pH*Concentration	1	177.3	177.3	177.3	1870.14	0.000		
	Dosage*Concentration	1	1121.2	1121.2	1121.2	11827.48	0.000		
3-Way	Interactions	1	662.3	662.3	662.3	6986.18	0.000		
	pH*Dosage*Concentration	1	662.3	662.3	662.3	6986.18	0.000		
Residual	Error	8	0.8	0.8	0.1				
	Pure	Error	8	0.8	0.8	0.1			
Total	15		15904.1						

**Table 6:** Comparison of adsorption efficiency (%) for the adsorption of heavy metal ions by MWCNTs.

Adsorbent	Adsorbates	Adsorptivity (%)	References
MWCNTs	Ag <sup>1+</sup>	99.80	Recent study
MWCNTs	Cd <sup>2+</sup> ,	10.80	(25)
MWCNTs	Mn <sup>2+</sup>	4.80	(26)
MWCNTs	Ni <sup>2+</sup>	49.00	(27)
MWCNTs	Pb <sup>2+</sup>	97.06	(28)
MWCNTs	Co <sup>2+</sup>	2.77	(29)

**CONCLUSION**

The results of present study clearly show that MWCNTs is effective in adsorption of Ag(I) ions. Adsorption efficiency was achieved up to 99.50 and 11.80 (%) Ag(I) ions from aqueous solutions in 1 h contact with initial concentration 10 and 100 mg/L, respectively. The adsorption of Ag(I) onto MWCNTs was characterized by SEM analysis. The factorial design method was employed for estimating the optimum values of pH, adsorbent dose, and initial

metal ions concentration. The statistical model and ANOVA results determined that pH was the most efficient factor in the adsorption process. Then pH-adsorbent dosage interaction and pH-initial concentration interaction, were also found highly significant. When the results were examined, the highest efficiency was obtained at pH 2. In the first stage of research, it have been defined the most significant parameters, that influence adsorption process and was possible to make a first optimization of the process using a screening design

of the adsorption process. MWCNTs has a potential to be used as an effective adsorbent for uptake of Ag(I) ions from aqueous media. The MWCNTs/Ag(I) binary structure has been supported by experimental results, which has the potential to be used in many areas. One of the important results is that the MWCNTs/Ag couple obtained by adsorption can be suggested as a catalyst for different reactions. In addition, the high capacity of MWCNTs to hold Ag(I) ions gives hope that they can be used in the industry.

## REFERENCES

- Nuhoglu Y, Malkoc E. Thermodynamic and kinetic studies for environmentally friendly Ni(II) biosorption using waste pomace of olive oil factory. *Bioresour Technol* [Internet]. 2009;100(8):2375–80. Available from: <http://dx.doi.org/10.1016/j.biortech.2008.11.016>
- Desai KR, Murthy ZVP. Removal of silver from aqueous solutions by complexation-ultrafiltration using anionic polyacrylamide. *Chem Eng J* [Internet]. 2012;185–186:187–92. Available from: <http://dx.doi.org/10.1016/j.cej.2012.01.072>
- Shreya, Verma AK, Dash AK, Bhunia P, Dash RR. Removal of surfactants in greywater using low-cost natural adsorbents: A review. *Surfaces and Interfaces* [Internet]. 2021;27(October):101532. Available from: <https://doi.org/10.1016/j.surfin.2021.101532>
- Fu L, Zhang L, Wang S, Peng J, Zhang G. Selective adsorption of Ag<sup>+</sup> by silica nanoparticles modified with 3-Amino-5-mercapto-1,2,4-triazole from aqueous solutions. *J Mol Liq* [Internet]. 2017;241:292–300. Available from: <http://dx.doi.org/10.1016/j.molliq.2017.06.028>
- Pan XH, Fu LX, Wang H, Xue Y, Zu JH. Synthesis of novel sulfhydryl-functionalized chelating adsorbent and its application for selective adsorption of Ag(I) under high acid. *Sep Purif Technol* [Internet]. 2021;271(March):118778. Available from: <https://doi.org/10.1016/j.seppur.2021.118778>
- Ihsanullah, Abbas A, Al-Amer AM, Laoui T, Al-Marri MJ, Nasser MS, et al. Heavy metal removal from aqueous solution by advanced carbon nanotubes: Critical review of adsorption applications. *Sep Purif Technol* [Internet]. 2016;157:141–61. Available from: <http://dx.doi.org/10.1016/j.seppur.2015.11.039>
- Oliveira LS, Franca AS, Alves TM, Rocha SDF. Evaluation of untreated coffee husks as potential biosorbents for treatment of dye contaminated waters. *J Hazard Mater*. 2008;155(3):507–12.
- Bădescu IS, Bulgariu D, Ahmad I, Bulgariu L. Valorisation possibilities of exhausted biosorbents loaded with metal ions – A review. *J Environ Manage*. 2018;224(July):288–97.
- Ubando AT, Africa ADM, Maniquiz-Redillas MC, Culaba AB, Chen WH, Chang JS. Microalgal biosorption of heavy metals: A comprehensive bibliometric review. *J Hazard Mater* [Internet]. 2021;402(May 2020):123431. Available from:
- <https://doi.org/10.1016/j.jhazmat.2020.123431>
- Geyikçi F. Basic red-5 adsorption on montmorillonite: Factorial design, equilibrium, kinetic and thermodynamic studies. *Acta Geodyn Geomater*. 2020;17(3):269–83.
- Geyikçi F. Adsorption of acid blue 161 (AB 161) dye from water by multi-walled carbon nanotubes. *Fullerenes Nanotub Carbon Nanostructures*. 2013;21(7):579–93.
- Tofighy MA, Mohammadi T. Adsorption of divalent heavy metal ions from water using carbon nanotube sheets. *J Hazard Mater* [Internet]. 2011;185(1):140–7. Available from: <http://dx.doi.org/10.1016/j.jhazmat.2010.09.008>
- Stylianou AG, Faidra GT, Zoi MS, Paraskevas P, Nikolaos AD. Optimization of the carbon nanotubes reinforcement in cement-based materials. *Procedia Struct Integr* [Internet]. 2021;37(C):485–91. Available from: <https://doi.org/10.1016/j.prostr.2022.01.113>
- Li M, Liu D. Mechanical and electrical properties of graphite/ carbon fiber/phenolic resin composite. *Adv Mater Res*. 2012;418–420:1452–5.
- Geyikçi F, Büyükgüngör H. Factorial experimental design for adsorption silver ions from water onto montmorillonite. *Acta Geodyn Geomater*. 2013;10(3):363–70.
- Alzahrani HS, Al-Sulami AI, Alsulami QA, Rajeh A. A systematic study of structural, conductivity, linear, and nonlinear optical properties of PEO/PVA-MWCNTs/ZnO nanocomposites films for optoelectronic applications. *Opt Mater (Amst)* [Internet]. 2022;133(June):112900. Available from: <https://doi.org/10.1016/j.optmat.2022.112900>
- Ruan L, Zhu L, Zhang X, Zhou C, Ali Alasmay F, Luque R, et al. A highly efficient, selective and stable PtCoNi/MWCNTs nanocatalyst for furfural hydrogenation to furfuryl alcohol under mild reaction conditions. *Fuel* [Internet]. 2023;333(P1):126222. Available from: <https://doi.org/10.1016/j.fuel.2022.126222>
- Ye C, Gong QM, Lu FP, Liang J. Adsorption of uraemic toxins on carbon nanotubes. *Sep Purif Technol*. 2007;58(1):2–6.
- Ren X, Chen C, Nagatsu M, Wang X. Carbon nanotubes as adsorbents in environmental pollution management: A review. *Chem Eng J* [Internet]. 2011;170(2–3):395–410. Available from: <http://dx.doi.org/10.1016/j.cej.2010.08.045>
- Zhang X, Yuan N, Xu S, Li Y, Wang Q. Efficient adsorptive elimination of organic pollutants from aqueous solutions on ZIF-8/MWCNTs-COOH nanoadsorbents: Adsorption kinetics, isotherms, and thermodynamic study. *J Ind Eng Chem*. 2022;111:155–67.
- Kavak D. Removal of boron from aqueous solutions by batch adsorption on calcined alunite using experimental design. *J Hazard Mater*. 2009;163(1):308–14.
- de Lima LS, Araujo MDM, Quinária SP, Migliorine DW, Garcia JR. Adsorption modeling of Cr, Cd and Cu on

activated carbon of different origins by using fractional factorial design. Chem Eng J [Internet]. 2011;166(3):881–9. Available from: <http://dx.doi.org/10.1016/j.cej.2010.11.062>

23. Alimohammady M, Jahangiri M, Kiani F, Tahermansouri H. Competent Heavy Metal Adsorption by Modified MWCNTs and Optimization Process by Experimental Design. J Environ Eng. 2018;144(11):1–16.

24. Zhou Y, Li Y, Liu D, Liu D, Xu L, Liu C. Adsorption optimization of uranium(VI) onto polydopamine and sodium titanate co-functionalized MWCNTs using response surface methodology and a modeling approach. Colloids Surfaces A Physicochem Eng Asp. 2021;627(January).

25. Li YH, Ding J, Luan Z, Di Z, Zhu Y, Xu C, et al. Competitive adsorption of Pb<sup>2+</sup>, Cu<sup>2+</sup> and Cd<sup>2+</sup> ions from aqueous solutions by multiwalled carbon nanotubes. Carbon N Y. 2003;41(14):2787–92.

26. Liang P, Liu Y, Guo L, Zeng J, Lu H. Multiwalled

carbon nanotubes as solid-phase extraction adsorbent for the preconcentration of trace metal ions and their determination by inductively coupled plasma atomic emission spectrometry. J Anal At Spectrom. 2004;19(11):1489–92.

27. Yang S, Li J, Shao D, Hu J, Wang X. Adsorption of Ni(II) on oxidized multi-walled carbon nanotubes: Effect of contact time, pH, foreign ions and PAA. J Hazard Mater. 2009;166(1):109–16.

28. Wang HJ, Zhou AL, Peng F, Yu H, Chen LF. Adsorption characteristic of acidified carbon nanotubes for heavy metal Pb(II) in aqueous solution. Mater Sci Eng A. 2007;466(1–2):201–6.

29. Pyrzyńska K, Bystrzejewski M. Comparative study of heavy metal ions sorption onto activated carbon, carbon nanotubes, and carbon-encapsulated magnetic nanoparticles. Colloids Surfaces A Physicochem Eng Asp. 2010;362(1–3):102–9.